To My Mother

DECLARATION

I hereby declare that the matter embodied in the thesis entitled "**Some studies on vortices with density stratification**" is the result of investigations carried out by me at the Engineering Mechanics Unit, Jawaharlal Nehru Centre for Advanced Scientific Research, Bangalore, India under the supervision of **Prof. Rama Govindarajan** and that it has not been submitted elsewhere for the award of any degree or diploma.

In keeping with the general practice in reporting scientific observations, due acknowledgment has been made whenever the work described is based on the findings of other investigators.

Harish N Dixit

CERTIFICATE

I hereby certify that the matter embodied in this thesis entitled "**Some studies on vortices with density stratification**" has been carried out by **Mr. Harish N Dixit** at the Engineering Mechanics Unit, Jawaharlal Nehru Centre for Advanced Scientific Research, Bangalore, India under my supervision and that it has not been submitted elsewhere for the award of any degree or diploma.

Prof. Rama Govindarajan
(Research Supervisor)

Acknowledgments

This thesis would not have been possible without the support, encouragement, guidance and criticisms of many people.

I would first like to thank my parents and the rest of my family for keeping their faith in me. The decision to stay back in India for a PhD was a tough and lonely decision to make, and I thank all the people who believed in me. The work ethic of my mother in particular has been an inspiration for me all these years. I thank Appa for imbibing in me an ability to think and argue rationally and logically. My sisters and my brothers-in-law have all been amazingly supportive. And finally, I thank my wife Gomathi for not just being a great companion and friend, but also for sharing my work load, helping me with the thesis corrections and doing most of the chores at home during my final days here.

I thank Rama, my thesis advisor, for putting up with me all these years. She has been wonderful and kind to me, and I will always cherish my friendship with her. She has helped me in my work at various stages, gave me the freedom to explore many tangents along the way, and introduced me to the fascinating subject of hydrodynamic stability theory. I also thank her for being very generous with facilities in the lab and the department, especially the EMU library. This has helped all the students in the department immensely. I also thank her for proof-reading this thesis, correcting many errors, and suggesting possible applications of my work.

I thank Prof. Narasimha for many discussions which has always been very exciting. I first heard of JNC after reading one of his popular science articles. I thank Ganesh for teaching me boundary-layer theory and many other aspects of fluid mechanics. I have had many memorable scientific discussions with him which have brought a lot of clarity to my work. I also thank other faculty in EMU for raising questions during my presentations and poster sessions which has helped me improve my work. I especially thank Prof. Deshpande for providing me valuable computer time on his workstation. I thank Prof. O.N. Ramesh for the maths classes in his office and for general discussions and Prof. Sengupta for the GFD course.

I thank Andrew Gilbert, Univ. of Exeter who willingly agreed to write the Newton fellowship proposal with me. He was also very supportive of my decision to join Prof. Homsy for my post-doc. I also thank Professors Jacques Vanneste and Jean-Marc Chomaz for agreeing to referee our Newton fellowship proposal. I thank Prof. Sherwin Maslowe for discussions on waves and many other topics, and Prof. Jonathan Healey on instabilities in stratified shear flows.

I am immensely grateful to uncle BJ for nurturing in me a deep interest in science. Dada and Lalta aunty were always interested in listening to me about my work. I thank my teacher, Dr. Babu for being such a wonderful friend all these years, and for my early lessons in fluid mechanics. Special thanks to Prasad Perlekar who helped me greatly with my DNS code. I thank Sameen and Vinod for helping me in the early days, and Vinod's Linux interests were very helpful to many in the lab.

A very special thanks to Anubhab. He has been a teacher of sorts to me all these years. I have been lucky to have worked on a research problem which overlapped with Anubhab's interests, and this provided us with ample opportunity to discuss various aspects of stability theory, often benefiting my own research.

Ratul has been another special friend here, especially since we started our PhD journey together. He was always there to share the highs and the lows, and I developed an interest in western classical music talking to him. Discussions with Mukund, both technical and non-technical were always fun, especially on music. Sumesh shared my interests in evolutionary biology, and our bird-watching sessions were memorable. Working with Srikanth on a research problem different from my thesis has been a learning experience. I thank him for the collaboration. I thank Prof. Amitabh Joshi for allowing me to ask him all kinds of silly questions on evolutionary theory, and also for the books.

I thank the IISc (Phys. dept.) film society for screening some extraordinary films. I developed a deep appreciation to the art of film-making. I thank the complab, academic and adminstrative staff for making life very comfortable for the students. Special thanks to the administrative officer, Mr.Jayachandra, hostel staff members Mr. Suresh and Mr. Nagaraj for their help.

I thank my lab mates (past and present in no particular order): Anjana, Raji, Vijay, Rajaram, Debu, Pinaki, Kaushik, Kirti, Ashish, Rajapandiyan, Aditya, Vivek N P, Bale, Gayathri, Ponnu, Shastry, Vivekanand, Rakshith, Priyanka, Dhiraj, Saurabh, Saikishan, etc. for making the lab a fun place to work. I thank my dear friends Chintu, Teju and Naveen for pestering me with conference calls, and Josena, Datta, Urmi, Venky, Claudy, Rinki, Paaty and many others for keeping the mood upbeat.

And finally, I thank my music teachers, Mani sir and Ramamani Mam for their love, and of course the music. I also thank my music colleagues, Nagaraj sir, Karthik, Rangarajan sir, Sampath sir, Raghu, Ramesh sir and many others for the practice sessions. The Sunday practice sessions with Mani sir was always a very satisfying experience.

Thanks to all my relatives here in Bangalore, it became a second home to me. I especially thank uncle Jayaram, Uma aunty, cousins Aparni, Vinay, Shashi and Gopi for being there for me.

Abstract

The effects of density stratification on the stability and evolution of vortices is investigated. Baroclinic vorticity generated due to density inhomogeneities can have important implications for the behaviour of vortices. In atmospheres and oceans, due to strong effects of density stratification and rotation, the flow can be considered to be in a quasi two-dimensional state. Typically, large scale vortical structures are accompanied by an inverse cascade of energy owing to the two-dimensional nature of the flow field. In these situations, density stratification occurs along the vortex axis. We have analysed the effect of density variations on a single vortex, and then considered the interaction of two such vortices in a general stratified medium. A combination of linear stability analysis and direct numerical simulation of the nonlinear Navier-Stokes equations have been carried out. When density variations occur in the plane of the vortex, it is shown in this thesis that small scale instabilities arise in the flow resulting in a strong direct cascade of energy. Such variations occur in a variety of situations, example in aircraft trailing vortices in a stratified medium, in cyclones/hurricanes travelling across regions of strong density gradients as would be encountered when we move in meridional directions or across the ocean-land interface, and also in polar vortices. In all the single vortex instabilities, gravity is completely neglected, and density effects arise from the inertial terms in the governing equations. The results are also valid for sharp density interfaces in the presence of weak gravity.

We begin with the linear stability of the classical piece-wise continuous mixing layer profile. Though a great deal of work has been undertaken using the 'Rayleigh' method in normal mode analysis, often, the physical mechanisms of these instabilities is not made clear. An exception is the kinematic mechanism for the instability of a vortex sheet dealt with by Batchelor in his classic text. A similar understanding in more general barotropic and baroclinic instabilities is still lacking. The linear wave interaction mechanism attempts to fill this gap in our understanding. We solve an initial value problem analytically to obtain further insight into the instability mechanism. Specifically, the temporal evolution of the initial disturbance into a normal mode is analysed. We then extend these ideas to the stability of a simple stratified shear flow problem with two interfaces, one with a vorticity jump and the other with a density jump. The phase relationship between the waves at these interfaces is explicitly calculated.

We extend the above analysis to a cylindrical geometry. The problem we investigate is the stability of a vortex with radial density distribution. Baroclinic vorticity is generated in this geometry due to the presence of centrifugal forces. A heavy-cored vortex, where density decreases monotonically away from the vortex axis is a potentially unstable configuration. Similarly, a light-cored vortex is expected to be stable due to the stabilizing effect of a centrifugal buoyancy force. But it is shown that even a light-cored vortex

can be unstable, contrary to common intuition. The entire range of vortex profiles of smoothness varying from a Rankine vortex to a Gaussian vortex with analogous density profiles are studied. This is carried out by defining a single parameter family of vorticity and density profiles, all having the same circulation. In the case of a Rankine vortex with a step density jump, we again interpret instabilties in terms of wave-interactions between Kelvin modes of the vortex and internal waves due to density jump. For smooth profiles which do not possess discrete Kelvin modes, we resort to the ideas of quasi-modes. Quasi-modes are exponentially decaying eigenmodes of the inviscid stability problem with a *wave-like* response, and are a manifestation of a peculiar cooperative effect of the continuous spectrum modes localized at the critical layer. It is suggested in this thesis that quasi-modes of the vortex interact with internal waves leading to a linearly unstable flow. A detailed analysis of quasi-modes of all the vortex profiles is carried out.

Having analysed the effect of a circular density interface, we then study the effect of a flat density interface in the neighbourhood of a vortex. Due to differential rotation outside the vortex core, the density interface winds itself into a spiral. Baroclinic vorticity in the form of a vortex sheet accumulates at this spiral interface. Using a simple model, we predict that the vortex sheet strength increases logarithmically in time, and this results in a faster-than-exponential instability of this sheet, typically of the form $t^{\sigma t}$ where σ is a suitable growth rate. We identify two instabilties in this problem, the spiral Kelvin-Helmholtz (SKH) instability of the vortex sheet and a centrifugal Rayleigh-Taylor (CRT) instability of the density interface. Inviscid and viscous stability analysis of suitable model velocity profiles are carried out, which is in good agreement with direct numerical simulations. These instabilities eventually amplify at the edge of the vortex, and lead to significant generation of small scales. The primary vortex is destroyed in this process and a final turbulence-like state ensues. Gravity further enhances the instability, and direct numerical simulations are carried out to corroborate this.

Using direct numerical simulations, we then extend the above results to understand the interaction of two co-rotating vortices in a linearly stratified fluid. Merger of two equal co-rotating vortices in a homogenous fluid is a well studied problem, and the merger process is attributed to the distortion of the vortex cores, and subsequent generation of vorticity filaments. But in a stratified fluid, organised sheet-like structures as well as additional filamentary debris are created due to a baroclinic torque. It is shown that the rate of merger crucially depends on the Reynolds and Froude number used. At high levels of stratification, the two vortices may repel each other, and merger can be prevented. Within the Boussinesq approximation, the centroid of vorticity is invariant during the evolution process. The merger process is associated with each vortex describing a spiral orbit, and the resultant merged vortex is formed at the vorticity centroid of the system. Inclusion of the full non-Boussinesq effects disrupts this symmetry, and the two vortices are shown to describe helical paths.

Some preliminary investigations were also carried out in three dimensional flows. The full 3D dispersion relation for a Rankine vortex with step density jump are obtained. In 3D, a Rankine vortex supports an infinite number of Kelvin modes, and therefore the possibilities of wave-interactions with internal waves is significantly enhanced. A detailed analysis of the dispersion relation is beyond the scope of this thesis.

Publications

Journal

1. "Vortex-induced instabilities and accelerated collapse due to inertial effects of density stratification", Harish N Dixit and Rama Govindarajan, *J. Fluid Mech.*, 646, 2010, 415–439. *Appeared on the cover of J. Fluid. Mech.*

2. "Stability of a vortex in radial density stratification: role of wave interactions", Harish N Dixit and Rama Govindarajan. *Submitted to J. Fluid Mech..*

3. "Vortex merger in a density stratified fluid: Boussinesq and non-Boussinesq effects", Harish N Dixit and Rama Govindarajan. *Under preparation.*

Proceedings

1. "Shedding behaviour in flow past an inline oscillating square cylinder", T. Srikanth, Harish N Dixit and Rama Govindarajan, *presented at the IUTAM symposium on Bluff Body Wakes and Vortex Induced Vibrations*, Capri Island, Italy, June 22 - 25 2010.

2. "Instabilities due a vortex at a density interface : Gravitational and Centrifugal Effects", Harish N Dixit and Rama Govindarajan, *Proc. of the 7th IUTAM symposium on Laminar Turbulent Transition*, Stockholm, Sweden, June 23 - 26, 2009.

3. "Vortices and the effects of atmospheric density stratification", Harish N Dixit and Rama Govindarajan, *Proc. of ICEAE, IISc Centenary Conference*, Bangalore, India, May 18 - 22, 2009.

4. "Flow past a rectangular cylinder in a stratified fluid", Harish N Dixit, A. Sameen and Rama Govindarajan, *Proc. of Sixth Intl. Symposium on Stratified Flows, Perth, Australia (Ed: G.N Ivey,) pp 189-194*, December, 2006.

List of Figures

List of Tables

Contents

CHAPTER 1

GENERAL INTRODUCTION

The main subject of this thesis is the effect of density stratification on the structure and stability of vortices. Idealized problems are studied, and the analysis is restricted for the most part to two-dimensions. Though the contents of this thesis are not aimed at specific applications, it is useful to understand realistic situations where the results obtained here might be applicable. We therefore give a brief overview of a wide class of problems where an interplay between density stratification and vortex dynamics takes place. We first begin with a discussion on some geophysical flows. Detailed discussions on literature directly related to the present work are included at the beginning of each chapter.

The atmosphere and ocean are subject to two main forces: (i) coriolis force due to rotation of the planet, and (ii) density variations due to effects of gravity. These two features makes the study of these systems both interesting and intruiging. By and large, the two effects are studied independently as they are complicated enough to warrant a detailed study. The classic text of Greenspan (1968) is devoted to a detailed study of rotating fluids. Similarly, the classic texts of Turner (1973) and Yih (1973) focus on buoyancy effects due to density and temperature stratifications. In geophysical fluid dynamics literature, these two effects appear together, i.e. the influence of planetary rotation or the appearance of a rotating fluids like cyclones, and density stratification along the vertical. Meridional variations of density also arise due to temperature differences across latitudes. One such example is the formation of a *polar vortex* during winter, with density radially decreasing away from the vortex core as shown in figure 1.1. The left and right panels show the temperature contours and satellite image of tropospheric clouds over Antartica. Virtually any vortex that is in motion in the atmosphere encounters these variations. The study of such vortices is important to understand their impact on climate and pollutant dispersion. Another feature of these vortices is the sharp vorticity gradient at their edges. It has been known that the edge of the polar vortex is very steep, and vorticity inside this region rapidly homogenizes, reaching constant values which are 2 or more times greater that the surroundings (Vallis (2006), page 575). This suggests that models employing piece-wise discontinuous vorticity profiles like a Rankine vortex might be a good starting point.

Such vortices are susceptical to what is known as a 'baroclinic instability' process. In fig.(1.2), we present a schematic showing the evolution of a cold mass of fluid on a non-rotating and a rotating planet. This schematic is adapted from Nadiga & Aurnou (2008), an excellent expository article on baroclinic instability. We discuss this phenomenon in brief here and encourage the reader to view the original article for more details. In the absence of planetary rotation, the cold (heavier) mass of air settles down due to gravity as shown in the left panels. But when the same mass of air is on a rotating planet, it experiences a coriolis force, $\mathbf{F_{cor}} = -2\boldsymbol{\Omega} \times \mathbf{u}$, where $\boldsymbol{\Omega}$ is the planet's angular velocity and $\mathbf{u}$ is the velocity of fluid. This force deflects fluid parcels to the right of

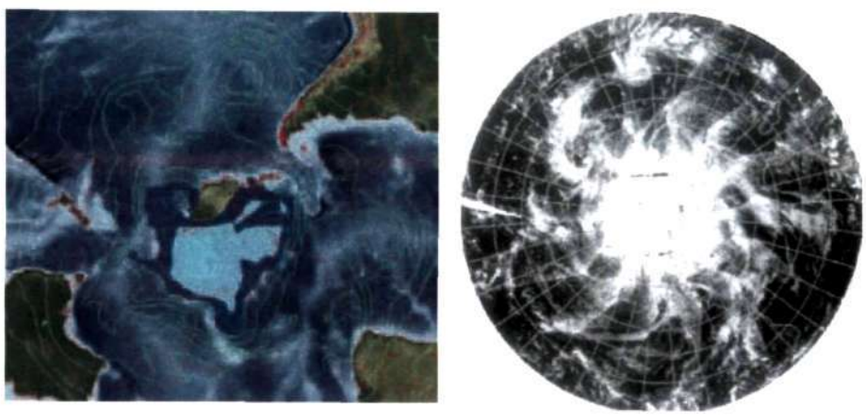

Figure 1.1: (a) The distribution of temperature in the southern-hemisphere atmosphere in winter at midlevel in the troposphere (temperature in degrees Celsius on the 500 millibar pressure surface at 1200 GMT on 25 August 2008. A cold air mass is shown in blue and light blue, centered over Antarctica. The surrounding temperature field is shown via light green line contours. Because of rotation, the cold Antarctic air mass does not simply respond to gravity by settling and flowing outwards and below warmer lower latitude air. Instead, rotational effects give rise to an azimuthal "thermal wind flow" that circulates around the cold air mass. The thermal wind can, however, become unstable and develop meanders (visible in green line contours). (b) NASA image showing tropospheric clouds over Antarctica that trace out a pattern of meanders that are qualitatively similar to those in (a). Source: Nadiga & Aurnou (2008)

their motion. The net effect of coriolis force is that gravitational settling can now be arrested reaching a 'thermal wind' balance (Vallis (2006)). But this balanced condition is usually unstable to perturbations in the zonal direction leading to what is referred to as baroclinic instability (see Pedlosky (1987); Vallis (2006)), which makes the cold air leave the central core forming spiral eddies. This results in significant mixing in the horizontal direction. Laboratory experiments have been carried out by Saunders (1973) by creating density variation in the radial direction using salt-water and fresh-water, initially separated by a cylindrical diaphragm. The whole apparatus is set in circular motion to replicate the rotation of the planet. Upon attaining a solid-body rotation, the diaphragm is removed. This creates a configuration very similar to that shown in fig.(1.2). He noticed that the primary vortex disintegrated into smaller parts. A series of similar experiments spanning two decades were also carried out by Hide in an annular apparatus. Water was used in his experiments and horizonal temperature differences were created across the annulus and the apparatus was set into a solid-body rotation (see Hide (1953, 1957, 1967, 1977)). The motivation for these experiments were not only in the general circulation of the atmosphere, but also in understanding the origin of earth's magnetic field from the motion of its liquid core. Hide noticed that the nature of the flow depended on a non-dimensional parameter characterising the strength of gravitational

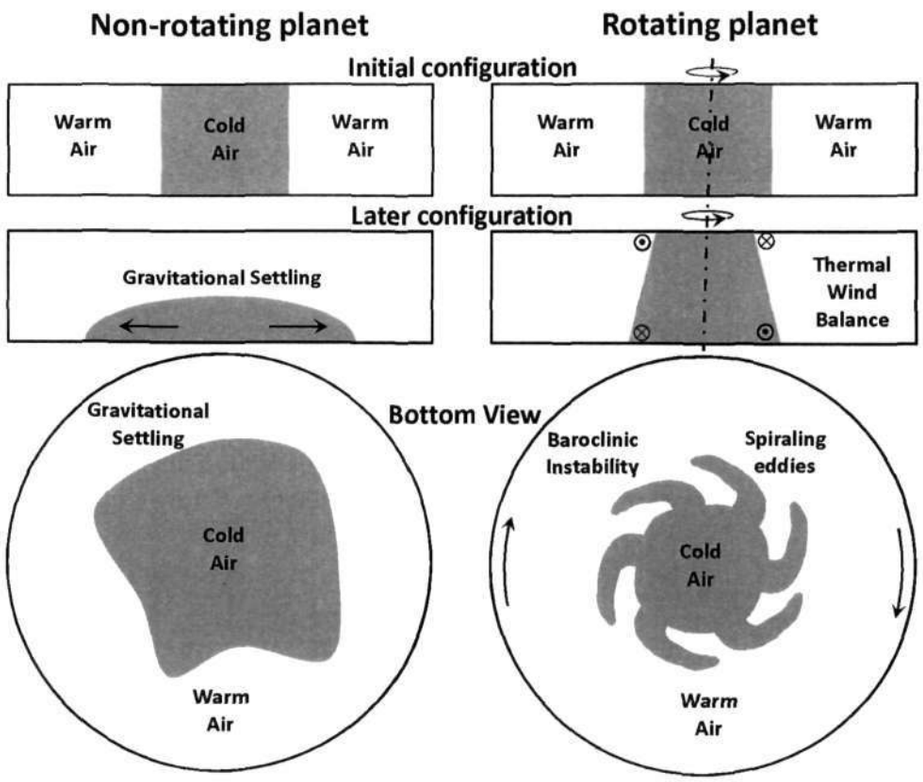

Figure 1.2: Schematic showing the settling of a dome of cold air on a rotating and non-rotating planet. Time increases down the page.

force to centrifugal force:

$$\Theta = \frac{2gd}{\Omega^2(b-a)^2}\left[\frac{\rho(T_a)-\rho(T_b)}{\rho(T_a)+\rho(T_b)}\right], \tag{1.1}$$

where $\rho(T)$ is the density of the water at temperature T, b and a is the radius of outer and inner cylinders respectively. He further noted that when Θ fell below a critical value, $\Theta_{crit} \approx 1.58$, the motion was predominanly in the horizontal direction. Wave-like motions were noticed in the azimuthal direction, and the wave-number decreased with decreasing Θ. The above points suggest that for a rapidly rotating system, the motion is predominantly two-dimensional in nature, dominated by effects of centrifugal force. Moreover, most of these earlier works were carried out with a fixed angular velocity, where shear effects are completely absent. For an arbitrary distribution of angular velocity where shear effects cannot be ignored, the role of stratification becomes non-trivial. In studies concerning planar geometry, it is well known that an unbounded couette flow,

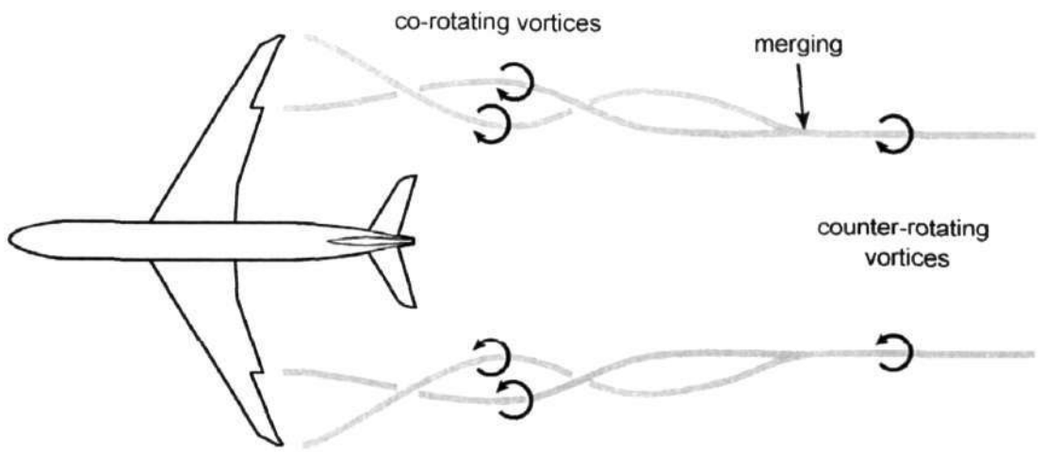

Figure 1.3: Aircraft trailing vortices when the aircraft is in a high-lift configuration (flaps deflected, and flow is from left to right). The scale in the horizontal direction is compressed by a factor of 5 to 10. Source: Meunier *et al.* (2005)

growth rates of Rayleigh-Taylor instability are not altered. But, on considering a region of varying shear, like in a Holmboe geometry (see Holmboe (1966)), Rayleigh-Taylor instability can be stabilized in a suitable parameter range. In plasma physics literature, it was shown recently (Sen & Storer (1997), Sen *et al.* (1998)) that flow curvature, i.e. variation of shear, can stabilize instabilities including the Rayleigh-Taylor instability. This point will be discussed in greater detail later in the thesis, first with a simpler planar geometry. Subsequently, we explore stabilization and destabilization in the more complicated vortex geometry with radial density stratification. In this thesis, no rotation of the entire system is imposed.

In this thesis, simple models of the two situations described above are studied, namely a vortex in a radial density stratification and a vortex at a linear density interface. The study will also be of relevance to situations including counter-rotating vortex pairs and can be extend to those. While this extension is not carried out in this thesis, the application is described briefly below. A vortex at a flat density interface could be relevant in understanding the impact of horizontal/latitudinal/meridional temperature (density) gradients on motion and weakening of tropical cyclones. The role of latitudinal temperature gradients to climate change has been discussed in Rind (1998), and its role in eddy transport has been discussed in Loon (1979). It is possible that sharp changes in horinzontal temperature gradients could also have an important role in the physics of tropical cyclones (see Chan (2005).

An important application of vortex stability studies is the problem of aircraft trailing vortices. In the context of vortex stability, it can be roughly said that this field began with the pioneering work of Lord Kelvin (see Kelvin (1867, 1880)) in his quest for a vortex theory of atoms. His theory of atoms was a failure, but was the starting point for hydrodynamic stability of vortices. In the last four decades, there has been a resurgence in vortex stability studies, and recent reviews of the topic can be found in Ash & Khorrami

(1995), Rossi (2000) and Jacquin *et al.* (2003). A schematic view of the trailing vortex configuration is shown in fig.(1.3). The mechanics of generation of these vortices, well described in standard texts (see Anderson (2001); von Kármán (1954)) involves the roll-up of a vortex sheet into a dipole. Moore & Saffman (1973) showed that this process obeys a self-similar evolution in the absence of density variations. Near the centre of the spiral, viscous effects become important, resulting in the formation of a circular vortex core. Three dimensional stability analysis of these vorticex pairs has received a great deal of attention. The pioneering work of Crow (1970) showed, for a dipole, the presence of a long wavelength instability, in the form of bending waves along the vortex axis. This result is now eponymously known as Crow instability. This result generated a huge interest in the aircraft industry and a conference titled Aircraft Wake Turbulence in 1971 to discuss the implications of this instability. Extensions of Crow's result were soon found in the short wave length limit by Moore & Saffman (1975) and Tsai & Widnall (1976). Generalization of this result were obtained by Bayly (1986); Pierrehumbert (1986); Waleffe (1990) who showed that any elliptical flow in a straining field is susceptical to a short-wavelength axial instability (see Kerswell (2002) for more details). Apart from the hazards posed by trailing vortices for other aircrafts, there has been efforts to understand the impact of aircraft contrails on the environment.

In high-lift configurations, two additional vortices of opposite sign also emanate as shown in figure (1.3). These additional vortices merge with their neighbours to form a single dipole system. The problem of merger of two co-rotating vortices has attracted a great deal of attention since the 1980's. This problem is especially relevant in understanding the process of inverse cascade of energy in two-dimensional turbulence. Saffman & Szeto (1980), Meunier *et al.* (2002) and others showed that merger of two inviscid vortex patches always occurs if the vortex size exceeds a certain critical fraction of the separation distance between them. Statistical models of two dimensional turbulence have often involved emperical estimates for this critical fraction (see Carnevale *et al.* (1991)).

One of the primary interests of this work is the influence of stratification on vortices. Scorer & Davenport (1970) were the first to address the problem of descent of a vortex pair in a stratified atmosphere, and their model predicted an accelerated descent of the vortex pair. As the vortices more downwards, baroclinic vorticity is generated along the streamline separating the two vortices from rest of the ambient fluid. Their model predicts that the vortex separation distance R decreases with time as

$$R = R_1/\cosh(At), \tag{1.2}$$

and therefore the descent velocity increases as

$$W = W_1 \cosh(At). \tag{1.3}$$

The exponential acceleration of the vortices was confirmed by Crow (1974) for weak stratifications. But the assumption of constant circulation has been questioned by Tsang (1971) using laboratory experiments. Saffman (1972) was also very critical of this assumption. Using a model where the distance betwen the vortices was kept constant and circulation was allowed to vary, Saffman arrived at a completely different prediction, that

the descent height oscillates with a time period $2\pi/N$ as

$$H = H_0 \sin(Nt), \tag{1.4}$$

where N is the Brunt-Vaisala frequency. Narain & Uberoi (1974) attemped to model entrainment of the ambient field and showed that trailing vortices first decelerate and come to rest, and then are accelerated upwards. Accurate experiments were carried out by Sarpkaya (1983) to test the above theoretical predictions, but his experiments had the drawback that they were carried out with low aspect ratio wings making the flow three dimensional. Oscillations of wake height as predicted by Saffman were not seen. The wake velocity was shown to decrease with time, in variance with the predictions of Scorer & Davenport (1970) and Crow (1974). The experimental results are similar to the predictions of Narain & Uberoi (1974), but that comparison was unfortunately not made by Sarpkaya. We skip a discussion on the early numerical calculations of Hill (1974) and Hecht *et al.* (1981) and focus on the detailed two-dimensional calculations of Spalart (1996). As in the theoretical analysis, he considers a pair of compact vortices in a linear density stratification. He finds good agreement with Sarpkaya's experiments at short time for the descent height of the vortices. In other words, he does not find good agreement with either Scorer & Davenport (1970), Crow (1974) or Saffman's theories.

This discussion puts the present work in a better perspective. The thesis is divided into the following chapters. In chapter 2, we consider a simple planar geometry to understand instabilities in stratified shear flows. We begin by considering a piece-wise continuous velocity profile which supports a Rossby wave at the vorticity jump location. Similarly, a discontinuous density profile supports neutral waves for stable stratification, and growing waves for unstable stratification. But, when the two profiles are juxtaposed, it will be shown that a combined vorticity-density jump problem supports unstable waves even when the flow is stably stratified. The instability can be shown to be due to the interaction of neutral modes of the two interfaces considered separately.

In chapter 3, we extend the analysis of chapter 2 to a circular geometry, i.e. an axisymmetric vortex with an axisymmetric density distribution. It is shown that a light-cored vortex can be unstable in spite of the 'stable stratification' of density. Using a model flow consisting of step jumps in vorticity and density, we show that a wave-interaction mediated by shear is the mechanism for the instability. Exact dispersion relations are obtained in this case. The physical mechanism involved in the instability process is examined in detail. We then extend the analysis to a smooth vortex and density profile where the instability is described as an interaction of 'quasi-modes' of the vortex profile and internal waves of the density profile. A detailed analysis is carried out for a wide range of vortices, from a Rankine vortex to a Gaussian vortex. Gravity is completely neglected in the analysis to emphasise the role of centrifugal force. The unstable stratification case, where density decreases radially away from the vortex axis is similar to the polar vortex problem discussed earlier. The phenomena of 'critical layer absorption' discovered by Booker & Bretherton (1967) in a planar stratified shear flow is shown to occur even for a light-cored vortex. Full numerical simulations of Navier-Stokes equations are finally presented to reveal the existance of stable non-linear non-axisymmetric structures in the flow.

The equations derived for a Rankine vortex with step-density jump in the previous chapter are extended to 3D in chapter 4. Because a 3D vortex supports many Kelvin modes, unlike the 2D vortex, it is of great interest to understand the role of wave-interactions. The 3D dispersion relation is derived in here, but a full analysis of this relation is beyond the scope of the thesis. It is shown that the derived relation reduces to the well-known 3D dispersion relation of a homogeneous Rankine vortex.

In chapter 5, we return to 2D and consider the evolution of a flat density interface in the neighbourhood of a vortex. This geometry is an idealised version of a vortex in a meridionally stratified atmosphere. The interface winds into a tight spiral leading to certain instabilities. A simplified model is constructed elucidating the essential physics in the problem. Inviscid and viscous stability analysis are also carried out to obtain growth rates of these instabilities. Direct numerical simulations are then carried which corroborate reasonably well with the model predictions.

The analysis of chapters 3 and 5 is now extended to a more complicated problem of interaction of two identical vortices in a stratified environment in chapter 6. When two vortices having the same sense of rotation are placed close to each other, they merge to form a single vortex. But when placed in a stratified environment, additional vorticity is generated due to the baroclinic effects of density. The position and intensity of this additional vorticity in space and time now dictates the evolution of the merger process. The problem is studied with the Boussinesq approximation, and also without it. For weak stratifications under Boussinesq approximations the presense of certain symmetries will be discussed. In certain cases, it is found that merger process accelerates, and in a few other cases, merger is completely prevented. Considering the effect of full non-Boussinesq effects in the flow, non-symmetric flow patterns were found. This work is still in progress and some of the existing results will be discussed.

In chapter 7, we make some concluding remarks. Some directions for future work are also offered. The extensions of the present work into three-dimensional flows, both for stability analysis and direct numerical simulations are discussed.

Note: Variables are separately defined in each chapter and do not get carried over, unless specified.

CHAPTER 2

INSTABILITY IN A STRATIFIED SHEAR FLOW

Scope of this chapter

The aim of this chapter is to gain a clear understanding of the linear wave-interaction mechanism. Our main interest is to understand the interaction between a Rossby wave and a surface-gravity wave. The ideas of wave-energy are introduced, which serve as a powerful yet simple means to understand the outcome of the interaction. Simplified model profiles are discussed here, which will then be used to discuss the more complicated vortex problem to be discussed in the next chapter.

2.1 Linear Wave Interaction

Throughout this thesis, our attention is restricted to wave phenomena which can be described by linear theory. Before we proceed, it is helpful to clarify the definition of waves and 'discrete modes'. This will be helpful in later chapters when we introduce the ideas of 'continuum modes' and 'quasi-modes'. Waves are well-defined physical manifestations in a flow, and for the simplest forms in which we are interested in, they possess a well-defined wave-length, λ and a phase-speed, c. The phase speed in general can depend on the wave-length (dispersive waves), and the relationship characterizing this dependence is called the dispersion relation, given by

$$\mathcal{D}(\omega, k) = 0. \tag{2.1}$$

The above equality gives us the dependence of frequency, $\omega = kc$ on the wavenumber, $k = 2\pi/\lambda$. Only for simple geometries, can this relationship be calculated analytically. In inviscid unstratified flows, if the velocity profile does not possess a vorticity extremum, i.e. it is non-inflectional, then according to Rayleigh's inflection point theorem (see Drazin & Reid (1981)), the flow is stable to infinitesimal perturbations. Even if the profile has an inflection point, the physical mechanism leading to instability is usually not clear. A simple kinematic mechanism explaining instability of a vortex sheet was known for a long time (see Batchelor (1980)), but an equivalent explanation for broad (piece-wise continuous) profiles has become clear only recently. One way of understanding instabilities in shear flows is to view it as a linear wave-interaction of two free waves.

Taylor (1931) was among the first to note that two free waves can interact and give rise to an instability. He further observed that 'stable' density stratification can give rise to instabilities in a three layer fluid model. But, a clear physical understanding of this process was lacking at his time, as can be remarked from his statement: *'It is curious that the effect of stratification in density gives rise to unstable waves for certain velocities when the same waves in a homogeneous fluid would be stable'*. The first detailed study of wave-interactions was carried out by Hoskins *et al.* (1985), who showed that for a homogeneous

shear layer with two vorticity interfaces, instability is due to a linear wave-interaction of counter-propagating Rossby waves riding at these interfaces. An exhaustive survey of stratified shear flow instabilities with broken-line profiles is given in Howard & Maslowe (1973). But at the time of that survey, a kinematic understanding of the instability process in terms of wave interactions was not clear. The wave-interaction mechanism was extended to stratified shear flows by Baines & Mitsudera (1994) and Harnik *et al.* (2008). The focus of Baines & Mitsudera (1994) was still the homogeneous problem, whereas in Harnik *et al.* (2008), the vorticity and density jump locations coincide. We will first review the wave-interaction mechanism in detail for a homogeneous flow. Additionally, we solve an initial value problem to follow the short time evolution of the disturbance.

2.1.1 Rayleigh equation

We consider the stability of small amplitude two-dimensional perturbations to an inviscid shear flow. The flow is in the x-direction, and the base-flow velocity $U(y)$ is purely a function of the vertical coordinate y. We use Cartesian (x, y) coordinates, with the corresponding velocity perturbation components (u, v). The two common approaches of solving the linearized stability equations are to either use a normal-mode form of solution, or solve an initial value problem (IVP). We will do the former here, and discuss the IVP treatment later in this section. We assume solutions of the form

$$q = \mathrm{Re}\left[Q(y)e^{i(kx-\omega t)}\right], \tag{2.2}$$

where q represents any flow quantity and Re represents the real-part. Here y is the direction along which mean flow quantities are allowed to vary, x is the homogeneous direction. The above form of the solution is just a mode from the Fourier decomposition. A single equation for the vertical perturbation velocity for an incompressible, inviscid homogeneous flow can be derived, and is the well known Rayleigh's equation (see Drazin & Reid (1981), Schmid & Henningson (2001)).

$$(U - c)\left(D^2 - k^2\right)v - U''v = 0, \tag{2.3}$$

with boundary conditions

$$v \to 0 \qquad \text{as} \qquad y \to \pm\infty. \tag{2.4}$$

Here the D and prime denote differentiation with respect to y and are used interchangeably. The streamfunction, ψ is related to the vertical velocity using the relation

$$v = \partial\psi/\partial x = ik\psi. \tag{2.5}$$

Discrete modes are just regular wave-like solutions of the linear governing equations. A simple example is the waves on a string, which supports a countably-infinite set of discrete modes. In reality, a multitude of waves can be found in nature, which can be both linear and non-linear (Whitham (1974)). All wave phenomena are associated with a restoring mechanism in the system. It is useful to define various classes of waves depending on the restoring mechanism present in the system. For example, presence of

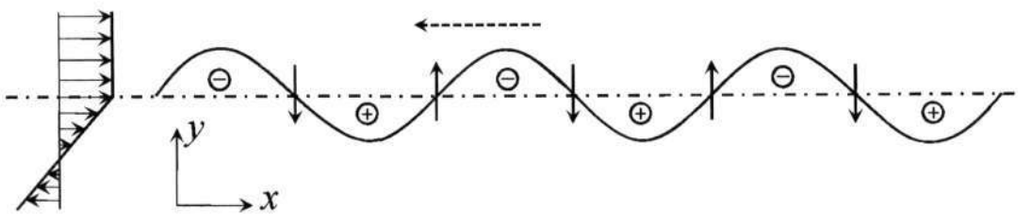

Figure 2.1: Vorticity jump profile (left panel), and the Rossby-wave mechanism shown in the right panel. The vertical arrows indicate the maximum vertical velocity, and the dashed horizontal arrow indicates the direction of propagation of the wave.

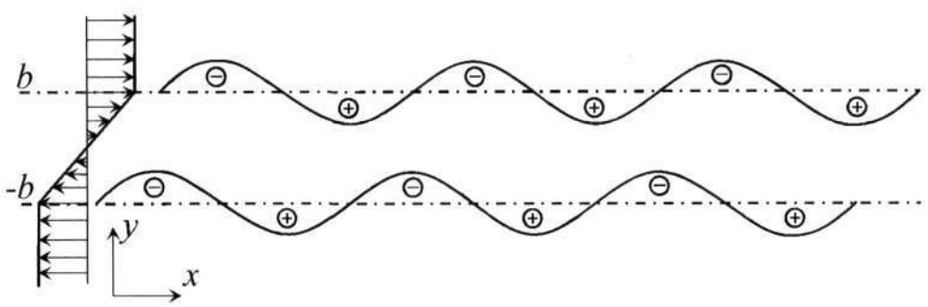

Figure 2.2: A mixing layer profile with a normal mode solution.

a vorticity gradient in the system supports what is called as a 'vorticity' or a 'Rossby' wave. In geophysical flows, vorticity is suitably replaced by isopynic potential vorticity. Similarly, discontinuities in density support a 'surface' wave. Water ripples is a common example. When density varies continuously in the system, surface waves are replaced by 'internal gravity' waves. Throughout this thesis we use the term internal gravity wave (IGW) even when referring to a surface wave. This minimizes confusion when we consider smooth density profiles later in the thesis.

Before we discuss the problem of wave-interaction between an internal gravity wave and a Rossby wave in the next section, we first consider the simpler problem of interaction between two Rossby waves. We follow the discussion of McIntyre (Rossby-wave propagation and shear instability, GEFD Summer school, Cambridge) and Hoskins *et al.* (1985) closely. Additionally we solve an IVP to clarify the physical mechanism. Consider a vorticity jump at some arbitrary location which supports a discrete neutral wave. The interface is a material line which may be perturbed to a wave-like form as shown in figure (2.1).

Since vorticity above the interface is zero, and below the interface is negative, the perturbation causes a positive vorticity anomaly, q' below the interface, and negative anomaly above it. These are shown by encircled signs. It has to be noted that the interface is a material contour. The vertical arrows show the direction of induced velocity field obtained from the q' field. The vertical velocity pattern is offset a quarter-wavelength from the interface displacement position. As time progresses, the disturbance u and

v causes the undulations to move to the left with respect to the local base flow at the interface without change of shape and amplitude. The neutrality condition is in accordance with the Rayleigh stability criterion which states that a necessary condition for instability in an inviscid fluid is that the sign of U'' change sign at some y. Thus, the present geometry supports a neutral Rossby wave moving to the left as shown by the dashed arrow. A key point is to be noted here. The disturbance velocity field, which is in quadrature with the interface displacement, cannot make the interface grow by itself. For growth of the wave, an external disturbance field needs to be provided. The simplest way to do this would be to place another vorticity jump, a certain distance below. This yields the well-known mixing layer profile studied by Rayleigh (1894), and is shown in figure (2.2). The basic idea is to interpret the instability in this profile as being due to a linear wave interaction of two Rossby waves at $y = \pm b$. If the two waves were considered separately, then they would propagate in opposite directions relative to each other. The disturbance velocity field of each wave slows down the wave at the opposite interface, such that the two waves are stationary with respect to each other. This new pattern is a normal-mode solution of the system. In the final frozen pattern, if there exists a component of v in-phase with the interface displacement, then the amplitude of such a disturbance would grow with time indicating instability. Such an in-phase component can be created due to the presence of the other wave. To quantify this, we decompose the total velocity into a component in-phase with the displacement, and a component displaced by a quarter wavelength from it. The in-phase component now can continually force the interface position leading to an instability.

The general solution of the Rayleigh equation for this flow can be written as

$$\psi = \begin{cases} A\sinh(2kb)e^{-k(y-b)} & (y > b), \\ A\sinh(k(y+b)) + B\sinh(k(b-y)) & (-b < y < b), \\ B\sinh(2kb)e^{k(y+b)} & (y < -b), \end{cases} \tag{2.6}$$

where A and B are arbitrary coefficients which depend on ω. The dispersion relation can be written as

$$\left(\frac{c}{U}\right)^2 = \frac{1}{4k^2b^2}\left[(2kb-1)^2 - e^{-4kb}\right]. \tag{2.7}$$

Skipping algebraic details, it can easily be shown that

$$\frac{B}{A} = \left(e^{2kb} - \frac{U\sinh(2kb)}{kb(U-c)}\right). \tag{2.8}$$

From this, the phase shift in the interface displacement (or vorticity) at $y = \pm b$ can be easily written as

$$\alpha = \arg\left(\frac{B}{A}\right) + 2\tan^{-1}\left(\frac{-c_i}{U}\right). \tag{2.9}$$

This phase-difference is responsible for an instability in the system. Detailed discussion of this mechanism is given in Hoskins *et al.* (1985) and Baines & Mitsudera (1994). The effect of density variation on a single Rossby wave propagation has recently been treated in Harnik *et al.* (2008). The phase-locking of two free waves into a normal-mode solution can be observed from the solution of an initial value problem.

2.1.2 Initial Value Problem

Instead of the normal mode form of the solution, we may assume the vertical velocity to be of the form

$$v(x,y,t) = \hat{v}(y,t)e^{ikx}. \tag{2.10}$$

The governing differential equation now takes the form

$$\left(\frac{\partial}{\partial t} + ikU\right)(\hat{v}'' - k^2\hat{v}) - ikU''\hat{v} = 0. \tag{2.11}$$

Defining a Laplace transform of $\hat{v}$, i.e.

$$\tilde{v}(y,s) = \int_0^\infty \hat{v}(y,t)e^{-st}dt, \tag{2.12}$$

the final differential equation reduces to

$$\tilde{v}'' - k^2\tilde{v} - \frac{ikU''v}{s+ikU} = \frac{\hat{\phi}_0}{s+ikU}, \tag{2.13}$$

where

$$\hat{\phi}_0 = \left(D^2 - k^2\right)\hat{v}_0. \tag{2.14}$$

Let $G(y,y')$ be the Green's function of the homogeneous part of equation (2.13),

$$\left[(D^2 - k^2) - \frac{ikU''}{s+ikU}\right]G(y,y') = A\delta(y-y'), \tag{2.15}$$

where A is an arbitrary constant. The velocity field $\tilde{v}$ can then be calculated as

$$\tilde{v} = \int_{-\infty}^{\infty} G(y,y')\hat{\phi}_0\, dy'. \tag{2.16}$$

The Green's function is defined as

$$G(y,y') = \begin{cases} \dfrac{\tilde{v}_2(y)\tilde{v}_1(y')}{ik(U(y')-c)W(c)} & \text{if } y' < y, \\ \dfrac{\tilde{v}_1(y)\tilde{v}_2(y')}{ik(U(y')-c)W(c)} & \text{if } y' > y, \end{cases} \tag{2.17}$$

where $\tilde{v}_1$ and $\tilde{v}_2$ are the solution of the homogeneous part of equation (2.13) satisfying $\tilde{v}_1(-\infty) = 0$ and $\tilde{v}_2(\infty) = 0$, c is the phase-speed and $W(c) = \tilde{v}_1 D\tilde{v}_2 - \tilde{v}_2 D\tilde{v}_1$ is the Wronskian. Therefore G is a continuous function of y.

IVP with a single vorticity interface

First, let us consider a single vorticity interface as shown in figure (2.1) and calculate the response of an arbitrary disturbance. For convenience, the interface position is chosen to be at $y = 0$, and $U = U_0$ for $y > 0$, and $U = U_0 + \gamma y$ for $y < 0$. The jump in the vorticity across $y = 0$ is given by $\Delta U' = -\gamma$. Equation (2.15) governing the Green's

function reduces to

$$\left[(D^2 - k^2) - \frac{ik(\Delta U')\delta(y)}{s + ikU}\right] G^R(y, y') = A\delta(y - y'), \tag{2.18}$$

where G^R represents the Green's function describing a single Rossby wave propagation. For $|y| > 0$, the above equation reduces to

$$\left(D^2 - k^2\right) G^R(y, y') = A\delta(y - y'), \qquad y' > 0. \tag{2.19}$$

The general solution of this equation satisfying the boundary conditions at $\pm\infty$ is given by

$$G^R(y, y') = \begin{cases} a_1 e^{-ky} & \text{if } y > y', \\ a_2 e^{-ky} + a_3 e^{ky} & \text{if } 0 < y < y', \\ a_4 e^{ky} & \text{if } y < 0. \end{cases} \tag{2.20}$$

The constants a_1, a_2, a_3, a_4 are calculated by imposing the usual conditions on the Green's function. $G^R(y, y')$ is continuous across $y = 0$ and $y = y'$, i.e.

$$\left[G^R\right]_{y'^-}^{y'^+} = 0, \qquad \left[G^R\right]_{0^-}^{0^+} = 0, \tag{2.21}$$

Integrating equation (2.18) across $y = 0$ and $y = y'$ yields the relations

$$\left[\frac{dG^R}{dy}\right]_{y'^-}^{y'^+} = A, \qquad \left[\frac{dG^R}{dy}\right]_{0^-}^{0^+} = \frac{ik(\Delta U')}{s + ikU_0} G^R(0, y'), \tag{2.22}$$

Using equations (2.20), (2.21) and (2.22), G^R takes the form

$$G^R(y, y') = \frac{A}{2k}\left[\frac{i\Delta U'}{2(s + ikc)} e^{-k(|y|+|y'|)} - e^{-k(|y|-|y'|)}\right], \tag{2.23}$$

where $c = U_0 + \Delta U'/2k$. Having obtained the Green's function, it is now possible to calculate $v(x, y, t)$ using the inverse Laplace transform of $\hat{v}(k, y, t)$:

$$\begin{aligned} v(x, y, t) &= \int_{-\infty}^{\infty} \hat{v}(k, y, t) e^{ikx} dk \\ &= \frac{e^{ikx}}{2\pi i} \int_{-\infty}^{\infty} \hat{\phi}_0(y') \int_{\sigma - i\infty}^{\sigma + i\infty} \frac{G(y, y')}{s + ikU(y')} e^{st} ds dy' \end{aligned} \tag{2.24}$$

Using $G^R = G$ in the above equation, we get

$$\begin{aligned} v(x, y, t) = \frac{e^{ikx}}{2\pi i}\frac{A}{2k} \int_{-\infty}^{\infty} \Bigg\{ & \hat{\phi}_0(y') \left[\frac{\Delta U'}{2k(c - U)} e^{-k(|y|+|y'|)} - e^{-k(|y-y'|)}\right] e^{-ikUt} \\ & - \hat{\phi}_0(y') \frac{\Delta U'}{2k(c - U)} e^{-ikct} e^{-k(|y|+|y'|)} \Bigg\} \end{aligned} \tag{2.25}$$

The above result describes the evolution of an arbitrary disturbance $\phi_0(y')$, and would

involve contributions from both discrete spectrum (a single wave at $y = 0$) and the continuous spectrum. This can be used a starting point in a more detailed analysis of the interaction of discrete and continuous spectrum modes, as was carried out by Sazonov (1989). Instead of a constant velocity above the interface, one can easily repeat the analysis with two different values of shear, γ_1 and γ_2 on either side of the interface. Then, as a special case, when the shear on either side becomes equal ($\gamma_1 = \gamma_2$), the flow would then reduce to a Couette profile, and the above solution would correspond to the solution of Case (1960). Since our main aim is to understand the evolution of the discrete mode at $y = 0$, we impose a vortex sheet at $y = 0$, i.e.

$$\hat{\phi}_0(y') = B\delta(y). \tag{2.26}$$

The discrete mode velocity field thus obtained takes the simple form

$$v(x, y, t) = \frac{iAB}{4\pi k} e^{-k|y|} e^{ik(x-ct)}. \tag{2.27}$$

This would exactly be the form of solution obtained by solving the Rayleigh equation using a normal-mode approach. Also, we can identify c with the phase-speed of the wave which can be written as

$$c = U_0 - \frac{\gamma}{2k}. \tag{2.28}$$

For the profile shown in figure (2.1), we have $\gamma > 0$. Therefore the speed of the wave with respect to the base flow, i.e. $c - U_0 < 0$, indicating that the wave travels leftward with respect to to they local mean flow, consistent with the kinematic view discussed earlier.

IVP with a mixing-layer profile

We now consider the stability of arbitrary disturbances with a mixing layer profile shown in figure (2.2). Setting $U_0 = 1$ and $\gamma = -1$, and adding another vorticity interface of opposite sign, the mean flow profile is defined as

$$U^{ML} = \begin{cases} 1 & \text{if } y > 1, \\ y & \text{if } -1 < y < 1, \\ -1 & \text{if } y < -1, \end{cases} \tag{2.29}$$

where the superscript ML denotes a mixing layer profile. Therefore, $U'' = \delta(y + 1) - \delta(y - 1)$. A normal-mode solution of the Rayleigh equation (2.3) yields the eigenvalues

$$c^{ML} = \pm\frac{1}{2k}\left[(1 - 2k)^2 - e^{-4k}\right]. \tag{2.30}$$

The flow is neutrally stable for $k > 0.639$ as can be seen in figure (2.3(a)). The corresponding phase-speeds of the unstable modes are plotted in figure (2.3(b)). These are compared with corresponding free wave phase speeds obtained by taking the limit $k \to \infty$ in the mixing-layer eigenvalues. The free wave solutions therefore take the simple form

$$c^{free} = \pm\left(1 - \frac{1}{2k}\right). \tag{2.31}$$

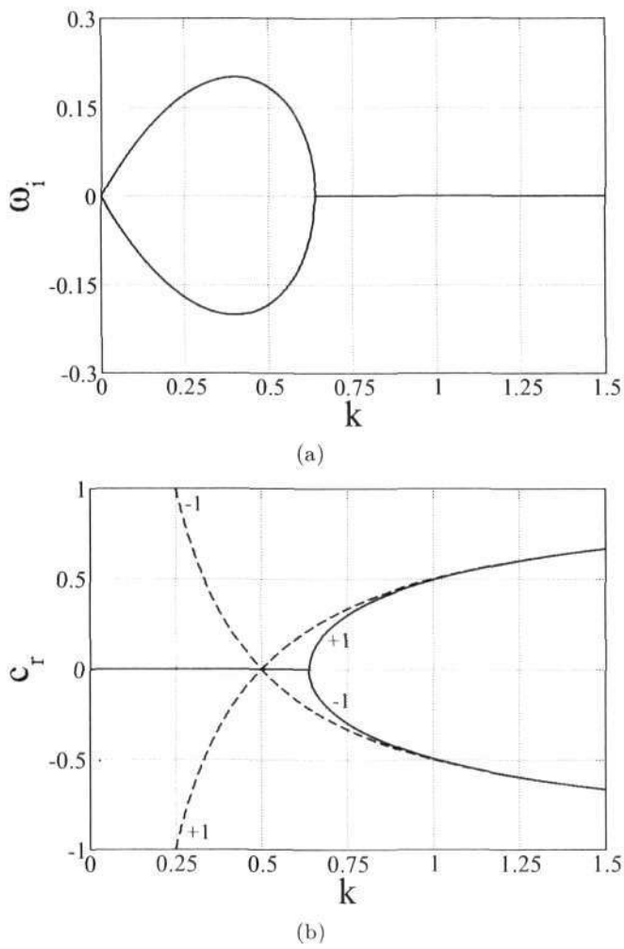

Figure 2.3: (a) Growth and decay rates of the two normal modes, $\Im(c^{ML})$. The flow is neutrally stable for $k > 0.639$. (b) Comparison of phase-speeds of the two normal modes for a mixing layer profile (solid lines) with the phase-speeds for two free waves (dashed lines) riding at $y = \pm 1$.

The phase-speed obtained from the IVP calculation for a single Rossby wave exactly matches with this solution. Focusing attention on the waves moving on the upper (+1) interface, the phase-speed of the free wave changes sign at $k = 0.5$. As expected, for large k, the normal modes of the mixing layer profile reduce to the free wave phase-speeds. But an important feature to be noticed is that the phase-speeds of the mixing layer profiles are always less then their free-wave counterparts in magnitude. This is clear for $k > 0.639$ where the waves for a mixing layer profile travel to the right slower than the corresponding free wave counterparts. In the IVP calculation to be presented below, it will be shown that an initial wave-like perturbation at the two interfaces indeed evolves like free-waves. Hence, the disturbance at $y = 1$ is expected to travel to the left for $y < 0.5$, and to the right for $y > 0.5$.

For this profile, equation (2.15) simplifies to

$$\left[(D^2 - k^2) - \frac{ik(\delta(y+1) - \delta(y-1))}{s + ikU}\right] G^{ML}(y, y') = A\delta(y - y'), \tag{2.32}$$

When $|y| \neq 1$, the Green's function satisfies equation (2.19). The general solution of this equation in various regions of the flow can be written as

$$G^{ML}(y, y') = \begin{cases} a_1 e^{-ky} & \text{if } y > 1, \\ a_2 e^{-ky} + a_3 e^{ky} & \text{if } y' < y < 1, \\ a_4 e^{-ky} + a_5 e^{ky} & \text{if } -1 < y < y', \\ a_6 e^{ky} & \text{if } y < -1. \end{cases} \tag{2.33}$$

As mentioned earlier, $G^{ML}(y, y')$ is continuous across $y = -1, y', 1$, i.e.

$$\left[G^R\right]_{-1^-}^{-1^+} = 0, \qquad \left[G^{ML}\right]_{y'^-}^{y'^+} = 0, \qquad \left[G^R\right]_{1^-}^{1^+} = 0, \tag{2.34}$$

Integrating equation (2.32) across $y = -1, y', 1$ yields the relations

$$\begin{aligned} \left[\frac{dG^{ML}}{dy}\right]_{-1^-}^{-1^+} &= \frac{ik}{s - ik} G^{ML}(-1, y'), \\ \left[\frac{dG^{ML}}{dy}\right]_{y'^-}^{y'^+} &= A, \\ \left[\frac{dG^{ML}}{dy}\right]_{1^-}^{1^+} &= \frac{-ik}{s + ik} G^{ML}(1, y'), \end{aligned} \tag{2.35}$$

Using equations (2.33), (2.34) and (2.35), G^{ML} takes the form

$$\begin{aligned} G^{ML}(y,y') &= \frac{iAe^{-k|1+y|}}{k}\left[\frac{s+ik}{g(s)}\right]\left\{\left(1+\frac{i}{2(s+ik)}\right)e^{-k|1+y'|}-\frac{ie^{-2k}}{2(s+ik)}e^{-k|1-y'|}\right\} \\ &+ \frac{iAe^{-k|1-y|}}{k}\left[\frac{s-ik}{g(s)}\right]\left\{\left(1+\frac{i}{2(s-ik)}\right)e^{-k|1-y'|}-\frac{ie^{-2k}}{2(s-ik)}e^{-k|1+y'|}\right\} \\ &- \frac{A}{2k}e^{-k|y-y'|} \end{aligned} \tag{2.36}$$

where $g(s) = 4(s^2+k^2)+4is-1+e^{-4k}$. Disturbance velocity is now calculated using equation (2.24). We do not write the explicit solution here as it is too lengthy. This solution would describe the evolution of any arbitrary disturbance. But our primary goal is to understand the evolution of disturbances at the two interfaces $y = \pm 1$, and subsequently observe the emergence of unstable/stable normal modes at long times. Hence, we solve here only a simplified problem. To excite purely discrete waves at the two interfaces, the initial condition is chosen to be of the form

$$\hat{\phi}_0(y') = B_1\delta(y'-1)+B_2\delta(y'+1), \tag{2.37}$$

where B_1 and B_2 are arbitrary constants. In particular, this initial condition corresponds to vortex sheets at $y = \pm 1$, and B_1 and B_2 control the initial strength and the phases of the two vortex sheets. Now the vertical velocity reduces to the calculation of two simple integrals,

$$v(x,y,t) = \frac{e^{ikx}}{2\pi i}B_2\int_{\sigma-i\infty}^{\sigma+i\infty}\frac{G(y,-1)}{s-ik}e^{st}ds + \frac{e^{ikx}}{2\pi i}B_1\int_{\sigma-i\infty}^{\sigma+i\infty}\frac{G(y,1)}{s+ik}e^{st}ds. \tag{2.38}$$

Having obtained $v(x,y,t)$, we now plot contours of streamfunction for two different values of k. It has already been mentioned above the free waves at the two interfaces change their direction of propagation at $k = 0.5$. Hence we show the evolution of streamfunction for $k = 0.4$ and $k = 0.6$. The contour plots are plotted for one wavelength. We choose $B_1 = 1$ and $B_2 = i$ such that the vortex sheets at $y = \pm 1$ are displaced by a quarter-wavelength from each other. In figure (2.4), streamfunction contours are plotted with $k = 0.4$ for various times. As time progresses, disturbance at $y = 1$ travels to the left, and at $y = -1$ travels rightwards, in agreement with the evolution of free waves. The last figure in the panel is close to the large-time normal mode pattern. For $k = 0.6$, free waves travel rightwards (leftwards) at the upper (lower) interface. The IVP solution at this wavenumber indeed confirms this behaviour, as shown in figure (2.5).

The above analysis shows that waves on the two interfaces indeed behave like free waves at short times evolving with the free wave phase-speeds. The disturbance velocity field of each wave slows the other one down such that the two waves come to rest relative to each other and form a normal-mode solution.

The kinematic understanding of linear wave-interaction can also be investigated using the ideas of wave-energy, a quantity which can have both positive and negative values. A wave is said to possess negative energy if its introduction into a medium lowers the total

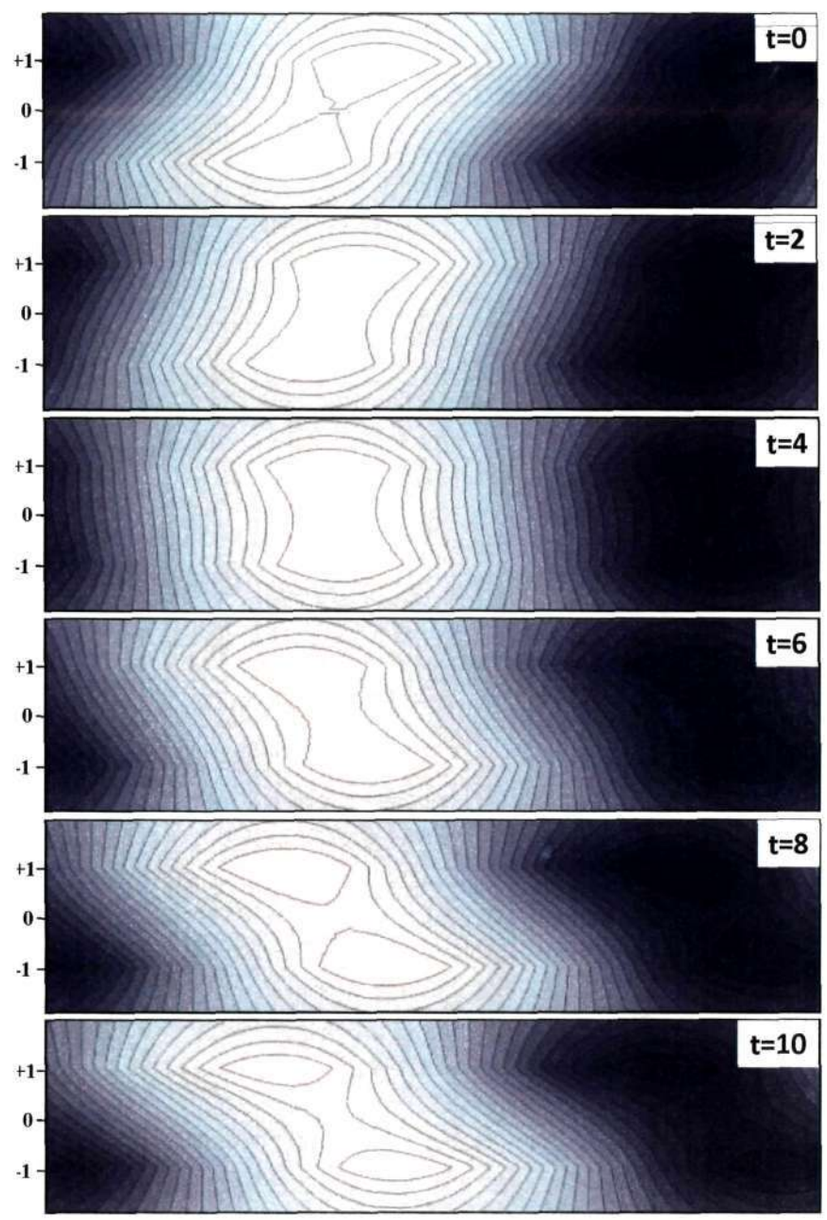

Figure 2.4: Evolution of streamfunction contours with time for an initial condition consisting of two vortex sheets at $y = \pm 1$ with $k = 0.4$. As time increases (downwards in the figure), disturbance at $y = 1$ travels to the left and at $y = -1$ travels to the right. But the speed of evolution continually slows down eventually reaching a steady-state pattern at $t \approx 10$.

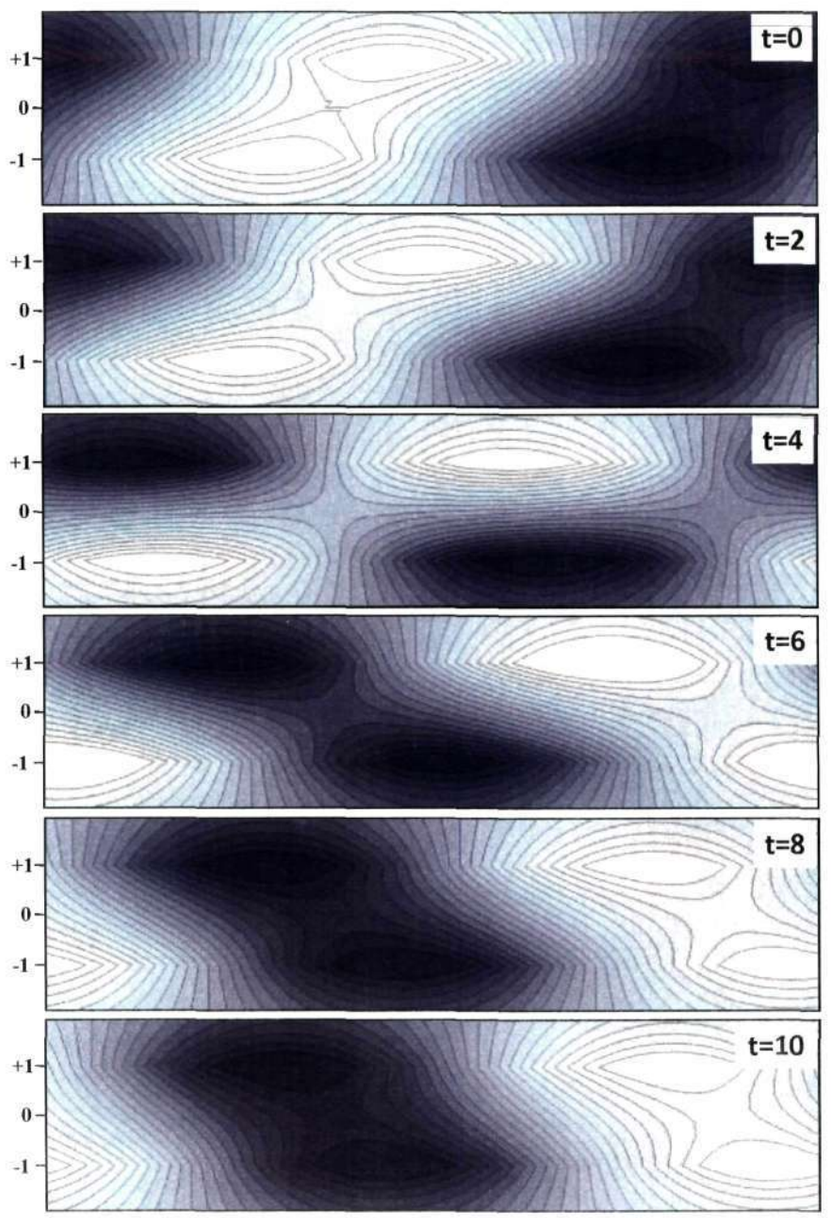

Figure 2.5: Same as figure 2.4 but with $k = 0.6$. In this case, the disturbance at $y = 1$ travels to the right and at $y = -1$ travels to the left.

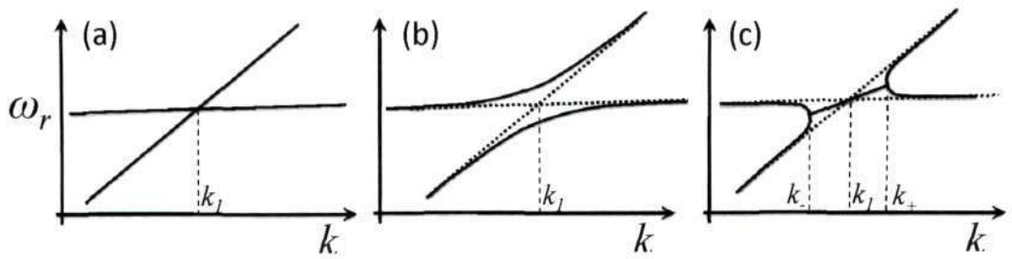

Figure 2.6: Schematic of possible wave-interactions possible for two free waves.

energy of the medium. For example, the kinetic energy of a stratified shear flow before the introduction of a perturbation is given by

$$KE_0 = \int_{-\infty}^{\infty} \rho(y)\mathbf{U}^2 dy \tag{2.39}$$

where $\rho(y)$ is the density and $\mathbf{U}$ is the mean flow. On introducing a disturbance velocity field (waves), $\mathbf{v}$, the kinetic energy changes to

$$KE_1 = \int_{-\infty}^{\infty} \rho(y)(\mathbf{U} + \mathbf{v})^2 dy \tag{2.40}$$

Therefore, the change is kinetic energy is given by $KE_1 - KE_0$. The same argument can be extended to potential energy. If the total energy after the introduction of a wave is lower than before it, then the wave is said to be associated with a negative energy, or simply called as a negative energy wave. Once it is recognized that waves can possess both negative and positive energies, then it easy to show that if energy is extracted from the system, then the negative energy wave increases in amplitude indicating instability. Cairns (1979) introduced these idea in instabilities of parallel flows, though the basic ideas were contained in the works of Landahl (1962) and Benjamin (1963) in the context of boundary layer flow over a flexible surface, and also in Acheson (1976) in his discussion on over-reflection. The idea is powerful mainly because of its predictive capabilities. If two free-waves have the same frequency, i.e the dispersion relations of the two waves intersect, then it is possible to predict the outcome of the combined instability problem. For example, in the above mixing layer profile, the two waves (solved independently) at $y \pm b$ possess opposite wave energies, and their dispersion curves intersect as shown schematically in figure (2.6). From the dispersion relation of each free wave, the wave-energy can be calculated using the Cairns formula:

$$\varepsilon = \frac{1}{4}\frac{\partial D}{\partial \omega}|\eta_0|^2, \tag{2.41}$$

where $|\eta_0|$ is the wave-amplitude. To derive this formula, one subtracts the total kinetic and potential energies of the system before and after the introduction of the wave. Another way to arrive at the same result is to use Whitham's averaged Lagrangian formulation (see Whitham (1974)) as was done in Ostrovskii *et al.* (1986). At the point of

interaction, $k = k_1$, if the two modes have the same sign of wave-energy, then the outcome is expected to be of form (b) in fig.(2.6). The resulting dispersion curves are distorted but remain neutral. Whereas, if the modes possess wave-energy of opposite sign, then an instability is expected as shown by the form (c) in fig.(2.6). In the region between k_+ and k_- the frequency in the form of complex conjugates, with one growing and one decaying mode. The ideas of wave-energetics are explored in detail in Craik (1985) and Fabrikant & Stepanyants (1998). These ideas will be used later in this chapter and in the next chapter. We now proceed to consider an interaction between a Rossby wave and an internal wave.

2.2 Taylor-Goldstein equation

For flows with density inhomogeneity, one usually employs the well-known Boussinesq approximation. In this approximation, the effects of density are neglected in all the terms in the momentum equation, but retained only in the gravity forcing term. We first write the density as

$$\tilde{\rho}(x, y, t) = \rho_m + \bar{\rho}(y) + \rho(x, y, t). \tag{2.42}$$

Here $\tilde{\rho}$, the total density is a function of all space and time, and is decomposed into three parts. The first part, ρ_m is a vertical mean density, and assumes a fixed number. $\bar{\rho}$ is a function of just the vertical coordinate, and superposed on this, is a small fluctuating component ρ, which varies in both space and time. We assume that $\rho << \rho_m, \bar{\rho}, \tilde{\rho}$. For a simple linearly varying density profile, i.e. $\bar{\rho} \propto y$, bounded between heights y_1 and y_2, ρ_m is usually related to $\bar{\rho}$ as

$$\rho_m = \bar{\rho}\left(\frac{y_1 + y_2}{2}\right). \tag{2.43}$$

The choice of ρ_m is made by convenience. Substituting these into the governing equations of motion leads to the Taylor-Goldstein equation derived independently by Taylor (1931), Goldstein (1931) and Haurwitz (1931).

$$v'' + \left[\frac{N^2}{(U-c)^2} - \frac{U''}{(U-c)} - k^2\right] v = 0, \tag{2.44}$$

where N is the Brunt-Vaisala frequency defined as

$$N^2 = -\frac{g}{\rho_m}\frac{d\bar{\rho}}{dy}. \tag{2.45}$$

In many geophysical applications, density is stably-stratified and varies either linearly or exponentially in the vertical direction. As a result, the Brunt-Vaisala frequency is non-zero for all heights. For stable density stratification, it can be shown from equn.(2.44) that internal gravity waves are supported by the system (see e.g. Cohen & Kundu (2004)). These waves are usually undamped in the far-field and homogeneous boundary conditions are not satisfied in the vertical direction. Therefore, more complicated boundary conditions need to be employed when solving equn.(2.44) in a bounded domain. In this work, we consider a situation where the density jumps from ρ_1 to ρ_2 at some arbitrary

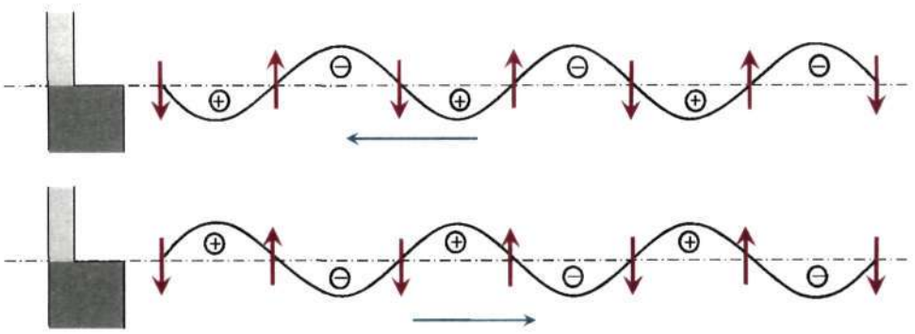

Figure 2.7: A parallel flow analogue of the stability of a Rankine vortex with density jump outside the vortex core.

location, say, $y = 0$ for convenience. This gives us a delta-function profile for the Brunt-Vaisala frequency. Therefore internal waves are supported only at this location and the disturbance decays to zero far away from this interface. ρ_1 corresponds to the density of the upper layer fluid ($y > 0$), and ρ_2 corresponds to the density of the lower layer fluid. When $\rho_1 < \rho_2$, the flow is said to be in a statically-stable configuration. When $\rho_1 > \rho_2$, the flow supports unstable waves, this is commonly known as the Rayleigh-Taylor instability (RTI). The full dispersion relation obtained by solving equn.(2.44) with $U = 0$ takes the form

$$c = \pm \left[\frac{g(\rho_2 - \rho_1)}{k(\rho_2 + \rho_1)} \right]^{1/2}. \tag{2.46}$$

Clearly, two normal modes are supported at the density interface. For unstable stratification, the solutions are purely imaginary and complex conjugates of each other. Therefore in the absence of any background flow, the unstable RTI waves are standing waves. For stable stratification, both the eigenvalues are real and are of opposite sign. To understand the mechanism of Rossby-gravity wave interaction, it is first important to understand the kinematics of density wave propagation. To do this, we write the linear equations governing vorticity and density anomalies,

$$\frac{D\zeta}{Dt} = -N^2 \frac{\partial \eta}{\partial x}, \tag{2.47}$$

$$\frac{D\rho}{Dt} + v \frac{d\bar{\rho}}{dy} = 0, \tag{2.48}$$

$$\frac{D\eta}{Dt} = v, \tag{2.49}$$

where $D/Dt = \partial/\partial t + U\partial/\partial x$, ζ is the vorticity anomaly and η is the interface displacement. Assuming a normal mode form of the solution, $D/Dt = -i(\omega - kU)$. This reduces

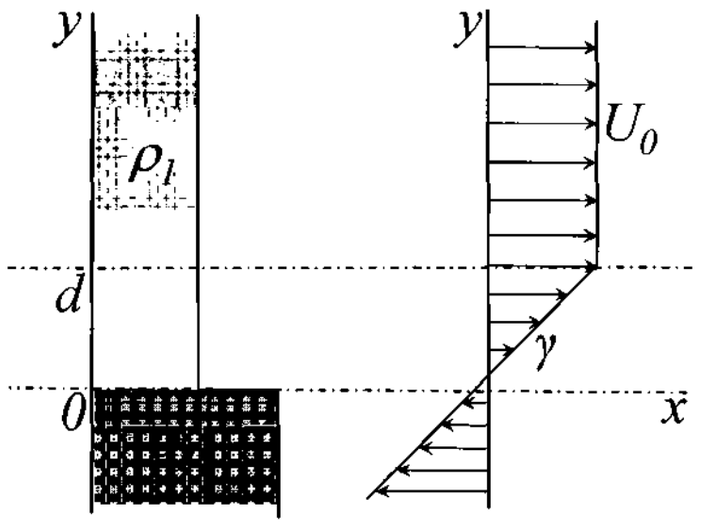

Figure 2.8: A parallel flow analogue of the stability of a Rankine vortex with density jump outside the vortex core.

the above equation to the simple form

$$\zeta = \frac{-iN^2}{k(c-U)}\frac{\partial \eta}{\partial x}, \tag{2.50}$$

$$= \frac{N^2}{(c-U)}\eta. \tag{2.51}$$

With $U = 0$, and stable density stratification, $N^2 > 0$ and c is real. For $c < 0$, ζ and η are always in anti-phase, and for $c > 0$, ζ and η are exactly in phase with each other. The two cases are shown schematically in figure 2.7. The vorticity anomaly for the upper panel in this figure is exactly analogous to the Rossby wave schematic shown in figure 2.1. Therefore, using the same kinematic arguments, it can be shown that the upper panel in figure 2.7 travels to the left, and the lower panel travels to the right. In terms of wave-interaction, it will be shown in the next section that the Rossby wave of figure 2.1 and the rightward traveling density wave interact, leading to an instability.

2.3 Rossby-Gravity wave interaction

We now consider the problem of interaction of a Rossby wave with an internal gravity wave. For simplicity, we employ the standard Boussinesq approximation. We employ here the kinematic wave-interaction ideas discussed in section 2.1 to show that a neutral Rossby wave and a neutral interface interact giving rise to exponential growth. The construction of flow geometry requires two key ingredients: (i) a vorticity jump which supports a neutral wave riding on it, (ii) a stable density jump which supports two neutral waves traveling in opposite directions, and riding at the density discontinuity. As

discussed in the previous section, an instability is now possible due to an interaction of two oppositely moving waves, which may become stationary relative to each other due to the action of shear. A schematic of the geometry is shown in fig.(2.8), and was first studied by Baines & Mitsudera (1994). This problem has also been studied by Fabrikant & Stepanyants (1998) in the context of an the air boundary layer over an ocean surface. The base flow can be written as:

$$U = \begin{cases} U_0 & \text{if } y > d, \\ U_1 = U_0 + \gamma(y - d) & \text{if } y < d, \end{cases} \tag{2.52}$$

where γ is the shear rate.

$$\tilde{\rho} = \begin{cases} \rho_1 & \text{if } y > 0, \\ \rho_2 & \text{if } y < 0. \end{cases} \tag{2.53}$$

For stable density stratification, $\rho_1 < \rho_2$. The governing equation now is the Taylor-Goldstein equation (2.44). The flow is unbounded in the vertical direction, and we use homogeneous boundary conditions on v. The general solution is

$$v = A \exp(-k|y|) + \exp(-k|y - d|). \tag{2.54}$$

The coefficient A is obtained by matching pressure on either side of the density interface.

$$A = \frac{-\exp(-kd)}{\left[1 - \dfrac{(\omega - kU_0 + \gamma kd)^2}{gk}\dfrac{(\rho_2 + \rho_1)}{(\rho_2 + \rho_1)}\right]}. \tag{2.55}$$

The complete dispersion relation, $\mathcal{D}(\omega, k, d, \rho)$ takes the form:

$$\left[(\omega - kU_0 + \gamma kd)^2 + \frac{gk(\rho_1 - \rho_2)}{(\rho_1 + \rho_2)}\right][2(\omega - kU_0) + \gamma] = \frac{gk(\rho_1 - \rho_2)}{\rho_1 + \rho_2}\gamma e^{-2kd}. \tag{2.56}$$

The right hand terms indicate the coupling between the two interfaces at $y = 0$ and at $y = d$. Defining a suitable Richardson number,

$$J = \frac{g}{\gamma^2 d}\frac{(\rho_2 - \rho_1)}{(\rho_2 + \rho_1)} \tag{2.57}$$

which quantifies the effect of density contrast, the growth rate contours are plotted in the $J - k$ plane, and is shown in fig.(2.9).

In the absence of shear, the first interface loses identity, and we recover the IGW solution at $y = 0$. In the absence of any density stratification ($\rho_1 = \rho_2$), IGWs disappear, and we recover the discrete mode riding on the vorticity interface at $y = h$ along with the continuous spectrum, i.e. for a given k, an uncountable number of frequencies can be supported by the system depending on the location of the origin we choose. The continuous spectrum modes are exactly analogous to the modes described in Case (1960). We return to this point later in the section where we show that the continuous spectrum modes of the homogeneous problem destabilize. The crucial term which determines the strength of the coupling is e^{-2kh}. If the interfaces are very far apart, then no instability

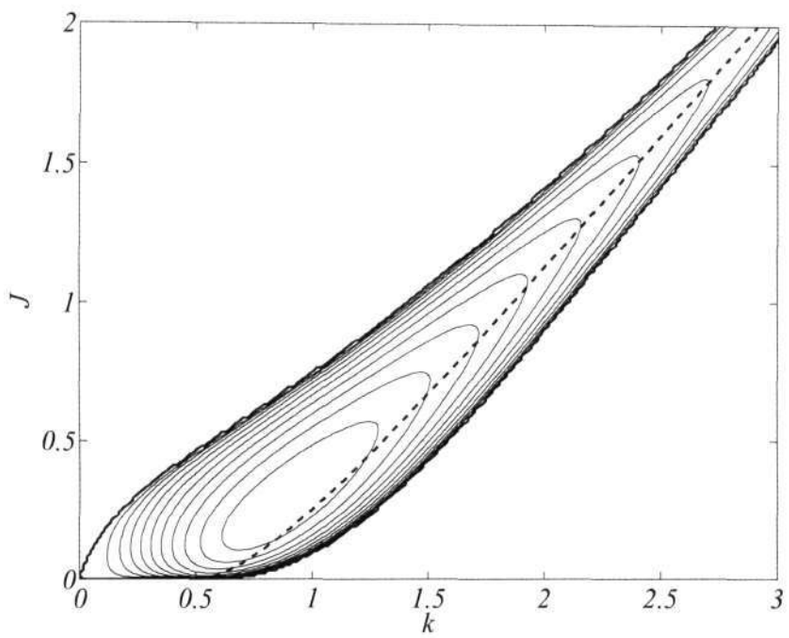

Figure 2.9: Stability diagram showing twelve equally spaced contours with a spacing of 0.0136. The thick solid line is the neutral curve, and the dashed line is the resonance condition for free waves of Baines & Mitsudera (1994). The region outside these contours is neutrally stable.

arises, and we recover the neutral solutions on each interface. A surprising result is obtained when the interfaces are brought very close to each other. This is the limit of $kh \to 0$. Writing an asymptotic expansion for small kh, the lowest order equation gives

$$\omega_0 = kU_0 - \frac{\gamma \pm \left[\gamma^2 - 16gk\left(\frac{\rho_1 - \rho_2}{\rho_1 + \rho_2}\right)\right]^{1/2}}{4}. \tag{2.58}$$

For closely spaced interfaces, this shows that stable density stratification does not lead destabilize. Physically, as the interfaces are brought very close to each other such that the spacing between them becomes much smaller than the wavelength of the waves, then shear becomes ineffective in adjusting the phase speeds of the two waves for interaction.

According to Baines & Mitsudera (1994), the phase relationship between interface displacement and vertical velocity is the key to understand the wave interaction mechanism. Instead of studying the phase relationship of free waves, we focus on the complete dispersion relation (2.56) to understand the underlying phase relationships between various quantities.

From equn.(2.54), the vertical velocity and interface displacement at the lower (density) interface is given by

$$v_0 = (A + \exp(-kd))e^{i(kx - \omega t)}, \tag{2.59}$$

$$\eta_0 = \frac{i(A + \exp(-kd))}{\omega - kU_0 + \gamma kd} e^{i(kx-\omega t)}, \tag{2.60}$$

and for the upper (vorticity) interface is given by

$$v_d = (A\exp(-kd) + 1)e^{i(kx-\omega t)}, \tag{2.61}$$

$$\eta_d = \frac{i(A\exp(-kd) + 1)}{\omega - kU_0} e^{i(kx-\omega t)}. \tag{2.62}$$

The phase difference is now given by

$$\alpha_i = \tan^{-1}\left[\frac{\mathrm{Re}(v_i)}{\Im(v_i)}\right] - \tan^{-1}\left[\frac{\mathrm{Re}(\eta_i)}{\Im(\eta_i)}\right], \qquad i : 0, d, \tag{2.63}$$

where $\mathrm{Re}, \Im$ correspond to real and imaginary parts. Figure 2.10 shows how the phase difference changes for various Richardson numbers as a function of wavenumber for both the interfaces. As the Richardson number is decreased, the phase angle between η and u_r approaches the near-perfect case of $\alpha_i = 0$. Clearly, the neutral region is marked by the angle's α_0, α_d fixed at 90^0. The same phase difference appears in the kinetic energy equation in the buoyancy flux term. The equations for the perturbation kinetic T', potential, V and total energies E, for an incompressible inviscid fluid take the form (see Gill (1982))

$$\frac{\partial T}{\partial t} + U\frac{\partial T}{\partial x} = -\overline{uv}\frac{dU}{dy} - g\overline{\rho v}, \tag{2.64}$$

$$\frac{\partial V}{\partial t} + U\frac{\partial V}{\partial x} = g\overline{\rho v}, \tag{2.65}$$

$$\frac{\partial E}{\partial t} + U\frac{\partial E}{\partial x} = -\overline{uv}\frac{dU}{dy}. \tag{2.66}$$

Here, $T' = \rho_0(u^2 + v^2)/2$, $V = g^2\rho^2/2\rho_0 N^2$ and $E = T' + V$. Total energy can grow only due to an exchange with the mean flow through a Reynolds stress term. Nonetheless, kinetic energy can increase at the expensive of potential energy through the buoyancy flux term, $g\overline{\rho v}$.

$$\overline{\rho v} = \iint \rho v \; dxdy, \tag{2.67}$$

$$= \iint \frac{-iv}{\omega - kU}\frac{d\rho_0}{dy} v \; dxdy. \tag{2.68}$$

$$\tag{2.69}$$

For a sharp density interface, $d\rho_0/dy = \Delta\rho\delta(y)$. Also using the relation $D\eta/Dt = v$, we get

$$\overline{\rho v} = \frac{\Delta\rho}{2}|\eta||v|\cos(\alpha_i). \tag{2.70}$$

This shows that no exchange of energy from kinetic to potential forms can take place when the phase difference between interface displacement and vertical velocity is 90^0.

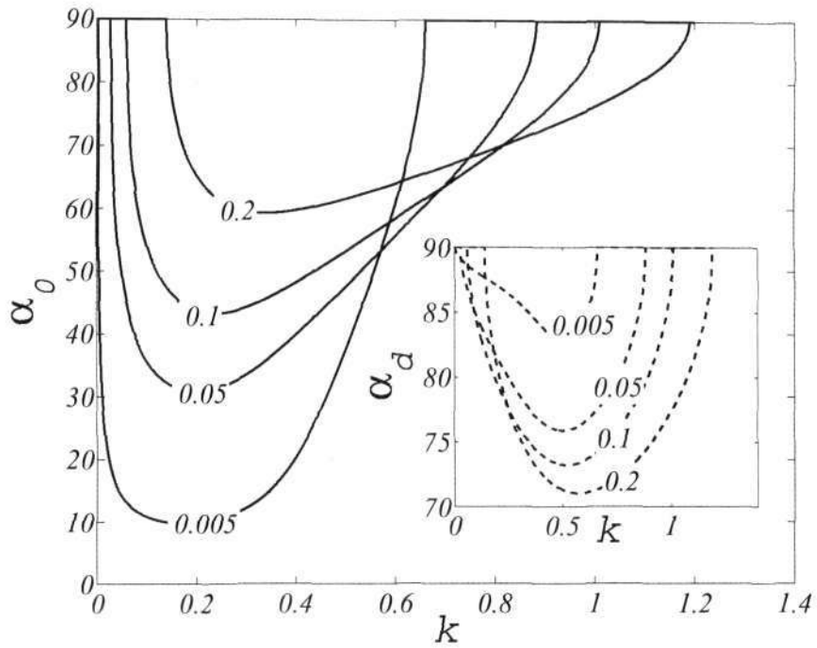

Figure 2.10: Phase difference between interface displacement and in-phase vertical velocity calculated at the interfaces for various Richardson numbers. Solid lines correspond to density interface (subscript 0), and dashed lines correspond to vorticity interface (subscript d).

We now obtain some approximate solutions to equation (2.56). The limit of small kd has already been discussed. We now write approximate solutions to the cubic-dispersion equation in the small J limit. It is convenient to re-write equn.(2.56) in the following non-dimensional form:

$$\omega^3 + a_0\omega^2 + a_1\omega + a_2\omega J + a_3 + a_4 J = 0, \tag{2.71}$$

where $a_0 = 2k + 1/2$, $a_1 = k^2 + k$, $a_2 = -k$, $a_3 = k^2/2$ and $a_4 = -k(1 - \exp(-2k))/2$. The wavenumber k has been non-dimensionalized by the interface spacing d. At small J, the lowest order equation, obtained by setting $J = 0$, reduces to the form

$$\left(\omega_0 + \frac{1}{2}\right)(\omega_0 + k)^2 = 0. \tag{2.72}$$

The roots of this equation are purely real. The first root $\omega_0^{(1)} = -1/2$ corresponds to a free wave on the vorticity interface at $y = d$. The other two roots, $\omega_0^{(2,3)} = -k$, reduce to the continuous spectrum obtained by considering $U = c$ in the Rayleigh stability equation. Using generalized functions, the corresponding eigenfunctions for these roots are simply the Green's function of the Rayleigh operator. It also has to be emphasized that the inviscid continuous spectrum in the present problem exists only for $y < d$. Now

we introduce a small density discontinuity at $y = 0$ characterized by a small Richardson number. The asymptotic expansion for small J for the first solution can be written as

$$\omega^{(1)} = \omega_0^{(1)} + J\omega_1^{(1)} + O(J^2), \tag{2.73}$$

where $\omega_1^{(1)} = -k\exp(-2k)/(2(k-1/2)^2)$. This solution diverges at $k = 1/2$, which is exactly equal to the free-wave interaction obtained by setting $\omega_1^{(0)} = \omega_1^{(2,3)}$. An inner solution for this root can be obtained near $k = 1/2$. But we are specifically interested in the two roots, $\omega_0 = -k$. Because this root has a multiplicity of two (Nayfeh (1985)), the asymptotic form for small J away from $k = 1/2$, the outer solution, can be written as

$$\omega_{outer}^{(2,3)} = \omega_0^{(2,3)} + J^{1/2}\omega_1^{(2,3)} + O(J), \tag{2.74}$$

where

$$\omega_1^{(2,3)} = \pm i\left[\frac{k}{\frac{1}{2}-k}\left(k - \frac{1}{2} + \frac{1}{2}e^{-2k}\right)\right]^{1/2}. \tag{2.75}$$

This solution again diverges at $k = 1/2$. An inner solution can be obtained near $k = 1/2$ as a solution of the equation

$$\omega_1^2\left(\frac{1}{2} - k + J^{1/3}\omega_1\right) = -J^{1/3}\frac{k}{2}e^{-2k}, \tag{2.76}$$

and the expansion in the inner region takes the form

$$\omega_{inner}^{(2,3)} = \omega_0^{(2,3)} + J^{1/3}\omega_1^{(2,3)} + O(J). \tag{2.77}$$

The regular form of this expansion clearly suggests that the continuous spectrum modes destabilize upon introducing density inhomogeneity in the system. Due to the presence of shear below the vorticity interface, continuous spectrum is localized in this region. In other words, the role of shear is therefore to facilitate the existence of a continuum of modes, which subsequently destabilize for any density inhomogeneity.

2.4 Summary

The main goal of this chapter was to gain a physical understanding of instabilities in shear layers and stratified shear flows. The stability of a mixing layer profile was therefore revisited, and an initial value problem was solved. The role of wave interactions was examined in detail. The linear wave interaction mechanism is shown to give a physical picture of the instability process. The IVP calculation of the mixing layer profile showed that wave-like disturbances on the two interfaces $y = \pm 1$, initially travel like free waves, slowing each other down and eventually freeze into a normal mode structure. We then considered the stability of a model stratified shear flow. The physical mechanism of internal wave propagation was discussed in detail. The interaction of a Rossby wave with a stable density interface was then studied. Specifically, we showed how a neutrally stable

Rossby wave can interact with a neutrally stable density wave leading to exponential growth. This is the simplest problem where we can explicitly show how stable density stratification can destabilize a flow. In the next chapter, the wave-interaction ideas are extended to a vortex geometry.

CHAPTER 3

STABILITY OF RADIALLY STRATIFIED VORTEX

Scope of this chapter[1]

In this chapter, we extend our study of density stratified flows to a rotating flow. We consider an exactly analogous problem to the one studied in the previous chapter, but now for an axisymmetric swirling flow. We study the stability of this flow with an axisymmetric density distribution. We restrict our study to two dimensions and neglect gravity. If gravity were present, then the problem would not be analytically tractable. Hence the simplification. A schematic of the flow geometry is shown in fig.(3.1).

Two specific configurations are studied, one, where density of the fluid decreases monotonically away from the vortex axis leading to a heavy-cored vortex, and two, where density increases monotonically away from the vortex axis leading to a light-cored vortex. The latter configuration receives the bulk of our attention in this study. Earlier studies have revealed that heavy-cored vortices can be unstable to a Rayleigh-Taylor instability (RTI) which eventually splits the vortex into smaller, but stronger vortices. It has been mentioned in earlier studies that shear outside the vortex core can stabilize the RTI. Here we show that shear acts as a destabilizing agent for light-cored vortices, a result not found earlier. Starting with a simple piece-wise model, the origin of this non-intuitive destabilization is clarified. A closer examination of the critical layer is necessary to understand instability in this case, and asymptotic solutions for growth rate are given at small Atwood number. The instability is shown to be due to a linear wave interaction between a discrete Kelvin wave and an internal wave due to density contrast. The simplified model is then extended to consider smooth vorticity and density profiles, where it is argued that the same wave interaction mechanism is now supported due to the presence of *quasi-modes*. It is shown that continuous spectrum modes of the flow profile destabilize upon introduction of a density inhomogeneity in the system in a certain range of radii immediately outside the core. We then study the nonlinear stages using full direct numerical simulations. The initial exponential instability of light-cored vortices is arrested due to a restoring centrifugal buoyancy force leading to stable non-axisymmetric structures in the flow.

3.1 Review of relevant literature

Density variation in the neighbourhood of vortices occurs in many natural systems and technological applications. A large scale geophysical vortex can be subjected to strong density variations, often along its axis, and occasionally perpendicular to it. The latter

[1] A large portion of this chapter's contents have been submitted for publication in J. Fluid Mech.

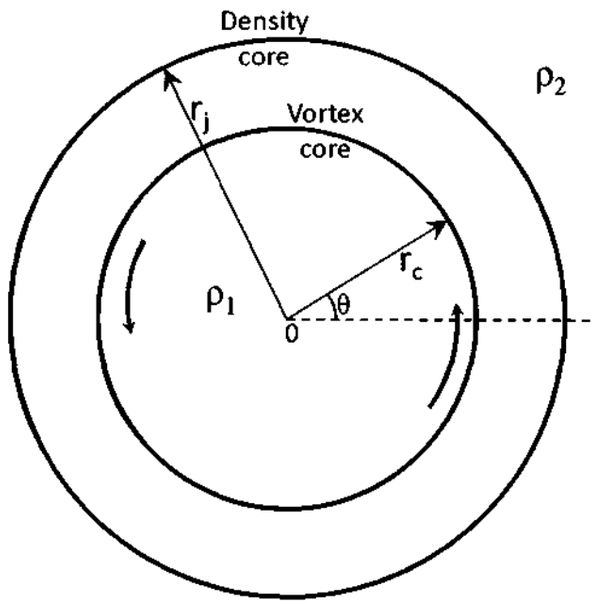

Figure 3.1: A schematic view of an axisymmetric vortex with an axisymmetric density distribution. Solid circles indicated the location of the vortex cores, either sharp or smooth. r_c and r_j are the radii of vortex and density cores respectively. Density at the vortex axis is ρ_1 and far-field density is ρ_2.

configuration, especially in the form of an axisymmetric flow with radial density variations, has been the subject of numerous papers, and is under study here. A heavy-cored vortex, where the density is a monotonically decreasing function of radius, can undergo a centrifugal Rayleigh-Taylor instability (CRTI), analogous to the Rayleigh Taylor instability (RTI) that occurs when a heavy fluid is placed above a lighter fluid. Just as gravity acting downwards triggers the RTI, centrifugal acceleration acting radially outwards renders the heavy-cored vortex flow potentially unstable. However, unlike the classical RTI which can exist without a mean flow, centrifugal forces are generated due to the vortex, and this makes the analogy incomplete. A more direct theoretical analog of the planar RTI is a radial density variation in a flow which is entirely in solid-body rotation, where shear is absent. Such a configuration was investigated by Fung & Kurzweg (1975) with an algebraically varying density. They also study the 3D stability of a radially stratified Rankine-type vortex, but the density jump was fixed at the edge of the core. This work was a generalization of the earlier study of Uberoi *et al.* (1972) on the stability of a Rankine vortex. In later work, Fung (1983) studied the stability of a three layer rotating fluid, each region with a fixed angular velocity and density. This is analogous to the planar three layer fluid first considered by Taylor (1931). In geophysical flows, there is an interest in understanding the baroclinic instability process, discussed in detail in Vallis (2006). It was shown by Saunders (1973) experimentally that radial density variation in a baroclinic vortex drives a CRTI. For an idealized compressible fluid rotating in a

pipe, Gans (1975) considered density variations in the radial direction, and noted that the stability depends on a 'centrifugal Richardson number'.

In all the above studies, shear does not play a role. We shall see below how the presence of shear in a vortical flow can have important implications for the stability of the system. In particular, it will be shown that shear can cause the destabilization of a light-cored vortex, or stabilize a heavy-cored vortex. The latter situation finds some mention in Joly *et al.* (2005), but the former has not been seen before, to our knowledge. In parallel flows, various combinations of density stratification and shear have been well investigated. As an extension of the popular semi-circle theorem of Howard (1961), a semi-ellipse criterion for plane stratified flows was derived by Kochar & Jain (1979) to define the possible range of phase speeds. This theorem was shown to hold for the cylindrical case as well by Fung (1983), and applies to the present flow of a vortex with radial density stratification.

Kurzweg (1969) was one of the earliest to consider non-axisymmetric disturbances, and derived a sufficient condition for stability for a smooth vortex. The stability of a heavy-cored Gaussian vortex with a Gaussian density distribution was studied by Sipp *et al.* (2005) and Joly *et al.* (2005). These studies are complimentary to each other. While the former show that a competition between 3D centrifugal instabilities and 2D Rayleigh-Taylor instabilities can occur, the latter restrict their analysis to two dimensions and include the nonlinear stages of RTI. Here, in agreement with Coquart *et al.* (2005) they show that wave-like motions on the vortex core amplify and result in the breakdown of the vortex into multiple parts, reminiscent of the breakdown of a baroclinic vortex observed by Saunders (1973). The number of parts is governed by the wavenumber of the linear perturbation. These workers found that CRTI is stabilized for density core sizes comparable to the vortex core, and realized that shear has a role to play in the stabilization. Incidentally, a similar mechanism was predicted by Lees (1958) in boundary layer flow over a convex surface.

Importantly, Joly *et al.* (2005) noted that a light-cored Gaussian vortex, where density increases monotonically away from the vortex centre, is always stable. Our work confirms their result for a Gaussian vortex, but we show that the smoothness of the vortex profile plays a crucial role, so a light-cored vortex is not always stable. This result may appear counter-intuitive at first sight, but is shown to be a natural consequence of wave interactions. Using a Rankine vortex and a step density jump located at a given radial location, we explicitly show that the Kelvin wave supported at the edge of the vortex core is allowed, due to shear, to interact with density waves, leading to stabilization/ destabilization. For a Gaussian vortex however, shear and vorticity gradient co-exist everywhere, and this clouds the interaction between the two. In our recent work on a more generic density stratification (Dixit & Govindarajan (2010)), we obtained one instance of a Rankine vortex surrounded by lighter fluid immediately outside the core, where a configuration which is unstable in terms of density stratification is rendered neutrally stable. A desire to understand this result motivated the present study.

In chapter 2, it was shown that a neutral Rossby wave and a neutral internal wave can interact with each other causing an instability. In the present flow, the interaction is between Kelvin waves riding on the vortex core, and internal waves riding on the density interface. The Kelvin waves are analogous to Rossby waves due to a potential vorticity

gradient, and are sometimes referred to by this name (see McWilliams *et al.* (2003); Schecter & Montgomery (2003)). We neglect gravity, so the internal waves are caused solely by centrifugal forces. The wave interaction is easy to obtain analytically when both vorticity gradient and density profiles are imposed in the form of step functions. However, smooth vorticity profiles with monotonically decreasing vorticity do not support discrete Kelvin waves. We hypothesize that the wave interaction mechanism is now between the quasi-modes from the vorticity field and internal waves from the density field. For this we follow the work of Briggs *et al.* (1970) and of Schecter *et al.* (2000) showing that when a piecewise continuous profile is smoothened, discrete modes are replaced by quasi-modes, which are a collective response of the continuous spectrum modes. A detailed mathematical treatment of quasi-modes in boundary layer flows is available in Shrira & Sazonov (2001), along with a discussion on the usage of piecewise linear approximations in stability theory.

The present work is the first to our knowledge where a quasi-mode, which is exponentially decaying, and a neutral discrete mode are shown to interact to give exponential growth. However there have been some studies which have investigated the interaction between continuous spectrum modes and discrete modes. Voronovich *et al.* (1998*a*,*b*) study the interaction of boundary layer quasi-modes with internal gravity waves in the ocean. Similarly Voronovich & Rybak (1978) and Romanova & Shrira (1988) study the interaction of boundary layer quasi-modes with gravity-capillary waves at an air/water interface. Sazonov (1989) showed that the resonant interaction between discrete spectrum and continuous spectrum modes leads to a linear growth of disturbances in time, and provided a physical interpretation of this algebraic instability. Vanneste (1996) also considered an interaction between discrete (regular) and continuous (singular) spectrum modes, and clarified that when dealing with continuous spectrum interaction, one needs to consider a packet of these modes together. As a result, contribution of continuous spectrum modes appear in terms of integrals over the physical domain, with quasi-modes being a special case.

The chapter is organized as follows. The problem is formulated in section 3.2. Base flow profiles and the governing equations are discussed here. The case of a Rankine vortex with step density jump is considered in section 3.3, and the mechanism is elaborated for heavy and light cored vortices. We then extend the stability of light-cored vortices to smooth profiles in section 3.4. Landau poles for various vorticity profiles are extracted, and their connection to quasi-modes is discussed. A linear initial value problem is solved numerically for comparison. Results from direct numerical simulations for light-cored vortices are presented in section 3.6 and concluding remarks are made in section 3.7.

3.2 Formulation

We consider the range of vorticity profiles from a Rankine to a Gaussian vortex. The density jump may also be step-like or smooth, and can be located at any radial location.

3.2.1 Base flow profiles

We define a family of vorticity profiles with the same circulation as that of a Gaussian vortex of core size a. The vorticity profile depends on a single parameter n in the following way,

$$Z = Z_0 \exp\left[-\left(\frac{r}{\delta_z}\right)^{2n}\right]. \tag{3.1}$$

The core size δ_z is defined as

$$\delta_z = a\left[\frac{n}{\Gamma(1/n)}\right]^{1/2}, \tag{3.2}$$

so that the circulation takes a fixed value of $\pi Z_0 a^2$ for all n. At $n = 1$, we obtain a Gaussian profile, and as $n \to \infty$, the profiles assume a step-like shape as shown in fig.(3.2). The total circulation is given by

$$\Xi \equiv 2\pi \int_0^\infty Z(r) r dr = \frac{\pi Z_0 \delta_z^2}{n}\Gamma(1/n) \tag{3.3}$$

where Γ is the gamma function. While we keep the numerical values of Z_0 and a fixed at 1 for simplicity, we retain these variables in the algebra for generality. The effect of smoothness can also be studied by imposing hyperbolic tangent profiles of varying width (see e.g. Hall *et al.* (2003)), but the present family was chosen for two reasons. The Gaussian profile at $n = 1$ makes for straightforward comparison with earlier work, and it is easier in (3.1) rather than with a tanh to enforce the same circulation for each profile. We believe our conclusions are valid for all types of smooth profiles. Since the vorticity for any n is monotonically decreasing, i.e.,

$$\frac{dZ}{dr} < 0, \tag{3.4}$$

for all r, discrete vorticity (Kelvin) modes do not exist (see Briggs *et al.* (1970)) except when $n = \infty$. In this limit we get a Rankine vortex, which supports a single discrete mode due to a vorticity discontinuity at $r = a$. An artifact of the family of profiles thus constructed is a small variation of the core size with n. From equation (3.2) we find that the core size δ_z is equal to unity for Rankine and Gaussian profiles, but is slightly higher for intermediate profiles, with a maximum of about 1.06 at $n \approx 2.17$.

Unless otherwise specified, density profiles are defined analogous to vorticity profiles as

$$\bar{\rho} = \rho_2 + (\rho_1 - \rho_2)\exp\left[-\left(\frac{r}{\delta_\rho}\right)^{2n}\right], \tag{3.5}$$

where δ_ρ is the density core size, ρ_1 is the density near the vortex centre and ρ_2 is the far-field value. We further define the location of the density interface, r_j, as

$$r_j = \frac{\delta_\rho}{\delta_z} a. \tag{3.6}$$

When $r_j > a$, the density core is larger than the vortex core. Another artifact of these

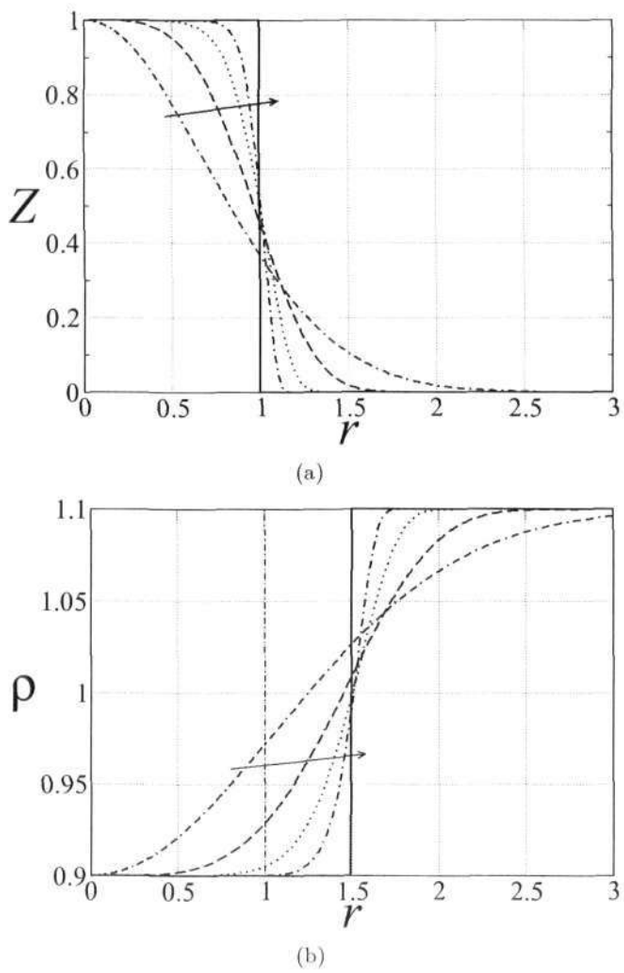

Figure 3.2: (a) Vorticity and (b) density profiles as functions of n. From left to right (indicated by arrow), $n = 1, 2, 4, 8, \infty$ going from a Gaussian to a step profile. In this representative figure, the core sizes for vorticity and density are chosen as $a = 1$ and $r_j = 1.5$ respectively, and the Atwood number $At = 0.1$.

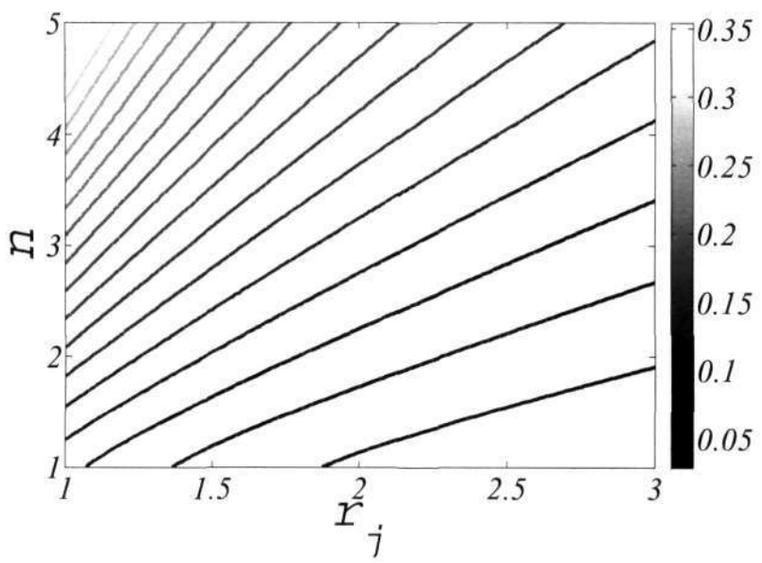

Figure 3.3: Dependence of the maximum density gradient, $\rho'(r)|_{max}$ on n and r_j. This value is a measure of the interface steepness, and internal wave properties depend on it.

profiles is that the density gradient varies with n and r_j. The maximum in the density gradient, $\rho'(r)|_{max}$, plotted in figure (3.3), is a measure of profile steepness. It can be seen that varying the location of the density jump affects the gradient value, and this becomes severe for large n. To overcome this difficulty, and more importantly, to estimate the effect of smoothing the vorticity profile alone, we make use of *tanh* density profiles in the stability analysis of section 3.4, defined by

$$\bar{\rho} = \frac{1}{2}\left[(\rho_1 + \rho_2) - (\rho_1 - \rho_2)\tanh\left(\frac{r - r_j}{\delta_t}\right)\right]. \tag{3.7}$$

For these profiles, steepness does not depend on r_j but is controlled by the factor δ_t, fixed here at a value of 0.1.

3.2.2 Governing equations

The appropriate governing equations are the two-dimensional Navier-Stokes equations in $r - \theta$ coordinates. A small amplitude perturbation (u'_r, u'_θ, ρ') is imposed on the axisymmetric base vorticity and density profiles. Using a Fourier decomposition in the azimuthal direction, i.e.,

$$[u'_r, u'_\theta, \rho'](r, \theta, t) = \mathrm{Re}\{[\tilde{u_r}, \tilde{u_\theta}, \tilde{\rho}](r, t)\exp[im\theta]\}, \tag{3.8}$$

the system of equations for $\tilde{\mathbf{y}} = [\tilde{u_r} \;\; \tilde{\rho}]$ can be written in the form

$$\frac{d}{dt}\mathcal{M}\tilde{\mathbf{y}} = -\mathbf{i}\mathcal{N}\tilde{\mathbf{y}}, \tag{3.9}$$

where the operators are given by

$$\mathcal{M} = \begin{bmatrix} \bar{\rho}\mathcal{L} + (\mathcal{D}\bar{\rho})r^2\mathcal{D}^* & 0 \\ 0 & 1 \end{bmatrix}, \tag{3.10}$$

$$\mathcal{N} = \begin{bmatrix} \bar{\rho}m(\Omega\mathcal{L} - r\mathcal{D}Z) + (\mathcal{D}\bar{\rho})m(\Omega r^2\mathcal{D}^* - rZ) & -im^2r\Omega^2 \\ -i\mathcal{D}\bar{\rho} & m\Omega \end{bmatrix}, \tag{3.11}$$

$$\mathcal{L} = r^2\mathcal{D}^2 + 3r\mathcal{D} - (m^2 - 1). \tag{3.12}$$

The azimuthal velocity component $\tilde{u_\theta}$ can be computed from $\tilde{u_r}$ using the continuity equation. Here $\Omega(r)$ is the angular velocity of the base state, $\mathcal{D} = d/dr$ and $\mathcal{D}^* = \mathcal{D} + 1/r$. The boundary conditions are that perturbations decay to zero at the vortex axis and as $r \to \infty$. The perturbation vorticity $\zeta(r,t)$ is related to $\tilde{u_r}$ and $\tilde{u_\theta}$ as

$$\zeta(r,t) = \frac{1}{r}\frac{\partial(r\tilde{u_\theta})}{\partial r} - \frac{im}{r}\tilde{u_r}. \tag{3.13}$$

For a normal mode in time,

$$[\tilde{u_r}(r,t), \tilde{u_\theta}(r,t), \tilde{\rho}(r,t)] = [u_r(r), u_\theta(r), \rho(r)]\exp[-i\omega t], \tag{3.14}$$

and a single equation in u_r can be written as

$$\mathcal{D}(\bar{\rho}r^2\mathcal{D}^*u_r) + \left[\frac{m^2r\Omega^2\;\mathcal{D}\bar{\rho}}{\left(\omega - \dfrac{mU}{r}\right)^2} + \frac{mr\;\mathcal{D}(\bar{\rho}\mathcal{D}^*(r\Omega))}{\left(\omega - \dfrac{mU}{r}\right)} - m^2\bar{\rho}\right]u_r = 0. \tag{3.15}$$

This equation is analogous to the Taylor-Goldstein equation for planar flow (Drazin & Reid (1981)), and has been derived earlier by Fung & Kurzweg (1975) and others. The boundary conditions are $u_r = 0$, at $r = 0$ for $m \geq 2$, and at $r \to \infty$. We will consider only wavenumbers $m \geq 2$ as $m = 1$ is only a translational mode in 2D, and does not alter the dynamics. The centrifugal acceleration $r\Omega^2$ in the first term in the bracket is analogous to gravity in a planar flow. Thus, unlike in the planar situation, internal waves supported by density inhomogeneity do not have an existence independent of the flow.

3.3 Stability of a Rankine vortex with density jump

The limit $n \to \infty$ corresponding to a Rankine vortex with a step density jump allows for analytical solutions, and is therefore considered in some detail. We keep the location of the density jump arbitrary. When the vorticity is constant everywhere, i.e., the flow is in solid-body rotation, Fung (1983) showed that no instability can occur when $D\bar{\rho} > 0$,

an intuitive result. We repeat this proof for clarity. Substituting $\Omega(r) = \Omega_0$, $c = \omega/m$ and $u_r = \Psi/r$ in equation (3.15), we get,

$$\mathcal{D}(\bar{\rho} r \mathcal{D}\Psi) + \left[\frac{-m^2\bar{\rho}}{r} + \Lambda \mathcal{D}\bar{\rho}\right]\Psi = 0, \tag{3.16}$$

$$\text{where } \Lambda = \frac{\Omega_0^2}{(c-\Omega_0)^2} + \frac{2\Omega_0}{(c-\Omega_0)}. \tag{3.17}$$

Equation (3.17) along with homogeneous boundary conditions at $r = 0$ and ∞ forms a Sturm-Liouville system, so Λ is purely real, with the same sign as $\mathcal{D}\bar{\rho}$. Rewriting (3.17) as

$$c = \Omega_0\left[\frac{(1+\Lambda) \pm \sqrt{1+\Lambda}}{\Lambda}\right], \tag{3.18}$$

we see that a density jump from light to heavy is always stable, since Λ is now positive and so c has only real solutions. Note however that the reverse case of a heavy core is not unstable unless $\Lambda < -1$.

On the other hand, for the irrotational flow near a point vortex, where angular velocity varies as $\Omega = \Gamma/r^2$, we get

$$\Lambda = \frac{1}{(c-\Omega)^2}. \tag{3.19}$$

Again we arrive at the result that there is no instability when $\mathcal{D}\bar{\rho} > 0$, but when $\mathcal{D}\bar{\rho} < 0$, there is always an instability. In our flow, a density jump placed at $r << a$ or $r >> a$ respectively resemble the limits of solid body rotation or a point vortex. A positive density jump being stable in either of these limits, one may expect a light-cored vortical flow to be stable wherever the jump is placed. This will be shown below to be not true. The reason is that while equation (3.15) can be reduced to equation (3.17) either inside or outside the vortex core, it still is not a Sturm-Liouville system as homogeneous boundary conditions are not satisfied at $r = a$, a region of non-zero vorticity gradient. There is thus an opportunity for different behaviour if the jump is placed at $r \sim a$.

The $n \to \infty$ limit may be described as

$r \le a$	$a < r \le r_j$	$r > r_j$
$Z = Z_0$	$Z = 0$	$Z = 0$
$\Omega = \Omega_0$	$\Omega = \Omega_0 a^2/r^2$	$\Omega = \Omega_0 a^2/r^2$
$\bar{\rho} = \rho_1$	$\bar{\rho} = \rho_1$	$\bar{\rho} = \rho_2$

(3.20)

The general solution of equation (3.15) in the above three regions is in the form of $r^{(m-1)}$ and $r^{(-m-1)}$. In appendix A, the eigenfunctions u_r are given along with the necessary steps for the derivation of the dispersion relation. Non-dimensionalizing ω by the maximum core vorticity Z_0, a cubic eigenvalue equation can be obtained from equation (3.15) as follows:

$$\omega^3 + a_2\omega^2 + a_1\omega + a_0 = 0, \tag{3.21}$$

where

$$a_2 = \frac{1}{2}\left(1 - m(1+2\left(\frac{a}{r_j}\right)^2) + At\left(\frac{a}{r_j}\right)^{2m}\right), \tag{3.22}$$

$$a_1 = \frac{m}{4}\left(2(m-1)\left(\frac{a}{r_j}\right)^2 - 2At\left(\frac{a}{r_j}\right)^{2m+2} + (m+At)\left(\frac{a}{r_j}\right)^4\right), \tag{3.23}$$

$$a_0 = \frac{m(m-1)}{8}\left(At\left(\frac{a}{r_j}\right)^{2m+4} - (m+At)\left(\frac{a}{r_j}\right)^4\right), \tag{3.24}$$

and $At = (\rho_1 - \rho_2)/(\rho_1 + \rho_2)$ is the Atwood number. In the homogeneous fluid limit of $At = 0$, equation (3.21) is solved to give a 2D Kelvin mode, $\omega_0^{(1)}$, on the vortex core boundary, and a single continuous spectrum mode, $\omega_0^{(2,3)}$, at any $r = r_j$ given by

$$\omega_0^{(1)} = (m-1)/2, \qquad \omega_0^{(2,3)} = \frac{ma^2}{2r_j^2}. \tag{3.25}$$

The subscript 0 denotes the case of $At = 0$[2]. The discrete mode is obtained due to a non-zero vorticity gradient at $r = a$. The critical radius for the Kelvin mode is obtained by equating the two solutions of equation (3.25) giving

$$r_c = a\sqrt{\frac{m}{m-1}}. \tag{3.26}$$

The angular speed of the base flow at this radius is equal to that of the Kelvin mode. In a frame of reference rotating with this speed, disturbance waves rotate in opposite directions on either side of r_c. The continuous spectrum outside the core can result in interesting behaviour for $At \neq 0$. Romanova (2008) for instance showed that the continuous spectrum modes of a homogeneous flow can become unstable eigenmodes in the presence of density stratification. We therefore restrict out study to the region $r_j > a$.

3.3.1 Heavy-cored Rankine vortex

We first consider $At > 0$, which means that fluid within r_j is heavier than that outside it. Following the standard methods of solving a cubic equation (Press *et al.* (1992)), a criterion for instability can be derived. As the general criterion is cumbersome, we give here the small At approximation, retaining up to $O(At)$. For instability we require

$$\mathcal{P} = \left(1 - m + m\left(\frac{a}{r_j}\right)^2\right)^3\left(1 - m + m\left(\frac{a}{r_j}\right)^2 - \left(\frac{a}{r_j}\right)^{2m}\right) > 0. \tag{3.27}$$

Figure (3.4) shows curves of $\mathcal{P}$ plotted as a function of r_j/a. The zero crossing occurs when the jump is placed exactly at the critical radius, i.e., $r_j = r_c$. As the Atwood

[2]The continuous spectrum of a Rankine vortex is studied in detail in forthcoming work of A. Roy and G. Subramanian.

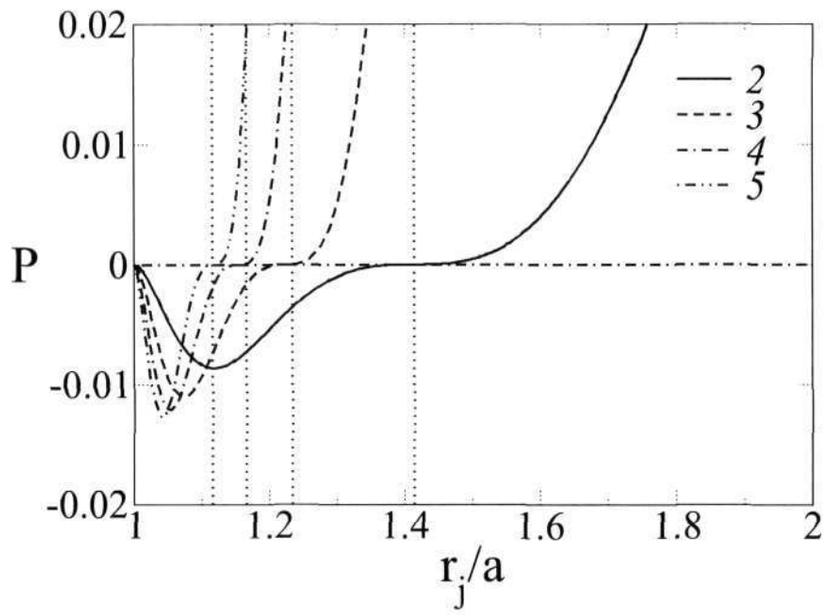

Figure 3.4: Curves of $\mathcal{P}$ from equation (3.27) plotted as a function of the density jump location r_j/a for various wave numbers. In the limit of small At the flow is unstable when $\mathcal{P} > 0$. The dotted vertical lines indicating the zero crossings of $\mathcal{P}$ coincide in each case with the critical radius for the Kelvin mode obtained from equation (3.26).

number increases, a jump placed anywhere outside r_c becomes increasingly unstable, and the unstable range encroaches within r_c as well, but the flow is neutrally stable for a range of r_j immediately outside the Rankine core. This can be seen in fig.(3.5(a)) where the growth rate is plotted as a function of the Atwood number for a fixed wavenumber $m = 2$. Fig. 3.5(b) shows that a neutral region exists for all m. Here no assumption is made on the smallness of At. The complete dispersion relation in the $At - r_j/a$ plane for $m = 2$ is plotted in fig.(3.6) where a region of stabilization can clearly be seen for small At and r_j/a. For a density jump which coincides with the core, i.e., $r_j = a$, equation (3.21) reduces to the simple form

$$\omega = \frac{m}{2} - \left[\frac{(1+At)}{4}\left(1 \pm \sqrt{1 - \frac{4mAt}{(1+At)^2}}\right)\right]. \tag{3.28}$$

Therefore instability occurs at the core only if

$$m > \frac{(1+At)^2}{4At}. \tag{3.29}$$

When $m = 2$, this condition is met when $At > 0.171$, and for $m = 3$, when $At > 0.101$. A physical explanation of this stabilization is given in section 3.3.3.

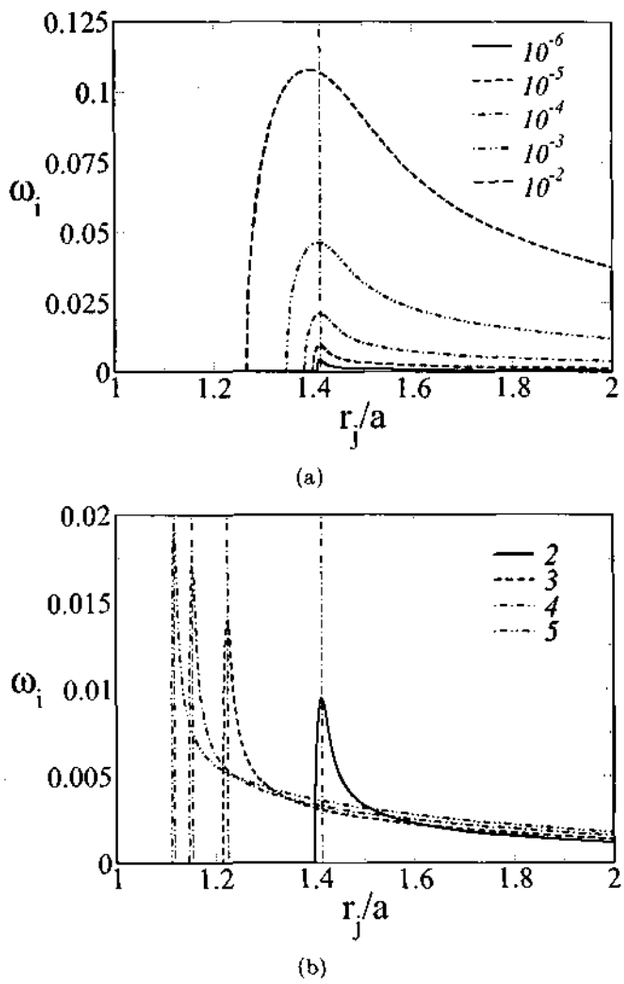

Figure 3.5: Growth rate for a heavy-cored Rankine vortex as a function of density jump location. (a) For various Atwood numbers for $m = 2$. At increases upwards in powers of 10 starting from 10^{-2}. (b) At fixed $At = 10^{-5}$ for various m. In both plots, the dash-dot vertical lines indicate the critical radius obtained from equation (3.26).

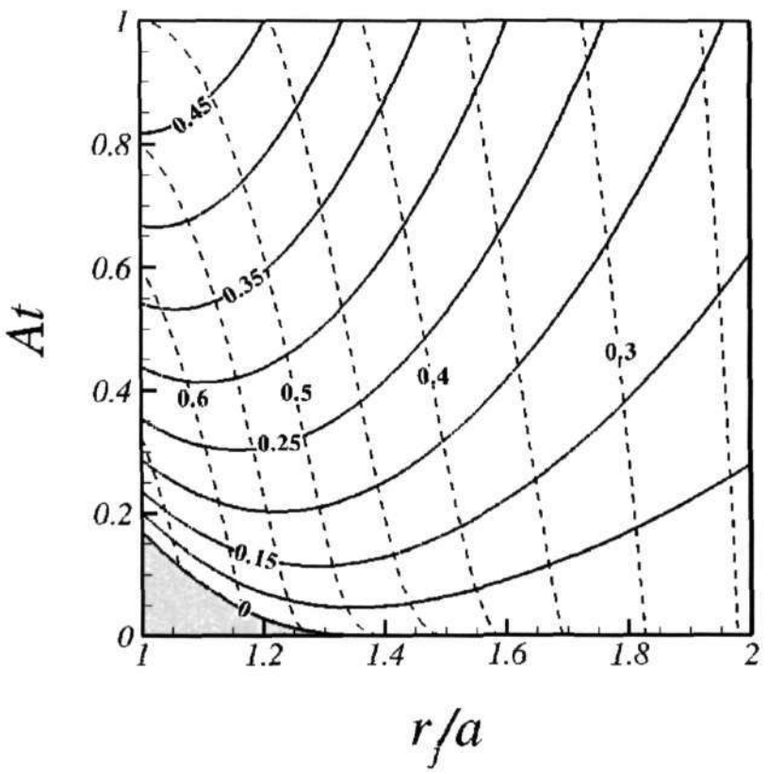

Figure 3.6: Contours of growth rate in the $At-r_j/a$ plane for heavy-cored vortex ($At > 0$). Only the region outside the core is indicated, since a density jump within the core would be stable. Solid lines indicate growth rate, and dashed lines the frequency. Gray shading represents neutral regions.

3.3.2 Light-cored Rankine vortex

If unstable density stratification can be stabilized, then the natural question that arises is whether the reverse is also true, i.e. can a light-cored vortex flow ever be unstable. To put the present results in perspective, it is re-emphasized that the earlier work of Sipp *et al.* (2005) and Joly *et al.* (2005) did not find any destabilization for any density contrast using Gaussian profiles. In this subsection we see that a Rankine core with a step density jump can be unstable. In the next section, we show that instability occurs only for steep profiles.

For a light-cored vortex, $At < 0$. At low $(-At)$, instability now occurs when $\mathcal{P}$ in equation (3.27) is less than 0. From equation (3.26) and fig.(3.7), it is again seen that instability first occurs at the critical radius as the Atwood number is increased (negatively) from zero. Instability is now confined to the region immediately outside the core as shown in figures 3.8(a) and 3.8(b). The three solutions of equation (3.21), named $\omega^{(1)}$, $\omega^{(2)}$ and $\omega^{(3)}$ may be obtained from series expansions in Atwood number. We derive an outer solution denoted by a superscript o, valid away from the critical radius and an

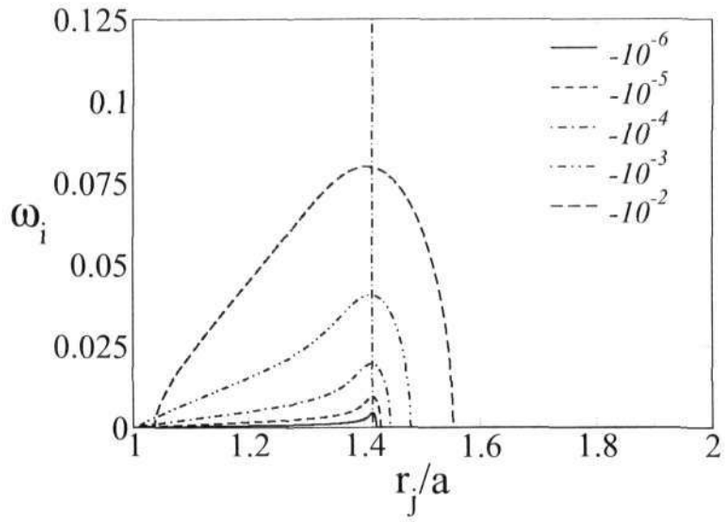

Figure 3.7: Variation of growth rate with Atwood number for $m = 2$. The vertical dash-dot line indicates r_c.

inner solution, denoted by a superscript i, valid in the neighbourhood of the critical radius.

The first solution, corresponding to the Kelvin wave riding on the vortex core boundary in the homogeneous case, takes the asymptotic form

$$\omega^{(1),o} = \omega_0^{(1),o} + (-At)\ \omega_1^{(1),o} + O(-At)^2, \tag{3.30}$$

where

$$\omega_0^{(1),o} = \frac{m-1}{2} \quad \text{and} \tag{3.31}$$

$$\omega_1^{(1),o} = \frac{(m-1)\left(\frac{a}{r_j}\right)^{2m}\left[(m-1) - 2m\left(\frac{a}{r_j}\right)^{2m} + m\left(\frac{a}{r_j}\right)^4\right]}{2(m-1)^4 - 4m(m-1)\left(\frac{a}{r_j}\right)^2 + 2m^2\left(\frac{a}{r_j}\right)^4}.$$

This solution diverges at the critical radius r_c, but since it gives rise to no instability, that neighborhood is not studied in detail. The other two solutions, which describe the continuous spectrum modes localized at $r = r_j$, take the asymptotic form

$$\omega^{(2,3),o} = \omega_0^{(2,3),o} + (-At)^{1/2}\ \omega_1^{(2,3),o} + O(-At), \tag{3.32}$$

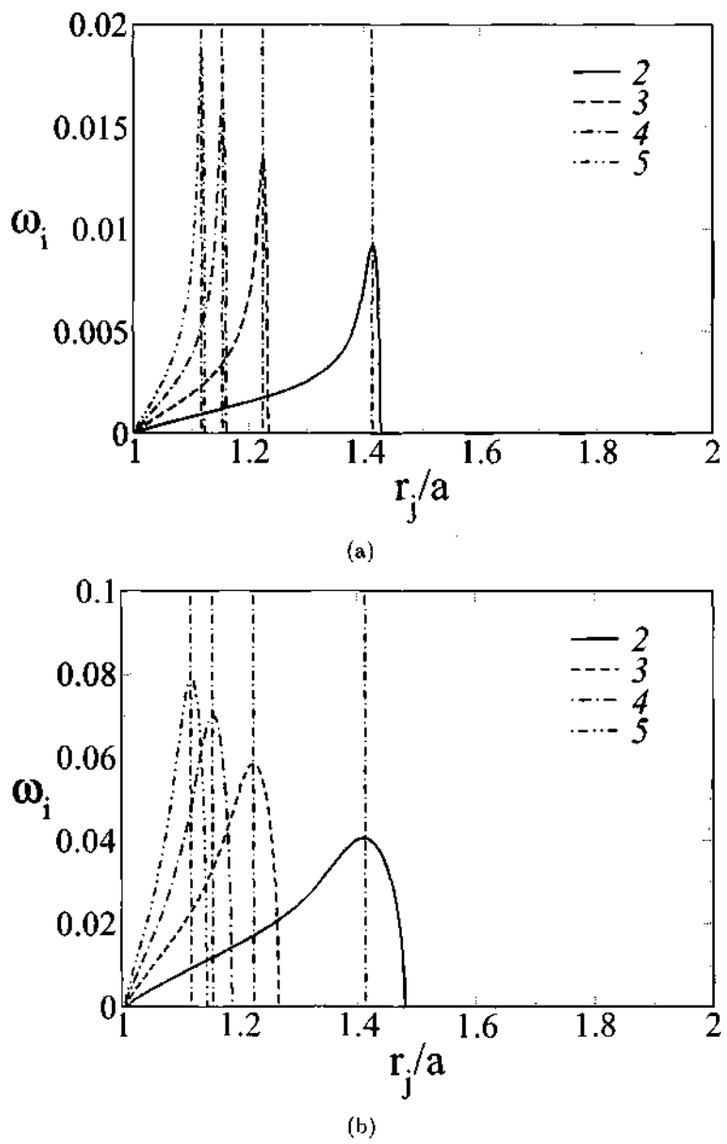

Figure 3.8: (a) Variation of growth rate with the jump location for a light-cored Rankine vortex at (a) $At = -10^{-5}$, (b) $At = -10^{-3}$. The dash-dot vertical line indicates r_c.

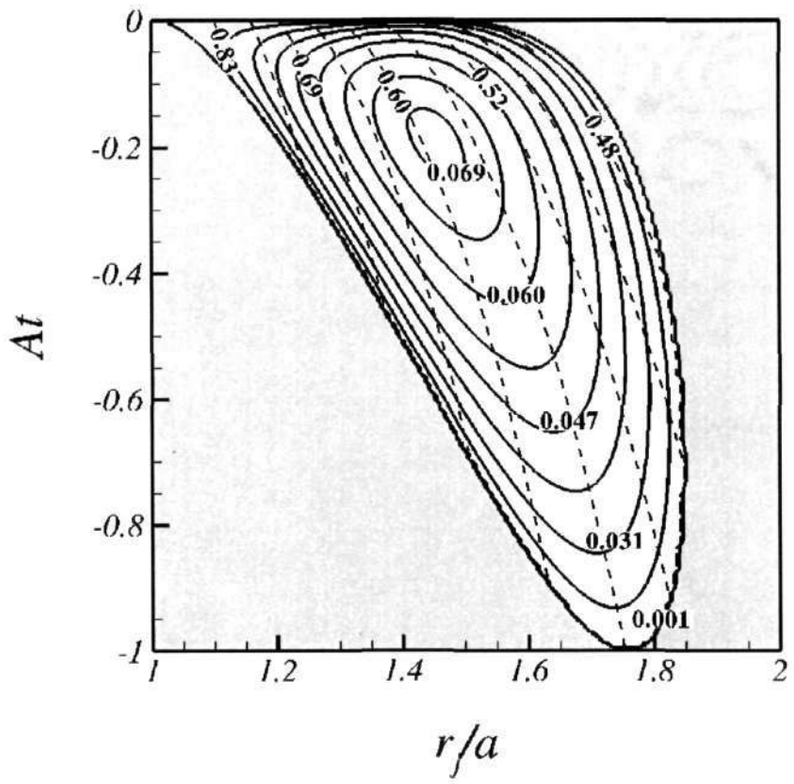

Figure 3.9: Contours of growth rate in the At-r_j plane for a light-cored vortex ($At < 0$). Solid lines indicate growth rate and dashed lines indicate frequency. The gray shading represents a neutral region.

with

$$\omega_0^{(2,3),o} = \frac{ma^2}{2r_j^2}, \qquad \text{and} \tag{3.33}$$

$$\omega_1^{(2,3),o} = \pm \left[\frac{-3\left(\frac{a}{r_j}\right)^{2m+4}(2m^2+m) - 3m(m-1)\left(\frac{a}{r_j}\right)^4 + 4m^2\left(\frac{a}{r_j}\right)^6}{12(m\left(\frac{a}{r_j}\right)^2 - (m-1))} \right]^{1/2}.$$

These solutions too diverge at the critical radius. An inner solution in this neighborhood takes the asymptotic form

$$\omega^{(2,3),i} = \omega_0^{(2,3),i} + (-At)^{1/3}\omega_1^{(2,3),i} + O(-At)^{2/3}, \tag{3.34}$$

where the correction term $\omega_1^{(2,3),i}$ is obtained as a solution to the equation

$$\omega_1^2\left(\frac{m}{2}\left(\frac{a}{r_j}\right)^2-\frac{m-1}{2}+(-At)^{1/3}\omega_1\right) \tag{3.35}$$
$$=(-At)^{1/3}\,\frac{m}{8}\left(\frac{a}{r_j}\right)^4\left(m\left(\frac{a}{r_j}\right)^2-(m-1)-\left(\frac{a}{r_j}\right)^{2m}\right).$$

Thus a continuous spectrum mode localized at $r = r_j$ becomes unstable with a growth rate increasing as $|At|^{1/2}$ when $r_j >> r_c$. In a small region around the critical radius of the Kelvin wave the growth rate increases faster, as $|At|^{1/3}$.

3.3.3 Physical Mechanism

In Sections 3.3.1 and 3.3.2, we showed that a heavy-cored Rankine vortex can be stabilized and a light-cored Rankine vortex destabilized. We now examine the physical mechanism behind this process. Our argument proceeds as per the wave-interaction mechanism proposed in many earlier studies on other shear flows, e.g. for counter-propagating Rossby waves (Hoskins *et al.* (1985)). The mechanism relies on the existence of two differentially moving free[3] waves, which can slow each other down relatively until they settle into a normal mode. In our flow, the interaction is between internal waves at the density interface and a Kelvin wave on the Rankine vortex. To understand these, we examine separately a radial density interface around a point vortex, and a Rankine vortex in a homogeneous density. The replacement of the Rankine vortex by a point vortex of the same circulation ($= \Omega_0 a^2$), is valid in the limit $r_j >> a$, and incidentally at low Atwood numbers, is also found to be good for r_j near the vortex core. Solving equation (3.15), the dispersion relation reduces to

$$\omega_p = \frac{m\Omega_0 a^2}{r_j^2}\left[1 \pm i\left(\frac{At}{m}\right)^{1/2}\right], \tag{3.36}$$

where the subscript p denotes a point vortex. When $At = 0$, the eigenvalue reduces to the corotation frequency at $r = r_j$. For a point vortex, whether or not $At = 0$, and independently of the eigenvalue, the vortex sheet strength takes the simple form of the continuous spectrum mode for a point vortex

$$\zeta_{j,p} = -2ir_j^{-m-1}\delta(r - r_j). \tag{3.37}$$

The interface displacement is given by

$$\eta_{j,p} = \frac{ir^{-m-1}}{\omega_p - m\Omega_0\dfrac{a^2}{r_j^2}}. \tag{3.38}$$

[3]Free waves are neutral waves having an independent existence. They are associated with perturbation vorticity localized in space. The 2D Kelvin mode of a Rankine vortex is an example.

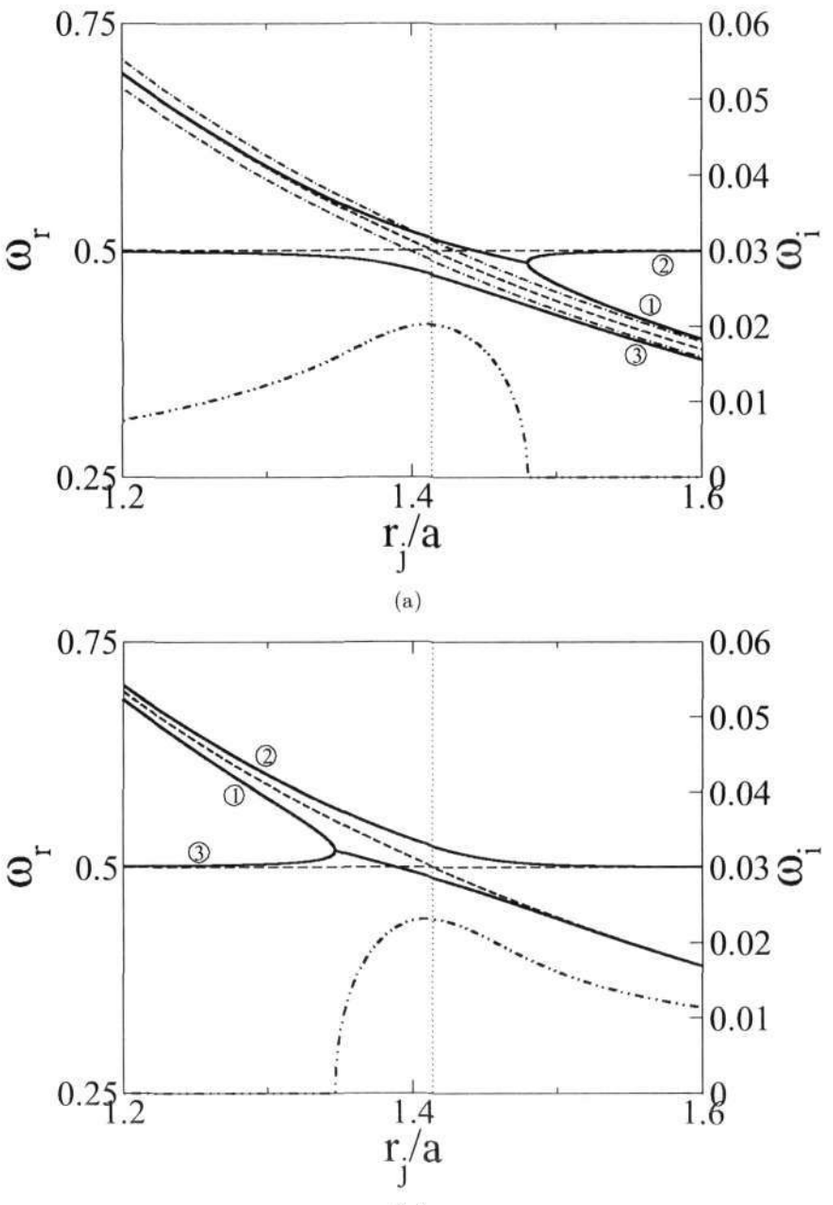

Figure 3.10: Variation of frequencies (solid lines) and growth rates (dash-dot-dot) with radial location of the density jump for (a) light and (b) heavy cored vortices with $m = 2$ and $At = \mp 10^{-3}$. The dashed curves are obtained by putting $At = 0$ corresponding to equation (3.25) and the vertical dotted line shows r_c. In (a), dash-dot curves indicate the frequencies obtained for a point-vortex system using equation (3.36).

To understand the wave-interaction mechanism, it is necessary to examine the phase difference between the two interfaces and their corresponding vortex sheets. With a point vortex, when $At < 0$ (light-core), the flow is always neutrally stable, and the vortex sheet strength, $\zeta_{j,p}$ is either in phase or anti-phase with $\eta_{j,p}$. The two neutral modes travel in opposite directions with respect to the local mean flow at r_j as shown in the dash-dot lines in figure (3.10(a)). But when $At > 0$ (heavy-core), the flow is always unstable and $\zeta_{j,p}$ is at a maximum at the nodes of the interface. Both unstable and stable modes are stationary with respect to the local mean flow (figure 3.10(b)). A homogeneous Rankine vortex offers a Kelvin wave of frequency $(m-1)\Omega_0$, shown by the horizontal dashed line in the figure. The eigenfunctions for the internal and Kelvin waves consist of vortex sheets at $r = r_j$ and $r = a$ respectively. The density wave of branch 1 for $At < 0$, which travels faster than the local mean flow, would be capable of interacting with the Kelvin wave to cause an instability. The three eigenvalue branches of the combined system, of a Rankine vortex with a density jump, are shown by solid lines in the same figure. At large r_j, branches 1 and 3, as expected, approach the point vortex solutions. The frequencies of branches 1 and 2 in fig. 3.10(a), and 1 and 3 in fig. 3.10(b), combine at a certain radius to give eigenvalues which are complex conjugates. The growth rates corresponding to the unstable one are shown by the dash-dot-dot lines. Using the eigenfunctions given in Appendix A, interface displacements and perturbation vorticity now take the forms

$$\eta_a = \frac{ia^{-m-1}}{\left[\left(\frac{r_j}{a}\right)^{2m}(\omega-(m-1)\Omega_0)-\Omega_0\right]}, \tag{3.39a}$$

$$\eta_j = \frac{ir^{-m-1}}{\omega - m\Omega\dfrac{a^2}{r_j^2}}, \tag{3.39b}$$

$$\zeta_a = \frac{2i\Omega_0 a^{-m-1}}{\left[\left(\frac{r_j}{a}\right)^{2m}(\omega-(m-1)\Omega_0)-\Omega_0\right]}\delta(r-a), \tag{3.40a}$$

$$\zeta_j = \frac{-2ir_j^{-m-1}\left[\left(\frac{r_j}{a}\right)^{2m}(\omega-(m-1)\Omega_0)\right]}{\left[\left(\frac{r_j}{a}\right)^{2m}(\omega-(m-1)\Omega_0)-\Omega_0\right]}\delta(r-r_j). \tag{3.40b}$$

For the purposes of the physical argument, ω above may be replaced by the point vortex eigenvalue.

Before describing an unstable light-cored vortex, it is useful to understand the neutral configuration, and our focus is on solution branches 1 and 2, which interact. For the Kelvin mode η_a and ζ_a are always in-phase. But the phase difference between η_j and ζ_j depends on r_j as well as on ω, which in turn depends on At. Using $\omega \approx \Omega_0 a^2/r_j^2$ and the

definition of r_c, we rewrite ζ_j as

$$\zeta(r_j) = -i \left[\frac{2r_j^{-m-1} \left(\frac{r_j}{a}\right)^{2m} ma^2}{\left(\frac{r_j}{a}\right)^{2m} ma^2 \left(\frac{1}{r_j^2} - \frac{1}{r_c^2}\right) - 1} \right] \left(\frac{1}{r_j^2} - \frac{1}{r_c^2}\right) \delta(r - r_j). \qquad (3.41)$$

The factor in the square brackets in equation (3.41) is negative for all r_j, and therefore the two vortex sheets at r_j and a are in-phase for $r_j > r_c$ and in anti-phase for $r_j < r_c$. The former was seen above to be in a neutral configuration. A schematic view of the twin vortex-sheet configuration supporting a neutral solution is shown in figure (3.11(a)). A positive (negative) interface displacement at the outer vortex sheet is associated here with a negative (positive) vorticity anomaly. Maximum radial and tangential velocities are indicated by straight solid and dashed arrows respectively. There is no component of u_r either abetting or impeding the interface displacement. This is the character of all neutral waves. If one rotates the Kelvin wave, being the faster moving, in the anti-clockwise direction, it can be worked out that the outer vortex sheet will respond so as to return the system to the original phase.

On the other hand when $r_j < r_c$, the vortex sheets are of opposite sign. For a growing mode, the interfaces should be positioned such that η_j lags η_a to within half a wavelength. In the most dangerous case, η_a and η_j are in anti-phase as shown in figure (3.11(b)). Here the disturbance velocity from the inner sheet causes η_j to grow. The Kelvin mode thus acts as a source of energy, absent in the point vortex case. This is the essential mechanism for the instability of a light-cored vortex. In other words, for a neutral wave, the kinematic condition, $D\eta/Dt = u_r$, results in the interface displacement and the normal velocity being always out of phase, i.e. there is no production of disturbance energy. Once the waves interact and a phase-locking occurs, η and u_r need no longer be out of phase, and an instability can result.

We now consider a heavy-cored vortex, and it is natural to begin with the unstable case. When $r_j >> a$, the growth rate for the Rankine vortex case is well described by the point vortex solution. The interface is subjected to the classical centrifugal Rayleigh-Taylor instability. Disturbance vorticity at the nodes of the unstable interface drives the interface progressively away from its initial position. Using $\omega \simeq \Omega_0 a^2/r_j^2$, it is easy to show that the two interfaces are displaced by a half-wavelength and the vortex sheets are in-phase with each other. This scenario is shown in figure (3.12(a)). The disturbance field from the Kelvin wave at $r = a$ adds to the growth of the density interface. This resonance is most fruitful near the critical radius r_c causing the growth rate to exceed the point vortex growth rate. We finally consider the stabilization of the heavy-cored vortex. For $r_j < r_c$, the frequency of the interacting branch 1 now satisfies the inequality $(m-1)\Omega_0 < \omega_r < m\Omega_0 a^2/r_j^2$. Therefore, this internal wave travels faster than the Kelvin wave. Using equations (3.39) and (3.40), we can shown that the two interfaces are perfectly in-phase with each other in the neutral configuration. Moreover, the vorticity disturbance created at the crests and troughs of the interfaces are exactly out-of-phase with each other. Such a configuration is seen in figure (3.12(b)), and u_r does not abet or

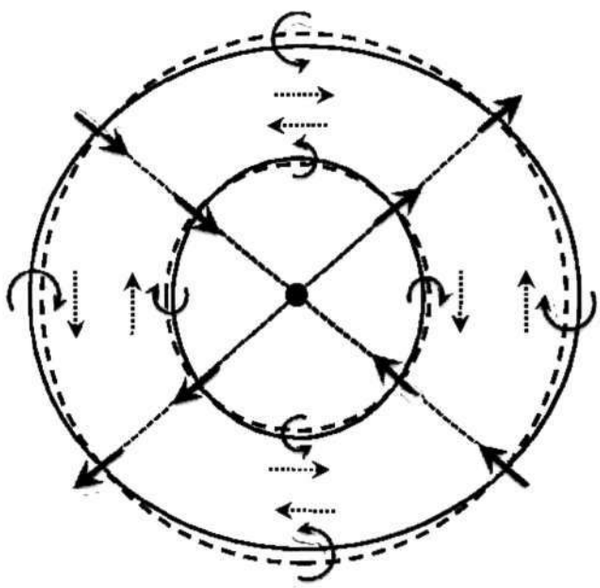

(a)

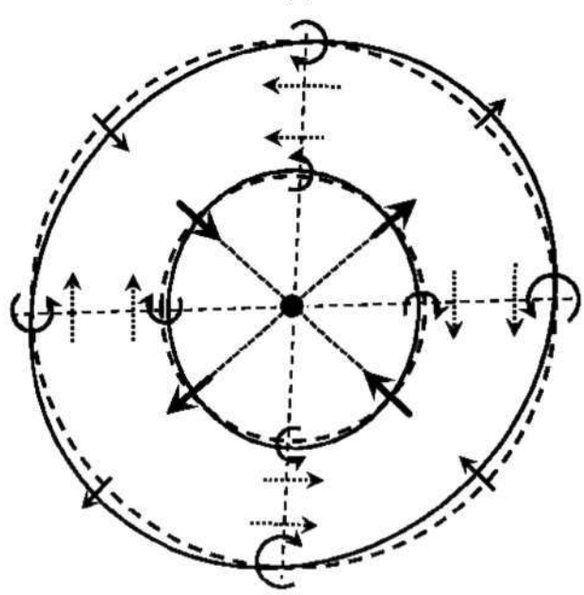

(b)

Figure 3.11: (a) Neutral configuration showing the interface position for the two waves at $r = a$ and $r = r_j$ for a light-cored Rankine vortex. The dashed and solid line circles indicate unperturbed and perturbed interfaces respectively. The straight solid arrows indicate the induced velocity at the nodes of the interfaces and dashed arrows indicate the direction of the tangential velocity disturbance. The circular arrows denote the disturbance vorticity, anticlockwise being positive and clockwise negative. (b) Unstable configuration for a light-cored Rankine vortex. The radial disturbance velocity from the inner vortex sheet destabilizes the outer sheet.

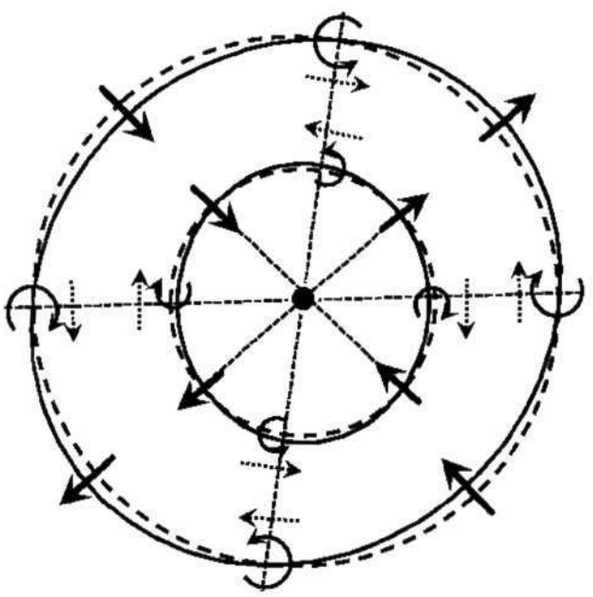

(a)

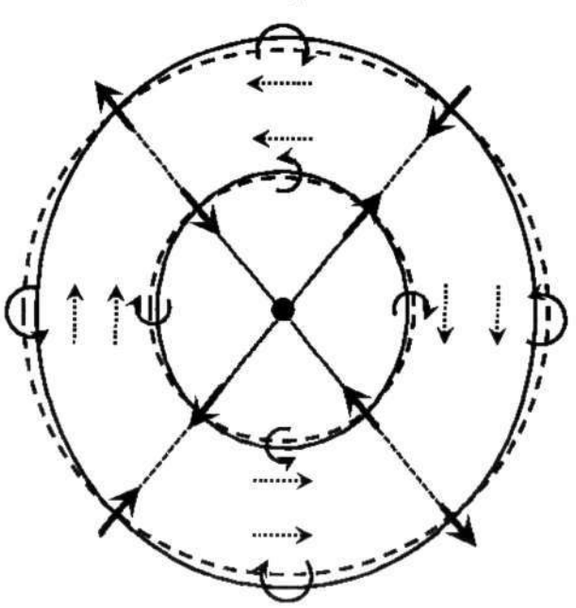

(b)

Figure 3.12: (a) A schematic of the centrifugal Rayleigh-Taylor instability of a heavy-cored Rankine vortex. The Kelvin mode at $r = a$ further reinforces the RTI, causing the growth rate to increase beyond the point vortex case. (b) Neutral configuration showing the interface position for the two waves at $r = a$ and $r = r_j$ for a heavy-cored Rankine vortex. The convention is the same as used in figure (3.11(a)).

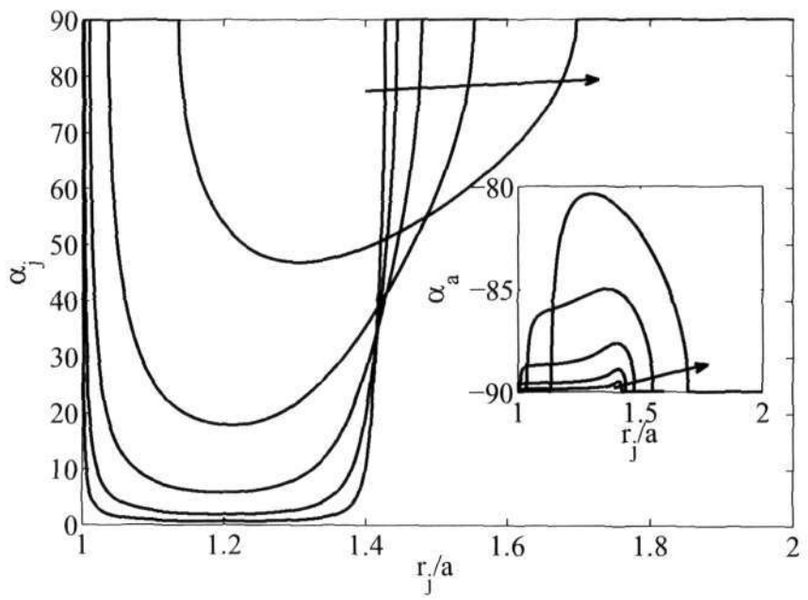

Figure 3.13: Phase difference, α_j and α_a, between interface displacement and radial velocity at $r = r_j$ and $r = r_a$ respectively. The Atwood number for the curves increases from 10^{-5} to 10^{-1} in powers of 10 as indicated by the arrow. For $m = 2$, an angle of 90^0 represents a half wavelength displacement in the azimuthal direction.

impede the interface displacement, i.e. the essential mechanism of RTI is now removed, resulting in a neutral state.

Figure (3.13) shows the variation of phase-angle at both the interfaces for various Atwood numbers as a function of density interface position for a light-cored Rankine vortex. Since $m = 2$ in all our analysis, a half wavelength displacement in the azimuthal direction is represented by an angle of 90^0. For the smallest At considered, the two interfaces behave like free waves and this results in near-perfect phase-locking below the critical radius. The phase-angle at $r = a$ shown in the inset departs marginally from the neutral wave condition, i.e. $\alpha_a \approx -90^0$. This indicates that it is the density interface that is destabilized, rather than the vortex core.

We now demonstrate that the relative signs of the disturbance vortex sheets in the present flow conform to the mechanism described. The vortex sheet strength for the unstable mode are calculated from the cubic dispersion relation. The case of a heavy-cored vortex is shown in figure (3.14). For comparison, the homogenous case given by equation (3.41) is also plotted. Clearly, for low At, the sheet strength changes sign in the neighbourhood of the critical layer. More importantly, the second vortex sheet is positive for $r_j \gtrsim r_c$. The reverse would be true for a light-cored vortex. In line with the wave-interaction mechanism, at low At, we find an instability for $r_j < r_c$ for a light core and for $r_j > r_c$ for a heavy core.

The kinematic picture described above is in agreement with the wave-energetic view-

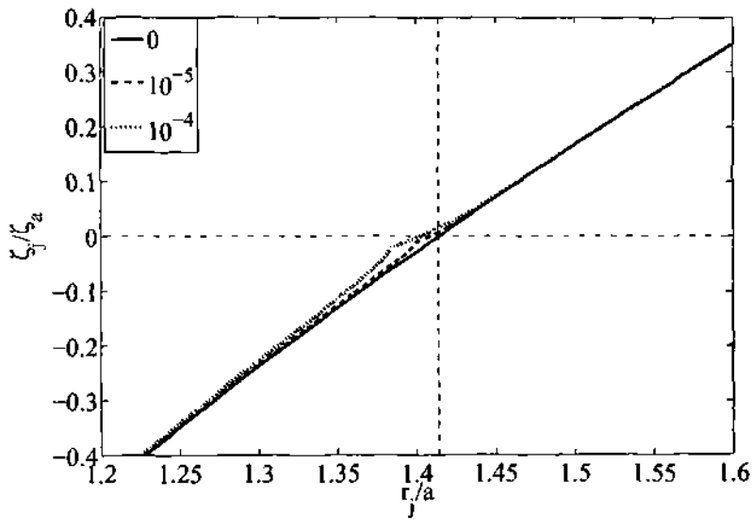

Figure 3.14: Vortex sheet strengths for a heavy-cored Rankine vortex for various At. The vertical dashed line indicates the location of the critical radius r_c. In the vanishing At limit, the sheet strength changes sign across r_c.

point of linear wave-interactions. The wave-energy concepts first developed in plasma physics were introduced into hydrodynamics by Cairns (1979). A detailed discussion of wave-energetics is given in Craik (1985) and Fabrikant & Stepanyants (1998). The wave energy can be calculated from the dispersion relation using the formula

$$\mathcal{E} = \frac{1}{4}\omega\frac{\partial D}{\partial \omega}|\eta_0|^2, \tag{3.42}$$

where $\mathcal{E}$ is the wave energy, D is the cubic dispersion relation of equation (3.21) multiplied by a negative sign, and η_0 is the interface displacement amplitude. Instability occurs when the dispersion curves of two waves with oppositely signed wave energies intersect. It can be shown that the two internal waves from the density field are associated with positive wave energies. Also as Fukumoto (2003) showed, the Kelvin mode is associated with a negative wave energy. Their interaction resulting in instability is thus in agreement with the wave energetic idea.

3.4 Stability of smooth profiles

Given that a light-cored Rankine vortex with step density jump can be unstable, but a light-cored Gaussian vortex with a Gaussian density distribution is not (Joly *et al.* (2005)), it is clear that the smoothness of the profile has a crucial role to play. In Section 3.4.1 we demonstrate that for smooth profiles too, instabilities similar to that for a Rankine vortex can exist, if the variation in the mean flow is rapid enough. With increasing smoothness however, the corresponding growth rates decrease and, at some

smoothness, instabilities vanish. How may this be explained, i.e., what happens to the mathematical construct of free waves we created above, when the discontinuities, as in real life, are smoothed out?

As shown by Briggs *et al.* (1970) and is now well-known, smooth vorticity profiles do not have normal mode solutions. However, a subset of the continuous spectrum, lying in the vicinity of the critical radius of a related sharp profile, can take the place of the discrete mode. In other words, the collaboration of these continuous spectrum modes (which actually appear as singular wave-packet solutions) can lead to remarkably wave-like behaviour. When this happens, it is referred to as a quasi-mode (Briggs *et al.* (1970) Schecter *et al.* (2000) and others). These quasi-modes exhibit an exponential decay, much in the manner of a stable discrete wave, for a short time. At longer times we have the usual algebraic decay (Case (1960)) of the entire continuous spectrum. The exponential decay can often be associated with the least stable Landau pole. Landau poles are discrete eigenvalues of the inviscid (Rayleigh) stability equation, obtained from an analytic continuation into the complex plane. Since they exist in another Riemann surface they have to be distinguished from true eigenmodes. It is well-known now that when vorticity gradient at the critical radius is very small, then Landau poles indeed become quasi-modes, i.e., manifest wave-like behaviour in the physical Riemann surface. On physical grounds, the exponential damping has been interpreted as being due to a resonant wave-fluid interaction, analogous to the wave-particle interaction considered by Landau. Schecter *et al.* (2000) showed that this resonant damping is a result of the conservation of angular momentum, where phase-mixing of vorticity in the Kelvin's cat's eye at the critical layer leads to a decrease in the mode amplitude. The existence of quasi-modes can be ascertained by various qualitative measures as we shall see.

As the base vorticity becomes more spread out, its resemblance to a step vorticity change becomes weaker, and so does the connection between the displayed behaviour and the Landau pole. Consequently the behaviour will be seen to be no longer wave-like at high levels of smoothness. In particular, as Schecter *et al.* (2000) noted, a Gaussian vortex has no noticeable quasi-mode signature. In this case, an initial impulsive perturbation results in a spiral structure which does not resemble a normal mode. Secondly the pole lies so far from the real r line that a critical radius is not well-defined. Since the deviation from wave-like behaviour is gradual with increase in smoothness, a particular smoothness level at which a quasi-mode ceases to exist is not possible to define in this flow.

By various measures, we show that a profile less smooth than about $n = 4$ exhibits quasi-mode behaviour. More important, we show that quasi-modes possess another property of wave-like disturbances, in that like discrete waves, they can participate in interactions with other waves. Interestingly, the interaction in this case between an exponentially decaying quasi-mode of the vortex profile and a neutral internal wave results in exponential growth. This interaction can also be interpreted in terms of wave energies. Briggs *et al.* (1970) showed that quasi-modes possess negative wave-energy. Hence, the mode amplitude grows when energy is extracted from these waves, by either introducing friction (viscosity) in the system, or by introducing a positive energy wave. The former situation occurred in Briggs *et al.* (1970), while we let ourselves into the latter situation by introducing positive-energy waves due to density stratification.

3.4.1 Quasi mode - gravity wave interaction

We now present stability results on the family of smooth vorticity profiles described earlier. Equation (3.15) is solved in the domain $r = 0$ to R_{max}, which is fixed at 20 using the Chebyshev spectral collocation method. The collocation points defined in the domain $x \in [-1, 1]$ are mapped to a subset of the positive real line as $s = (x+1)/2$. The grid is clustered in regions of sharp density gradients based on the stretching formula given in Govindarajan (2004). To improve accuracy at small growth rates and to obtain Landau poles, the integration contour is deformed into the complex plane as follows:

$$r = \beta_1 \left[\frac{\sinh(\beta_2(s - y_0)) + \sinh(\beta_2 y_0)}{\sinh(\beta_2 y_0)} \right] - i\alpha(1 - x^2), \tag{3.43}$$

where

$$y_0 = \frac{1}{2\beta_2} \log \left[\frac{1 + (e^{\beta_1} - 1)\beta_1}{1 + (e^{-\beta_1} - 1)\beta_1} \right]. \tag{3.44}$$

Here β_1 represents the location where clustering is desired, β_2 determines the degree of clustering, and $\alpha < 0$ denotes the extent of deformation. For radially stratified vortices, we choose β_1 to coincide with the density jump location. For homogenous flows treated later in the chapter, β_1 is chosen to be equal to the critical radius. β_2 is fixed at 10 in all our calculations. It was seen above that instability for a Rankine vortex is highest when the density jump is placed at the critical radius. To get an estimate of the maximum growth rate, we again place the density jump at the critical radius, defined now as the real part of the Landau pole location of the homogeneous vortex, as described in detail later. In figure 3.15, growth rates for different Atwood numbers are shown as a function of profile steepness. For the Atwood numbers considered here, instability always vanishes for n less than about 6. On the other hand, for large n, the Rankine limit is approached. The density profiles here have the same n as the vorticity. To estimate how much of the stabilization at lower n is due to the smoothening of the density profiles, a steep *tanh* density profile, as given in equation 3.7, is used to obtain neutral stability curves, shown in the $n - r_j$ plane in figure 3.16. The steepening of the density profile does bring down the n at which instabilities vanish. Though its exact value is sensitive to At, for small At, this n value is always between 2 and 1. Henceforth we use only steep density profiles.

In the small At limit, waves from vortex and density profiles can be assumed to weakly modify each other. For large At, vorticity and density waves strongly influence each other, making it difficult to pin down a particular range of n for the transition to stability.

3.4.2 Landau poles and quasi-modes for a homogeneous vortex

To estimate how wave-like the vorticity perturbation is, we prescribe homogeneous density conditions in this subsection. Landau poles are recovered from a suitable analytic continuation of the dispersion relation, as discussed in Briggs *et al.* (1970). We then qualitatively estimate whether these are also quasi-modes of the system.

Figure (3.17) shows the frequency and decay rate as per the Landau pole as functions of the smoothness parameter n. For large n, the frequency approaches asymptotically the

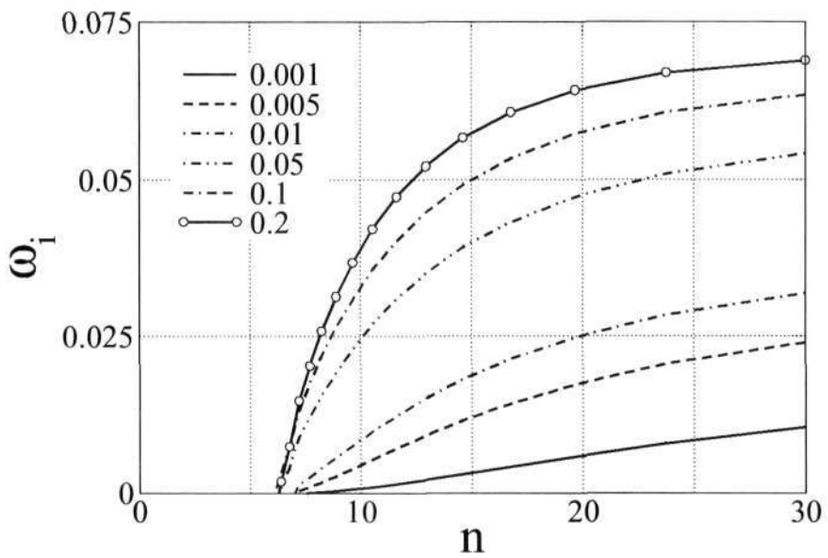

Figure 3.15: Growth rates obtained by varying the value of n for vortex and density profiles for different Atwood numbers. The density profiles are placed at r_c.

Kelvin mode frequency of a Rankine vortex. The decay rate increases dramatically for $n \lesssim 3.5$. Eventually at low enough n, we have $\omega_{q,i}/\omega_{q,r} \sim O(1)$, violating the assumption of small decay rate of Briggs *et al.* (1970) and Schecter *et al.* (2000), under which they are able to obtain quasi-modes. An examination of fig.(3.18) reveals that the critical point r_c too drifts rapidly away from the real-r axis for $n \lesssim 3.5$, so the approximation of the critical point by its projection on the real axis is not justified. We therefore expect that there should be no quasi-mode evident at low n, and apply some diagnostics to support this.

The first is the excitability test of Schecter *et al.* (2000). The excitability, which they define as

$$X_l = -\frac{\langle \vartheta_l, r^{m-1}\mathcal{D}Z(r)\rangle}{\langle \vartheta_l, \vartheta_l\rangle}, \tag{3.45}$$

is a measure of amplification of a given frequency in the perturbation. Here the inner product is defined as

$$\langle f, g\rangle = \int_0^\infty \frac{f^*(r)g(r)}{|\mathcal{D}Z(r)|} r^2 dr. \tag{3.46}$$

and the disturbance vorticity is considered in discretized form, for example in terms of Chebyshev polynomials, as

$$\zeta(r,t) = \sum_{l=1}^{N} a_l \vartheta_l(r) e^{-i\omega_l t}, \tag{3.47}$$

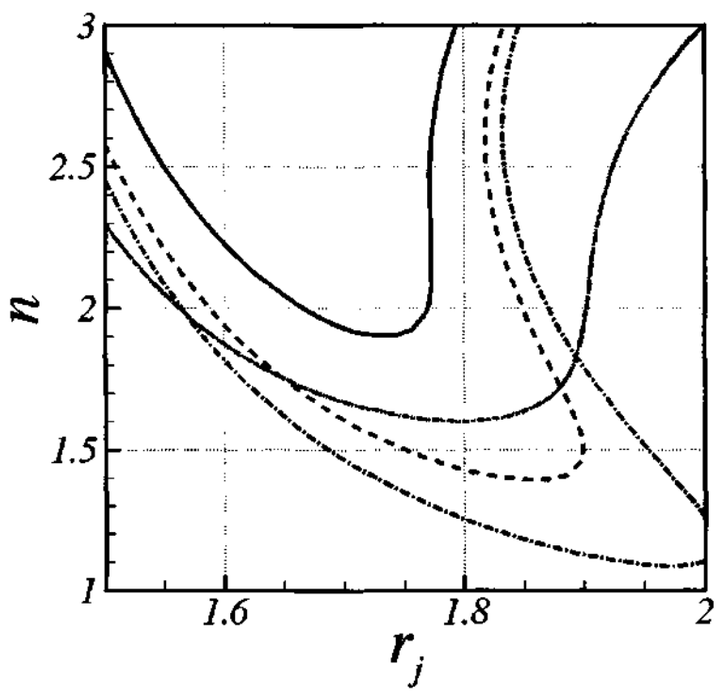

Figure 3.16: Neutral curves with *tanh* density profiles (equation (3.7)) of $\delta_t = 0.1$. solid line: At=-0.01, dashed line: At =-0.02, dash-dot line: At=-0.025. Dash-dot-dot line: $At = -0.05$ with the density profile according to equation (3.5) with $n = 10$.

where a_l are the expansion coefficients, ϑ_l the vorticity eigenfunction and ω_l is the frequency. In the case of steep *tanh* vortices, Schecter *et al.* (2000) obtained a Lorentzian-type excitability spectrum, with a peak at the Landau frequency. This is the signature of a quasi-mode. However for a Gaussian vortex, a broadband spectrum was obtained with no well-defined peak. Our results for the present profiles are in qualitative agreement, as seen in the excitability spectra in figure (3.19) for four vorticity profiles of decreasing steepness. Given its sharply peaked excitability spectrum, we estimate that a profile of $n = 4$ is steep enough to respond with a wave, and at some lower n, a quasi-mode no longer exists. In fact the excitability spectrum for $n = 4$ is fit well by a Lorentzian, with a peak at $\mathrm{Re}(\omega_q)$, where the subscript q stands for the Landau pole, that is orders of magnitude greater than for surrounding frequencies. For $n = 2$ and 1.5, there is only a shallow peak, while a Gaussian vortex behaves in accordance with Schecter *et al.* (2000).

Fabre *et al.* (2006), whose primary focus was 3D perturbations, provided a second diagnostic. They too noted that a Gaussian vortex does not have a quasi-mode in the 2D limit, displaying instead a broadband response. Their viscous L-branches (as they name them), the only modes which can possess a critical layer singularity, undergo a dramatic change in eigenmode structure as axial wavenumber is decreased (see their figure 14). For

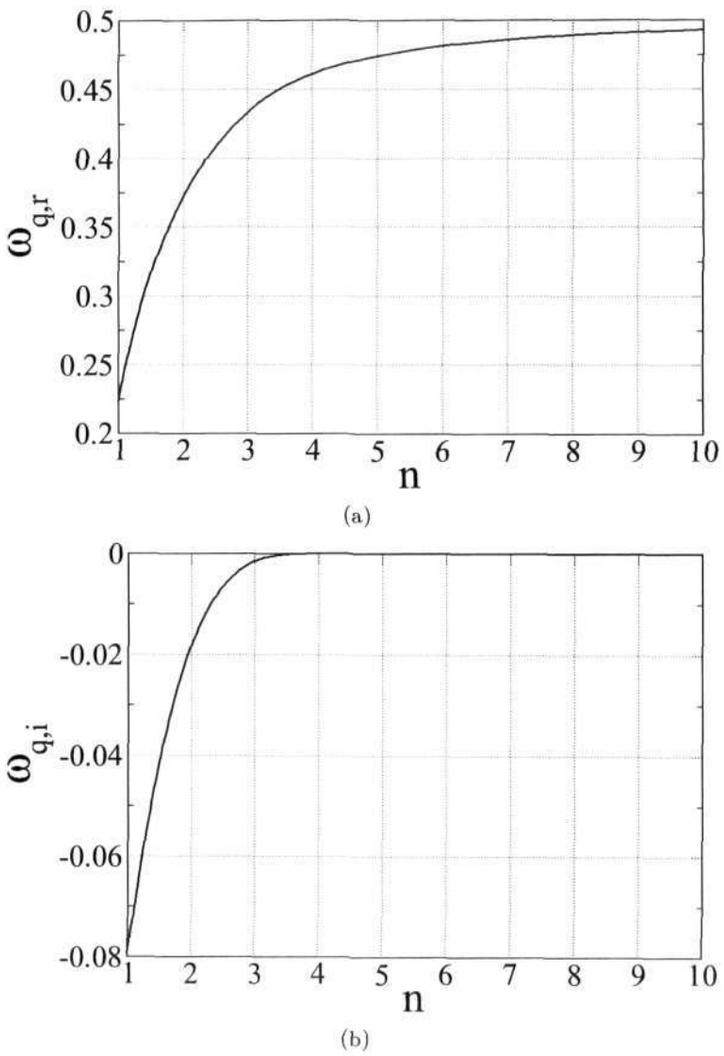

Figure 3.17: Variation of Landau pole ω_q for $m = 2$. Subscripts r and i indicate the real and imaginary parts. $\omega_{q,i}$ has a negative value for all n, but is too small to be visible when $n > 3.5$. A sudden drop in $\omega_{q,r}$ is obtained for $n \lesssim 3.5$.

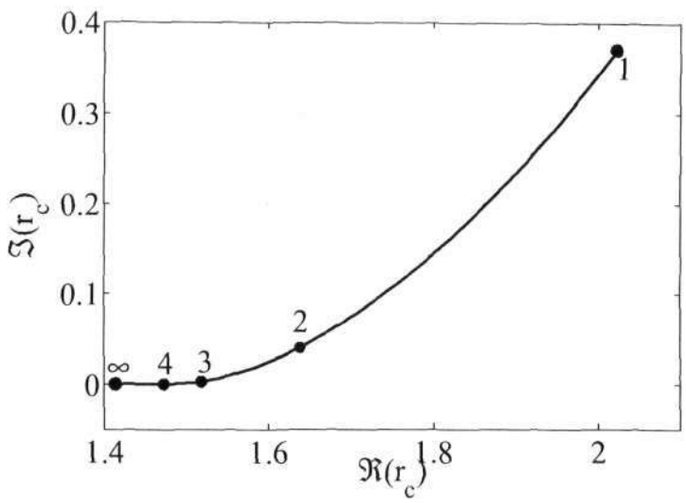

Figure 3.18: Location of the Landau pole in the complex r-plane for various values of n with $m = 2$. The limiting values for a Rankine vortex ($n \to \infty$) with critical radius at $\sqrt{2}$ and a Gaussian vortex ($n = 1$) along with a few intermediate values of n are indicated by bold circles. A large increase in $\Im(r_c)$ is obtained for $n \lesssim 3.5$.

small axial wavenumber and large Reynolds number, the disturbance is wound into a thin spiral structure outside the vortex core, notably with no perturbation in the core region. If a resonant wave-fluid interaction were taking place, we would have seen its signature in the form of a significant perturbation amplitude at the core. They further showed that these viscous L-branch solutions at large Re match the inviscid solutions of Sipp & Jacquin (2003) suggesting that the quasi-modes of the inviscid system become true eigenmodes of the viscous problem. Moreover, decay rates of these L-branch solutions rapidly increases with decreasing axial wavenumber, such that eventually $\omega_{q,i} \sim O(\omega_{q,r})$. This led Fabre *et al.* (2006) to conclude that there are no quasi-modes for a Gaussian vortex in the 2D limit. We extend the viscous stability study to other values of n, with the governing equations and method described in Dixit & Govindarajan (2010). The results at $Re = 10^5$ shown in figure (3.20) indicate that there are significant vorticity perturbations inside the core for $n \geq 2$, suggesting again that quasi-modes exist for steeper profiles.

3.4.3 Initial value problem

In the solution of an initial value problem, quasi-modes are associated with exponential decay of energy, where the decay rate is precisely that given by the Landau pole. This provides a third diagnostic. The linear equations (3.9-3.12) are solved with homogeneous boundary conditions at $r = 0$ and $r = R_{max}$. Radial discretization is given by equation (3.43) with $\alpha = 0$ and we use 3000 collocation points. The initial perturbation consists

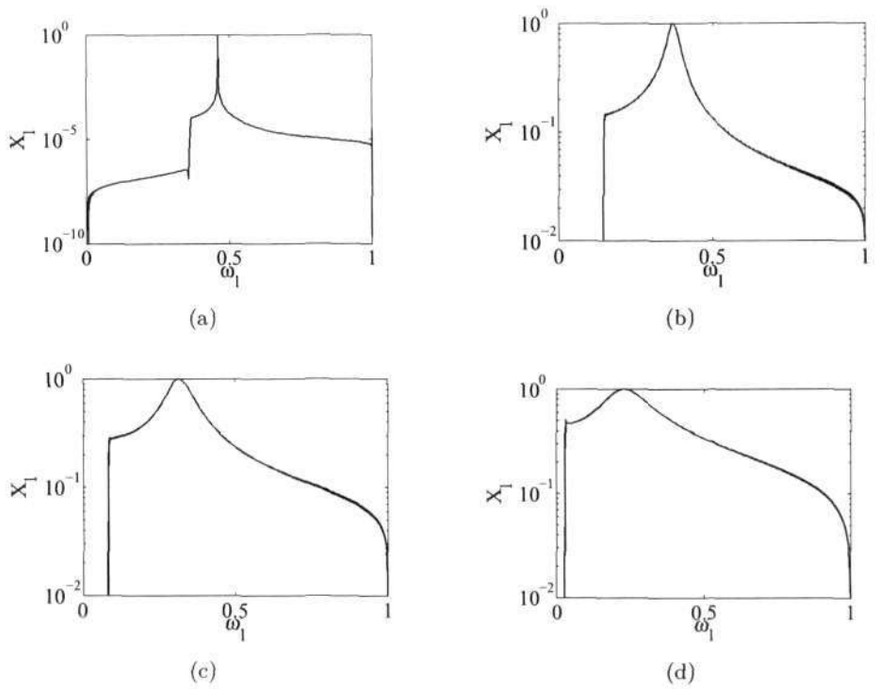

Figure 3.19: Excitability for vorticity profiles with (a) $n = 4$, (b) $n = 2$, (c) $n = 1.5$ and (d) $n = 1$. Note the change of vertical scale for (a). A sharply peaked excitability spectrum is indicative of a quasi-mode.

of a narrow ring of vorticity centered at the real part of the critical radius $\mathrm{Re}(r_c)$, with

$$\zeta(r,0) = \exp\left(\frac{-(r - \mathrm{Re}[r_c])^2}{\delta^2}\right). \tag{3.48}$$

A large number of vorticity profiles were studied, but we present only a few. We are

n	ω_q	r_c
3.5	$0.450 - 1.856 \times 10^{-4}i$	$1.490 + 0.307 \times 10^{-3}i$
3.0	$0.433 - 1.518 \times 10^{-3}i$	$1.518 + 0.266 \times 10^{-2}i$
2.47	$0.407 - 6.892 \times 10^{-3}i$	$1.567 + 0.133 \times 10^{-1}i$
2.0	$0.371 - 1.827 \times 10^{-2}i$	$1.638 + 0.406 \times 10^{-1}i$
1.5	$0.315 - 4.137 \times 10^{-2}i$	$1.766 + 0.118i$
1.0	$0.222 - 7.939 \times 10^{-2}i$	$2.022 + 0.370i$

Table 3.1: Variation of Landau pole for select values of profile smoothness. The critical location for these modes lies off the real axis, and is obtained by inverting the relation $\omega_q = m\Omega(r_c)$.

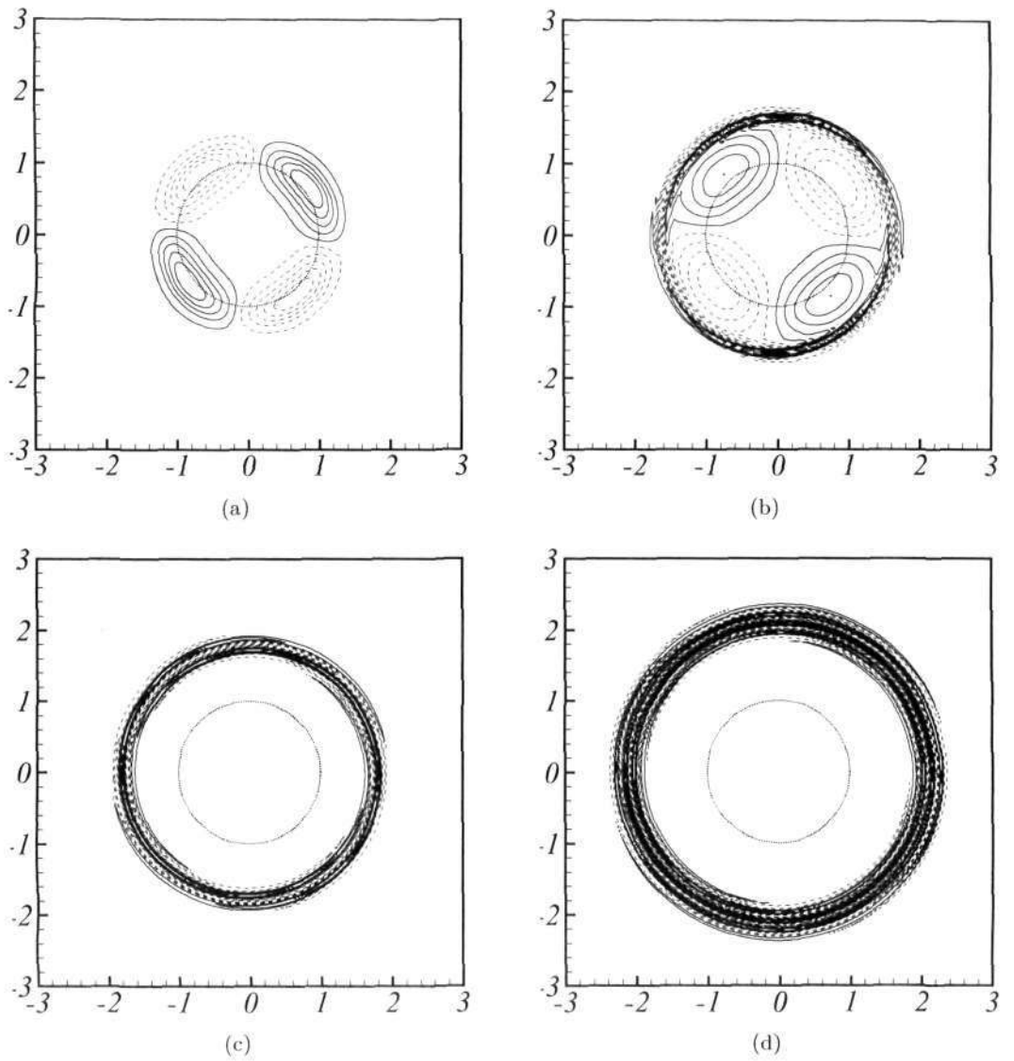

Figure 3.20: Vorticity eigenfunctions obtained from a viscous calculation at $Re = 10^5$. (a) $n = 4$, (b) $n = 2$, (c) $n = 1.5$ and (d) $n = 1$. The dotted circle at the centre indicates the vortex core size δ_z. Twelve equally spaced contour levels are plotted. Solid and dashed lines indicate positive and negative vorticity levels respectively.

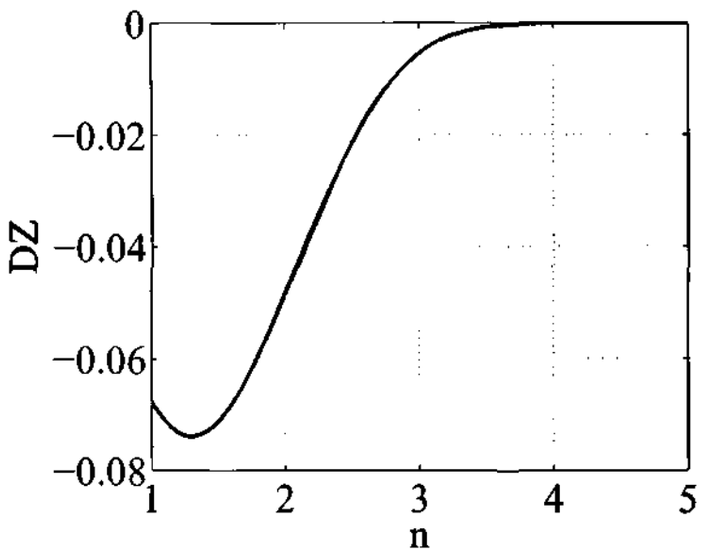

Figure 3.21: Vorticity gradient at the critical radius for various values of n. The solid line is the real part of $\mathcal{D}Z$ obtained by considering the complex r_c and the dotted line is obtained by calculating $\mathcal{D}Z$ at $r = \mathrm{Re}(r_c)$. The minima in these two cases are reached at $n = 1.3$ and $n = 1.6$ respectively.

n	$\mathrm{Im}(\omega_q)$	σ_q	σ_e
2.0	−0.01827	−0.01827	−0.01827
1.5	−0.04137	−0.04137	−0.0325
1.0	−0.07939	−0.054	−0.0245

Table 3.2: Comparison of decay rate obtained from multipole moment and energy with the Landau pole value for three different vortex profiles. The decay rate of energy for $n = 2$ vortex is in excellent agreement Landau pole value, but is poor for the other profiles.

specifically interested in the region between $n = 4$ and $n = 1$. One way to measure the strength of non-axisymmetric perturbations is to use the m^{th} multipole moment defined as

$$Q_m(t) = \int_0^\infty r^{m+1}\zeta(r,t)dr. \tag{3.49}$$

This quantity is a measure of the ellipticity of the vortex (for $m = 2$) and is related to the form of the streamfunction in the far-field, i.e.

$$Q_m(t) \sim 2mr^m\psi_m(t), \qquad (r \to \infty), \tag{3.50}$$

(see Bassom & Gilbert (1998); Turner & Gilbert (2007)). For comparison, Table 3.1 gives Landau pole values and their critical radii for a few vortex profiles. As seen in fig.(3.22), the decay rate obtained from the multipole moment, $Q_m(t)$, is in excellent

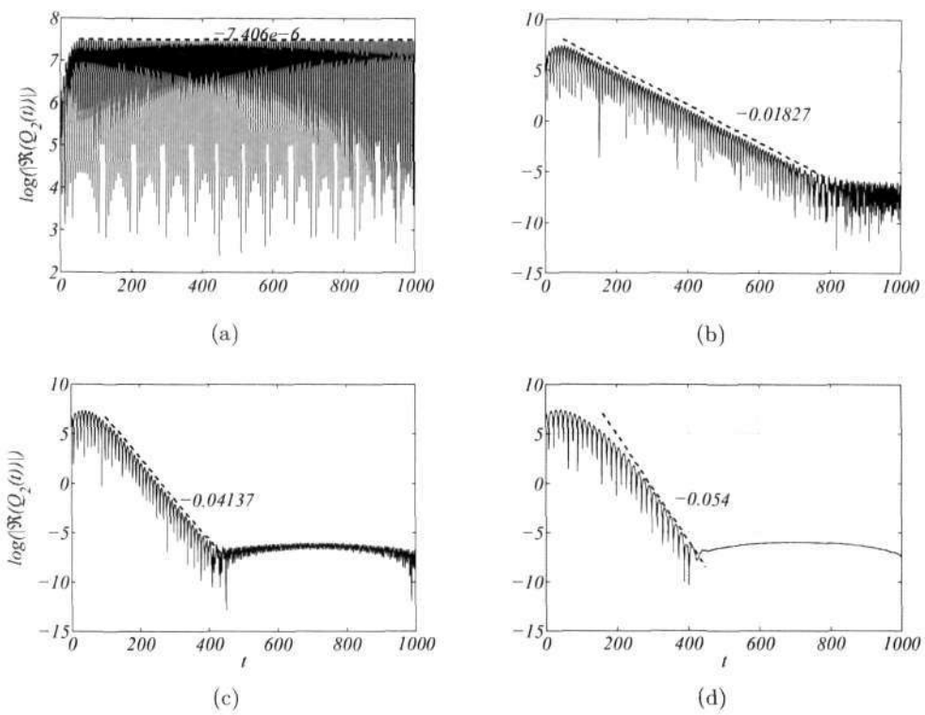

Figure 3.22: Evolution of quadrupole moment $|Re(Q_2(t))|$ for four different vortex profiles, (a) $n = 4$, (b) $n = 2$, (c) $n = 1.5$ and (d) $n = 1$. The dashed lines are fits for the exponential damping rate with the indicated decay rate.

agreement with Table 3.1 for profiles $n = 2$ and $n = 1.5$, but the agreement is not so good for $n = 1$. The exponential decay is seen to last for longer times as the profile is made steeper. The noise at late times is probably due to insufficient numerical resolution, since the disturbance field becomes progressively finer-scaled. A very small viscosity has been used to stabilize some of the calculations (as done by Turner & Gilbert (2007)).

Another useful quantity is the kinetic energy of the perturbations, defined as

$$E(t) = \int_0^\infty \frac{r}{m^2} \left(m^2 ||u_r||^2 + ||\mathcal{D}(ru_r)||^2 \right) dr. \tag{3.51}$$

At intermediate times, larger than the mean turn-over time, $E(t)$ being proportional to $\exp(-2\omega_{q,i}t)$ is a definitive demonstration of quasi-mode response. Figure 3.23 shows the evolution of normalized kinetic energy. After a short early transient, a clear exponential decay can be noticed, similar to the observations of Shrira & Sazonov (2001) in a boundary layer flow. A striking distinction between the decay of $Q_m(t)$ and $E(t)$ is the significantly shorter duration of exponential decay in $E(t)$. Decay rates σ_q and $2\sigma_e$, obtained by a fit of the exponential portions of $Q_m(t)$ and $E(t)$ respectively, are tabulated in Table 3.2. Again the decay of $Q_m(t)$ is in fair comparison with the Landau pole value, but the decay of energy is in poor agreement for $n = 1.5$ and $n = 1$ vortices. The

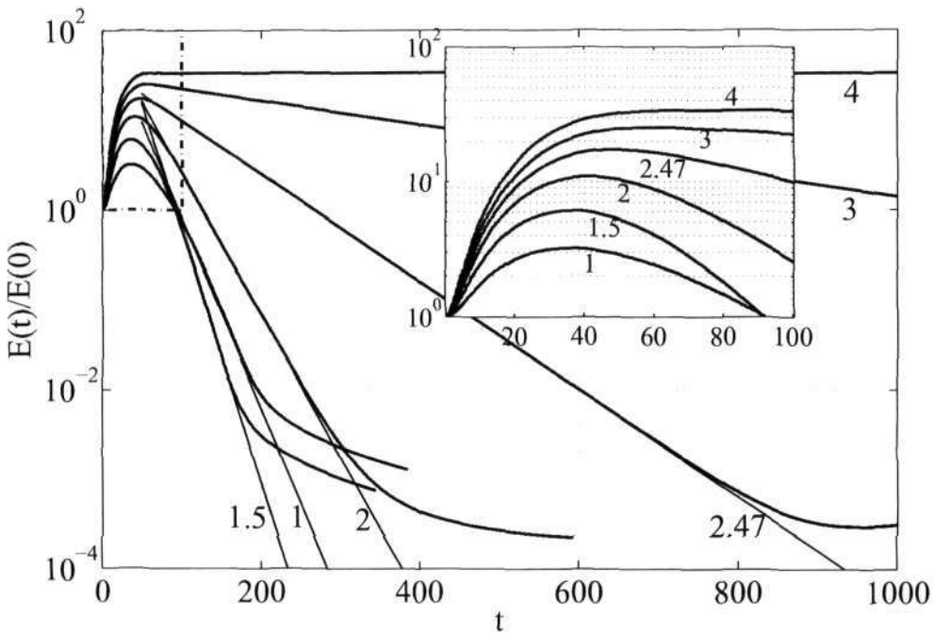

Figure 3.23: Evolution of disturbance kinetic energy $E(t)$ for $n = 1, 1.5, 2, 2.47, 3$ and 4 indicated by solid lines. An exponential fit of the form $e^{2\sigma t}$ is obtained and is shown for the first four curves. Values of σ obtained for $n = 1, 1.5, 2$ and 2.47 are -0.0245, -0.0325, -0.01827 and -0.006892. The inset shows the region near $t = 0$ indicated by a rectangle, where transient growth is obtained. Notice a monotonic increase in transient energy growth with n, but a non-monotonic variation in energy decay.

transient growth is seen in the inset of figure 3.23 to increase with increasing n at short times. But the exponential decay rate at intermediate times does not change monotonically with n, at $n = 1.5$ the decay is more rapid than at $n = 1$ or $n = 2$. The decay rate is expected to be directly related to $\mathcal{D}Z(r_c)$, and a corresponding non-monotonicity in that quantity in seen in fig.(3.21).

To compare the response of the initial value problem with the viscous stability calculations, a fixed time of 100, close to the beginning of the energy decay, is chosen. Figure 3.24 shows the contours of perturbation vorticity at $t = 100$ for four different values of n. Figures 3.24(a), 3.24(b) and 3.24(c) are remarkably similar to the viscous results shown in fig.(3.20), suggesting that quasi-modes indeed become eigenmodes of the viscous problem. Clearly, a lobed structure analogous to a Kelvin wave can be noticed at $r = a$ (shown by a dotted circle) for the $n = 4$ vortex. For an $n = 2$ vortex, weak lobes are noticed at the core boundary. Core perturbations completely vanish for an $n = 1.5$ vortex, and in the case of $n = 1$, the spiral region begins to engulf the vortex core with no visible wave-like pattern noticeable.

Having seen by all measures that no quasi-mode exists for $n < 1.5$, we now examine the light-cored vortex. Clearly from fig. 3.16, the instability vanishes for n between 2 and 1. We thus conclude that the existence of a quasi-mode is strongly correlated with

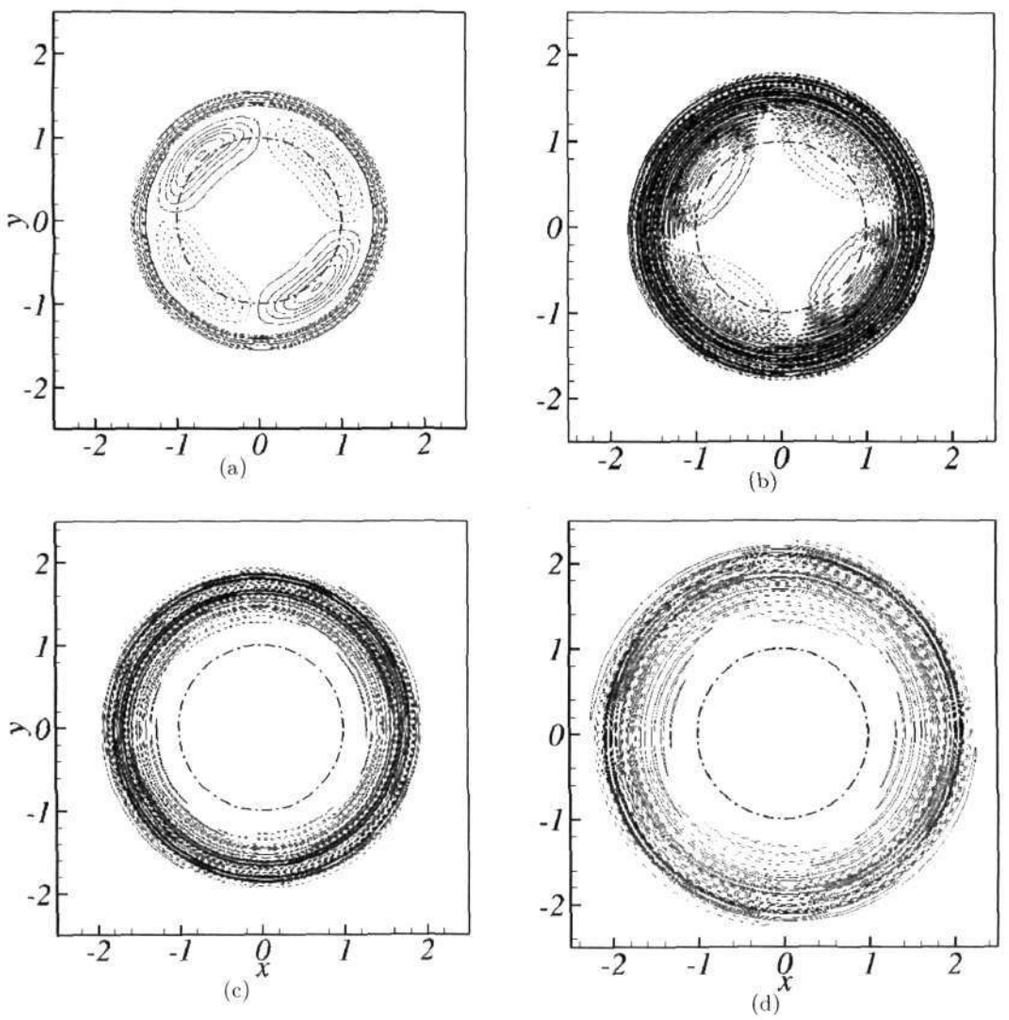

Figure 3.24: Contours of perturbation vorticity obtained from a linear initial value problem at $t = 100$. (a) $n = 4$, (b) $n = 2$, (c) $n = 1.5$ and (d) $n = 1$. 20 equally spaced contour levels between the maximum and minimum values are plotted. The positive levels are shown by solid lines and negative levels by dashed lines. The dotted circle shows the region of the vortex core. Note the change of scale for (d).

the existence of an instability. We surmise that the quasi-mode makes a wave interaction possible.

3.5 Critical layer absorption

It is often of interest to examine the structure of stable/neutral modes even if these are not the most dominant in terms of exponential growth. In this section, we study the structure of the eigenmodes of the continuous spectrum which are neutrally stable. If no contour deformation is carried out in the stability calculations, then a neutral spectrum is obtained. When the density profile is broad, internal waves can propagate in the radial direction, unlike in the step density jump case where the internal wave technically becomes a surface wave and is restricted to exist only on the density interface. But for smooth profiles, an interplay of shear and internal waves can lead to a remarkable behaviour near the critical layer of each mode, i.e., where $\omega = m\Omega$. It was first shown by Booker & Bretherton (1967) that in the presence of shear, internal waves get 'absorbed' in the critical layer. What really happens is that the group velocity vector of the internal waves becomes more and more tangential to the critical layer as the wave approaches it. And in a direction perpendicular to the critical layer, the solution becomes highly oscillatory. We will show below that the same is true even for a vortex geometry where internal waves are supported by restoring buoyancy forces. No assumptions are made on the vortex and density profile steepness. The analysis is similar to the one carried out in Booker & Bretherton (1967) and Nappo (2002) for a planar stratified shear flow.

We define a wave angular speed as

$$c = \frac{\omega}{m}, \tag{3.52}$$

and rewrite equation (3.15) as

$$\frac{d^2u_r}{dr^2}+\left(\frac{3}{r}+\mathscr{G}_0\right)\frac{du_r}{dr}-\frac{m^2-1}{r^2}u_r+\frac{3\Omega'+r\Omega''}{r(c-\Omega)}u_r+\frac{\mathscr{G}_0}{r}u_r+\mathscr{G}_0\frac{2\Omega+r\Omega'}{r(c-\Omega)}u_r+\mathscr{G}_0\frac{\Omega^2}{r(c-\Omega)^2}u_r=0, \tag{3.53}$$

where $\mathscr{G}_0 = \frac{1}{\bar{\rho}}\frac{d\bar{\rho}}{dr}$. Let us assume that a wave is approaching the critical level, r_c, from a region outside it as shown in figure (3.25). At a distance ξ outside r_c as shown in figure (3.25) and for $\xi/r_c << 1$, we expand the background angular velocity to second order in ξ. For simplicity, we do not expand the background density gradient, and neglect variations in $\mathscr{G}_0$. The effect of varying $\mathscr{G}_0$ can easily be incorporated if needed.

$$\Omega(r_c+\xi) = c+\left(\frac{d\Omega}{dr}\right)_{r=r_c}\xi+\frac{1}{2}\left(\frac{d^2\Omega}{dr^2}\right)_{r=r_c}\xi^2+... \tag{3.54}$$

This gives

$$\frac{1}{c-\Omega(r_c+\xi)} \approx -\frac{1-\left(\frac{1}{2}\right)\left(\frac{\mathscr{G}_2}{\mathscr{G}_1}\right)\xi}{\mathscr{G}_1\xi} \tag{3.55}$$

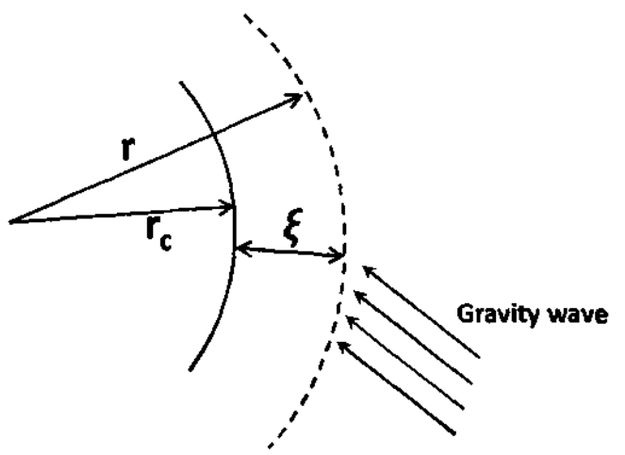

Figure 3.25: A sketch showing a gravity wave impinging a critical layer, r_c, from a region outside it.

where

$$\mathscr{G}_1 = \left.\frac{d\Omega}{dr}\right|_{r_c}, \tag{3.56a}$$

$$\mathscr{G}_2 = \left.\frac{d^2\Omega}{dr^2}\right|_{r_c}. \tag{3.56b}$$

Including equations (3.55), (3.56b) into equation (3.53), we get

$$\begin{aligned}
\frac{d^2u_r}{dr^2} &+ \left(\frac{3}{r_c+\xi} + \mathscr{G}_0\right)\frac{du_r}{dr} - \frac{(m^2-1)}{(r_c+\xi)^2}u_r \\
&+ \frac{3\mathscr{G}_1 + (r_c+\xi)a_2}{r_c+\xi}\frac{\left[1-\left(\frac{1}{2}\right)\left(\frac{\mathscr{G}_2}{\mathscr{G}_1}\right)\xi\right]}{\mathscr{G}_1\xi} \\
&+ \frac{\mathscr{G}_0}{r_c+\xi}u_r + \frac{\mathscr{G}_0}{r_c+\xi}\left(2c + 2\mathscr{G}_1\xi + \mathscr{G}_2\xi^2\right)\frac{\left[1-\left(\frac{1}{2}\right)\left(\frac{\mathscr{G}_2}{\mathscr{G}_1}\right)\xi\right]}{\mathscr{G}_1\xi}u_r \\
&+ \frac{\mathscr{G}_0}{r_c+\xi}\left(2c + 2\mathscr{G}_1\xi + \mathscr{G}_2\xi^2\right)^2\frac{\left[1-\left(\frac{1}{2}\right)\left(\frac{\mathscr{G}_2}{\mathscr{G}_1}\right)\xi\right]^2}{4\mathscr{G}_1^2\xi^2}u_r = 0.
\end{aligned} \tag{3.57}$$

For small ξ, we have up to second order in ξ,

$$\frac{1}{r_c+\xi} \approx \frac{1}{r_c} - \frac{\xi}{r_c^2}, \tag{3.58a}$$

$$\frac{1}{(r_c+\xi)^2} \approx \frac{1}{r_c^2} + \frac{\xi^2}{r_c^4} - \frac{2\xi}{r_c^3}, \tag{3.58b}$$

On substituting equations (3.58) into equation (3.57), we can verify that the dominant terms are $O(1/\xi^2)$. Keeping the first three orders, i.e., $O(1/\xi^2)$, $(1/\xi)$ and $O(1)$ and neglecting higher order terms, and taking the wave speed to be approximately equal to the local angular velocity at the critical layer, i.e., $c \approx \Omega_c$, we get

$$\frac{d^2u_r}{dr^2} + \delta\frac{du_r}{dr} + \left(\frac{R_c}{\xi^2} - \frac{\alpha}{\xi} + \gamma\right) u_r = 0, \tag{3.59}$$

where

$$R_c = \frac{\left(\frac{1}{\bar{\rho}}\frac{d\bar{\rho}}{dr}\right) r_c\Omega_c^2}{r_c^2\Omega_c'^2}, \tag{3.60}$$

is the local Richardson number, and

$$\alpha = \frac{3}{r_c} + \frac{\mathscr{G}_2}{\mathscr{G}_1} + \frac{a_0c^2}{r_c^2\mathscr{G}_1^2} + \frac{\mathscr{G}_0\mathscr{G}_2c^2}{r_c\mathscr{G}_1^3}, \tag{3.61a}$$

$$\gamma = \frac{4-m^2}{r_c^2} + \frac{6\mathscr{G}_2}{\mathscr{G}_1 r_c}\frac{\mathscr{G}_2}{2\mathscr{G}_1^2} + \frac{\mathscr{G}_0\mathscr{G}_2^2c^2}{4r_c\mathscr{G}_1^4} + \frac{\mathscr{G}_0\mathscr{G}_2^2c^2}{r_c^2\mathscr{G}_1^3}, \tag{3.61b}$$

$$\delta = \frac{3}{r_c} + a_0. \tag{3.61c}$$

3.5.1 Approximate solution

Equation (3.59) contains a regular singular point at the critical layer. To understand the behaviour of u_r near the critical layer, we therefore introduce the Frobenius expansion,

$$\begin{aligned} u_r(m, r_c+\xi) &= \sum_n c_n\xi^{n+\lambda} \\ &= c_0\xi^\lambda + c_1\xi^{\lambda+1} + c_2\xi^{\lambda+2} + ..., \end{aligned} \tag{3.62}$$

$$\begin{aligned} \frac{du_r}{dr} &= \sum_n c_n(n+\lambda)\xi^{n+\lambda-1} \\ &= c_0\lambda\xi^{\lambda-1} + c_1(\lambda+1)\xi^\lambda + c_2(\lambda+2)\xi^{\lambda+1} + ..., \end{aligned} \tag{3.63}$$

$$\begin{aligned} \frac{d^2u_r}{dr^2} &= \sum_n c_n(n+\lambda)(n+\lambda-1)\xi^{n+\lambda-2} \\ &= c_0\lambda(\lambda-1)\xi^{\lambda-2} + c_1(\lambda+1)\lambda\xi^{\lambda-1} + c_2(\lambda+2)(\lambda+1)\xi^\lambda + ..., \end{aligned} \tag{3.64}$$

Substituting these into equation (3.59), we get

$$\begin{aligned} &\xi^{\lambda-2}\left[\lambda(\lambda-1) + R_c\right]c_0 + \xi^{\lambda-1}\left[(\lambda(\lambda+1) + Rc)c_1 + (\delta\lambda - \alpha)c_0\right] \\ &\quad + \xi^\lambda[((\lambda+2)(\lambda+1) + R_c)c_2 + (\delta(\lambda+1) - \alpha)c_1 + \gamma c_0] = 0. \end{aligned} \tag{3.65}$$

For non-trivial solutions of equation (3.65), each coefficient of ξ must be zero. This leads to the recursive relations:

$$c_1 = \frac{(\alpha - \delta\lambda)c_0}{\lambda(\lambda+1) + R_c}, \tag{3.66a}$$

$$c_2 = \frac{\left\{\frac{[\alpha - \delta(\lambda+1)][\alpha - \delta\lambda]}{\lambda(\lambda+1) + R_c} - \gamma\right\} c_0}{(\lambda+2)(\lambda+1) + R_c}. \tag{3.66b}$$

The indicial equation is obtained from the first term of equation (3.65), i.e.,

$$\lambda(\lambda - 1) + R_c = 0. \tag{3.67}$$

$$\lambda = \frac{1}{2} \pm i\mu, \tag{3.68}$$

where

$$\mu = \sqrt{R_c - \frac{1}{4}}. \tag{3.69}$$

We see that the Frobenius exponents become complex for $R_c = \frac{\mathscr{G}_0\Omega_c^2}{r_c\mathscr{G}_1^2} > \frac{1}{4}$. We now expand equation (3.62) to second order,

$$\begin{aligned} u_r(m, r_c + \xi) &= c_0\xi^\lambda + c_1\xi^{\lambda+1} + c_2\xi^{\lambda+2} + ..., \\ &= c_0^+\xi^\lambda F(\xi) + c_0^-\xi^{\lambda^*}F^*(\xi), \end{aligned} \tag{3.70}$$

where

$$F(\xi) = 1 + \frac{c_1}{c_0}\xi + \frac{c_2}{c_1}\xi^2, \tag{3.71}$$

and c_0^+ refers to values using $\lambda = 1/2 + i\mu$ and c_0^- refers to values using $\lambda = 1/2 - i\mu$. We now know the values of all variables except c_0^+ and c_0^-. Taking the radial derivative of equation (3.70), we get

$$\frac{du_r}{dr} = c_0^+\xi^\lambda G(\xi) + c_0^-\xi^{\lambda^*}G^*(\xi), \tag{3.72}$$

where

$$G(\xi) = \frac{\lambda}{\xi} + \frac{c_1}{c_0}(\lambda+1) + \frac{c_2}{c_1}(\lambda+2)\xi \tag{3.73}$$

From equation (3.70) and (3.72), we get c_0^+ and c_0^- as

$$c_0^+ = \frac{F^*\left(\frac{du_r}{dr}\right) - G^*u_r}{H} \tag{3.74}$$

$$c_0^- = \frac{F\left(\frac{du_r}{dr}\right) - Gu_r}{H} \tag{3.75}$$

where $H = F^*G - FG^*$. We now examine the wave in a region just inside the critical radius. At a distance ξ inside the critical radius, we have

$$u_r(m, r_c - \xi) = c_0^+(-\xi)^\lambda F(-\zeta) + c_0^-(-\xi)^{\lambda^*} F^*(-\zeta), \tag{3.76}$$

$$\frac{du_r}{dr}(m, r_c - \xi) = c_0^+(-\xi)^\lambda G(-\zeta) + c_0^-(-\xi)^{\lambda^*} G^*(-\zeta). \tag{3.77}$$

We now need to carry the wave solutions across the critical layer. Because $(-\xi)^\lambda$, $(-\xi)^{\lambda^*}$ exhibit a branch-cut across the critical layer, we introduce a small imaginary part to the wave speed, c, i.e.

$$c = c_r + ic_i. \tag{3.78}$$

As the wave approaches the critical level from outside r_c, we expand the background angular velocity as

$$\begin{aligned} \Omega(r) &= \Omega(r_c) + \left.\frac{d\Omega}{dr}\right|_{r_c} (r - r_c) + ... \\ &= c_r + \mathscr{G}_1(r - r_c). \end{aligned} \tag{3.79}$$

As $r \to r_c$, the centrifugal (last) term in equation (3.53) dominates, and the dominant balance yields the simplified equation

$$\frac{d^2u_r}{dr^2} + \left(\frac{3}{r} + \mathscr{G}_0\right)\frac{du_r}{dr} + \frac{\mathscr{G}_0\Omega^2}{r[-\mathscr{G}_1(r - r_c) + ic_i]^2}u_r = 0. \tag{3.80}$$

Using $1/r \approx 1/r_c$ and $\Omega^2 \approx \Omega_c^2$, the above equation further simplifies to

$$\frac{d^2u_r}{dr^2} + \delta\frac{du_r}{dr} + \frac{R_c}{[(r - r_c) - \frac{ic_i}{\mathscr{G}_1}]^2}u_r = 0. \tag{3.81}$$

Now using equation (3.62) with $\xi = r - r_c - \dfrac{ic_i}{\mathscr{G}_1}$, the solution of equation (3.81) takes the form,

$$u_r(m, r - r_c) = F_1\left(r - r_c - \frac{ic_i}{\mathscr{G}_1}\right)^{\frac{1}{2}+i\mu} + G_1\left(r - r_c - \frac{ic_i}{\mathscr{G}_1}\right)^{\frac{1}{2}-i\mu}, \tag{3.82}$$

where F_1 and G_1 are arbitrary constants. As discussed in Nappo (2002), we switch to a polar form, schematically shown in figure (3.26),

$$r - r_c - \frac{ic_i}{\mathscr{G}_1} = pe^{i\varphi} \tag{3.83}$$

where

$$p = \sqrt{(r - r_c)^2 + \frac{c_i^2}{\mathscr{G}_1^2}}, \tag{3.84}$$

$$\varphi = \tan^{-1}\left[\frac{-c_i/\mathscr{G}_1}{r - r_c}\right]. \tag{3.85}$$

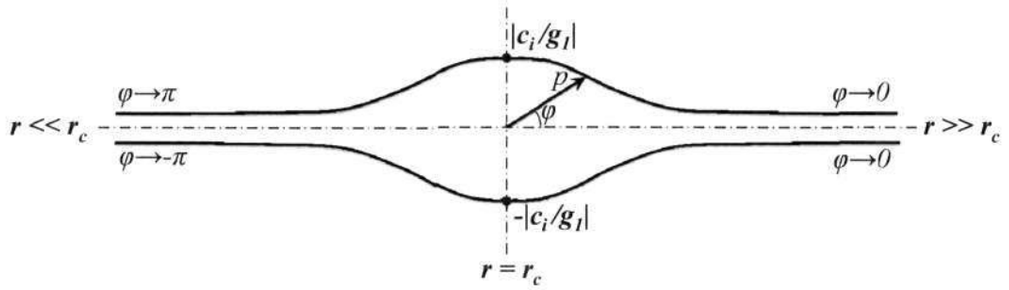

Figure 3.26: The possible paths that can be taken across the singularity $r = r_c$

For $r >> r_c$, $\varphi \to 0$, but for $r << r_c$, φ goes to either π or $-\pi$ depending on the sign of $\mathscr{G}_1 \left(= \frac{d\Omega}{dr}\Big|_{r_c}\right)$. We are mainly interested in stable angular velocity profiles which satisfy Rayleigh's centrifugal criteria, and hence $\mathscr{G}_1 < 0$. But the procedure is valid even for $\mathscr{G}_1 > 0$. We will therefore restrict the analysis only for $\mathscr{G}_1 < 0$. In this case, $\varphi \to \pi/2$ as $r \to r_c$, and therefore, we go above the singularity as shown in figure (3.26). On this contour, for $r << r_c$ and letting $c_i \to 0$, we have

$$\begin{aligned}(-\xi) = -(r - r_c - \frac{ic_i}{\mathscr{G}_1}) &\approx -(r - r_c) \\ &= (r - r_c)e^{i\pi} \\ &= \xi e^{i\pi} \end{aligned} \tag{3.86}$$

Therefore, $(-\xi)^\lambda = i\xi^\lambda e^{-\mu\pi}$, where we have used the positive branch of λ. To know what terms in equation (3.82) correspond to inward and outward moving waves, we calculate the wave stress. We first re-write u_r as

$$u_r = \xi^{1/2}\left(F_1 e^{i\mu\log\xi} + G_1 e^{-i\mu\log\xi}\right), \tag{3.87}$$

and using the continuity equation, $u_\theta = \dfrac{ir}{m}\left(\dfrac{\partial u_r}{\partial r} + \dfrac{u_r}{r}\right)$, we get u_θ as

$$u_\theta = \frac{r_c}{m}\xi^{-1/2}\left(\left(\frac{i}{2} - \mu\right)F_1 e^{i\mu\log\xi} + \left(\frac{i}{2} + \mu\right)G_1 e^{-i\mu\log\xi}\right). \tag{3.88}$$

Similar to planar stratified shear flow, the wave stress is given by (see Booker & Bretherton (1967))

$$\tau \propto \rho_0 \mathrm{Re}(u_r)\mathrm{Re}(u_\theta) \tag{3.89}$$

At the critical level, this simplifies to

$$\tau \propto (F_1^2 - B_1^2), \tag{3.90}$$

where we need to integrate over one wave-length in the azimuthal direction. Therefore, the F_1 term represents an outward moving wave contributing to a positive wave stress,

and the G_1 term represents an inward moving wave contributing to a negative wave stress. Above the critical level, we can write equation (3.82) as

$$u_r^+ = |r - r_c|^{1/2} \left(F_1' e^{i\mu \log|r-r_c|} + G_1 e^{-i\mu \log|r-r_c|} \right) \tag{3.91}$$

and below the critical level,

$$u_r^- = i|r - r_c|^{1/2} \left(F_1' e^{-\pi\mu} e^{i\mu \log|r-r_c|} + G_1 e^{\pi\mu} e^{-i\mu \log|r-r_c|} \right). \tag{3.92}$$

Clearly, for an outward (inward) moving wave, the strength of radial velocity u_r decreases (increases) by a factor of $e^{-\pi\mu}$ as the wave cross the critical layer. Similarly, the wave stress changes by a factor of $e^{2\pi\mu} = e^{2\pi\sqrt{R_c - 1/4}}$ across the critical layer. This large decrease in wave stress (and amplitude) appears like an absorption. It can also be verified that the group velocity of these waves also becomes nearly tangential to the critical layer. As we approach the critical layer, $r \to r_c$, due to the logarithmic term, the wave becomes highly oscillatory near r_c.

We now carry out a stability analysis of a light-cored Gaussian vortex with Gaussian density distribution to show the damping of waves across the critical layer. The same phenomenon can be observed even for other smooth profiles. The inviscid spectral calculation is identical to the one carried out in the previous section. In order to capture only neutral modes, and not quasi-modes, we do not deform the contour of integration. Figure (3.27) shows the eigenfunction obtained for two different frequencies. These frequencies were chosen for purely aesthetic reasons. Across the critical layer, shown with a vertical dotted line, a clear reduction in mode amplitude can be noticed. Also notice the strong oscillations as $r \to r_c$ resulting in a decrease in the radial wavenumber. This can also be seen from the logarithmic term present in the above solutions for u_r and u_θ. A more detailed description of this process, including a physical interpretation of the absorption process in terms of group velocity of a wave packet approaching the critical layer is given Booker & Bretherton (1967).

3.6 Non-linear stages

We now present results from a viscous direct numerical simulation to understand the non-linear stages of these instabilities. Even in stably stratified shear flows like the Holmboe instability, there continues to be interest in understanding these instabilities in the nonlinear regime (see the recent paper of Carpenter *et al.* (2010)). In the light of this interest in a parallel flow, it would be of interest to understand similar situations for a rotating flow. Only the results for light-cored vortices are presented, as the heavy-cored case has already been treated in Joly *et al.* (2005) and Coquart *et al.* (2005). In many flows, the non-linear pattern bears strong similarities with the most unstable mode obtained from a linear analysis. Heavy-cored vortices were shown by Joly *et al.* (2005) to split into m smaller but stronger vortices. But with stable stratification in light-cored vortices, it is interesting to know what would be the outcome of an exponentially growing instability. We find initial adherence to the linear growth rate followed by nonlinear saturation. However, unlike in the heavy cored case where the primary vortex splits

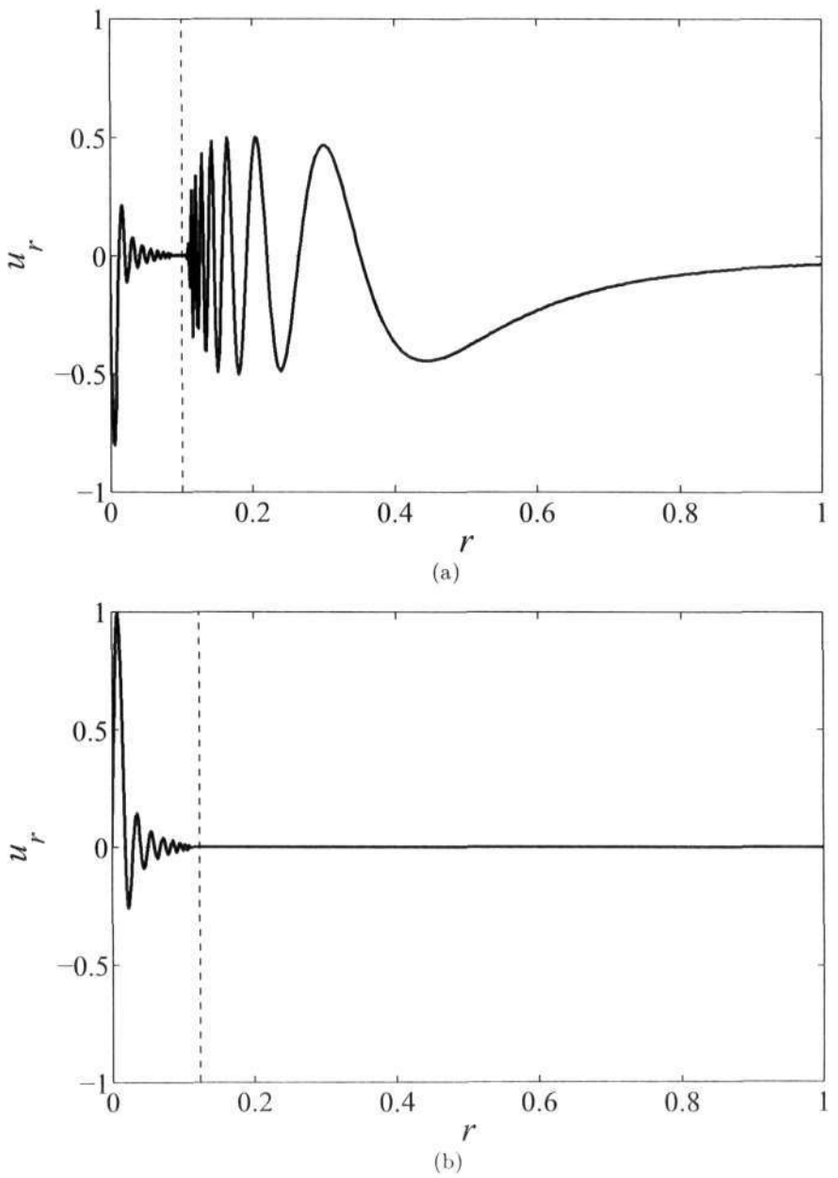

Figure 3.27: The u_r eigenfunction (solid) showing a significant reduction in the mode amplitude across the critical layer, shown with a vertical dashed line, for two different frequencies, (a)$\omega_r = 0.9949$, (b) $\omega_r = 0.9927$. The base flow is a light-cored Gaussian vortex with Gaussian density distribution, with $r_j/a = 0.5$.

into m parts, baroclinically generated vorticity creates m additional satellite vortices around the primary vortex, forming a stable non-linear structure. Incidentally, in an experimental realization of an unstratified tripolar vortex, van Heijst & Kloosterziel (1989); van Heijst *et al.* (1991) use an initial negative vorticity envelope. This envelope makes the vortex susceptible to barotropic instabilities. Carton *et al.* (1989) exploits these unstable modes to obtain stable tripolar vortices in their numerical simulations at constant density.

3.6.1 Numerical method and initial perturbation

The numerical method is a 2/3-dealiased pseudo-spectral code (Canuto *et al.* (1988)) solved in the vorticity-streamfunction formulation with periodic boundary conditions. This enforces a solenoidal velocity field. An additional equation is solved for the non-axisymmetric correction to the density field. The characteristic scales in the problem, as given in section (3.2.1) are determined by the vortex core size, δ_z, density core size, δ_ρ and circulation Ξ. For simplicity, we consider the transport coefficients to be constant. To enable comparison with the stability analysis presented in section 3.4, we consider a large Reynolds number, Re and Peclet number, Pe in the present simulations. This allows us to approach inviscid results with viscosity and diffusivity to stabilize the numerical scheme. The governing equations solved in cartesian coordinates can be written as,

$$\frac{d\tilde{Z}}{dt} = \frac{1}{\tilde{\rho}}\left(\frac{\partial\tilde{\rho}}{\partial y}\frac{d\tilde{u}}{dt} - \frac{\partial\tilde{\rho}}{\partial x}\frac{d\tilde{v}}{dt}\right) + \frac{1}{Re}\nabla^2\tilde{Z}, \tag{3.93}$$

$$\frac{d\tilde{\rho}}{dt} = \frac{1}{Pe}\nabla^2\tilde{\rho}. \tag{3.94}$$

Here d/dt represents the total derivative, $\tilde{Z}$ and $\tilde{\rho}$ are the total vorticity and density fields. The first term on the right-hand-side of equation (3.93) is responsible for baroclinic torque created by a misalignment of pressure and density surfaces. We use a unit Schmidt number, so $Re = Pe = \Xi/\nu$. A large value of 50000 was chosen. A domain size of $L = 8\pi$ in x and y directions was chosen and we use 1024^2 grid for all the cases. Periodicity enforces a net zero circulation in the flow, and hence the velocity field far away from the vortex axis is not accurately predicted. This prompts us to use a large domain size. This was found to be very important in order to capture the transient periods of the instability.

At $t = 0$, an initial perturbation is given to the vorticity and density fields.

$$\tilde{Z}(r,\theta,t) = Z(r) + \epsilon\ \hat{Z}(r,\theta,t), \tag{3.95}$$

$$\tilde{\rho}(r,\theta,t) = \rho(r) + \epsilon\ \hat{\rho}(r,\theta,t). \tag{3.96}$$

Here $[Z(r), \rho(r)]$ are the base-state vorticity and density profiles as defined in section 3.2, $[\hat{Z}(r,\theta), \hat{\rho}(r,\theta)]$ are perturbation vorticity and density fields normalized by $\max[\hat{Z}(r,\theta)]$, and ε controls the initial amplitude of the perturbation, to be discussed later. We fix the profile parameter n at 10 for both vorticity and density, as we did not wish to carry out a detailed parametric study for the present work. Other values of n are expected to

Run	n	At	m	δ_ρ/δ_z	ω_r(lin)	ω_i(lin)
1	10	-0.2	2	1.5	0.5803	0.04606
2	10	-0.5	2	1.5	0.6520	0.04377
3	10	-0.2	3	1.5	0.9874	0.02826
4	10	-0.5	3	1.5	1.0370	0.05190

Table 3.3: Description of the various parameters used in the numerical simulations. ω_r(lin) and ω_i(lin) are the frequencies and growth rates obtained from a linear stability analysis.

give qualitatively similar results. This choice of n was found to be ideal for the present problem as it provided a sufficiently large growth rate for a wide range of Atwood numbers which could be easily captured in the numerical simulations, and at the same time, the profile was sufficiently smooth to describe the steep gradients well while using a smaller number of total grid points. A larger value of n would require a much finer grid than used here.

An inviscid stability analysis was first carried out with a $n = 10$ vorticity and density profile. For simplicity, we fix the ratio of vortex and density core sizes at a value of 1.5. A viscous stability analysis at $Re = Pe = 50000$ did not produce any appreciable difference in the results. The numerical simulations carried out are listed in Table 3.3, but only a few representative results are presented. In figure 3.28, initial perturbations for vorticity and density fields are plotted for runs 1 and 3. The perturbations are organized as $2m$ spiral arms, and an additional rim of vorticity at the density interface can be noticed. This additional outer rim of vorticity is crucial to the formation of stable non-linear structures.

These perturbations are now added to base-state vorticity and density, and a small value of ϵ, fixed at 0.01 is used. Computations were also carried out with $\epsilon = 0.05, 0.1$. No appreciable difference was noticed in the results, but a shorter linear regime was obtained. With a value of $\epsilon = 0.01$, the peak vorticity perturbation value was $1/100$ of the base-state vorticity value at the vortex axis, and the peak density perturbation value was approximately $1/600$ of the average density value. These are small enough for linear dynamics to be captured well.

3.6.2 Results

In figures (3.29)-(3.30), we plot the full nonlinear time evolution of vorticity and density fields for run 1, which corresponds to a $m = 2$ perturbation with $At = -0.2$. At initial time, negative vorticity levels are about two orders of magnitude smaller than the maximum vorticity level. Time in these plots is non-dimensionalized by maximum vorticity value. After a very early transient adjustment of the perturbation field, an exponential growth ensues, whose rate is in good agreement with linear stability prediction. At $t = 40$, a ring of negative vorticity is formed around the vortex. This ring soon organizes itself into two satellite vortices. By $t = 80$, a fully developed tripolar vortex is formed, and at $t \approx 100$, saturation of $|Q_2(t)|$ is observed. To quantify the eccentricity of the perturbation field, we numerically calculate the multipole moment for $m = 2$. This is

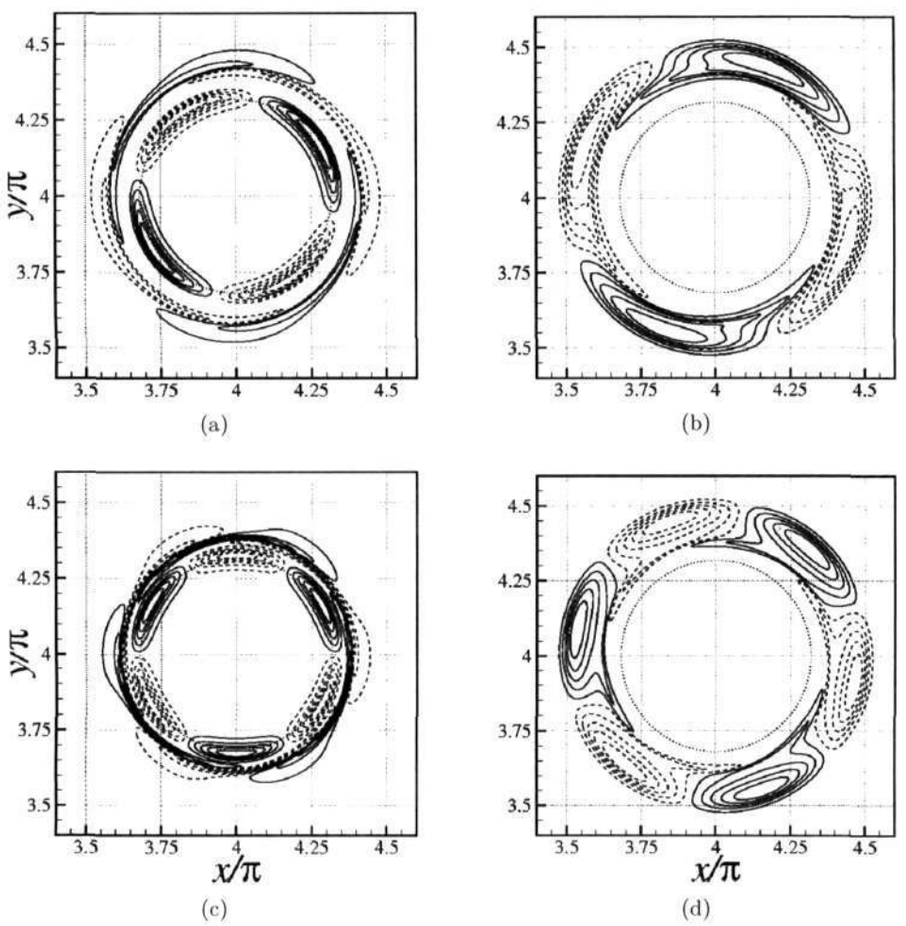

Figure 3.28: Vorticity (a, c) and density (b, d) perturbation corresponding to the most unstable mode for an $n = 10$ vortex. $At = -0.2$ and $m = 2$ for the first row, and $At = -0.5$ and $m = 3$ for the second row. Twelve equally spaced contours between maximum and minimum values plotted.

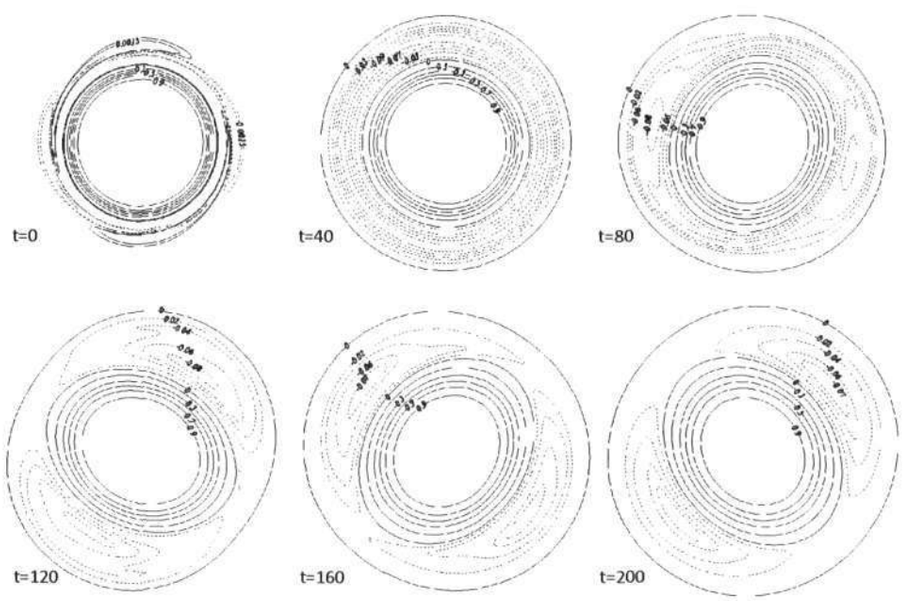

Figure 3.29: Vorticity contours at various times for Run-1 with $m = 2$ and $At = 0.2$. Notice the smallness of negative vorticity levels indicated with dashed lines. All figures are to same scale as shown in fig.(3.28). The nonlinear saturation into a tripolar state of an initially stably stratified configuration is evident.

plotted in fig.(3.31). Upon saturation, a flat region which survives for many turn-over time periods may be seen. The evolution of the square of the density fluctuations averaged over the simulation domain is plotted in fig.(3.32(a)). In our simulations, we directly calculate the non-axisymmetric part of the density field, $\hat{\rho}(x, y, t)$, and from this we obtain

$$\langle \hat{\rho}(t)^2 \rangle = \int_0^L \int_0^L \hat{\rho}(x, y, t)\ dxdy. \tag{3.97}$$

We additionally place monitor points across the density interface along a given radial line, and instantaneous values of total density were extracted at each time step. The time evolution of instantaneous density at five such monitor points is shown in fig.(3.32(b)). The first and last monitor points are far away from the density interface, and are placed inside and outside the density core respectively. At these two points, there is no change in density value up to an error of 10^{-6}. Whereas at other points, an oscillatory signal is obtained. Frequency spectrum yielded a dominant frequency of 0.57, which is in excellent agreement with the linear stability calculations. In fact, this rotation rate is seen to vary very little even for a fully developed tripolar vortex.

Because of the finite value of viscosity, vorticity in these satellites slowly homogenizes. At $t = 200$, the vorticity in the satellites is still an order of magnitude smaller than in the

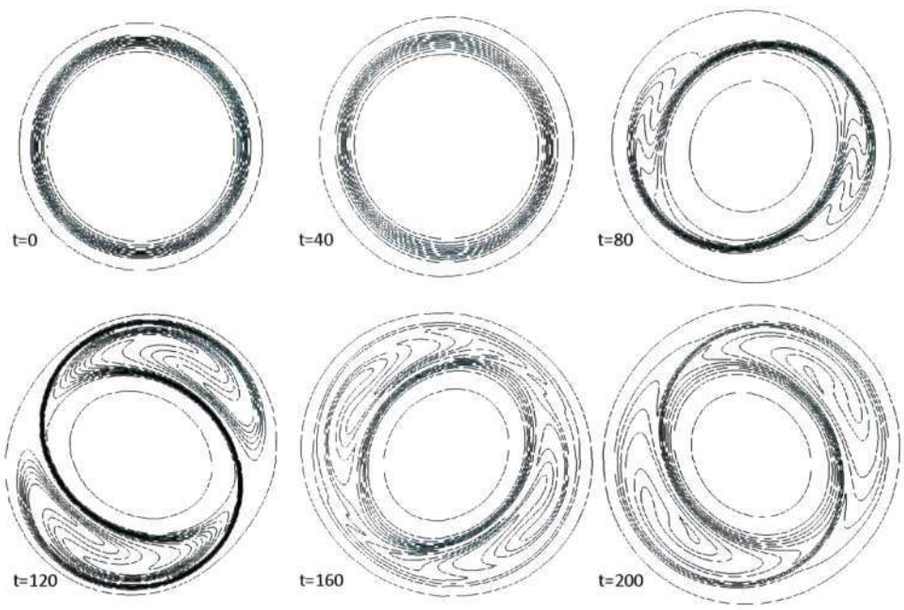

Figure 3.30: Density contours at various times for Run-1 with $m = 2$ and $At = 0.2$. 12 equally spaced contour levels between $\max(\bar{\rho})$ and $\min(\bar{\rho})$ are shown.

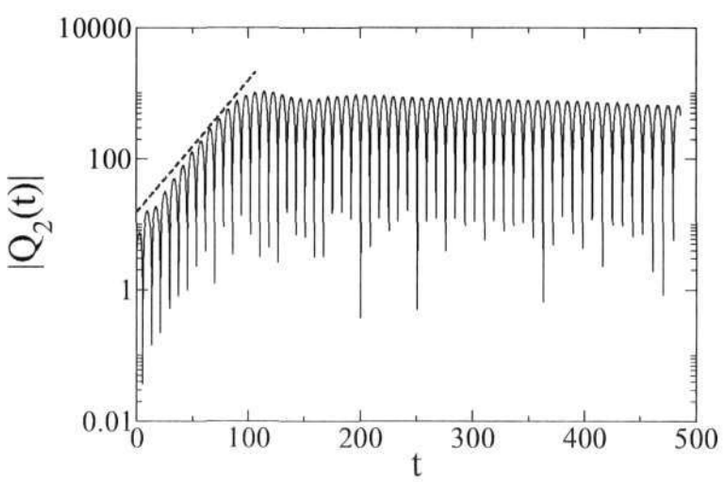

Figure 3.31: Multipole moment for Run-1 with $m = 2$ and $At = 0.2$. The dashed line indicates prediction from linear stability calculation and has a slope of 0.04606 as shown in table (3.3). The best fit for the numerical slope is approximately 0.051, in good agreement with the linear stability result. The flattening of $|Q_2(t)|$ at $t > 100$ corresponds to nonlinear saturation into a tripolar vortex.

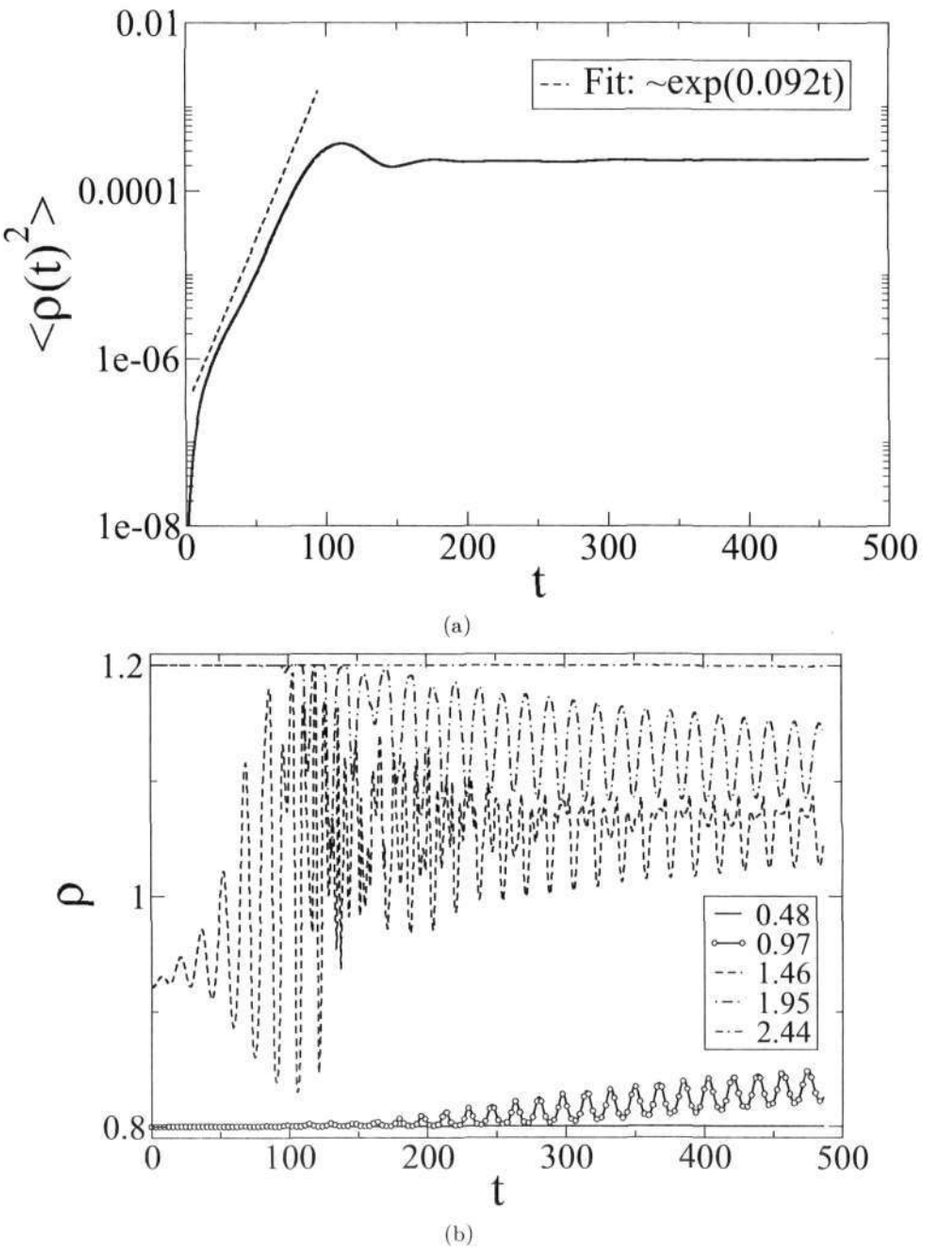

Figure 3.32: (a) Time evolution of $\rho(t)^2$ averaged over the entire domain, i.e $\langle \rho(t)^2 \rangle$ for Run-1 simulation with $m = 2$ and $At = 0.2$. (b) Time trace for the same case showing evolution of instantaneous density extracted from various monitor points placed along a radial line at radii 0.48, 0.97, 1.46, 1.95, 2.44. FFT spectrum yields a dominant frequency of 0.57, in excellent agreement with linear stability calculation shown in Table 3.3.

primary vortex. The whole structure slowly advects relative to the flow. Density contour plots in fig.(3.30) offer a good visualization of the flow field. The reversal of vorticity field in the satellites is clearly accompanied by density contours being twisted in the clockwise direction. The final tripolar vortex formed is observed to be stable for a very long period of time, and is only weakened slightly due to viscosity. Nonetheless, $Re = 50,000$ was observed to be a large enough value for inviscid dynamics to be captured. Smaller Reynolds number simulations were also carried out, and they yielded similar results.

3.7 Summary and Outlook

The primary focus of this work has been the stability properties of a radially density stratified vortex. The bulk of our attention is given to stable density stratification, i.e. a light-cored vortex, where density increases monotonically away from the vortex axis. Such a light-cored Rankine vortex is remarkably shown to become unstable when the density jump is placed at a radial location r_j immediately outside its core. Further, we show that for small Atwood numbers, instability growth rates of light-cored vortices are comparable to their heavy-cored counterparts. This result seems counter-intuitive, and moreover not in accord with the finding of Joly *et al.* (2005), that a light-cored Gaussian vortex is always stable. The difference is shown to arise from the steepness of the profiles. The instability is explained physically on the basis of a wave interaction mechanism. It is seen that shear is necessary for the interaction, so a density jump placed within a region of solid body rotation would be uninteresting. The interaction is strongest close to the critical radius r_c of the Kelvin wave. An expansion for small Atwood numbers shows that the growth rate of the instability scales as $|At|^{1/3}$ in the vicinity of the critical layer, and only as $|At|^{1/2}$ closer to the vortex core. Thus the instability appears first at r_c and is strongest in that vicinity. When r_j increases away from r_c there is a steep fall-off in the instability. Conversely, in a heavy-cored vortex, a jump placed in the region immediately outside the core, but within r_c, is stabilized. An Atwood number criterion for instability when the vorticity and density jumps coincide is derived. The physical mechanism leading to this destabilization/ stabilization of a light/ heavy-cored Rankine vortex is explained as a wave interaction. Further support for the mechanism is given by wave-energetic arguments. For a light core, two neutral waves interact to give exponential growth for a range of conditions, which may be predicted by our arguments.

The effect of smoothness of the profiles is studied by defining a class of vorticity and density profiles based on a parameter n. The limit $n \to \infty$ corresponds to a Rankine vortex and $n = 1$ represents a Gaussian vortex. For steep profiles, the instability is described as being caused by the interaction between the quasi-mode of the homogeneous vortex and an internal wave arising due to density inhomogeneity. A direct mathematical proof of this result was found to be too difficult at this stage, but this work demonstrates the feasibility of such an interaction within the linear regime. Using steep *tanh* density profiles, it is shown that instability vanishes for n between 1 and 2. To understand this range, we study the stability characteristics of a wide range of homogeneous vortex profiles. Due to a non-zero vorticity gradient at the critical radius, all smooth vortex profiles possess Landau poles with an exponentially decaying solution. In the large n limit, we show that these Landau poles become quasi-modes of the vortex, but for small

n, the exponential decay rate in an initial value problem departs from the Landau pole prediction. The eigenfunction structure in this case is dominated by a spiral outside the core with no vorticity inside it. This explains the absence of an instability in the work of Sipp *et al.* (2005) and Joly *et al.* (2005) where a Gaussian vortex with Gaussian density distribution was used.

The quasi-mode concept has been used earlier in interaction of boundary layer modes with 'true' eigenmodes of the system. In many such works, quasi-modes were studied in the context of non-linear resonant triad interactions. Here we show that it might be useful to interpret linear instabilities in smooth profiles through the same quasi-mode concept.

Due to an overall stabilizing influence in a light-cored vortex, it is useful to understand the effect of an unstable mode on the flow structure. Therefore, we study the nonlinear stages of these light-cored instabilities using direct numerical simulations. At short times, an exponential growth of the non-axisymmetric perturbation was observed which compared well with the linear stability analysis. Eventually, nonlinear saturation resulted in stable tripolar and quadrupolar vortices corresponding to $m = 2$ and 3 perturbations.

An extension of the present work to 3D flows would be interesting in many ways. Stratification can be considered both in the axial direction as has been recently studied by Le Dizès (2008) and Le Dizès & Billant (2009), and in the radial direction as done here. With constant axial stratification, internal gravity waves can radiate away from the vortex, leading to radiative instabilities. Moreover the fact that a 3D Rankine vortex supports an infinite number of discrete Kelvin modes tremendously increases the possibilities of wave interactions. The 3D equations have been derived, as discussed in the following chapter.

CHAPTER 4

3D STABILITY OF A RADIALLY STRATIFIED VORTEX

Scope of this chapter

In this chapter we derive the dispersion relation for three dimensional stability of a Rankine vortex with an axisymmetric density distribution. This chapter is an extension of the 2D analysis carried out in chapter 3. A detailed analysis of the dispersion relation is beyond the scope of this thesis.

4.1 Introduction

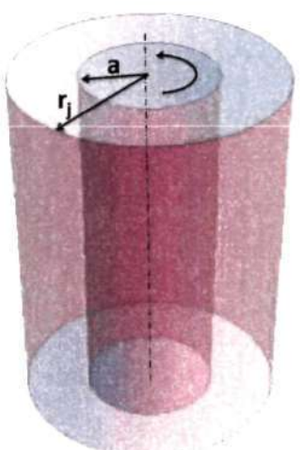

Figure 4.1: A schematic view of a 3D Rankine vortex, of core size, a with a circular density jump at $r = r_j$. Solid circles indicated the location of the vortex cores, either sharp or smooth. r_c and r_j are the radii of vortex and density cores respectively. Density at the vortex axis is ρ_1 and far-field density is ρ_2.

The 2D stability analysis of a Rankine vortex with circular density jump carried out in chapter 3 demonstrated the role of wave interactions in the instability of a light-cored vortex. To re-emphasize, the 2D Kelvin mode riding at the edge of the vortex core and an internal wave riding at the density interface can interact causing a weak instability. In a 3D problem, an infinite number of Kelvin modes are supported by the system. So, it is important to understand the role of wave-interactions in the 3D problem. Sipp *et al.* (2005) and Joly *et al.* (2005) motivate their 2D analysis with applications to

aircraft trailing vortices. It is well known that most of the dangerous instabilities in multiple vortices are three dimensional in nature. It is natural to inquire whether this is also true for a single vortex with radial density stratification. Uberoi *et al.* (1972) study the stability of a Rankine vortex with density varying across the vortex core. In this study, since the density jump location is kept arbitrary, the result of Uberoi *et al.* (1972) is obtained as a special case. There has been interest in 3D stability analysis of stratified vortices from a geophysical perspective, but most of the analysis concerns density variations along the axis of the vortex. As mentioned in chapter 1, geophysical vortices can sometimes experience radial density stratification, a polar vortex being a special case.

4.2 Governing equations

The base flow is an axisymmetric velocity field, $V(r)$ with an axisymmetric mean density distribution, $\bar{\rho}(r)$. The inviscid equations in cylindrical polar coordinates are given by

$$\frac{\partial u_r}{\partial r} + \frac{u_r}{r} + \frac{1}{r}\frac{\partial u_\theta}{\partial \theta} + \frac{\partial u_z}{\partial z} = 0, \tag{4.1a}$$

$$\frac{\partial u_r}{\partial t} + u_r\frac{\partial u_r}{\partial r} + \frac{u_\theta}{r}\frac{\partial u_r}{\partial \theta} + u_z\frac{\partial u_r}{\partial z} - \frac{u_\theta^2}{r} = -\frac{1}{\bar{\rho}}\frac{\partial p}{\partial r}, \tag{4.1b}$$

$$\frac{\partial u_\theta}{\partial t} + u_r\frac{\partial u_\theta}{\partial r} + \frac{u_\theta}{r}\frac{\partial u_\theta}{\partial \theta} + u_z\frac{\partial u_\theta}{\partial z} + \frac{u_r u_\theta}{r} = -\frac{1}{r\bar{\rho}}\frac{\partial p}{\partial \theta}, \tag{4.1c}$$

$$\frac{\partial u_z}{\partial t} + u_r\frac{\partial u_z}{\partial r} + \frac{u_\theta}{r}\frac{\partial u_z}{\partial \theta} + u_z\frac{\partial u_z}{\partial z} = -\frac{1}{\bar{\rho}}\frac{\partial p}{\partial z}, \tag{4.1d}$$

where u_r, u_θ and u_z are the velocities in the radial, azimuthal and axial directions respectively, and p is the total pressure. We perturb the vorticity and the density interface in the normal-mode form as follows:

$$r_1 = a + \epsilon_1 \exp[i(m\theta + kz - \omega t)], \tag{4.2a}$$

$$r_2 = r_j + \epsilon_2 \exp[i(m\theta + kz - \omega t)], \tag{4.2b}$$

This creates perturbation velocity and pressure fields in the form

$$u_r = f(r)\exp[i(m\theta + kz - \omega t)], \tag{4.3a}$$

$$u_\theta = V(r) + g(r)\exp[i(m\theta + kz - \omega t)], \tag{4.3b}$$

$$u_z = h(r)\exp[i(m\theta + kz - \omega t)], \tag{4.3c}$$

$$p = P + s(r)\exp[i(m\theta + kz - \omega t)], \tag{4.3d}$$

where the mean pressure P balances the base-flow centrifugal acceleration,

$$P = \int \frac{\bar{\rho}V^2}{r}dr. \tag{4.4}$$

Substituting velocities and pressure from equations (4.3) into equations (4.1), and expressing all velocity and pressure perturbations in terms of $h(r)$, we get,

$$f(r) = \frac{-i(\omega - mV/r)}{kD}\left[-\frac{dh}{dr}\left(\omega - \frac{mV}{r}\right) + \frac{mh}{r}\left(\frac{dV}{dr} + \frac{V}{r}\right)\right], \tag{4.5a}$$

$$g(r) = \frac{1}{kD}\left[\left(\frac{dV}{dr} + \frac{V}{r}\right)\left(\omega - \frac{mV}{r}\right)\frac{dh}{dr} + \frac{m}{r}\left(\frac{V^2}{r^2} - \left(\frac{dV}{dr}\right)^2 - \left(\omega - \frac{mV}{r}\right)^2\right)h\right], \tag{4.5b}$$

$$s(r) = \frac{\bar{\rho}h}{k}\left(\omega - \frac{mV}{r}\right), \tag{4.5c}$$

where

$$D = \frac{2V}{r}\left(\frac{dV}{dr} + \frac{V}{r}\right) - \left(\omega - \frac{mV}{r}\right)^2. \tag{4.6}$$

4.3 Base flow

The base-flow is a Rankine vortex with an axisymmetric density jump at $r = r_j$

$r \le a$	$a < r \le r_j$	$r > r_j$
$Z = Z_0$	$Z = 0$	$Z = 0$
$V = r\Omega_0$	$V = \Omega_0 a^2/r$	$V = \Omega_0 a^2/r$
$\bar{\rho} = \rho_1$	$\bar{\rho} = \rho_1$	$\bar{\rho} = \rho_2$

(4.7)

The ratio of the vortex size and density core size can be combined to define an 'aspect ratio' as

$$\lambda = \frac{a}{r_j}. \tag{4.8}$$

Substituting equations (4.5a), (4.5b), (4.5c) and (4.6) into the continuity equation, a single equation for $h(r)$ can be derived.

For $0 < r < a$,

$$r^2\frac{d^2h_1}{dr^2} + r\frac{dh_1}{dr} + (\nu^2 r^2 - m^2)h_1 = 0, \tag{4.9}$$

For $a < r < r_j$,

$$r^2\frac{d^2h_2}{dr^2} + r\frac{dh_2}{dr} - (\kappa^2 r^2 + m^2)h_2 = 0, \tag{4.10}$$

For $r > r_j$,

$$r^2\frac{d^2h_3}{dr^2} + r\frac{dh_3}{dr} - (\kappa^2 r^2 + m^2)h_3 = 0, \tag{4.11}$$

where

$$\nu^2 = k^2\left[\frac{4\Omega_0^2}{(\omega - m\Omega_0)^2} - 1\right]. \tag{4.12}$$

The subscripts 1, 2 and 3 denote the three regions in equation (4.7) in the direction

away from the vortex centre. The general solution in the three regions is given by

$$h_1(r) = C_{11}J_m(\nu r) + C_{12}Y_m(\nu r), \tag{4.13a}$$

$$h_2(r) = C_{21}I_m(kr) + C_{22}K_m(kr), \tag{4.13b}$$

$$h_3(r) = C_{31}I_m(kr) + C_{32}K_m(kr). \tag{4.13c}$$

J_m and Y_m are the Bessel functions of order m of first and second kind respectively, and I_m and K_m are the modified Bessel functions of first and second kind respectively (Abramowitz & Stegun (1965)). For finiteness of h_1 and h_3 as $r \to 0$ and $r \to \infty$ respectively, we require $C_{12} = 0$ and $C_{31} = 0$. To calculate the values of the constants in equations (4.13a, 4.13b, 4.13c), we use kinematic (continuity of u_r) dynamic (continuity of pressure) conditions at $r = a^{\pm}$ and $r = r_j^{\pm}$. The superscript $\pm$ denote the inner and outer surfaces of the interfaces.

At $r = a^-$, we have

$$\begin{aligned} u_{r_1}|_{r=a^-} &= \frac{\partial r_1^-}{\partial t} + \Omega_0 \frac{\partial r_1^-}{\partial \theta}, \\ &= -i\epsilon_1(\omega - m\Omega_0)e^{i(m\theta + kz - \omega t)}, \end{aligned} \tag{4.14}$$

Using equations (4.3a), (4.5a) and (4.13a), we get

$$C_{11} = \frac{\epsilon_1 k \left(4\Omega_0^2 - (\omega - m\Omega_0)^2\right)}{-\nu(\omega - m\Omega_0)J'_m(\nu a) + \dfrac{2m\Omega_0}{a}J_m(\nu a)}. \tag{4.15}$$

Similarly, for $r = a^+$

$$\begin{aligned} u_{r_2}|_{r=a^+} &= \frac{\partial r_1^+}{\partial t} + \Omega_0 \frac{\partial r_1^+}{\partial \theta}, \\ &= -i\epsilon_1(\omega - m\Omega_0)e^{i(m\theta + kz - \omega t)}. \end{aligned} \tag{4.16}$$

Using equations (4.3a), (4.5a) and (4.13b), we get the relation

$$C_{21}I'_m(ka) + C_{22}K'_m(ka) = \epsilon_1(\omega - m\Omega_0). \tag{4.17}$$

At $r = r_j^-$ and using equations (4.3a), (4.5a) and (4.13b), we get

$$C_{21}I'_m(kr_j) + C_{22}K'_m(kr_j) = \epsilon_2\left(\omega - m\Omega_0\lambda^2\right), \tag{4.18}$$

and $r = r_j^+$ and using equations (4.3a), (4.5a) and (4.13c), we get

$$C_{32} = \frac{\epsilon_2}{K'_m(kr_j)}\left(\omega - m\Omega_0\lambda^2\right). \tag{4.19}$$

Solving for C_{21} and C_{22} from equations (4.17) and (4.18), we get

$$C_{21} = \frac{-\epsilon_1(\omega - m\Omega_0)K'_m(kr_j) + \epsilon_2\left(\omega - m\Omega_0\lambda^2\right)K'_m(ka)}{K'_m(ka)I'_m(kr_j) - K'_m(kr_j)I'_m(ka)}, \tag{4.20}$$

and

$$C_{22} = \frac{\epsilon_1(\omega - m\Omega_0)I'_m(kr_j) - \epsilon_2\left(\omega - m\Omega_0\lambda^2\right)I'_m(ka)}{K'_m(ka)I'_m(kr_j) - K'_m(kr_j)I'_m(ka)}. \tag{4.21}$$

We now use the pressure continuity at $r = a$ and $r = r_j$. For $r < a$, we have

$$p_1 = \frac{\rho_1\Omega_0^2}{2}(r^2 - a^2) + \frac{\rho_1}{k}C_{11}J_m(\nu r)(\omega - m\Omega_0)e^{i(m\theta + kz - \omega t)}, \tag{4.22}$$

and for $a < r < r_j$, we have

$$p_2 = \frac{-\rho_1\Omega_0^2}{2}\left(\frac{a^4}{r^2} - a^2\right) + \frac{\rho_1}{k}\left(C_{21}I_m(kr) + C_{22}K_m(kr)\right)\left(\omega - m\Omega_0\lambda^2\right)e^{i(m\theta + kz - \omega t)}, \tag{4.23}$$

Equating p_1 and p_2 at $r = a$, we get the relation

$$C_{11}J_m(\nu a) = C_{21}I_m(ka) + C_{22}K_m(ka). \tag{4.24}$$

Using the expressions for C_{11}, C_{21} and C_{22}, we can express ϵ_2 in terms of ϵ_1, i.e.,

$$\epsilon_2 = \frac{\epsilon_1 W}{(\omega - m\Omega_0\lambda^2)Q(a;a)}\left[\mathcal{L} + \frac{(\omega - m\Omega_0)Q(r_j;a)}{W}\right] \tag{4.25}$$

where the notation $Q(\star;\star)$ is defined as

$$Q(\alpha;\beta) = K'_m(k\alpha)I_m(k\beta) - I'_m(k\alpha)K_m(k\beta), \tag{4.26}$$

and

$$\mathcal{L} = \frac{k\left(4\Omega_0^2 - (\omega - m\Omega_0)^2\right)J_m(\nu a)}{-\nu(\omega - m\Omega_0)J'_m(\nu a) + \dfrac{2m\Omega_0}{a}J_m(\nu a)}, \tag{4.27}$$

$$W = K'_m(ka)I'_m(kr_j) - I'_m(ka)K'_m(kr_j). \tag{4.28}$$

To obtain the dispersion relation by matching pressure across $r = r_j$. For $r > r_j$, we have

$$p_3 = \frac{-\rho_2\Omega_0^2}{2}\left(\frac{a^4}{r^2} - a^2\right) + \frac{\rho_2}{k}C_{32}K_m(kr_j)\left(\omega - m\Omega_0\lambda^2\right)e^{i(m\theta + kz - \omega t)}. \tag{4.29}$$

Equating p_2 and p_3 at $r = r_j$ and after some tedious algebra, we get the dispersion

relation as

$$
\begin{aligned}
&(\varrho-1)\Omega_0^2\left[\frac{W\mathcal{L}}{Q(a;a)(\omega-m\Omega_0\lambda^2)}+\frac{(\omega-m\Omega_0)}{(\omega-m\Omega_0\lambda^2)}\frac{Q(r_j;a)}{Q(a;a)}\right]\\
&+\frac{\varrho}{kr_j}\left[\frac{-(\omega-m\Omega_0)}{WQ(a;a)}(Q(a;a)Q(r_j;r_j)-Q(a;r_j)Q(r_j;a))+\mathcal{L}\frac{Q(a;r_j)}{Q(a;a)}\right](\omega-m\Omega_0\lambda^2)\\
&=\frac{1}{kr_j}\frac{K_m(kr_j)}{K'_m(kr_j)}\left[\frac{W\mathcal{L}}{Q(a;a)}+(\omega-m\Omega_0)\frac{Q(r_j;a)}{Q(a;a)}\right](\omega-m\Omega_0\lambda^2).
\end{aligned}
\tag{4.30}
$$

4.4 Special cases

We now show that the above dispersion relation reduces to the known results in literature under special cases.

4.4.1 $r_j = a$

In this limit, the density jump location coincides with the edge of the vortex core. With $r_j = a$, we have $\lambda = 1$, $W \equiv 0$ and $Q(r_j;a) \equiv Q(a;a)$. Equation (4.30) reduces to

$$
(\varrho-1)\Omega_0^2+\frac{\varrho}{ka}\mathcal{L}(\omega-m\Omega_0)=\frac{1}{ka}\frac{K_m(ka)}{K'_m(ka)}(\omega-m\Omega_0)^2. \tag{4.31}
$$

Substituting $\mathcal{L}$ from equation (4.27), the above equation reduces to

$$
(\varrho-1)\Omega_0^2-\varrho(\omega-m\Omega_0)\frac{\left(4\Omega_0^2-(\omega-m\Omega_0)^2\right)}{\nu a(\omega-m\Omega_0)\dfrac{J'_m(\nu a)}{J_m(\nu a)}-2m\Omega_0}=\frac{(\omega-m\Omega_0)^2}{ka\dfrac{K'_m(ka)}{K_m(ka)}}. \tag{4.32}
$$

After some re-arrangement, we get

$$
(\varrho-1)\Omega_0^2-\frac{\varrho\left[\dfrac{4\Omega_0^2}{(\omega-m\Omega_0)^2}-1\right]}{\nu a\dfrac{J'_m(\nu a)}{J_m(\nu a)}-\dfrac{2m\Omega_0}{(\omega-m\Omega_0)}}=\frac{1}{ka\dfrac{K'_m(ka)}{K_m(ka)}}. \tag{4.33}
$$

Using the definition of ν, we get

$$
(\varrho-1)\Omega_0^2-\frac{\varrho\nu^2}{k^2}\frac{1}{\nu a\dfrac{J'_m(\nu a)}{J_m(\nu a)}-\dfrac{2m\Omega_0}{(\omega-m\Omega_0)}}=\frac{1}{ka\dfrac{K'_m(ka)}{K_m(ka)}}. \tag{4.34}
$$

Equation (4.34) is the dispersion relation derived in Uberoi *et al.* (1972) with no axial flow along the vortex. Written in this form, it is easy to take the 2D limit ($k \to 0$) of the above equation.

4.4.2 $\varrho = 1$

Substituting $\varrho = 1$ in equation (4.30), we get

$$\left[\frac{-(\omega - m\Omega_0)}{WQ(a;a)}(Q(a;a)Q(r_j;r_j) - Q(a;r_j)Q(r_j;a)) + \mathcal{L}\frac{Q(a;r_j)}{Q(a;a)}\right] = \frac{K_m(kr_j)}{K'_m(kr_j)}\left[\frac{W\mathcal{L}}{Q(a;a)} + (\omega - m\Omega_0)\frac{Q(r_j;a)}{Q(a;a)}\right]. \tag{4.35}$$

The above relation does not reduce to the famous Kelvin's dispersion relation (see Kelvin (1880), Saffman (1992)) in spite of the fact that $\varrho = 1$ corresponds to a homogeneous flow. A similar situation was seen in chapter 3 where the 2D cubic dispersion relation, equation (3.21), did not reduce to the 2D Kelvin mode frequency. Instead, we recover the continuous spectrum frequency for a mode localized at $r = r_j$. The same is true of equation (4.35) where, in addition to the 3D Kelvin mode dispersion relation, we have a continuous spectrum mode localized at $r = r_j$. Note that this is only one family of continuous spectrum modes possible. A detailed analysis of the 3D continuous spectrum modes for a homogeneous Rankine vortex is contained in Roy & Subramanian (2009). To recover the Kelvin mode dispersion relation, we further substitute $r_j = a$ in equation (4.35) which reduces it to the form

$$\frac{\left(4\Omega_0^2 - (\omega - m\Omega_0)^2\right) J_m(\nu a)}{-\nu a(\omega - m\Omega_0)J'_m(\nu a) + 2m\Omega_0 J_m(\nu a)} = \frac{1}{ka}\frac{K_m(ka)}{K'_m(ka)}(\omega - m\Omega_0). \tag{4.36}$$

On suitable rearrangement, we get the well known 3D dispersion relation of a Rankine vortex without axial flow (see Saffman (1992), pp. 216).

$$\frac{k^2}{\nu^2}\left[\frac{\nu a J'_m(\nu a)}{J_m(\nu a)} - \frac{2m\Omega_0}{(\omega - m\Omega_0)}\right] = -ka\frac{K'_m(ka)}{K_m(ka)}. \tag{4.37}$$

4.5 Summary

In this chapter, we derived the dispersion relation for a 3D perturbations on a Rankine vortex with a circular density jump outside the vortex core. A detailed analysis of this dispersion relation is beyond the scope of this thesis. It is further shown that this relation reduces to existing dispersion relations published in literature, including the Kelvin's dispersion relation for a homogeneous Rankine vortex.

It would be of interest to carry out a similar study with axial density stratification as this problem would be greatly relevant to geophysical flows. Surprisingly, the stability of a single vortex with axial density stratification has received attention only recently (see Billant & Le Dizés (2009), Le Dizès & Billant (2009), Schecter & Montgomery (2004)). Most of the earlier studies were carried out in the framework of shallow water equations or other similar approximations.

CHAPTER 5

VORTEX AT A FLAT DENSITY INTERFACE

Scope of this chapter [1]

In the previous chapter, we have studied the stability of an axisymmetric vortex with an axisymmetric density distribution. This allowed the stability equations to be Fourier decomposed in the azimuthal direction, and hence led to a significant simplification in the analysis. One of the key findings of the previous chapter is that even light-cored vortices can be unstable with significant growth rates. In this chapter, we consider a more generic and realistic problem of a vortex encountering a flat density interface as shown in fig.(5.1).

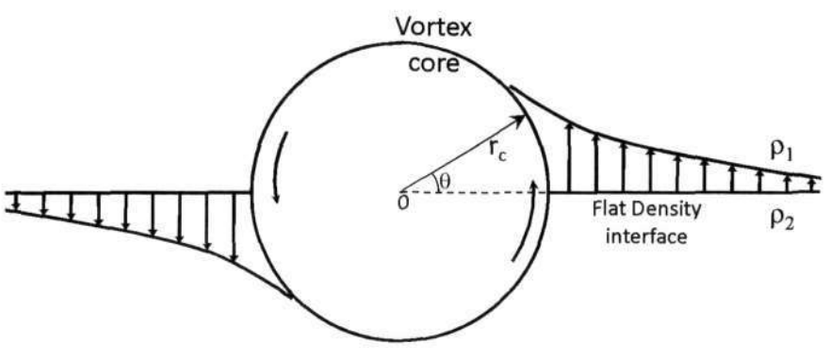

Figure 5.1: A schematic view of an axisymmetric vortex placed at a flat density interface. The density interface will wind-up into a spiral due to differential rotation indicated by vertical arrows.

As time progresses, the density interface winds itself into an ever-tighter spiral. We show that this results in a combination of a centrifugal Rayleigh-Taylor (CRT) instability and a new spiral Kelvin-Helmholtz (SKH) type of instability. The SKH instability arises because the density interface is not exactly circular, and dominates at large times. Our analytical study of an inviscid idealized problem illustrates the origin and nature of the instabilities. In particular, the SKH is shown to grow slightly faster than exponentially. The predicted form lends itself for checking by a large computation. From a viscous stability analysis using a finite-cored vortex, it is found that the dominant azimuthal wavenumber is smaller for lower Reynolds number. At higher Reynolds numbers, disturbances subject to the combined CRT and SKH instabilities grow rapidly, on the inertial timescale, while the flow is stable at low Reynolds numbers due to homogenization of density. Our direct numerical simulations are in good agreement with these studies in

[1]The contents of this chapter appeared in J. Fluid Mech. (2010), Vol. 646, pp. 415-439.

the initial stages, after which non-linearities take over. At Atwood numbers of 0.1 or more, and a Reynolds number of 6000 or greater, both stability analysis and simulations show a rapid destabilization. The result is an erosion of the core, and breakdown into a turbulence-like state. In studies at low Atwood numbers, the effect of density on the inertial terms is often ignored, and the density field behaves like a passive scalar in the absence of gravity. The present study shows that such treatment is unjustified in the vicinity of a vortex, even for small changes in density when the density stratification is across a thin layer. The study would have relevance to any high Peclet number flow where a vortex is in the vicinity of a density-stratified interface.

5.1 Introduction

Vortical structures are subject to instabilities of various kinds, a common cause for the instability being the existence of other vortical structures in the neighborhood. The Crow instability (Crow (1970)) for a counter-rotating vortex pair of small core is well-known. Vortices of finite core, rendered non-axisymmetric (often elliptic) by the strain field of their neighbours, are then unstable to shorter wave-length disturbances (see e.g. Kerswell (2002)). Miyazaki & Fukumoto (1992) and Itano (2004) studied the effect of stratification of density perpendicular to the vortex axis on these elliptical instabilities. Both found that stratification suppresses the elliptical instability. When placed in a density-stratified fluid with the stratification parallel to their axes, systems of two or more vortices display the zig-zag instability (Billant & Chomaz (2000)). An important effect of density stratification, acting through such instabilities or otherwise, is to flatten out the structures and make the flow quasi two-dimensional. This property, and the variety of applications, has made the dynamics of vortical structures in a density-stratified environment a subject of much interest. The instabilities mentioned above are all three-dimensional, and involve more than one vortex. Under the Boussinesq approximation, a perpendicular density stratification has been studied in two dimensions by Brandt & Nomura (2007) in the context of vortex merger. It is shown that at a Prandtl number of 1 and Reynolds numbers above 2500, a stable density stratification aids vortex merger by speeding up their approach towards each other.

The present study is of a lone vortex with its axis perpendicular to the plane of density stratification, with no gravity. For this geometry the dominant effects are again expected to be of two-dimensional nature. An initially flat density interface is wound up into an increasingly tightened spiral by the vortex, similar to how it would advect a patch of passive scalar (see for example Flohr & Vassilicos (1997); Moffatt & Kamkar (1983)). The scaling of the spiral is derived here analytically in a more direct fashion than in earlier studies. It is shown that two kinds of instabilities, of a Rayleigh-Taylor and Kelvin-Helmholtz types are then triggered. The former arises from a mechanism similar to the centrifugal-acceleration driven Rayleigh-Taylor instability of a vortex with a heavy core, as studied by Fung (1983); Fung & Kurzweg (1975); Greenspan (1968); Saunders (1973); Sipp *et al.* (2005) and Joly *et al.* (2005). The novelty here is that we have heavy to light and light to heavy jumps occurring alternately, and the resulting flow is still unstable. The latter arises purely from the fact that the density interface, being spiral, is not quite circular. Both instabilities would be missed upon neglecting inertial

effects due to density variations, i.e., we need to include non-Boussinesq effects. Gravity is unnecessary in this process, and if it existed, would only act to aid the instability in some regions and slow it down in others. Here, and in the following, by the term 'non-Boussinesq', we mean the inclusion of density stratification effects in inertial terms. Note that for simplicity we neglect variations in the transport coefficients.

A work of relevance that must be discussed here is that of a stratified mixing layer of Reinaud *et al.* (2000). By an inviscid simulation, it is shown that this flow disintegrates into turbulence. The process begins with the creation of vorticity braids by the traditional KH mechanism. Subsequently, baroclinic torque enhances the vorticity in portions of the braid and decreases it in others. The vorticity-enhanced regions are further susceptible to a secondary instability, which speeds up the disintegration of the mixing layer. An extension of this study to three-dimensional viscous situations by Fontane & Joly (2008) showed an increase in the growth of the instability. Importantly the mechanism of vorticity enhancement, due to centrifugal forces, is similar to that of the vorticity creation we shall see in the spiral interfaces below. The present work however addresses a different flow situation, of density interfaces in the vicinity of vortices. We show that the density interfaces that initially respond passively to the vortex, can ultimately be the cause for the destruction of the main vortex itself. The simplicity of the model configuration allows the analytical treatment of section 5.2, showing the density interfaces to form Lituus spirals, where the baroclinic vorticity may be estimated as a function of distance from the central vortex core, and time. The instability of the model basic flow is studied, and the effect of various parameters, including viscosity, evaluated. We show that sharp density interfaces can lead to non-Boussinesq effects even at low Atwood numbers. It is also seen that the net effect of alternately placed stabilizing and destabilizing density jumps is one of rapid destabilization.

We begin in section 5.2.1 with the simplest model, of a point vortex at a sharp density interface. The flow is taken to be inviscid with zero density diffusion. We discuss the formation and evolution of the spiral, and a scale for the density-homogenized region close to the core. For studying the instabilities, the density jumps are first modeled as circular, and then in section 5.2.2 as spirals. With the replacement of a point vortex by a Rankine vortex (section 5.2.3), conditional stabilization is obtained at the edge of the vortex core, while in the interior, the growth rate is constant. In the above, analytical solutions were obtained using step changes in density and vorticity. In section 5.3, the effect of viscosity, and of smooth vorticity and density profiles are considered. The eigenvalue problem is solved using Chebyshev collocation, and the dominant azimuthal wave-number and growth rates are obtained for various conditions. Section 5.4 consists of direct numerical simulations, of inviscid flow, and of viscous flow at finite diffusivity, by a spectral method. The inviscid simulations include a small hyper-viscosity and hyper-diffusivity which cut-off numerical (and other) contributions to high wave-numbers. Linear effects are displayed up to some time, with good qualitative agreement with the predictions of sections 5.2 and 5.3. Afterwards vortex roll-up and other nonlinear effects are seen, including the appearance of a turbulence-like state at later times.

The predictions made here have relevance whenever a vortex and a relatively sudden density change co-exist in the same neighborhood. A cyclone close to a coastline, moving towards it with a velocity component parallel to it, could be one such situation. The

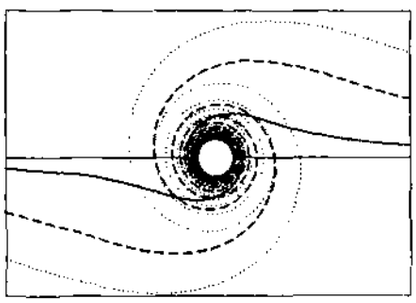

Figure 5.2: Evolution with time of an initially horizontal density interface due to a point vortex at the origin. The dotted line is at a later time than the dashed line, which in turn has evolved from the solid line. At finite Peclet number, the density would be homogeneous within a radius of $r_h \sim Pe^{1/3}(\kappa t)^{1/2}$, indicated by the grey circle.

actual contribution of the present instability in weakening the cyclone are unclear, since a cyclone is a complicated entity with barriers which protect it from annihilation, but it would be revealing to examine this problem using the non-Boussinesq equations. Other situations where this mechanism could apply would be in modifying submarine signatures or in an aircraft trailing vortex descending in a stratified atmosphere.

5.2 Inviscid stability analysis

5.2.1 A point vortex and a sharp density interface

Consider a point vortex of circulation Γ located at an initially straight density interface, with a jump $\Delta\rho$ in density across it. The flow is taken to be inviscid, and with zero diffusivity ($\kappa = 0$) of the density field. The initial interface is represented as a horizontal line in figure 5.2 but, since we do not take gravity into consideration, its orientation does not matter. The point vortex causes a spiralling of the density interface, whose evolution is shown in the same figure. Note that each point on the interface moves in a circular path at an azimuthal velocity $U = \Gamma/(2\pi r)$, where r is its radial distance from the vortex. In the initial phase of the dynamics, the interface advects passively, until its configuration allows instabilities to set in. This will be confirmed in the numerical simulations of the full equations in section 5.4.

At a given time t, let r_n be the radial location where the interface has completed n full rotations as shown in fig.5.3. Then $n = \Gamma t/4\pi^2 r_n^2$, and the spacing λ_n between two zero crossings for density jumps of same sign is given by

$$\lambda_n = r_n - r_{n+1} = \sqrt{\frac{\Gamma t}{4\pi^2 n}} - \sqrt{\frac{\Gamma t}{4\pi^2 (n+1)}}. \tag{5.1}$$

To obtain the spacing between jumps of opposite sign, $n+1$ must be replaced by $(n+1/2)$

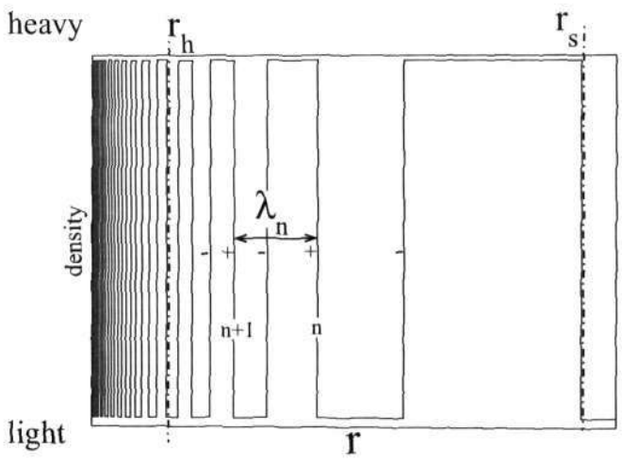

Figure 5.3: An instantaneous radial cross-section of the density profile showing the r^3 scaling of the spacing λ between neighbouring density jumps. If the diffusivity were to be finite, the density would be homogenized to its average value at radial distances below r_h. Both the homogenized front and the location r_s of the largest spiral move radially outward with time as $t^{1/2}$. For large Pe, $r_s >> r_h$.

in the above formula. For large n, the spacing between successive turns of the spiral thus scales as

$$\lambda_n \sim \frac{r^3}{\Gamma t}. \tag{5.2}$$

Figure 5.3 shows an instantaneous density profile at time t in a radial cross-section across the spiral structure. The density jumps alternately to the values ρ_l and $\rho_h = \rho_l + \Delta\rho$ of the light and heavy fluid respectively. In accordance with equation (5.2), the spacing between successive jumps rapidly increases away from the origin with an r^3 scaling. If for a moment we take the diffusivity κ to be small but non-zero, corresponding to a finite Peclet number $Pe \equiv \Gamma/\kappa$ and a diffusion length scale $l_d \sim (\kappa t)^{1/2}$, we see that for $\lambda_n < l_d$, diffusion would have erased the jumps, and homogenized the density to its average value $\rho_{ave} = (\rho_l + \rho_h)/2$. The radius r_h of this homogenized front would scale, given equation (5.2), as

$$\frac{r_h}{l_d} \sim Pe^{1/3} \tag{5.3}$$

while inertia would dictate that the spiral extend up to a radial distance

$$r_s \sim l_d Pe^{1/2}. \tag{5.4}$$

The instantaneous size r_s of the spiral may be taken, for example, to be equal to the location where the interface has completed one rotation. For a Peclet number tending to infinity, we expect many density jumps to exist between r_h and r_s. By different and more general approaches, Moffatt & Kamkar (1983), Rhines & Young (1983), Flohr & Vassilicos (1997) and Bajer *et al.* (2001) had obtained scaling equivalent to equation (5.3) for the accelerated diffusion of passive scalars near a vortex, due to the accumulation of

discontinuities. Incidentally Gilbert (1988) showed how spiral structures forming around coherent vortices affect the spectrum of two-dimensional turbulence.

We now study the linear stability of an instantaneous snapshot of the flow, taking the base flow to be slowly varying in time. The assumption is akin to the parallel flow approximation in space for spatially developing flows such as in boundary layers, and is valid when the change in the structure is much slower than the frequency of the dominant disturbance, which we shall see to be the case for disturbances of high azimuthal wavenumber. We first approximate the spiral density interface by concentric circles of radii $r_j, j = 1,2,3....n$ which are spaced as $r_j - r_{j-1} \sim r_j^3$. The fact that the spiral is different from a series of circles is also important, and instructive to study separately. This is done in section 5.2.2. Here n step changes in density are under consideration, and the density (for $r > r_h$) is given by

$$\bar{\rho} = \rho_{ave} \pm \frac{(-1)^j}{2}\Delta\rho \qquad r_{j-1} < r < r_j. \tag{5.5}$$

The density of the innermost layer, just beyond r_h, hops between ρ_l and ρ_h with time, and subsequent jumps alternate in sign. The vorticity and density balance equations are given in the inviscid, infinite Peclet number limit by

$$\bar{\rho}\frac{\mathcal{D}Z}{\mathcal{D}t} = -\nabla\bar{\rho} \times \frac{\mathcal{D}\mathbf{u}}{\mathcal{D}t}. \tag{5.6}$$

$$\frac{\mathcal{D}\bar{\rho}}{\mathcal{D}t} = 0, \tag{5.7}$$

where $\mathcal{D}/\mathcal{D}t \equiv \partial/\partial t + \mathbf{u}\cdot\nabla$, and $\mathbf{u} = (u_r\mathbf{e}_r, u_\theta\mathbf{e}_\theta)$, Z and ρ denote the velocity vector (of radial and azimuthal components), the vorticity and the density respectively. The flow is taken to be incompressible, so $\nabla\cdot\mathbf{u} = 0$. If the density in equation (5.6) were to be replaced by its average value, that would constitute a neglect of non-Boussinesq effects. The right hand side would then be zero, and the flow would remain irrotational forever except at the origin. For small Atwood number

$$\mathcal{A} \equiv \frac{\Delta\rho}{\rho_h + \rho_l}, \tag{5.8}$$

this approximation is made most often, but we shall see that not making this approximation is crucial to obtaining the correct, and dramatic, dynamics of this flow.

Linearising equation (5.6) about the base flow, assuming the perturbations to be of normal mode form, e.g., $\hat{u}_r = u_r(r)\exp[i(m\theta - \omega t)]$, and eliminating u_θ, we get

$$\left\{\frac{r^2\bar{\rho}}{m^2}\left(\omega - \frac{mU}{r}\right)\left(u_r' + \frac{u_r}{r}\right) + \frac{r\bar{\rho}}{m}\left(U' + \frac{U}{r}\right)u_r\right\}' - \bar{\rho}\left(\omega - \frac{mU}{r}\right)u_r$$
$$-\bar{\rho}\frac{2U}{m}\left(u_r' + \frac{u_r}{r}\right) = \frac{-U^2\bar{\rho}'}{r(\omega - mU/r)}u_r. \tag{5.9}$$

Around a point vortex, the mean azimuthal velocity $U = \Gamma/(2\pi r)$, and the primes denote differentiation with respect to the radial coordinate r. The step changes in

density shown in equation (5.5) correspond to delta functions in its derivative, $\rho' \equiv (-1)^{j+1}\Delta\bar{\rho}\delta(r - r_j)$. Away from the discontinuities, equation (5.9) may be simplified to

$$\mathcal{I}u_r \equiv \left(\omega - \frac{mU}{r}\right)\left[r^2 u_r'' + 3ru_r' - (m^2-1)u_r\right] + mrZ'u_r = 0 \tag{5.10}$$

For a point vortex, the gradient of the vorticity $Z' = 0$ for $r > 0$ (but Z' assumes non-zero values in section 5.2.3). The solutions are of the form

$$u_r = P_j r^{m-1} + Q_j r^{-m-1}, \qquad j = 0, 1, \cdots n. \tag{5.11}$$

Since u_r is a linear eigenfunction, one of the constants P_j, Q_j may be fixed arbitrarily. The remaining $2n+1$ constants and the unknown eigenvalue ω may be resolved as follows. The perturbed density interfaces are located at $r = (r_j + \hat{\eta}_j), j = 1, 2, 3...n$. Integrating equation (5.9) between $\eta_j - \epsilon$ and $\eta_j + \epsilon$ for $\epsilon \to 0$ we get n jump conditions

$$\Delta_\eta\left\{\frac{r^2\bar{\rho}}{m^2}\left(\omega - \frac{mU}{r}\right)\left(u_r' + \frac{u_r}{r}\right) + \frac{r\bar{\rho}}{m}\left(U' + \frac{U}{r}\right)u_r\right\} = \left(\frac{-U^2 u_r}{r(\omega - mU/r)}\right)_\eta \Delta_\eta(\bar{\rho}) \tag{5.12}$$

where

$$\Delta_\eta\{f\} = f|_{r_j+\eta_j+0} - f|_{r_j+\eta_j-0}. \tag{5.13}$$

Recognizing that u_r is continuous at each interface, and decays to zero both at $r = 0$ and as $r \to \infty$, gives $n+2$ more conditions. The system may then be simplified into a dispersion relation for ω in the form of a polynomial of degree $2n$.

For a single circular density jump at $r = r_1$ the dispersion relation is

$$\omega = \frac{m\Gamma}{r_1^2} \pm \sqrt{-\frac{m\Gamma^2}{r_1^4}\frac{(\rho_0 - \rho_1)}{(\rho_0 + \rho_1)}}, \tag{5.14}$$

and the frequency and growth rate of the perturbation are given respectively by the real and imaginary parts of ω. The flow is unstable to perturbations of any azimuthal wavenumber when $\rho_0 > \rho_1$, i.e., when there is heavy fluid inside and light fluid surrounding it. This result is perfectly analogous to a planar Rayleigh-Taylor instability (see e.g. Drazin & Reid (1981)), with gravity replaced by the centrifugal acceleration at a given radius. We shall return to this in section 5.2.3. It may also be derived from Rayleigh's criterion for centrifugal instability, modified to account for density. In this context, von Kármán (see Lin (1955)) proposed that $d(\bar{\rho}U^2r^2)/dr \geq 0$ for stability. Yih (1961) showed that the above criterion is neither necessary nor sufficient, and that $d\bar{\rho}/dr \geq 0$ and $d(U^2r^2)/dr \geq 0$ are required separately, for stability. Other stability criteria have been formulated, notably by Howard & Gupta (1962); Leibovich (1969) for axisymmetric and non-axisymmetric disturbances. A comprehensive review is given in Sipp *et al.* (2005). Fung (1983); Fung & Kurzweg (1975) wrote down expressions similar to ours above for simple artificially prescribed circular RT+KH situations.

In the present flow, $4\pi^2U^2r^2 = \Gamma^2$ is constant for $r > 0$, while Yih's first criterion is violated when light fluid surrounds heavy. The perturbation eigenfunction describes a

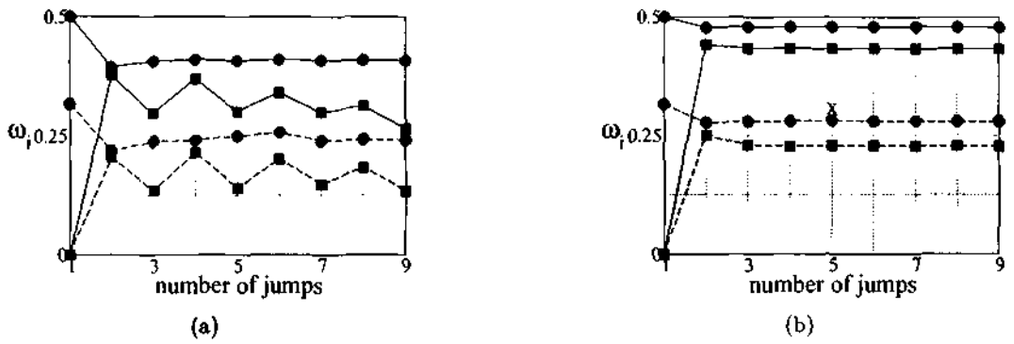

Figure 5.4: Maximum growth rate of disturbance as a function of the number of density jumps. The solid lines correspond to $m = 5$ and the dashed lines to $m = 2$. The circles show the growth rate with the innermost fluid layer being heavy, at $\rho_h = 1.05$, while squares are for this layer being light, at $\rho_l = 0.95$. The first two jumps are located at (a) $r_1 = 0.1, r_2 = 0.102$ (b) $r_1 = 0.1, r_2 = 0.105$, with the remaining jumps spaced out as r^3. The growth rate has been normalized by Γ/r_1^2.

circular vortex sheet at r_1 of strength

$$\Delta u_\theta = -2iu_r,$$

which is independent of the density difference. When the density difference $\Delta\rho$ goes to zero, the system would support a neutral mode with the above eigenfunction, one among the continuous spectrum of non-Kelvin modes (Roy & Subramanian (2009)). Just as a disturbance of small wavelength in a boundary layer does not perceive the downstream growth of the boundary layer, a disturbance of large azimuthal wavenumber riding on the interface at a certain radial location does not perceive the time variation in the spiral structure of the interface. At low wavenumbers too, our results shown in figure 5.4 indicate that the growth rate of the instability is insensitive to the spacing between the jumps, so a frozen interface approximation appears to be valid here too. However, for completeness, a global instability analysis accounting for the time variation of the spiral would be warranted.

Figure 5.4 shows the growth rate ω_i of the instability with multiple density jumps of size $\Delta\rho = \pm 0.1$, obtained using Mathematica. The single jump ($n = 1$) result is as in equation (5.14). In the two jump case, the second jump, being of opposite sign, partially neutralizes the first. When the initial jumps are very closely spaced, the growth rate oscillates with the addition of jumps as shown in figure (5.4(a)), but when they are not too close (figure 5.4(b)), the growth rate after the first few jumps is insensitive to further addition of either a stabilizing or a destabilizing jump. Note that the growth rate of the instability is substantial, of the same order of magnitude as the inverse of the inertial time scale, whether the first jump is positive or negative. In other words, the flow is quite unstable irrespective of whether the central region is light or heavy. This result is different from the requirement of a heavy core in earlier work on a single stratified layer (Joly *et al.* (2005); Sipp *et al.* (2005)). The eigenfunctions in the radial and azimuthal

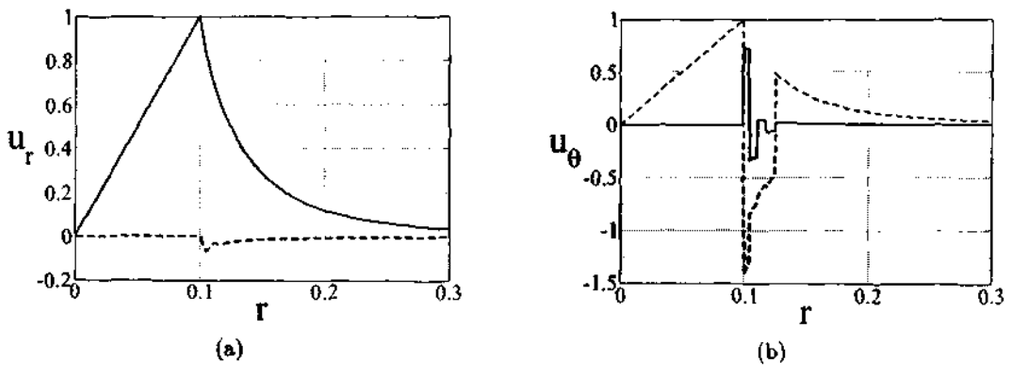

Figure 5.5: (a) Radial and (b) azimuthal eigenfunctions for a point vortex with 5 density jumps placed with an r^3 spacing, corresponding to the point marked **X** in figure 5.4(b). The solid and dashed lines show the real and imaginary parts respectively.

direction corresponding to five jumps with a heavy inner layer are shown in figure 5.5, the behaviour is as expected.

5.2.2 Deviation of a spiral density interface from a circular interface

We have so far assumed the density interface to be in the form of several concentric circles, while it actually is two continuous spirals originating from the flat interface on either side of the vortex. At a given time t, the spiral interface created by a point vortex is described in cylindrical polar coordinates by

$$\theta_s = \frac{\Gamma t}{2\pi r^2}. \tag{5.15}$$

The instantaneous interface is thus a pair of Lituus spirals (one among the Archimedean class of spirals), one of which is shown in figure 5.7. From equation (5.15) we may obtain the angle α between the spiral and a circle sharing the same origin and radius as

$$\tan\alpha = \frac{\pi r^2}{\Gamma t}, \tag{5.16}$$

so the assumption of a circular interface is better at smaller radii or late times. A schematic view of the instability mechanism is given in fig.(5.6) showing that instability occurs due to the misalignment of density gradient vector and centrifugal acceleration vector. Vorticity is generated at these intersection points of spiral and streamline. Returning to the vorticity equation (5.6) and assuming that the effect of the circulation Γ of the point vortex is far greater on the basic flow than of that which is newly created, we may write

$$\frac{\mathcal{D}Z}{\mathcal{D}t} \simeq -\frac{\nabla\bar{\rho}}{\bar{\rho}} \times \left[\frac{U^2}{r}\mathbf{e}_r\right]. \tag{5.17}$$

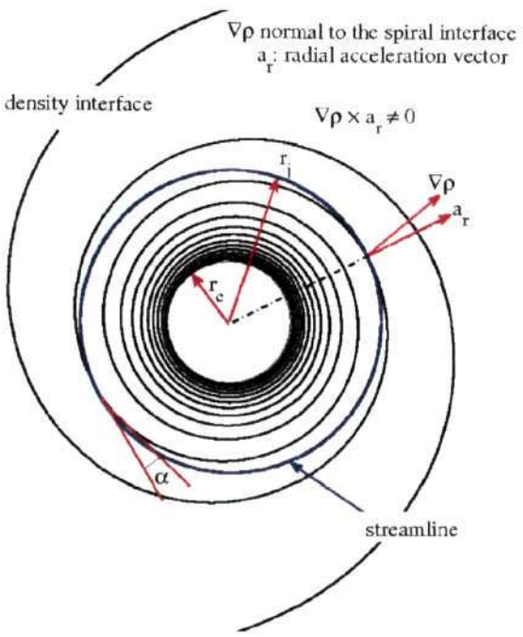

Figure 5.6: Physical mechanism for the cause of instability. Blue circle indicates a streamline, and solid black line is the position of the density interface. Also indicated are the density gradient vector, $\boldsymbol{\nabla}\rho$ and centrifugal force, $a_r = U^2/r$. (indicated with red arrows). Geometrically, it can be seen that $\boldsymbol{\nabla}\rho \times a_r \neq 0$ for any circular streamline.

Under this approximation, the streamlines remain circular. In section 5.4 this approximation is shown to be valid even up to the nonlinear regime at later times (figure 5.20(a)). We see that vorticity is created whenever the gradient of the density is not strictly radial, i.e., for any deviation from a circular interface. Note that this too is a non-Boussinesq effect. Since $\nabla\bar{\rho} = \pm\Delta\rho\delta(r\theta - r\theta_s)\mathbf{n}$, where $\mathbf{n}$ is a unit vector in the direction normal to the spiral, using equation (5.16) we may write

$$\frac{\mathcal{D}Z}{\mathcal{D}t} \simeq \frac{\pm\Delta\rho}{\rho_{ave}}\frac{U^2}{r}\frac{1}{(1+4\theta_s^2)^{1/2}}\delta(r\theta - r\theta_s). \tag{5.18}$$

The above equation may be integrated in time at a given r, i.e., moving with the interface on its circular path, to give

$$Z(r,t) = \mp\mathcal{A}U\log(2\theta_s + (1+4\theta_s^2)^{1/2})\delta(r\theta - r\theta_s) \equiv \Delta U_\theta\delta(r\theta - r\theta_s). \tag{5.19}$$

At high θ_s, i.e., at large time at a given radius, we have

$$\Delta U_\theta \simeq \mp\mathcal{A}U\log(\frac{2\Gamma t}{\pi r^2}). \tag{5.20}$$

At every unstable density jump, negative vorticity is created and vice versa, resulting in heavier fluid travelling faster and lighter fluid slower. A spiral Kelvin-Helmholtz (SKH)

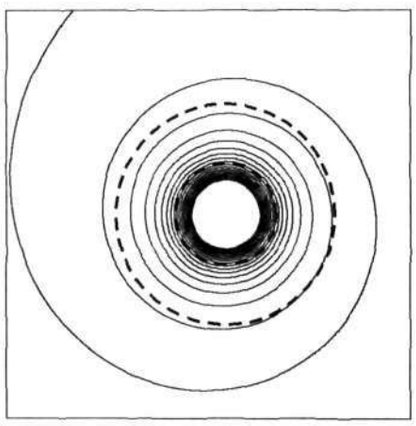

Figure 5.7: A Lituus spiral describing the instantaneous shape of one side of the density interface. The dashed lines describe circles. It is seen that the assumption of a circular jump made hitherto is better at smaller radii, or at later times at a given radius.

instability thus ensues, and combines with the centrifugal Rayleigh-Taylor (CRT) instability. We shall see in figure 5.20(b), section 5.4 that such jumps in the azimuthal velocity are obtained in the full numerical solution as well. For a single jump, approximating it to be circular for the purpose of studying the instability, we now have the dispersion relation

$$\omega = \frac{m}{r_1(\rho_0+\rho_1)}\left[\rho_0 U_0 + \rho_1 U_1 \pm \sqrt{\frac{(\rho_1 U_1^2 - \rho_0 U_0^2)(\rho_0+\rho_1)}{m} - \rho_0\rho_1(U_0-U_1)^2}\right], \quad (5.21)$$

where $U_0 = U$ and $U_1 = U + \Delta U_\theta$. The first term under the square root sign would reduce to a radial gravity term if we set the velocity difference to zero. The second term under the square root sign is responsible for the SKH instability. At short times, ΔU_θ is small, so the instability reduces to the Rayleigh-Taylor one of equation (5.14). At large times or at low Atwood number, instability growth would be dictated by the velocity jump ΔU_θ. Given that ΔU_θ increases logarithmically in time, we have a spiral Kelvin-Helmholtz instability with a slightly faster than exponential growth rate, i.e., $u_r \sim t^t$.

Table 5.1 compares disturbance growth rates between a purely CRT instability and a combined CRT and SKH instability. Depending on the time chosen, the growth rates for the combined instability can become extremely large. In any case, the combined instability has a larger growth rate than the CRT alone. Note that the interface is unstable everywhere, irrespective of the local sign of the density jump.

In the work of Reinaud *et al.* (2000), the flow is of mixing layer type, and therefore already unstable. Baroclinic torque in that case serves to increase the vorticity in one part of the mixing layer allowing a secondary instability to set in, thus contributing to a speeding up of the break-up process. In contrast, the SKH is a primary instability, with the vortex sheets entirely generated by baroclinic torque. In combination, the SKH and CRT instabilities rapidly destabilize a flow which would otherwise survive for an extremely long time.

j	$\Delta\rho$	$(\Delta U_\theta)_j$	ω_i (CRT alone)	ω_i (CRT+SKH)
1	0.1	-0.805	0.5	0.6469
2	-0.1	0.720	0.4783	0.5364
3	0.1	-0.634	0.4795	0.5568
4	-0.1	0.547	0.4789	0.5407

Table 5.1: Rates of instability growth for a purely centrifugal Rayleigh-Taylor instability and a combined CRT and SKH instability with multiple jumps. Larger growth rates are obtained for the combined instability. The number of jumps is denoted by j. The size of the density jump $\Delta\rho$ and that of the last velocity jump $(\Delta U_\theta)_j$ across the interface are fixed arbitrarily. At later times or lower radius, ΔU_θ would be much higher, so the SKH can give rise to extremely large disturbance growth rates. Here $r_1 = 0.1$, $r_2 = 0.105$ and $m = 5$. Column 4 corresponds to the uppermost curve in figure5.4(b).

5.2.3 Rankine vortex

The point vortex is replaced by a Rankine vortex, with a core of radius r_c and constant vorticity Z_0. The vorticity outside is zero. As will be seen in the numerical simulations in section 5.4, the exact form of the vorticity does not affect the results much so long as it is concentrated within a small core. The approach for obtaining disturbance growth rates is as before, except that we obtain a polynomial equation for ω which is one order higher, e.g. a cubic for a single jump in the place of the quadratic (equation 5.14).

As expected, a jump far away from the core responds exactly as to a point vortex, so the primary effect of a finite core is in the case where a jump is placed in the vicinity of the core. As can be seen in figure 5.8(a) the instability growth rate is constant and has a large value when the density jump is placed inside the core. This could ultimately lead to the destruction of the core. Configurations similar to the one in this subsection, i.e., instabilities due to heavy-cored vortices, were studied by Joly *et al.* (2005); Sipp *et al.* (2005). In both, Gaussian vorticity and density profiles were used instead of the discontinuous profiles used here. Due to this, quantitative comparisons with their results cannot be made. Qualitatively, in their case too, instability with large growth rate was found. For density jumps inside the core, growth rate saturates at a large value as the location of the density jump approaches the origin. A similar feature was observed by Joly *et al.* (2005) (see their fig.6(a)) when the density core was made very small.

When the density jump is placed close to the edge of the core, figure 5.8(a) shows that the instability vanishes suddenly. This result is in qualitative agreement with Sipp *et al.* (2005), who found stabilization when the density-stratified layer overlapped with the region of high shear. A similar observation was made indirectly by Joly *et al.* (2005). This stabilization may be seen explicitly in the simplest case when the density jump is exactly placed at the edge of the Rankine core. There the growth rate is described by a quadratic rather than a cubic equation in ω, and written as

$$\omega = m\Omega_0 - \left[\frac{\Omega_0}{1+s}(1 \pm \sqrt{1 - m(1-s^2)})\right] \tag{5.22}$$

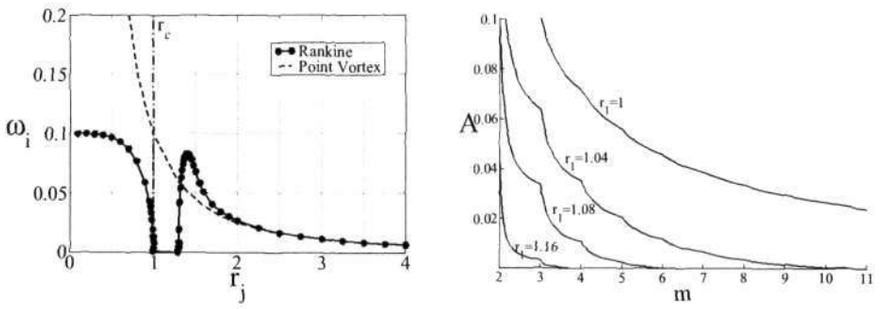

Figure 5.8: (a) Comparison of the growth rates due to a Rankine vortex with $r_c = 1$ and a point vortex for $\mathcal{A} = 0.005$ with $m = 2$ and (b) Stability domain in the $\mathcal{A} - m$ plane for various jump locations. The region above each curve is unstable, and solid lines between integer values of m are only to guide the eye.

where $s = \rho_l/\rho_h$. This puts a condition $m > 1/(1-s^2)$ for instability. The cubic equation in ω, when the two discontinuities are near each other but do not coincide, gives solutions consistent with this condition. From these solutions, we may say a little more about the neutral region seen in fig.5.8(a). As $\Delta\rho \to 0$, we recover the neutral Kelvin mode, and a mode with $\omega = mU/r$ in the continuous spectrum. When $\Delta\rho \neq 0$, apart from this Kelvin mode with modified frequency, two neutral waves are supported, which travel in a direction opposite to the previous continuous-spectrum mode. These additional waves are analogous to internal gravity waves in a planar problem with gravity. On either increasing $\mathcal{A}$ or m, these waves destabilize. Density variations within the vortex core and near the edge often give rise to interesting features, such as a destabilization of a lighter core in some cases. These are being studied, and are not discussed further here to avoid diversion from our present focus.

In this idealized model, the instability grows indefinitely for any $\mathcal{A}$ as $\omega_i \sim \sqrt{m}$. In reality, at high Peclet number, a mode with azimuthal wavelength comparable to the thickness of the density-stratified layer will grow faster than the others, similar to what would happen in a planar situation (Drazin & Reid (1981)). Diffusivity and viscosity would further affect the results, as shown in the next section.

5.3 Viscous stability analysis

Rather than a parametric study, which is very tedious given the number of parameters involved in the viscous problem, the purpose of this section is to present characteristic results, some of which will serve for comparison with the numerical simulations of section 5.4. We restrict ourselves to Atwood numbers between 0.05 and 0.2, and the relevant Reynolds numbers are 2000 and above. We present results for (i) the effects of viscosity on the CRT instability with one and two density jumps, and (ii) the effect of viscosity, interface thickness, and Atwood number separately on the combined CRT and SKH instability for two jumps. This is deemed sufficient since it has been demonstrated in

section 5.2 that the result for multiple jumps is well approximated by that for two jumps in either order. We again assume that the density interface is circular, and introduce vortex sheets at the density interface as described. The edge of the Rankine vortex, and the density profile within each density interface are made smooth by specifying $Z/Z_0 = (1-\tanh((r-r_c)/d))/2$ and $\bar{\rho}/\rho_a = 1 \pm \mathcal{A}\tanh((r-r_j)/d)$ in the neighbourhood. For simplicity the smoothing parameter d is kept the same for vorticity and for each density interface. The equations are non-dimensionalized by the vortex core size, r_c as the characteristic length scale, and the velocity at the edge of the core, U_c as the characteristic velocity scale. The Reynolds number is defined as $Re \equiv \Gamma/\nu$, the Peclet number as $Pe \equiv \Gamma/\kappa$ where ν and κ are the kinematic viscosity and scalar diffusivity respectively, and the circulation $\Gamma = 2\pi U_c r_c$. The Atwood number is defined as $\mathcal{A} \equiv \Delta\rho/(\rho_h + \rho_l)$. The densities are scaled by the average density $\rho_a = (\rho_h + \rho_l)/2$, ρ_h and ρ_l being the heavy and light densities respectively. In this study the Schmidt number $Sc = \nu/\kappa$ is held constant at 10. Higher values of Sc are expected to show similar behaviour. The stability equations in the non-dimensional form may now be written as:

$$\bar{\rho}r^2\mathcal{I}u_r + \bar{\rho}'r^3\left[\left(\omega - \frac{mU}{r}\right)(r\frac{d}{dr} + 1) + mZ\right]u_r + im^2rU^2\rho = \frac{i}{Re}\mathcal{N}u_r, \tag{5.23}$$

$$\left(\omega - \frac{mU}{r}\right)r^2\rho = -iu_r r^2\bar{\rho}' + \frac{i}{Pe}\mathcal{M}\rho, \tag{5.24}$$

where the operator $\mathcal{I}$ is as defined in equation (5.10), and

$$\mathcal{N} \equiv r^4\frac{d^4}{dr^4} + 6r^3\frac{d^3}{dr^3} + (5-2m^2)r^2\frac{d^2}{dr^2} - (1+2m^2)r\frac{d}{dr} + (m^2-1)^2, \tag{5.25}$$

$$\mathcal{M} \equiv (r^2\frac{d^2}{dr^2} + r\frac{d}{dr} - m^2). \tag{5.26}$$

The boundary conditions are $u_r = u_r' = 0$ at $r = 0$ and $r \to \infty$, as valid for $m \geq 2$. Note that since we are restricted to two dimensions, the $m = 0$ mode is unphysical, and $m = 1$ is only a translational mode causing no change in the structure of the vortex. Equations (5.23-5.26) are solved as an eigenvalue problem by a Chebyshev collocation method, with a grid stretching in the density-stratified layer as used in a different context in Khorrami *et al.* (1989). A typical computational domain size was $25r_c$ and good accuracy was obtained with 800 collocation points. The stability calculations were validated by repeating some of the cases of Joly *et al.* (2005), and very good agreement was obtained.

In instabilities of this kind, the azimuthal wavenumber m_{max} at which the growth rate is maximum is usually the most noticeable feature even after the flow becomes nonlinear (Coquart *et al.* (2005); Joly *et al.* (2005); Saunders (1973)). We therefore devote some attention to this parameter, and first examine how it varies with Reynolds (or equivalently, Peclet) number for a single density jump in CRT instability. In planar RT instability, increasing viscosity progressively stabilizes short wavelength perturbations, and therefore reduces the wavenumber of the "most dangerous" mode (see Chandrasekhar

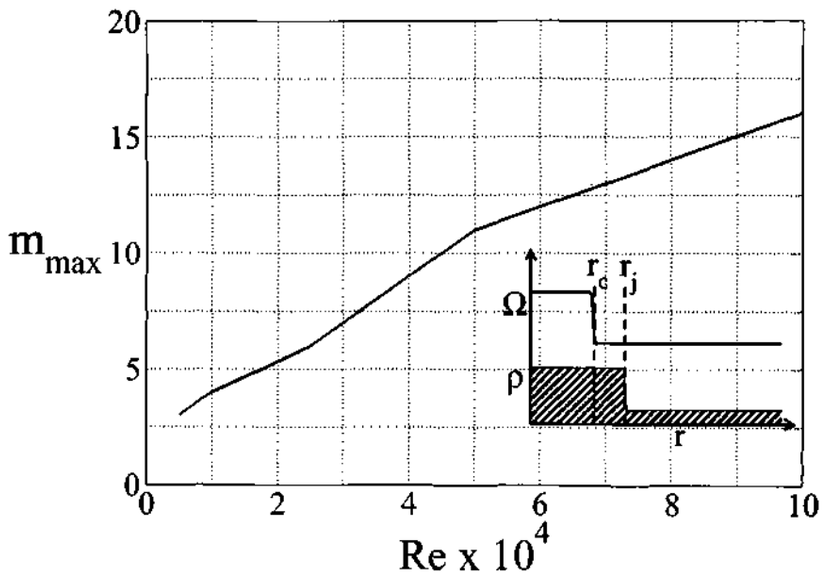

Figure 5.9: Effect of Reynolds number on a single density-jump CRT instability. The azimuthal wavenumber corresponding to maximum disturbance growth rate is shown, with $d = 0.02r_c$, $r_j = 2r_c$, $\mathcal{A} = 0.05$. A schematic of the base flow profile is shown in the inset.

(1961); Duff *et al.* (1962)). The same physics may be expected in CRT, and figure 5.9 shows that m_{max} increases with Reynolds number for a fixed base flow. There was no surprise in the qualitative dependence of the single jump CRT instability on the interface thickness d. The maximum growth rate (not shown) occurs for the thinnest profile, and with an increase in d the instability saturated at a smaller wavenumber, roughly as $d^2 \sim 1/m$, the reason for this scaling is unclear at his point.

We now examine the effect of introducing a second density jump, with the inner jump destabilizing and the outer one stabilizing. The thickness of the jumps is fixed at $d = 0.02r_c$. Figure 5.10 shows the frequency and growth rate of the CRT instability as functions of m and Re. The highest Reynolds number shown is close to the inviscid result (not shown). The growth rate, the m_{max} and the range of unstable modes all increase as the Reynolds number increases, as is to be expected. The frequency on the other hand remains similar to the inviscid predictions, showing a very weak dependence on Reynolds number.

So far, only the effects of density have been considered. We now allow both CRT and SKH instabilities to operate in combination. As a suitable base state, we chose the flow field at a non-dimensional time, which is 30 for the results presented. Choosing the location of the first jump then dictates that of the second, using equation (5.1) and noting that $(n+1/2)$ should be used in place of $(n+1)$, since the second jump, belongs to

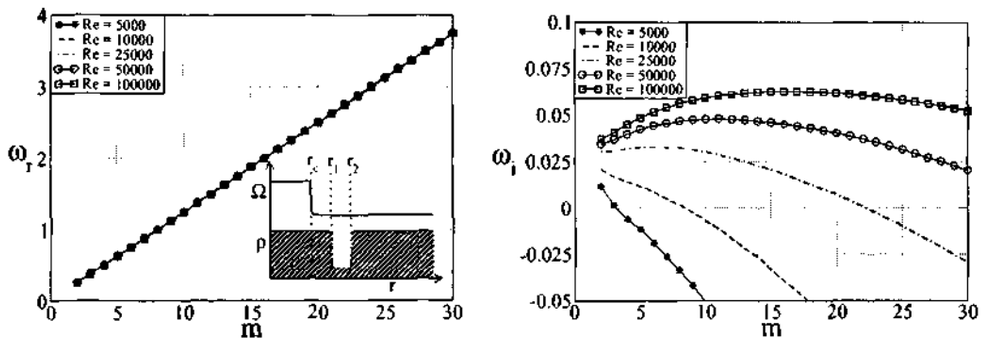

Figure 5.10: Frequency and growth rate of the most unstable CRT mode for a smooth vortex with two circular density jumps at $r_j = 2r_c$ and $r_j = 2.5r_c$. $\mathcal{A} = 0.05$, and $d = 0.02r_c$. The first jump is from heavy to light and the second jump from light to heavy. A schematic of the base flow profile is shown in the inset.

the spiral sheet originating from the opposite side. The vorticity generated at the density interfaces due to the baroclinic torque is in the form of thin spiral shear layers. Since the spectral collocation method requires smooth profiles to produce reliable results, we approximate them to be circular steep Gaussians of the sign of the density jump. The idealized base-flow vorticity is therefore prescribed to be

$$\frac{Z}{Z_0} = \frac{1}{2}\left(1 - \tanh\left[\frac{(r - r_c)}{d}\right]\right) \pm \sum P_j \exp\left[\frac{-(r - r_j)^2}{d^2}\right] \tag{5.27}$$

For simplicity, the same base-flow vorticity and density profiles are used to study the effects of viscosity. Though in reality, such an initial condition would relax on the viscous time-scale to a Gaussian distribution. Studying diffusive effects with jump-like profiles has been carried out in the past by Chandrasekhar (1961); Duff *et al.* (1962); Villermaux (1998). Hence only a qualitative comparison of these viscous results can be made with experiments or DNS. Figures 5.12(a) and 5.12(b) show growth rates from inviscid and viscous stability analysis respectively. The Atwood numbers used in the two cases are 0.2 and 0.1 respectively, which enable comparisons with simulations. The first jump is located at $1.3r_c$ and the location of the second is obtained to be $1.57r_c$ from equn. (5.1), which is rounded off to $1.6r_c$. For simplicity we use $P_1 = -P_2 = 1$ in equation (5.27), the value chosen to roughly agree with the sheet strengths in the simulations at $t = 30$ (see section 5.4, fig. 5.14). The constructed stability profiles are compared with the actual numerical simulation profiles shown in fig. 5.11. Also shown is the initial velocity profile in the simulations. To show that the jump sizes are indeed in good agreement, a slightly shifted stability profile is shown.

For the smallest thickness considered, $d = 0.01r_c$, the inviscid instability peaks at a very large value of m. For larger d, there is a non-monotonic variation of ω_i with m, which can be explained as follows. When the interfaces are thin, the dominant wavenumber is

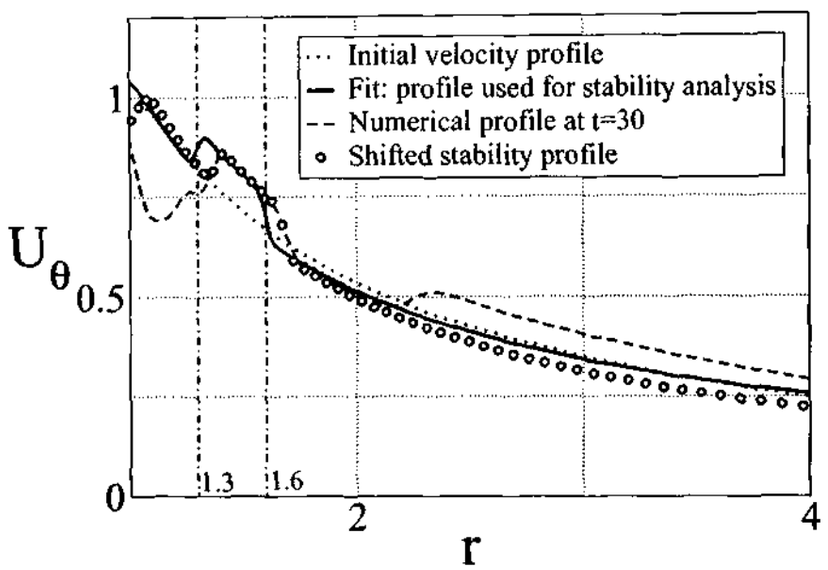

Figure 5.11: Azimuthal velocity profile outside the vortex core at t=30 (in the simulations shown in fig.5.14). The initial velocity profile used in the numerical simulations has been shown for reference, along with the profile used in the stability analysis. A similar profile would also be obtained at t=40 (shown in fig.5.14).

selected by their thickness, hence a large wavenumber instability is obtained. However, as the interface thickness becomes comparable to the distance between them, the fact that each interface contains a diffused vortex sheet makes the small wavenumber modes respond as to a wake-like base flow, and so the fastest growing azimuthal wavelengths are comparable to the interface spacing rather than the thickness. Very large wavenumbers again display increasing growth. A similar study with two density jumps was carried out (not shown) on the CRT instability alone, and no such behaviour was obtained in that case. The non-monotonic variation of the growth rate with m is thus a feature of the inviscid, combined CRT and SKH instability.

The major effect of viscosity (figure 5.12(b)) is that the dominant wavenumbers are now much smaller, in the range of 3 to 5, and decreasing with Reynolds number. Also with a decrease in Reynolds number, the growth rate drops considerably. These results will be seen below to be in agreement with simulations. A critical Reynolds number Re_{cr} is very difficult to define in this case since there are many parameters. An example each of stabilization due to decreasing Atwood number and increasing thickness are given by the dashed line and the filled circle in the figure respectively. Note that the growth rates in figure 5.12(b) are lower than in figure 5.12(a) in large part because of the lower Atwood number.

The KH instability is not studied here in isolation, since it is not relevant to our flow, but we remark that planar shear layers are insensitive to viscous effects at high Reynolds numbers Villermaux (1998).

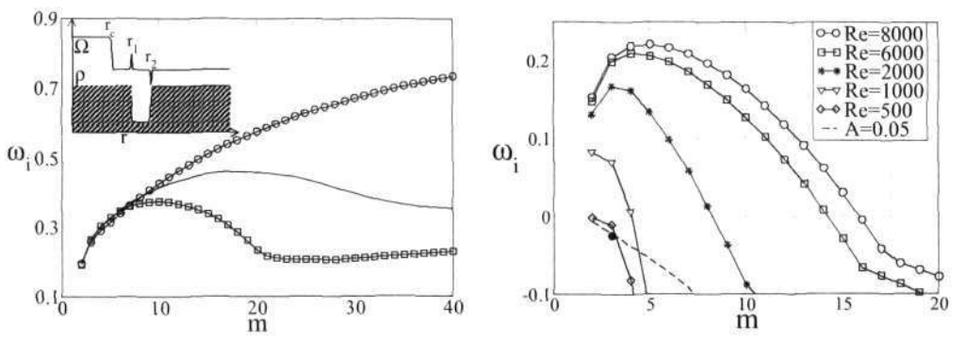

Figure 5.12: Growth rate for the combined CRT and SKH instability with a smooth vortex and two circular density and velocity jumps of same size at $r_1 = 1.3r_c$ and $r_2 = 1.6r_c$, (a) for varying thickness with inviscid analysis, $\mathcal{A} = 0.2$, circles: $d = 0.01r_c$, solid: $d = 0.02r_c$, squares: $d = 0.03r_c$. The base flow is shown schematically in the inset. (b) Viscous analysis at various Reynolds numbers for $\mathcal{A} = 0.1, d = 0.05r_c$. The dashed line is for $Re = 2000$ but with $\mathcal{A} = 0.05, d = 0.05r_c$. The lone black filled circle shows the highest growth rate for $Re = 2000, \mathcal{A} = 0.1, d = 0.2r_c, r_2 = 1.4r_c$.

5.4 Direct numerical simulations

The complete problem including non-Boussinesq effects is now solved by direct simulations. Again gravity is not considered. Both inviscid and viscous simulations are carried out, in cartesian coordinates in a doubly periodic domain using the Fourier pseudo-spectral method. In all the results presented here, we use 1536 collocation points in each direction without dealiasing. No visible difference was found with dealiasing. Results did not vary significantly for grid sizes of 1024 and 2048. The computational domain is $15\pi r_c$ for the inviscid simulations and $20\pi r_c$ for the viscous simulations, which is large compared to most numerical simulations found in literature. Varying it did not alter the features of the instability. In all the figures below, x and y shown corresponds to the actual domain size scaled by a factor of π. The effects of using periodic boundary conditions for problems involving an isolated vortex is discussed in Joly *et al.* (2005) and Josserand & Rossi (2007). The residual vorticity produced because of the imposition of the periodic boundary conditions is about 800 times smaller than the vorticity of the central core at early times. With the production of baroclinic vorticity, this residual vorticity becomes 3800 times smaller than the peak value of the vorticity in the flow field. Therefore, the results of our numerical simulations can be considered to be a faithful representation of an isolated vortex.

The time discretization is done through an Adams-Bashforth scheme. We split the total density field as $\bar{\rho} = \rho_i(y) + \rho(x, y, t)$ where ρ_i is the initial density field and ρ has information of the time evolution of the density. This allows ρ to remain a spatially periodic function, with a period equal to the domain size. As in section 5.2.3, we non-dimensionalize the governing equations using the vortex core size, r_c as the characteristic length scale, Z_0 as the characteristic scale for vorticity such that the circulation $\Gamma =$

$Z_0 \pi r_c^2$. In cartesian coordinates, the equations in velocity-vorticity formulation in the non-dimensional form are

$$\frac{\mathcal{D}Z}{\mathcal{D}t} = \frac{1}{\tilde{\rho}}\left(\frac{d\rho_i}{dy} + \frac{\partial \rho}{\partial y}\right)\frac{\mathcal{D}u}{\mathcal{D}t} - \frac{1}{\tilde{\rho}}\frac{d\rho}{dx}\frac{\mathcal{D}v}{\mathcal{D}t} + \frac{1}{Re}\nabla^q Z, \tag{5.28}$$

$$\frac{\mathcal{D}\tilde{\rho}}{\mathcal{D}t} = \frac{1}{Pe}\nabla^q \tilde{\rho}, \tag{5.29}$$

$$\frac{\partial u}{\partial x} + \frac{\partial v}{\partial y} = 0. \tag{5.30}$$

where q is the order of the diffusion term used, and densities are scaled by the average density. In the viscous case, $q = 2$ and $Re = \Gamma/\nu$ and $Pe = \Gamma/\kappa$ are the Reynolds and Peclet numbers respectively. In the inviscid simulations, hyperviscous diffusion of the vorticity and density fields is included by setting $q = 6$, and Re and Pe, defined respectively in this case as $\Gamma r_c^4/\nu_h$ and $\Gamma r_c^4/\kappa_h$. The hyperviscous Re and Pe were nearly 2×10^{11}. Using twice or half of these values did not change the results qualitatively. A similar approach was used, for example, by Neilsen *et al.* (1996) for studying inviscid vortex merger. The purpose of the hyperviscosity is to damp out spurious numerical modes of large wavenumber, and the diffusion it causes is found to be very weak, so these simulations are referred to here as inviscid. An initial vorticity in the form of a smoothed Rankine vortex, as in section 5.3 is used for the inviscid simulations. A Lamb-Oseen vortex with $Z = Z_0 \exp[-r^2/r_c^2]$ defines the initial vorticity in the viscous simulations. A range of Reynolds numbers from $Re = 500$ to $Re = 10000$ were studied, and three of them are shown here as being representative. For Re larger than the range studied, the resolution was found to be insufficient at later times to capture the thin spiral structures. And for Re smaller than 2000, dissipation was too rapid for the density gradients to play any significant role. The Atwood number was also varied from 0.05 to 0.4, and it was found that lower Atwood numbers required thinner interface thickness to display the instability. At $\mathcal{A} \leq 0.05$ this could lead to difficulties in numerical resolution. In each case, the vortex is placed at a horizontal interface separating fluids of different densities. The interface is in the form of a thin layer within which density varies in the vertical coordinate as a hyperbolic tangent. The straight interface is in contrast to the axisymmetric initial density profile with a heavy core in the numerical simulations of Joly *et al.* (2005). The nonlinear terms on the right-hand side of equation (5.28) are computed in physical space.

For comparison, we first carry out an inviscid simulation without any inertial effects due to density stratification. The density field is advected passively into Lituus spirals as is evident in figure 5.13. The vorticity field is not shown, but is practically unchanged from its initial configuration even at the final time. This also shows that for the simulations considered in this work, hyperviscous simulations suffice to reproduce inviscid behaviour.

We contrast this result with that from a full simulation including non-Boussinesq effects, shown in figure 5.14. It is immediately evident that density in this situation is not a "passive" scalar, even though the Atwood number is low and there is no gravity. The vorticity profile is completely different from the simulation shown in fig.5.13. Vorticity

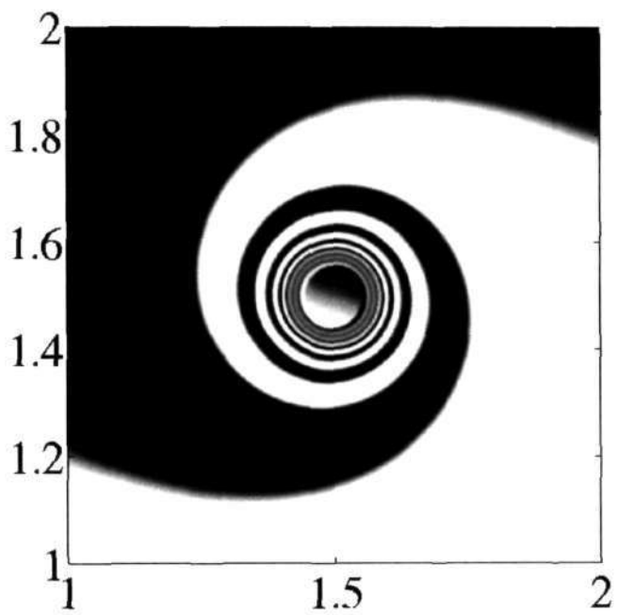

Figure 5.13: Density field forming a Lituus spiral around a Rankine vortex in an inviscid simulation treating the density field like a passive scalar. The vorticity field (not shown) is unchanged from its initial value. The black and white regions correspond to light and heavy fluid respectively. This image is formed at $t = 100$, by which time the flow will be seen to undergo a complete breakdown in the full simulations including non-Boussinesq effects. The time t is scaled by $\pi r_c^2/\Gamma$.

of alternating sign is now produced in the form of two interwound spirals, i.e., along the density interfaces, consistent with equation (5.19). The vorticity across an unstable density jump is negatively signed, while positive vorticity is produced across every stable density jump. The two spiral vortex sheets we now have are unstable in the Kelvin-Helmholtz sense. The combined action of this and the density jumps is evident in the instability displayed at later times. The instability, once visible, grows rapidly. The spiral vortex sheet then rolls up into blobs, indicative of the dominance of the SKH instability. A final breakdown soon follows. The Atwood number in this simulation was 0.2. Note that the time $t = 30$ of the stability analysis is well before the onset of instability as can be seen in fig.(5.14). At this time, the first visible jump in the simulations is located close to the value $1.3r_c$ used in figure 5.12(a). Consistent with equation (5.1) and the same figure, the second jump was found to occur at $1.57r_c$. The width of the vortex sheet was found to lie between $0.035r_c - 0.05r_c$ which is comparable to the largest value $d = 0.03r_c$ used in the stability analysis. The azimuthal wavenumber of about 11 as seen in the simulations corresponds to a wavelength of the same order of magnitude as the thickness of the interface. It compares well with a wavenumber of $8 - 12$ obtained from

the inviscid stability analysis for comparable interface thickness in fig.5.12(a).

A viscous simulation at $Re = 8000$ is shown in figure 5.15. Snapshots of the density field are also given for $Re = 6000$ and $Re = 2000$ in figure 5.16. The Schmidt number is fixed at 10 as in section 5.3, and the Atwood number is 0.1. The trend in fig.5.15 is very similar to that in the inviscid simulation. Note that the main vortex used here is Lamb-Oseen while the stability analysis is carried out with a Rankine vortex. We therefore make only qualitative comparisons in the viscous case. A direct comparison with the viscous stability results of fig. 5.12(b) cannot be made owing to differences in the base flow profiles. The original vortex is no longer discernible at the end of the simulation. This is in contrast to what happens when the density field is treated like a passive scalar at this Reynolds number, where the original vortex is slightly diffused but otherwise undisturbed. The inertial effects of density stratification thus act in accelerating the collapse of the vortex. Note that non-Boussinesq effects are strong even at low $\mathcal{A}$ because it is the size of the gradient of density which is important, not the density difference alone.

The instability is less clearly defined for $Re = 6000$, but one may discern that the selected wavenumber is even smaller, at about 5. No instability is visible at $Re = 2000$. A quantitative comparison of this result with the stability predictions is not straightforward due to the number of parameters involved which are sometimes difficult to estimate. The effective core becomes smaller in the simulations than the one we begin with, as discussed below, so the location of the jumps with respect to the core is difficult to estimate. The effective Atwood number in the central region decreases progressively due to the centrifugal forces making the core lighter. The thickness of the diffused layer is difficult to estimate from numerical results. Given the differences between the simulations and the idealizations made for stability analysis, both in viscous and in inviscid flow, we may conclude that a good qualitative agreement is achieved.

In order to compare the growth rate with stability analysis, the amplitude of oscillation of the interface was manually extracted from the numerical data. This was possible to do relatively reliably only for the inviscid simulations, and so we present results for only this case. The instability becomes visible after a time $t > 44$. The amplitude η of a given undulation was measured by hand at various times, after $t = 44$ when the instability becomes visible, till non-linear effects become important at $t \sim 53$. The superimposition of two such measurements at different phases is shown in fig.5.17. A exponential fit gives growth as $\exp(0.32t)$. At the time and innermost radius of onset of instability, it was estimated that the thickness of the spiral interface was approximately $0.05r_c$. In the instability predictions of fig.5.12(a), ω_i for this case is approximately 0.37. The jump in velocity in the stability analysis was prescribed to match the simulations, but there are still many differences between direct simulations and the stability analysis of a simplified problem. This comparison may thus be considered quite good. In section 1 the SKH disturbance amplitude was predicted to grow as t^{bt}. Given the small duration of the numerical instability is is difficult to differentiate between this and a pure exponential growth. A fit of this form is also shown in fig. 5.17, with $b \sim \omega_i / t_{avg}$ where $t_{avg} \approx 50$.

In the simulations, since we have a density interface of finite thickness, two points on the interface initially separated by a small distance l_0 are stretched apart due to the

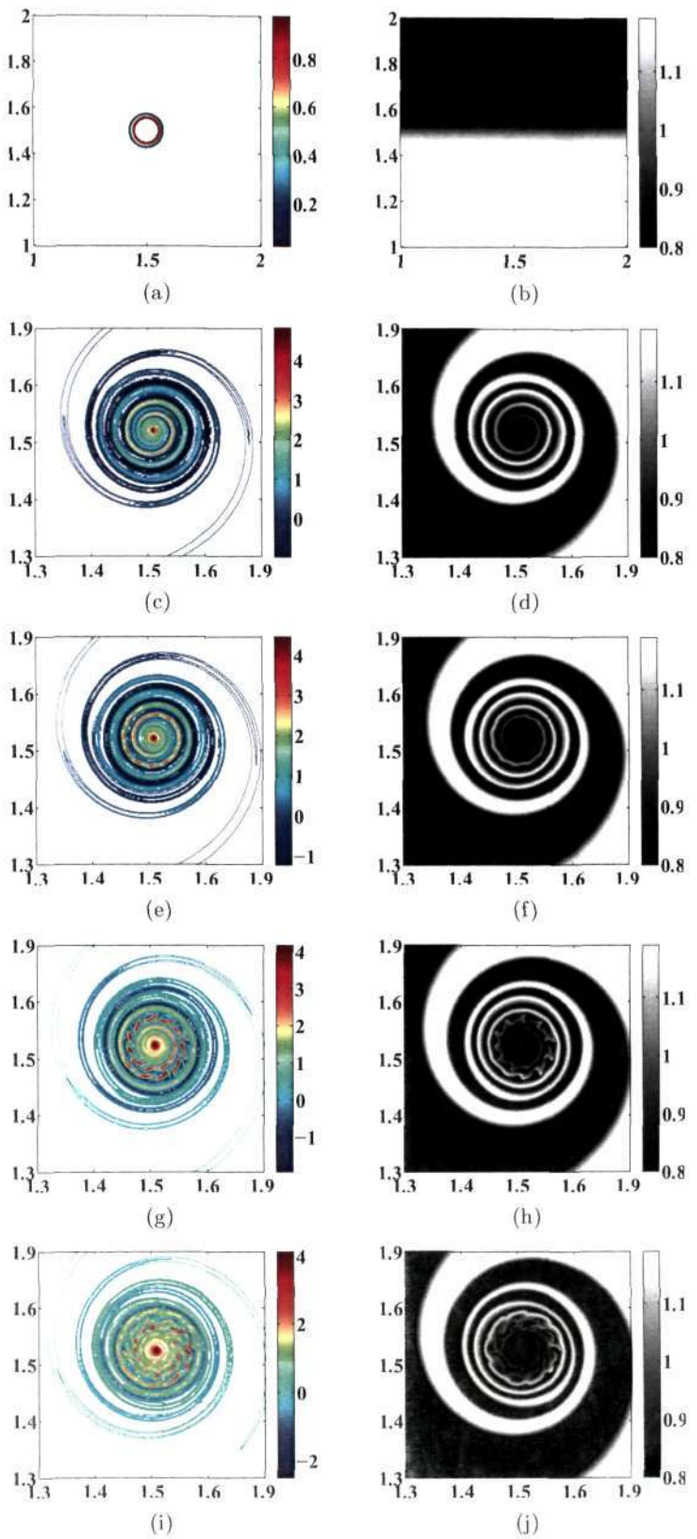

Figure 5.14: Evolution of the vorticity (a, c, e, g and i) and density (b, d, f, h and j) fields in the inviscid simulations. The time t, non-dimensionalized with respect to the period of rotation of the vortex core $\pi r_c^2/\Gamma$, is (a,b) 0, (c,d) 40, (e,f) 45, (g,h) 50 and (i,j) 55. Note that the scale for (a,b) is different from others. The Atwood number is 0.2.

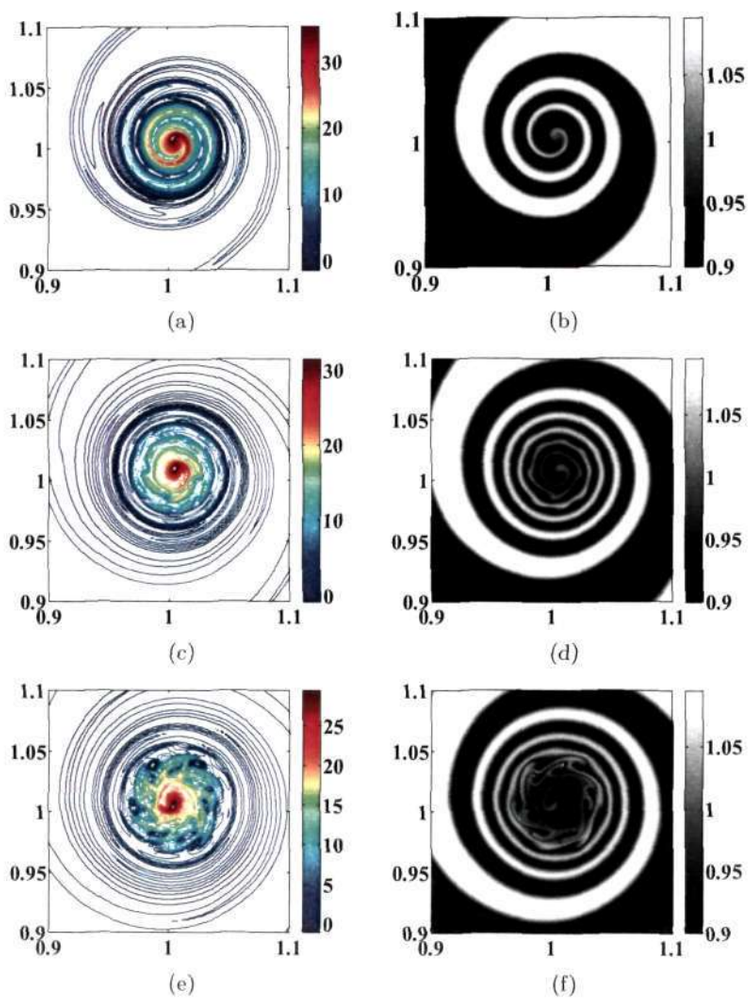

Figure 5.15: Evolution of the vorticity (a, c and e) and density (b, d and f) fields in the viscous simulations. The picture at the initial time is the same as that in figure 5.14, except that a Lamb-Oseen vortex is used here instead of a Rankine. The time, non-dimensionalized as before, is (a,b) $t = 40.7$, (c,d) $t = 76.4$, (e,f) $t = 96.76$. The Reynolds number is 8000, the Peclet number is 80000 and the Atwood number is 0.1.

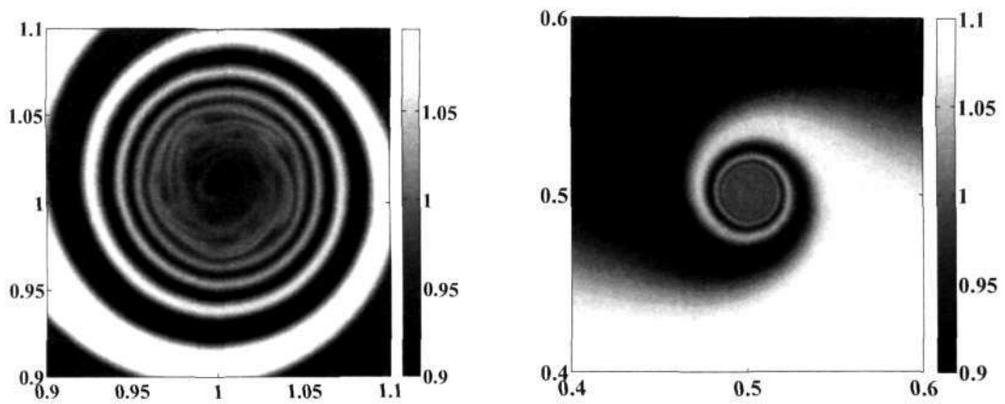

(a) (b)

Figure 5.16: Snapshot of the density field in a viscous simulations with (a) $Re = 6000$, $Pe = 60000$ and (b) $Re = 2000$, $Pe = 20000$. The instability in (a) is qualitatively similar to fig.5.15, whereas there is no instability in (b) owing to smaller centrifugal forces and more rapid homogenization.

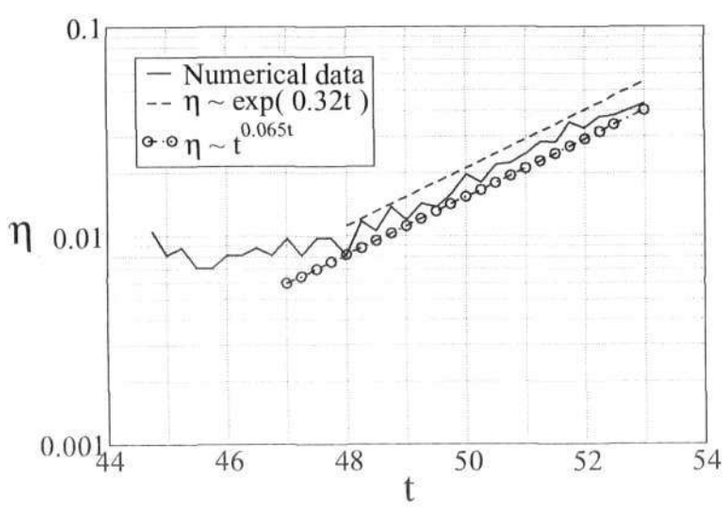

Figure 5.17: Growth rate extracted from the numerical simulation of fig.5.14. The straight line is an exponential fit. The stability analysis of fig.5.12(a) predicted a growth as $\exp(0.37t)$.

spiralling. We have from equation (5.15)

$$\frac{l(r,t)}{l_0} = \theta_s. \tag{5.31}$$

Due to this steepening of the density gradient, Gibbs oscillations were encountered at the later stages of these simulations which prevented the study of the complete breakdown of the vortex cores. Secondly, in the viscous simulations, at the Reynolds numbers considered, the grid is not sufficient to resolve all the scales up to the Kolmogorov scale. Hence, a correct fully turbulent state cannot be achieved in these simulations. Nevertheless, an examination of the energy spectrum is a useful indicator of the cascade effects. Figures 5.18(a) and 5.18(b) show the kinetic energy spectrum for the inviscid and the viscous simulations respectively, plotted against the scale $k = (k_x^2 + k_y^2)^{1/2}$. The difference between the inviscid and viscous spectra at the initial time is because in the latter we use a Lamb-Oseen vortex, while in the former, a Rankine vortex is used, which includes sharp changes in the velocity derivative at the edge of the vortex core. This produces a signal with sharp dips at the zeros of the Bessel function J_1 (Neilsen *et al.* (1996)). This is because the energy spectrum for an axisymmetric vortex is given by $E(k) = \frac{\pi}{k}\int \Omega(r) J_0(kr) dr$ (Gilbert (1988)), so for a Rankine vortex we get $E(k) \propto J_1(kr)$, and a steep *tanh* vorticity profile behaves similarly.

As time progresses, both spectra broaden and flatten, corresponding to the emergence of smaller scales. The final state is turbulence-like, but the simulations are insufficient to make more quantitative statements. In the case of gravity driven flows, an exchange takes place between the kinetic and potential energies, often with one growing at the expense of the other. It is instructive to construct an analogy to this process in the present system. The total energy, given by $E_t = \int\int \frac{\tilde{\rho}}{2}(u^2+v^2)\, dV$, is a conserved quantity in the absence of viscosity. Writing $\tilde{\rho} = \rho_{ave} + \hat{\rho}$ where ρ_{ave} is constant, we have

$$E_t = E + E_\rho \tag{5.32}$$

where $E \equiv \rho_0 \int_0^L \int_0^L (u^2 + v^2)/2 \; dxdy$ is the kinetic energy based on a constant density, i.e., the integrand is just the kinetic energy per unit mass, a useful quantity in stratified flows (Gill (1982)). The second term $E_\rho \equiv \int\int \frac{\hat{\rho}}{2}(u^2 + v^2)\, dV$ is analogous to a potential energy in a system with radial (centrifugal) gravity ($\sim \Gamma^2/r^3$), and arises solely due to inhomogeneity in the density field. Such a splitting of the total energy E_t highlights the contribution of the density variations, since the quantity E increases or decreases at the expense of E_ρ. Figures 5.19(a) and 5.19(b) show the evolution of E and enstrophy ($Z = \int_0^L \int_0^L \Omega^2 dxdy$) with time, normalized by their initial value. The residual vorticity is first subtracted from the total vorticity field, from which the velocity field is calculated. Both the energy and the enstrophy here are calculated in the physical space. The slight increase in E visible in the inviscid case is due to density variations acting as a source. In the viscous case this increase is offset by the dissipation. The net enstrophy in the inviscid case increases continuously since vorticity is generated continuously at the density interface. The viscous case shows a small increase at short times and a decay at long times. The difference in enstrophy production could arise from increased diffusion of the interface, and from the different initial vorticity distribution. From Kelvin's law, for

a given strength ΔU_θ of the vortex sheet, the vorticity created in the spiral (equation 5.21) would increase due to the stretching of the density interface by the factor given in equation (5.31). With this taken into account, the prediction of the total enstrophy is seen in figure 5.19(b) to agree well with the inviscid simulations up to some time. The prediction, being for a point vortex, is of arbitrarily scale so the scales are chosen to match the simulations.

The reduction in instability at large r is easily expected from our analysis, but it remains to be explained why the instability first begins at a specific radial location, as observed in figures 5.14 and 5.15. From equation (5.3) the homogenized region around a point vortex scales as $r_h \sim \kappa^{1/6}$ for a diffusive flow. In the hyperdiffusive case, similar arguments lead us to $r_h \sim \kappa_h^{1/18}$. The prefactor in these scalings is difficult to estimate, but we may appreciate that the homogenization in the two simulations is comparable, and not too small by the time the instability becomes visible. The instability thus appears just outside r_h, at the first surviving jump. In section 5.2.2, we assumed that the dominant effect on the base flow was from a central vortex, and that the streamlines would remain circular. The assumption is validated by the streamlines of the inviscid simulations plotted in figure 5.20(a). The radial variation of azimuthal velocity at $t = 50$ seen in figure 5.20(b), is also consistent with predictions. It is also noticed that the central vortex becomes significantly smaller and stronger at early times, while more or less maintaining its circulation constant. The reason for this is that the simulations begin with a straight density interface within the vortex core, which is rotated around at early times like a solid object. This results in the production of opposite-signed vorticity on two halves of the interface within the core, so one part of the core becomes stronger and the other weaker. The weaker part is then entrained by the stronger part to give a smaller and stronger core slightly shifted away from the original center. A similar drift due to an asymmetric vorticity distribution was seen by Bajer *et al.* (2004).

5.5 Discussion

It emerges from this study that the neglect of inertial effects of density stratification is often not valid in the vicinity of a vortex in density-stratified flows. This is the case even when the difference of density is small, so long as the interface is thin, making the density gradient significant, and even when gravity is absent. Non-Boussinesq effects are especially large in high Peclet number flows, and where density changes over a thin layer. This has been demonstrated by following the evolution of a system consisting of a lone vortex at an initially flat density interface. The evolution of this system into a spiral density interface at first, followed by vorticity generation everywhere on the spiral interface, giving rise to instability and breakdown is predicted by stability theory and shown to be in qualitative agreement with direct numerical simulations, both inviscid and viscous. The density field, which would merely have advected as a passive scalar if non-Boussinesq effects were neglected, now causes an instability of a combined centrifugal Rayleigh-Taylor and spiral Kelvin-Helmholtz type. The centrifugal term takes the place of gravity to cause the Rayleigh-Taylor instability. Unlike earlier work on CRT instability, the present flow is unstable in the Rayleigh-Taylor sense whether the innermost region is light or heavy. This is because the tightly wound spirals give rise to density jumps of alternating

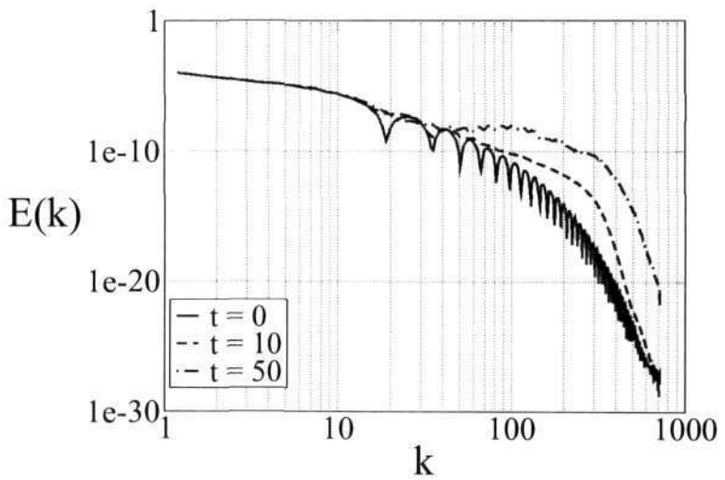

(a)

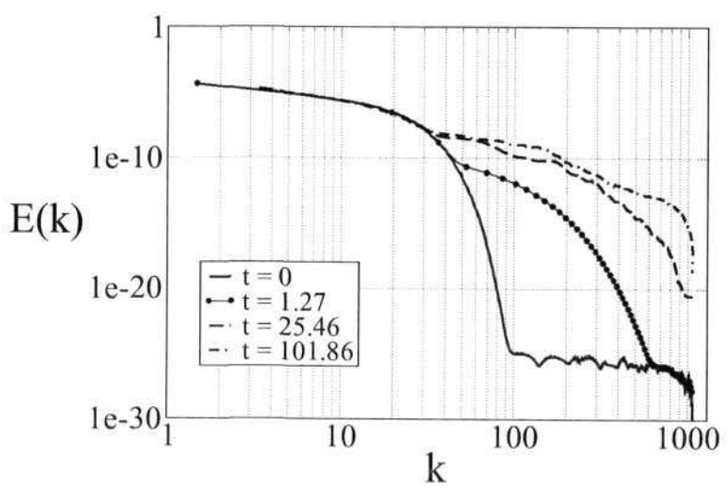

(b)

Figure 5.18: The energy spectrum for the (a) inviscid and (b) viscous simulations at $Re = 8000$.

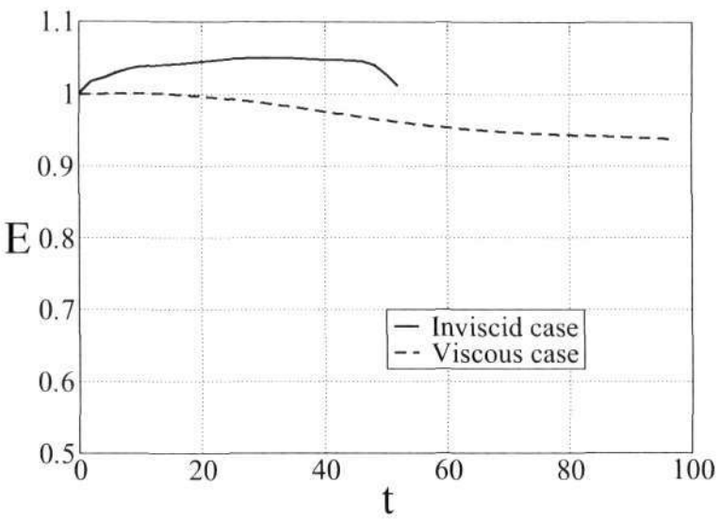

(a)

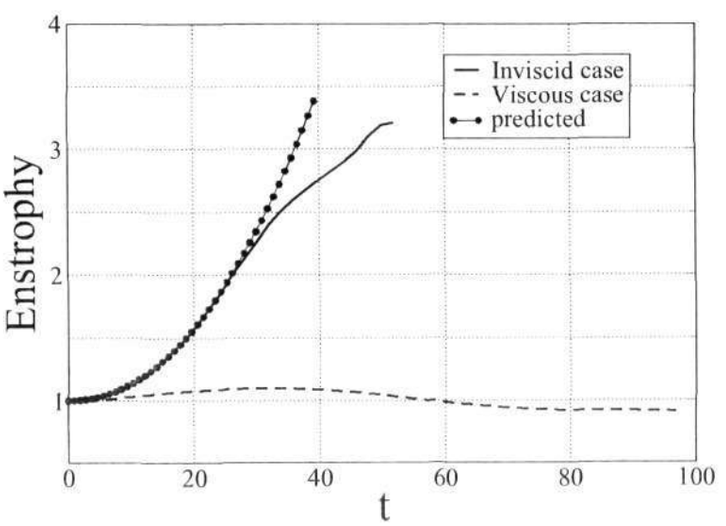

(b)

Figure 5.19: (a) Variation of E (kinetic energy based on a constant density) with time for the inviscid and viscous simulations. (b) Variation of total enstrophy with time. Solid line: inviscid simulations. Dashed line: viscous simulations at $Re = 8000$. Symbols: predictions based on section 5.2.2.

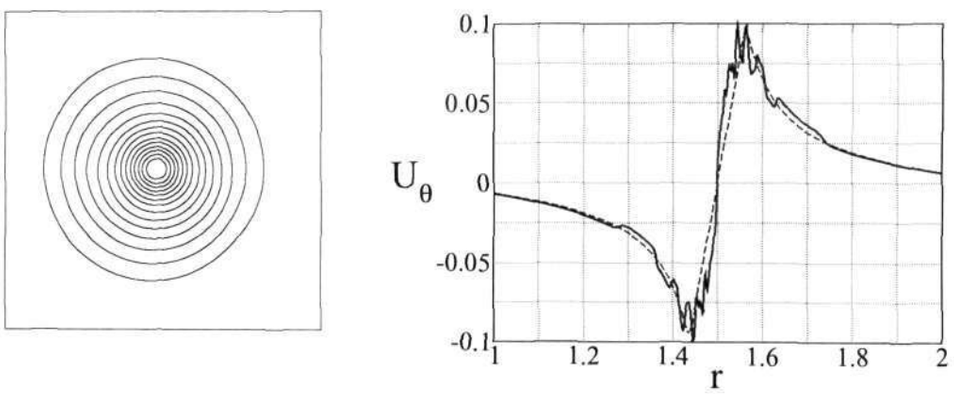

(a) (b)

Figure 5.20: (a) Nearly axisymmetric streamlines near the onset of instability for a Rankine vortex. The time is 50, and the corresponding vorticity and density profiles are shown in figures 5.14(g) and 5.14(h) respectively. (b) Azimuthal velocity for a Rankine vortex at the initial time (symbols) and at t=50 (solid line).

sign. The small deviation of the spiral from a perfectly circular shape means that the density gradient is not perfectly perpendicular to the centripetal acceleration. The result is two oppositely signed spiral vortex sheets whose strength increases logarithmically in time. The spiral Kelvin-Helmholtz instability which ensues therefore grows as t^t. Both instabilities give rise to large growth rates, with the SKH dominating at large times. Note that this prediction is made here by an idealized inviscid model. Physically, the continuous generation of fresh vorticity at the density interfaces stoking the already unstable exponential instability, leads one to expect a super-exponential behaviour. However the difference between the form t^t and that of a pure exponential growth is small, and the present simulations are not able to distinguish between them. A larger computation where the interface could be resolved better everywhere, and the growth rate could be gleaned to better accuracy, would be needed to check this prediction. At small interface thickness, the dominant m in inviscid SKH+CRT instability is dictated by the interface thickness. For higher interface thickness a flapping mode is observed, with significantly lower m. The viscous analysis shows that decreasing the Reynolds number, decreasing the Atwood number and increasing the interface thickness all have a stabilizing effect, as is to be expected. Decreasing the Reynolds number results in a reduction of the dominant wavenumber as well. A detailed parametric study for the viscous case is warranted.

The azimuthal wavenumbers seen in the viscous and inviscid simulations were in good qualitative agreement with the stability results. For $\mathcal{A} = 0.1$, no instability was noticed for $Re \leq 2000$, while the critical Reynolds number for this Atwood number and comparable thickness was slightly lower in the stability studies. The grid used in the present simulations is insufficient to completely resolve the final turbulence-like state, but the breakdown into a spectrum of small scales, and the annihilation of the original vortex are evident.

Since inertia and the effective gravity are dictated by the same scales in this flow, the effective Froude number based on $\Delta\rho$ is of $O(\mathcal{A}^{-1/2})$. For a thin density interface, the effective Froude number, which depends on the density gradient rather than on the density difference, would be much lower $\sim (\mathcal{A}\rho' r/\rho)^{-1/2}$, so density would play a lead role for thin interfaces.

The effect of continuous density stratification is studied in the following chapter in the context of vortex merger. The effect of three-dimensionality and the competition between the new instabilities which would then occur is also of interest, but is beyond the scope of this thesis.

CHAPTER 6

VORTEX MERGER IN A STRATIFIED FLUID

Scope of this chapter

So far, the emphasis has been on understanding the effects of baroclinic torque on a single vortex. In this chapter, we consider the effect of density stratification in a twin-vortex configuration. When two co-rotating vortices are placed near each other, they mix the neighbouring fluid around them, and merge to form a single vortex. In the presence of baroclinic vorticity, we show that this process can be significantly altered, and merger can sometimes be completely prevented.

6.1 Literature Survey

One of the simplest forms of interaction between vortices is the merger of two co-rotating vortices. In the last few decades, vortex merger has received a great deal of attention and forms one of the fundamental interaction processes in a turbulent flow. This becomes more apparent in two-dimensional turbulence where smaller eddies "merge" to form larger eddies as the flow evolves, and this is believed to be a fundamental mechanism for the transfer of energy to larger scales. Simultaneously, the merger of vortex cores is almost always associated with filamentary debris in the form of tight spirals with very thin cross sections. These filaments are believed to be a cause of the cascade of enstrophy to smaller scales. It has been felt that a better understanding of vortex merging could play a key role in developing and improving turbulence models incorporating physics at the level of vortex merging. Here we discuss some of the important works on vortex merger and the current state of understanding of this problem. The first detailed observations of vortex merging can be attributed to the experiments on mixing layers. Freymuth (1966) observed coalescence of vortices in a separated laminar boundary layer. More detailed observations were made by Winant & Browand (1974) who attributed the growth of a turbulent mixing-layer to vortex merger.

Most of the earlier work studied the process of vortex merger in a purely inviscid context in an unstratified flow. The first detailed analysis of vortex merger was due to Rossow (1977) who carried out inviscid numerical calculations on various vortex configurations including vortices in shear. His efforts were aimed at finding the best possible vortex configuration which would disperse the vortical structures in the wake of an aircraft. As shown in figure (6.1), when two vortices of same circulation Ξ and core size a are separated by a distance b, they rotate about a common centre because of the induced velocities of each on the other. It was found that for inviscid vortices, there exists a critical $(a/b)_{cr}$ below which merger does not occur (Saffman & Szeto (1980), Overman & Zabusky (1982), Griffiths & Hopfinger (1987), Meunier *et al.* (2002)). In the limit of $a/b \to 0$, the each vortex sees the other effectively as a point vortex. In this case, the two

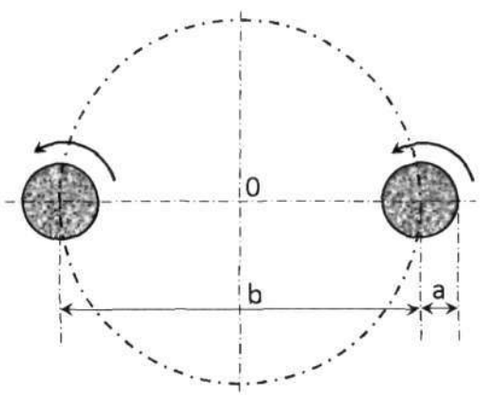

Figure 6.1: Schematic of a two dimensional intial vortex configuration which will lead to merger. The anti-clockwise arrows indicate the sense of vorticity, such that the two vortices describe an anti-clockwise revolution of period $2\pi^2 b_0^2/\Xi$ about the vorticity centroid '0'. Ξ is the circulation of each vortex.

vortices rotate about each other endlessly with a constant angular velocity. Such a configuration is referred to as an equilibrium configuration, as the vortices appear stationary in a frame rotating with the angular velocity of the two vortices. Inviscid vortices with finite core can undergo deformations, and the analogy with a point vortex may not hold in all cases. Saffman & Szeto (1980) find various non-circular equilibrium configurations and conclude that these configurations become unstable if the vortices are too close to each other. Deem & Zabusky (1978) in an earlier work had referred to these configurations as "V States". Overman & Zabusky (1982) carried out a detailed analysis using a contour dynamics method on these equilibrium configurations. They demonstrate that the merger of vortices is the result of an instability of a perturbed equilibrium configuration. A stability analysis of these equilibrium configurations was also carried out by Dritschel (1985), who also extended it to many vortices rotating about a common centre. For symmetric vortex pairs, to arrive at an equilibrium configuration, it suffices to analyze the deformation of just one vortex. To further simplify the calculations, the vortex was assumed to deform symmetrically about the line joining the two vortices. Cerretelli & Williamson (2003*a*) find many new uniformly rotating equilibrium configurations using the above assumptions. They extend previous work to cases where the vortices even touch each other. In reality, the assumption of symmetric deformation is not valid as the major axis of the vortex tilts from the line joining the vortex centers as shown in figure (6.2). This can be compared with figure (3) in Cerretelli & Williamson (2003*a*). Meunier *et al.* (2002) calculated the equilibrium shapes of two like-signed vortices with a non-uniform vorticity distribution to arrive at a more realistic critical separation distance which could be compared with their experiments. They attribute the merger of the vortices to the conservation of angular momentum as the filaments are ejected outside the core.

Griffiths & Hopfinger (1987) carried out detailed experiments on a like-signed vortex

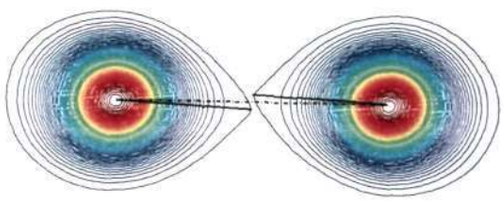

Figure 6.2: Tilt of the vortices from the line joining the vortex centers

pair to understand the merger process in both a baroclinic and a barotropic setting[1]. For barotropic vortices, they confirm the previous theoretical and numerical results on the critical separation distance. In the baroclinic case, they find this critical distance to depend on the internal Rossby radius, i.e., the radius at which rotational effects become as important as buoyancy forces. For Rossby radius larger than the core size, they find merger for larger separation distances.

In an unstratified flow, when the two vortices are kept sufficiently far, the process of merger can be divided into four stages as shown in figure 6.3. In the first stage, the viscous diffusive stage, the two vortices behave like point vortices rotating around each other about a common axis. Viscous diffusion acts on the vortex cores reducing over time, the value of a/b. In the second stage, the convective stage, which begins when a/b crosses a critical value, the vortices rapidly approach each other with the ejection of spirals of vorticity in the form of filaments. This stage is nearly independent of the Reynolds number and can be explained purely in an inviscid context. The third stage can be called the axisymmetrization stage where the vortex cores completely merge into each other, and the single final vortex relaxes towards an axisymmetric state. The final stage involves the viscous diffusion of the single vortex. We now discuss the literature concerning each individual stage of the merger process. In reality, these distinct phases can be observed clearly only for flows with very large Reynolds number (based on the vortex characteristics).

The first stage, as mentioned earlier, is a viscous stage with the size of the core increasing owing to viscous diffusion. Apart from this, each vortex is under the straining influence of the other vortex and therefore adapts to it. Le Dizès & Verga (2002) using direct numerical simulations studied this *adaptation* process for various vorticity profiles, and find two distinct relaxation processes. The first one is an inviscid process where the vortex rapidly adapts to the strain field of the other vortex. This is found to be profile dependent and is elucidated using the eccentricities of the vortex core. They show that the eccentricity exhibits a damped oscillation and attribute this to the damped Kelvin modes (*quasi-modes*) of each vortex (Le Dizès (2000)) resulting in a quasi-stationary state (in a rotating frame). Though the shape of the vortex in the numerical simulations is not strictly elliptical, unlike in the theoretical case (Le Dizès (2000)), a very good agreement is found between the two. The second phase is found to be a viscous diffusion of this

[1]In a barotropic case, isobars and isopycnals are parallel to each other, whereas in a baroclinic case, isobars and isopycnals cross each other, and this is a source of vorticity in the flow.

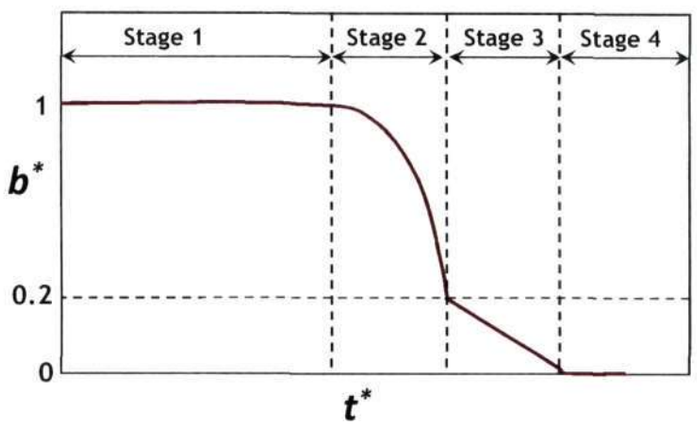

Figure 6.3: Schematic showing the variation of separation distance with time for an unstratified co-rotating vortex pair. The stages in the merger process are indicated.

state to that a Gaussian profile. The vorticity at the central saddle point is found to exhibit an $Re^{1/3}$ scaling. They attribute this to be similar to the cross-stream diffusion of a scalar in a shear flow (Rhines & Young (1983)).

The second stage is the key stage to the merger process and vortex merger actually begins at this stage. The bulk of the work on this stage has centered on explaining the critical a/b ratio, i.e., to quantify the onset of merger. Some important studies concerning this stage have been discussed earlier. The physical mechanism associated with merger was first discussed in detail by Melander *et al.* (1988). They view the flow in a co-rotating frame where three distinct regions can be identified, as shown in figure (6.3). The flow near the core is vorticity (Z) dominated and consists of closed streamlines around each vorticity maximum. This inner core region is surrounded by a band of fluid where each streamline encircles both vortex cores. This region is strain dominated and is called the exchange band. Surrounding this is are outer recirculation regions, sometimes referred to as the 'ghost' regions. These have an opposite sense of rotation as compared to the inner core or the exchange band region and exists only in the co-rotating frame. We will discuss various regions of flow in detail in section (6.5.1) where the physical mechanism leading to merger will be discussed.

To understand the influence of each region on the merger process, it is useful to extract these regions from the velocity field as was done by Brandt & Nomura (2006). The inner core and the exchange band region have the same sign of vorticity in the co-rotating frame, whereas the outer recirculation region has the opposite sign. The core and exchange band regions are distinguished by the the value of the second invariant of the velocity gradient tensor, $\Pi = (Z^2/2 - S^2)/2$ where S is the strain rate tensor. If $\Pi > 0$, the flow is vorticity dominated. This corresponds to the inner core regions. For $\Pi < 0$, the flow is strain dominated and this corresponds to the exchange band region. Using the value of Π, Brandt & Nomura (2006) identified various regions in the flow. They then showed that both the inner core region and the exchange band region

contribute to the merging, i.e. cause a decrease of b with time, though the dominant contribution is from the exchange band region. Huang (2005) also found a similar result using a vortex-blob calculation, though he refers to the exchange band region as a 'sheet-like' region. Cerretelli & Williamson (2003*b*) ascribe the merging velocity, i.e., the rate of decrease of b with time, to the anti-symmetric part of the vorticity field. This part can be attributed to the presence of filaments. But Fuentes (2005) finds that filamentation cannot always be the cause of merger, especially in steep vorticity profiles where merger begins before the onset of filamentation. As noted by Fuentes (2005), this contradiction is due to assumption that the separatrices dividing different flow regions are taken to be streamlines in the co-rotating Eulerian frame. This is true only for flows with a constant rotation rate. For unsteady cases, i.e., once the second stage of merger begins, the rotation rate changes with time, streamlines do not form separatrices. To define the separatrices more precisely, Fuentes (2005) analyses the Lagrangian flow geometry and finds that filamentation occurs when the stable manifold of a hyperbolic trajectory enters the vortex. His results corroborate previous results to a certain extent, in the sense that filamentation plays an important role in the merger process, but cannot be said to dictage its onset.

The third stage of the merger process has received very little attention. After a rapid decrease in separation distance in stage 2, an abrupt slowing down is observed, and the separation distance falls off at a much slower rate, and is sometimes referred to as the 'plateau stage'. At the beginning of this stage, though the vortices are very close to each other, two distinct maxima can be identified, and the streamlines are elliptical. During this stage, the elliptical streamlines relax towards an axisymmetric stage, and the process is therefore an advection-diffusion process, and not just a diffusion stage as noted by Cerretelli & Williamson (2003*b*). Therefore, in regions away from the centroid of the system where differential shear dominates the flow field, an accelerated diffusion, at a rate of $Re^{1/3}$ is expected to occur. In studies on axisymmetrization of a non-axisymmetric vortex, it is shown how this accelerated diffusion occurs (see Moffatt & Kamkar (1983), Rhines & Young (1983), Flohr & Vassilicos (1997), and references therein). But near the vortex centre, where differential shear vanishes, Bajer *et al.* (2001) showed that $Re^{1/2}$ is the relevant scaling to follow. Josserand & Rossi (2007) show that the duration of third stage lasts for a time proportional to $Re^{1/2}$.

The final stage of the merger process involves axisymmetrization and diffusion of the single merged vortex. In particular, a lot of filamentary debris still exists at the beginning of this stage which gets slowly diffused or is engulfed into the vortex at the centroid of the system. An very important point in merger studies is to understand the relation between the circulations of the pre-merged vortices to the circulation of the final merged vortex. Josserand & Rossi (2007) show that approximately (1/3) of the initial circulation is lost to filaments, and this value is independent of the Reynolds number. The non-axisymmetry in the vortex can be viewed as (damped) Kelvin modes riding on the vortex core. It has to be checked whether the axisymmetrization process involves quasi-mode damping for these profiles.

Atmospheric conditions such as stable density stratification can have an important role to play in the merger process. In the present work, we study the effect of stable density stratification on the interaction of two co-rotating vortices. In brief, we find

that apart from the Froude number, Fr which governs the strength of stratification, the Peclet number Pe, also plays an important role. For flows with $Fr \sim 1$, merger never occurs and, remarkably, the vortices actually move away from each other. Two distinct mechanisms are found to operate depending on the value of Peclet number. For flows with high Pe, spirals of density field enter the vortex core resulting in the breakdown of the vortex core. Whereas for flows with low Pe, the density field diffuses rapidly near the vortex core and no such breakdown was observed.

6.2 Governing equations

In the previous chapters of this thesis, baroclinic vorticity was generated entirely due to inertial effects of density stratification. Centrifugal forces played the role of buoyancy. We now consider a more realistic situation where gravitational acceleration is also included. Direct numerical simulations in two-dimensions are performed with a corotating Gaussian vortex pair in a stably stratified fluid. The initial background density stratification is taken to be linear. For simplicity, we further split the total density field, $\tilde{\rho}(x, y, t)$ in the following form (see Turner (1973)).

$$\tilde{\rho}(x, y, t) = \rho_0 + \bar{\rho}(y) + \rho'(x, y, t), \tag{6.1}$$

where x and y are the horizontal and vertical directions respectively. ρ_0 is a constant density value and $\bar{\rho}(y)$ is the vertical variation of the mean density about ρ_0. We prescribe linear stratification, i.e. $\bar{\rho}(y)$ has a linear dependence on the y coordinate. And ρ' is a time dependent perturbation density field generated due to the motion of vortices. The governing non-Boussinesq equations in the velocity-pressure formulation can be written as,

$$\nabla \cdot \mathbf{u} = 0, \tag{6.2}$$

$$\tilde{\rho}\left(\frac{\partial \mathbf{u}}{\partial t} + \mathbf{u} \cdot \nabla \mathbf{u}\right) = -\nabla P + \rho' \mathbf{g} + \tilde{\rho}\nu\nabla^2 \mathbf{u}, \tag{6.3}$$

$$\frac{\partial \rho}{\partial t} + \mathbf{u} \cdot \nabla \rho = \kappa \nabla^2 \rho. \tag{6.4}$$

In the above equations, ν is the kinematic viscosity, κ is the thermal diffusivity, and these quantities are taken to be constant. Gravity $\mathbf{g} = g\mathbf{e}_y$ where $\mathbf{e}_y$ is the unit vector in the vertical direction. The fluid is taken to be incompressible, and this allows us to define a streamfunction to solve the momentum equation in the vorticity-streamfunction formulation. Notice that the total density $\tilde{\rho}$ appears in the inertial acceleration terms. In situations where gravity term is larger than the inertial effects of density stratification, it is common to employ the Boussinesq approximation. This approximation is strictly valid when the following inequality is satisfied:

$$\rho' \ll \bar{\rho} \ll \tilde{\rho}, \tag{6.5}$$

In this limit, re-writing total density as

$$\tilde{\rho} = \rho_0 \left(1 + \frac{\rho'}{\rho_0} + \frac{\bar{\rho}(y)}{\rho_0}\right), \tag{6.6}$$

and retaining only the lowest order terms in the acceleration terms, we get the Boussinesq approximation. In many physical systems, $\rho_0 + \bar{\rho}(y) \approx \rho_0$ on an average. For example, in the oceans, $\rho_0 \approx 1000\ kg/m^3$, the density of fresh water, $\bar{\rho}(y)$ occurs due to salinity stratification, and there is a fluctuating ρ' everywhere in space due to fluid motions. In the atmospheres, this approximation is restrictive, and so caution needs to be employed when dealing with atmospheric flows. Retaining density only in the gravity term, we thus have the Boussinesq equations which take the form,

$$\rho_0 \left(\frac{\partial \mathbf{u}}{\partial t} + \mathbf{u} \cdot \nabla \mathbf{u}\right) = -\nabla P + \rho' \mathbf{g} + \rho_0 \nu \nabla^2 \mathbf{u}. \tag{6.7}$$

When gravity is small, or when the inequality (6.5) is not satisfied, inertial effects of density stratification cannot be ignored. This is certainly true very close to a vortex as we have seen in chapter 5 that inertial effects cannot be ignored. Even for flows when density variation is small, but the transition region from heavy to lighter fluid occurs rapidly, inertial effects of density stratification cannot be ignored. A common case is when sharp interfaces arise in a flow leading to large values of density gradient, baroclinic torque generated from inertial effects of density stratification become important. In the pure inertial limit, the governing equation (6.3) reduces to

$$\tilde{\rho} \left(\frac{\partial \mathbf{u}}{\partial t} + \mathbf{u} \cdot \nabla \mathbf{u}\right) = -\nabla P + \tilde{\rho} \nu \nabla^2 \mathbf{u}. \tag{6.8}$$

An important quantity of interest is the vorticity, $Z(x, y, t) = \boldsymbol{\nabla} \times \mathbf{u}$. The evolution equation for vorticity for a non-Boussinesq system is obtained by taking the curl of equation (6.3).

$$\frac{\partial Z}{\partial t} + \mathbf{u} \cdot \nabla Z = \frac{\nabla \tilde{\rho} \times \nabla P}{\tilde{\rho}^2} + \frac{g}{\rho_0} \frac{\partial \rho'}{\partial x} + \nu \nabla^2 Z, \tag{6.9}$$

where the streamfunction in the fixed frame is related to vorticity in the standard way,

$$\nabla^2 \psi = -Z. \tag{6.10}$$

Therefore the streamfunction in a rotating frame of reference, with angular velocity Ω_0 is given by

$$\psi_r = \psi - \frac{\Omega_0}{2} r^2. \tag{6.11}$$

The initial condition prescribed for vorticity in the simulations is two Gaussian vortices with centres at (x_1, y_1) and (x_2, y_2), and initial vortex radii of a_0. This can be written as

$$Z(x, y, 0) = Z_0 \left[\exp\left(\frac{-((x - x_1)^2 + (y - y_1)^2)}{a_0^2}\right) + \exp\left(\frac{-((x - x_2)^2 + (y - y_2)^2)}{a_0^2}\right)\right]. \tag{6.12}$$

The peak vorticity Z_0 is a function of the circulation Γ and the vortex radius, i.e., $Z_0 = \Xi/\pi a_0^2$. For simplicity, we take $y_1 = y_2 = 0$, and the initial vortex separation is given by $b_0 = |x_1 - x_2|$.

The non-dimensional numbers characterizing this flow are the Reynolds number, the Prandtl number and the Froude number. The first two are defined as before by

$$Re = \frac{\Xi}{\nu}, \tag{6.13}$$

$$Pr = \frac{\nu}{\kappa}. \tag{6.14}$$

The Peclet number, also used earlier in this thesis, is related to the Reynolds and Prandtl numbers by the simple relation,

$$Pe = RePr = \frac{\Xi}{\kappa}. \tag{6.15}$$

The Froude number is defined as

$$Fr = \frac{U_0}{Nb_0} = \frac{\Xi}{2\pi b_0^2 N}, \tag{6.16}$$

where N is the Brunt-Vaisala frequency given by

$$N^2 = -\frac{g}{\rho_0}\frac{d\bar{\rho}}{dy}. \tag{6.17}$$

In the above equations, U_0 is a relevant characteristic velocity, and is calculated from the initial angular velocity of the two vortices assuming them to be similar to point vortices. In the above case we get $U_0 = \Xi/2\pi b_0$. The initial time period for a system of point vortices is given by $T_{ref} = 2\pi^2 b_0^2/\Xi$. We investigate the flow for a wide range of Reynolds, Froude and Prandtl numbers. In all the simulations in this chapter, the background density stratification is taken to be linear. Also, all the results are presented in terms of the non-dimensional time $t^* = t/T_{ref}$.

It is useful to remember a few important points regarding Pr and Fr. At large Pr, momentum diffuses much more rapidly than density, whereas at small Pr, the reverse is true. Therefore, when using a low Pr fluid, the effect of stratification is reduced due to rapid homogenization of density gradients, thus killing the source of baroclinic torque. Also, strong stratification occurs for small Fr. An $Fr = 1$ indicates that the time scale associated with rotation of the vortices and the time scale associated with density oscillations, i.e., $1/N$, are comparable. Therefore, at this Fr, stratification effects will be felt very strongly. But clearly, small Fr and small Pr have competing effects. We will show some results later in this chapter that strongly stratification effects can be overcome by using a small Pr fluid.

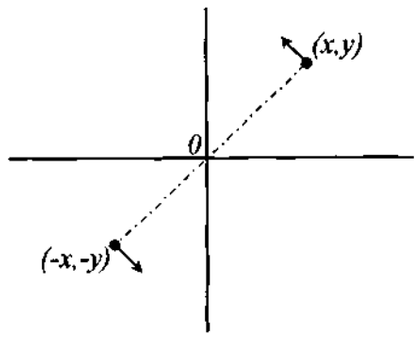

Figure 6.4: Points (x, y) and $(-x, -y)$ have the same vorticity for a symmetric density profile.

6.3 Symmetries in a Boussinesq system

The buoyancy force is related to the differences in the density field from a mean time invariant density profile. In the present scenario, the mean density profile is assumed to vary linearly in the vertical coordinate. Consider the following set of transformations as shown in figure (6.4):

$$(x, y) \rightarrow (-x, -y), \quad (u, v) \rightarrow (-u, -v), \quad Z \rightarrow Z^*, \quad (\rho, \rho') \rightarrow (\rho^*, \rho'^*). \tag{6.18}$$

$$\frac{\partial Z^*}{\partial t} + \mathbf{u} \cdot \nabla Z^* = \frac{g}{\rho_0} \frac{\partial \rho'}{\partial x} + \nu \nabla^2 Z^*. \tag{6.19}$$

$$\frac{\partial \rho^*}{\partial t} + \mathbf{u} \cdot \nabla \rho^* = \kappa \nabla^2 \rho^*. \tag{6.20}$$

The above equations are satisfied by the following transformations for Z and ρ, i.e.

$$Z^*(x, y) \rightarrow Z(-x, -y), \tag{6.21}$$

$$\rho^*(x, y) \rightarrow -\rho(-x, -y), \tag{6.22}$$

$$\rho'^*(x, y) \rightarrow -\rho'(-x, -y). \tag{6.23}$$

Because of this symmetry in vorticity, the centroid of vorticity is preserved in a Boussinesq system. In the present context of vortex merger, it would mean that a successful merger of vortices would lead to a single merged vortex at the origin, i.e. the vorticity centroid of the initial configuration. In the presence of baroclinic torque, it is evident from equations (6.21), (6.22) and (6.23) that this symmetry will no longer be preserved. Thus, as will be shown later, symmetry is broken when employing the non-Boussinesq equations.

6.4 Effect of gravity on a single vortex

Since gravity has not been taken into consideration in earlier chapters, before we deal with the two vortex case, we first discuss the effect of gravity on a single vortex. This section can also be viewed as an extension to chapter 5, where, in the absence of gravity, small scale instabilities were shown to arise along the spiral density interface. Here, we briefly treat the same problem with Boussinesq approximation. Gravity is chosen to act perpendicular to the axis of the vortex. Though idealized, an understanding of this problem will be useful in the early evolution of aircraft trailing vortices in a stratified environment (see Crow (1974), Narain & Uberoi (1974), Saffman (1972)), and in the interaction of a vortex with a sharp density interface (see Linden (1973), Dahm *et al.* (1989)).

Linden (1973) used the problem of a vortex ring impacting a thin density interface as a model problem for understanding turbulent entrainment. For the same problem, Dahm *et al.* (1989) showed that the dynamics is governed by two non-dimensional parameters, $(a/\delta)At$ and R where a is the vortex core size, δ is the characteristic thickness of the density interface, At is the Atwood number and $R \equiv (a^3 g/\Xi)$ characterizes the ratio of centrifugal acceleration to gravity. Dahm *et al.* (1989) also showed that the flow is weakly influenced by Reynolds and Weber numbers. A direct comparison with their results is difficult due to two primary reasons: (i) the present geometry is too idealized to represented the interaction of an impacting vortex ring, and (ii) the value of At and R used in their analysis is different from the present simulations. Though, a detail investigation is worthwhile especially, since Linden (1973) used a similar problem to understand turbulent entrainment and is beyond the scope of this thesis. Our main aim is to study the roll-up process of the density interface as seen in chapter 5 and understand its impact on the structure and evolution of the vortex.

We solve the Boussinesq equations with a *tanh* vortex placed at a vertically stratified *tanh* density interface. Vorticity and density profiles in this case are defined as

$$Z(r) = \frac{Z_0}{2}\left(1 - \tanh\left[\frac{r-a}{\delta}\right]\right) \tag{6.24a}$$

$$\bar{\rho}(y) = \rho_0\left(1 - \frac{\Delta\rho}{2\rho_0}\tanh\left(\frac{y}{\delta}\right)\right) \tag{6.24b}$$

where Z_0 is the peak value of voricity, ρ_0 is the average density, a is the vortex core size, δ is the thickness of the vorticity and density interfaces. The Atwood number can be defined as $At = \Delta\rho/(2\rho_0)$. To keep things brief, we only present one sample result here, viz., for $At = 0.2$, $a/\delta = 20$, and $Fr = 4.6$, based on the maximum density gradient in the flow. Since the dynamics is predominantly inviscid, we use hyperviscosity in our simulations. The time evolution of vorticity and density is given in figure (6.5). At short times, the vortex remains axisymmetric winding the thin density interface into a spiral. Baroclinic vorticity in the form of thin vortex sheets gets generated along the density interface. Eventually, this vorticity grows and becomes comparable to the primary vortex. This vortex sheet is susceptible to a Kelvin-Helmholtz type of instability and rolls up into smaller vortices of sign opposite to the primary vortex as can be seen at $t^* = 68.7$. Moreover, local regions of unstable density configurations are created making the flow

suceptible to Rayleigh-Taylor instabilities. The smaller vortices strain the primary vortex elongating it. At low levels of gravity, the strain field of the smaller vortices results in an oscillation of the primary vortex, now elliptical.

A simple model based on point vortices is constructed here capuring the most essential physics. Due to the simplicity of the model, we will not attempt to compare the results of the model quantitatively with the DNS results.

Consider an idealised three vortex system as shown schematically in figure (6.6). Motivated by simulations, the effet of baroclinic torque has been clubbed into two point vortices here. Let Ξ be the circulation of the primary vortex placed at the origin. And let ϵ represent the strength of baroclinically generated vorticity, which is generated at a distance b from the origin. The rate of generation of baroclinc vorticity is given by

$$\frac{d\epsilon}{dt} = -\frac{\Delta\rho}{\rho_0}\frac{g}{\delta}\cos(\theta+\phi), \tag{6.25}$$

where the density gradient is simplified as $\nabla\rho \approx (\Delta\rho)/\delta$, g is the acceleration due to gravity, ϕ is the angle made by the density gradient (normal to the interface) with the line joining the vortices, and θ is the angle made by the line joining the vortices with the horizontal. The induced velocity of vortex 2 due to the primary vortex 1, and vortex 3, is obtained by using the Biot-Savart law,

$$V = \frac{\Xi}{2\pi b} - \frac{\epsilon(t)}{4\pi b}. \tag{6.26}$$

Differentiating this with respect to time, we get

$$\frac{dV}{dt} = \frac{1}{4\pi b}\frac{\Delta\rho}{\rho_0}\frac{g}{\delta}\cos(\theta+\phi). \tag{6.27}$$

The rate of rotation of the line joining the vortices is given by $\dot{\theta}(t)$ where the overhead dot represent derivative with time. Therefore $\ddot{\theta} \equiv \dot{V}/b$. This reduces the above equation to a non-linear oscillator equation,

$$\frac{d^2\theta}{dt^2} = \frac{1}{4\pi b^2}\frac{\Delta\rho}{\rho_0}\frac{g}{\delta}\cos(\theta+\phi), \tag{6.28}$$

with the initial conditions

$$\theta(0) = 0, \qquad \dot{\theta}(0) = \frac{\Xi}{2\pi b^2}. \tag{6.29}$$

Equation (6.28) is solved using the standard MATLAB program ode45, which uses an adaptive Runge-Kutta time-stepping. A parametric study for various values of b and $g' = g\Delta\rho/\rho_0$ was carried out. The time evolution of angle $\theta(t)$ for three arbitrarily chosen value of gravity is shown in figure (6.7). For increasing g, the system settles into a stable oscillation about the vertical. The amplitude and time period of this oscillation varies inversely with gravity. From the solution of $\theta(t)$, the baroclinic vorticity generated can be obtained as

$$\epsilon(t) = 2\Xi - 4\pi b^2\dot{\theta}. \tag{6.30}$$

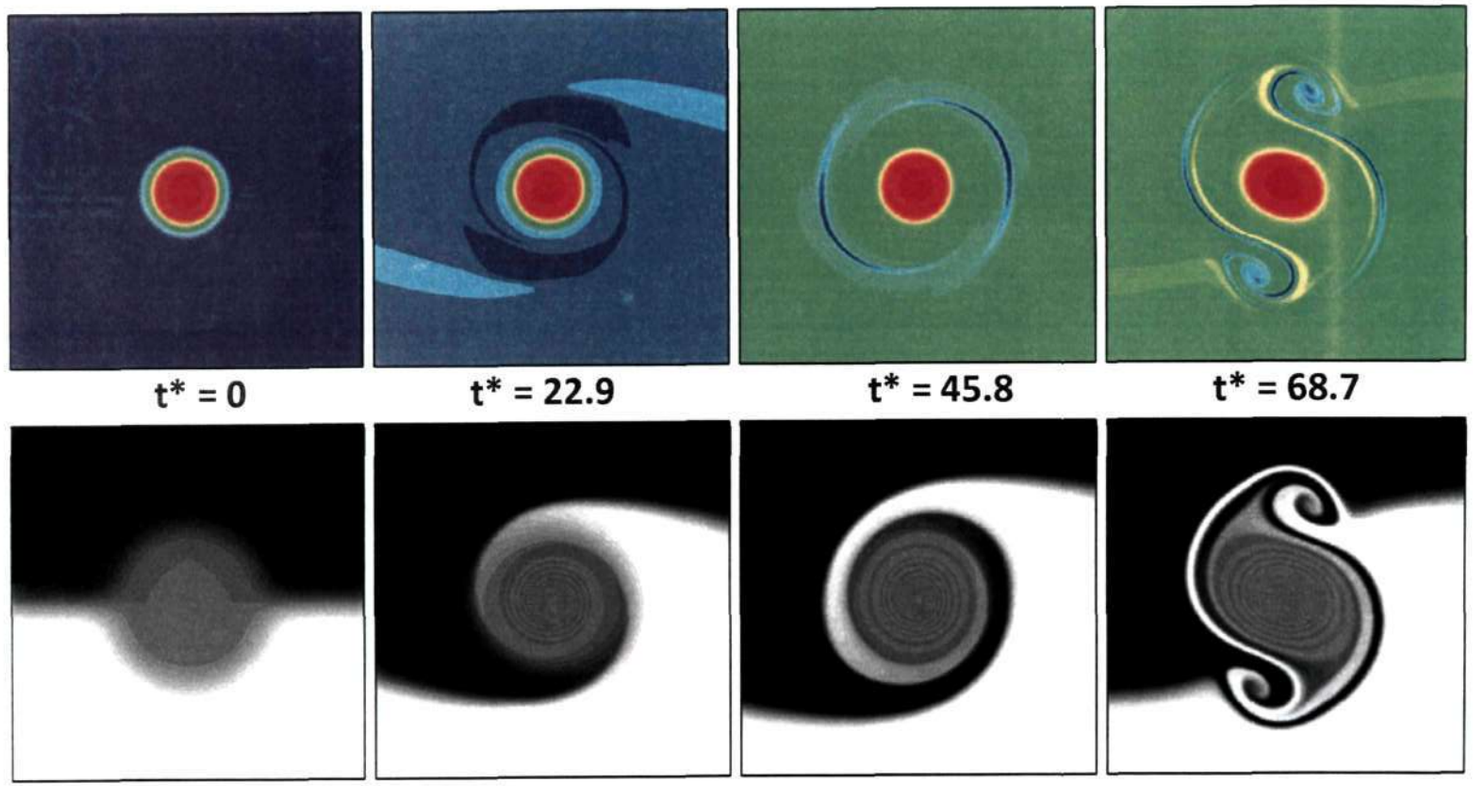

Figure 6.5: Evolution of vorticity (color) and density (gray scale) for a *tanh* vortex placed a vertically stratified *tanh* density interfac. Time is non-dimensionalized by circulation timescale of the vortex, $Fr = 4.6$ based on the maximum density gradient.

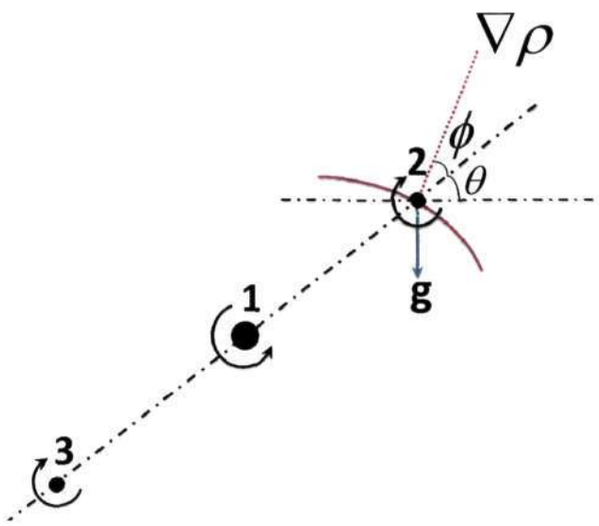

Figure 6.6: Three vortex model showing the primary vortex 1 and baroclinically generated vortices 2 and 3. The red curve is the density interface with $\nabla\rho$ being the direction of density gradient normal to it. ϕ is the angle made by $\nabla\rho$ with the line joining the vortices, and θ is the angle subtended by the vortices with the horizontal.

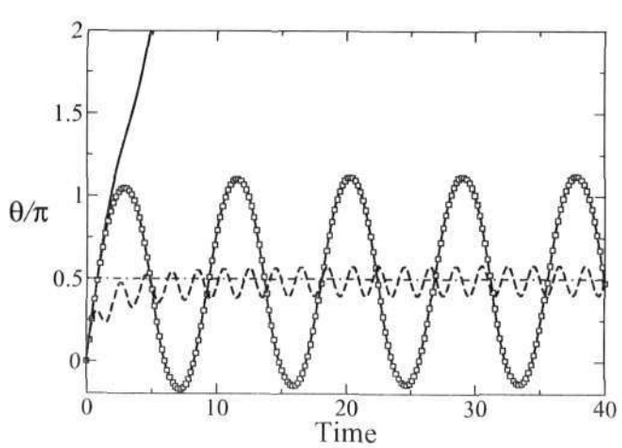

Figure 6.7: Evolution of angle, θ made by the line joining the vortices for increasing values of stratification. Increasing g reduces the time period of oscillation.

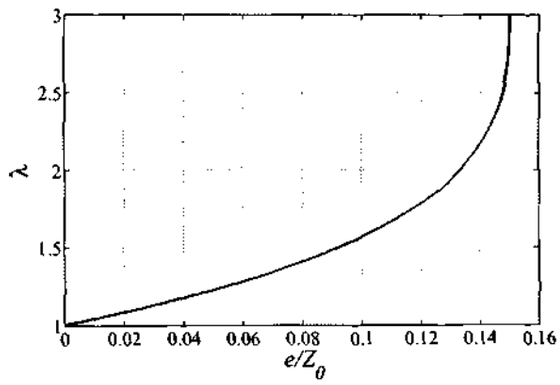

Figure 6.8: Variation of aspect ratio with imposed strain rate. At $e/Z_0 > 0.15$, the aspect ratio diverges.

This imposes a time dependent strain field on the primary vortex. The non-dimensional strain-rate experienced by the primary vortex 1 is given by

$$\frac{e}{Z_0} = \frac{\epsilon(t)}{\Xi}\left(\frac{a}{b}\right)^2, \tag{6.31}$$

The stability of an elliptic vortex patch to an external strain field was studied by Moore & Saffman (1971). They find two stable elliptical solutions for $|e/Z_0| < 0.15$, but for $|e/Z_0| > 0.15$, no solutions of elliptical form were found. The variation of aspect ratio as a function of imposed strain field in their analysis reduces to

$$\frac{e}{Z_0} = \frac{\lambda(\lambda-1)}{(\lambda^2+1)(\lambda+1)}, \tag{6.32}$$

and is shown in figure (6.8). Clearly, when the strain field reaches 0.15, the aspect ratio diverges. For values of strain greater than 0.15, no solutions were found, possibly indicating that stable steady elliptical vortex patches cannot exist. We calculate the strain rate obtained in our model as a function of b and gravity. This is shown in figure (6.9). The values of circulation, $\Delta\rho$ were chosen to match the simulation. The region inside the thick black curve corresponds to strain rates higher than 0.15. Clearly, for very small gravity, the induced strain rate is too weak and a stable elliptical vortex results. Similarly, for large b, the point vortices are too far apart to influence the primary vortex. An interesting aspect of this plot is the region for small b and small gravity. For small gravity, a higher value of b appears to be more dangerous than a lower b. More work needs to carried out, both in terms of simulations, and improved modelling to understand these results better. This preliminary analysis, however, leads us to expect a completely different behaviour at higher levels of gravity. We now return to the vortex merger problem.

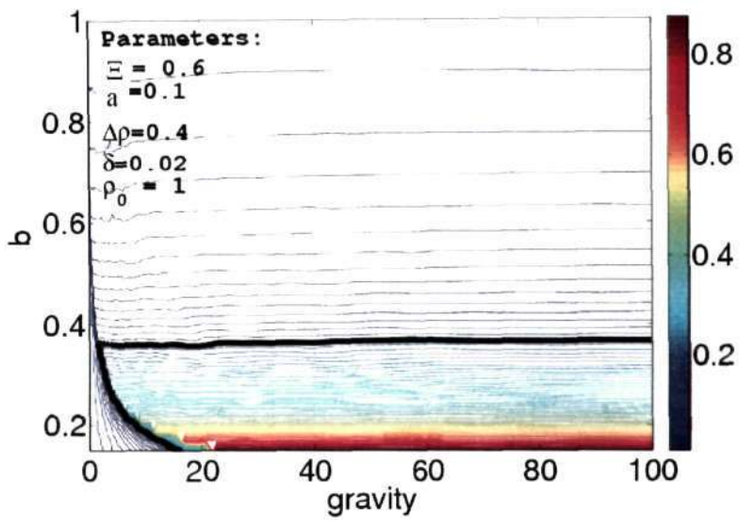

Figure 6.9: Variation of aspect ratio with imposed strain rate. At $e/Z_0 > 0.15$, the aspect ratio diverges.

6.5 Merger in a homogeneous fluid

The merger of a two co-rotating vortices in an unstratified fluid is a well studied problem now. To enable comparisons with the stratified flow cases, we present here results from a few numerical simulations at various Reynolds numbers. In all the simulations carried out, the initial vortex size and initial separation distance were kept fixed at 0.1 and 1 respectively. Figure 6.10 shows the time evolution of the vorticity field in a homogeneous fluid for $Re = 5000$. The advection of each vortex by the other causes the two vortices to rotate about the centroid of vorticity in an anti-clockwise direction. At short times, the vortices behave like point vortices rotating with a constant angular velocity. During this time, in response to the straining field from the other vortex, both the vortices undergo distortions at their core boundaries. Le Dizès & Verga (2002) showed that these distortions eventually relax and the vortices reach an equilibrium shape. They further showed that this relaxation is associated with the exponentially damped Landau poles of a Gaussian vortex, discussed in Chapter 3. By $t^* \approx 1.875$, filaments ejected from diametrically opposite ends of each vortex become clearly visible. In fact, though not noticeable clearly, pronounced deformations occur near the centroid of vorticity. This is associated with a tilt in the vortices as shown in figure 6.2, a fact recognized in the early work of Melander *et al.* (1988). This tilt has been neglected in the theoretical predictions of critical core size for merger in the inviscid contour deformation calculations of Saffman & Szeto (1980) and Meunier *et al.* (2002). In a related work, Kimura & Herring (2001) studied the axisymmetrization of a two-dimensional elliptic vortex, and showed that palinstrophy, i.e. square of the vorticity gradient, in two dimensions plays a similar role as enstrophy in three-dimensions. For an elliptic vortex, palinstrophy growth leads to ejection of filaments from the ends of the major axis. Brandt & Nomura (2007) used

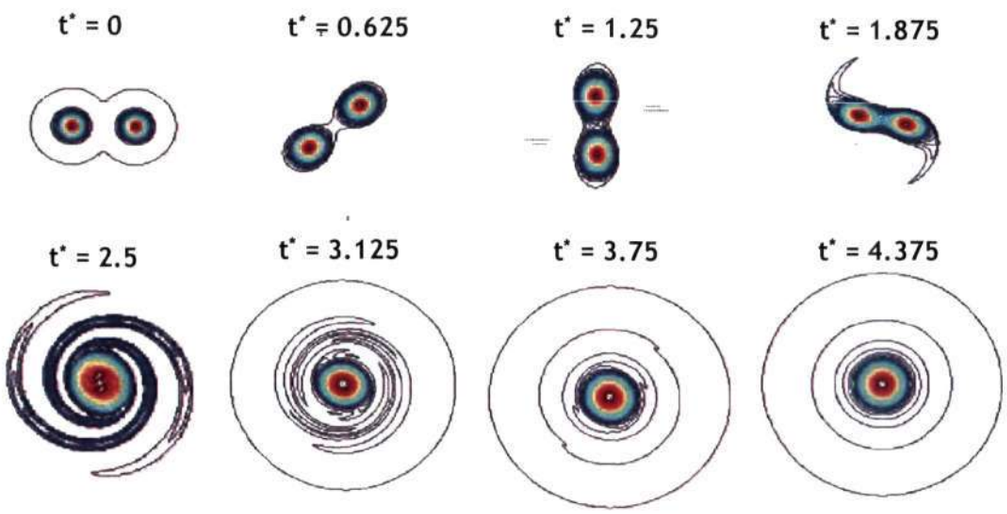

Figure 6.10: Vorticity contours for $Re = 5000$, $Fr = \infty$. The time, t^* indicated is non-dimensionalized by the reference time scale, T_{ref}.

these ideas to explain the tilt created in the vortices. These ejected filaments eventually grow to engulf both the vortices, and lead to rapid merger of the two vortices. We will examine the physical mechanism leading to merger later in the section. The instantaneous vorticity profiles are plotted in figure (6.11) at various times. The final merged vortex, at the end of the third stage has a core size which is approximately twice the original core radius.

In figure (6.12(a)), the variation of separation distance between the two vortices with time is indicated for various Reynolds numbers. Various stages of merger, as shown in the schematic figure (6.3) can clearly be observed, especially at large Reynolds number. In figure 6.12(b), the number of rotations completed by each vortex is shown as function of time. For example, at $Re = 10000$, each vortex completes nearly five complete rotations with a constant angular velocity, and then undergoes an abrupt change in rotation rate. No such abrupt transition in visible for b^*, but clearly, at $t^* > 5$, the value of b^* drops very rapidly to a value of 0.25. This is the second stage of merger, also referred to as the "convective merger stage". To identify a "merging time", i.e., the time when the convective merging process begins, we follow the method of Meunier *et al.* (2002) to calculate a critical core size and a critical time. The procedure is as follows. It is assumed that the second stage of merger is nearly independent of Reynolds number, i.e., is a purely inviscid process. Moreover, during the first stage which is governed mainly by viscous diffusion, the vortex core sizes are taken to increase with time as

$$a^2 = 4\nu t + \text{constant}, \tag{6.33}$$

where t is a non-dimensionalized time based on the rotation timescale of two point vortices of equal circulation separated by a distance b_0. It is convenient to choose the time origin

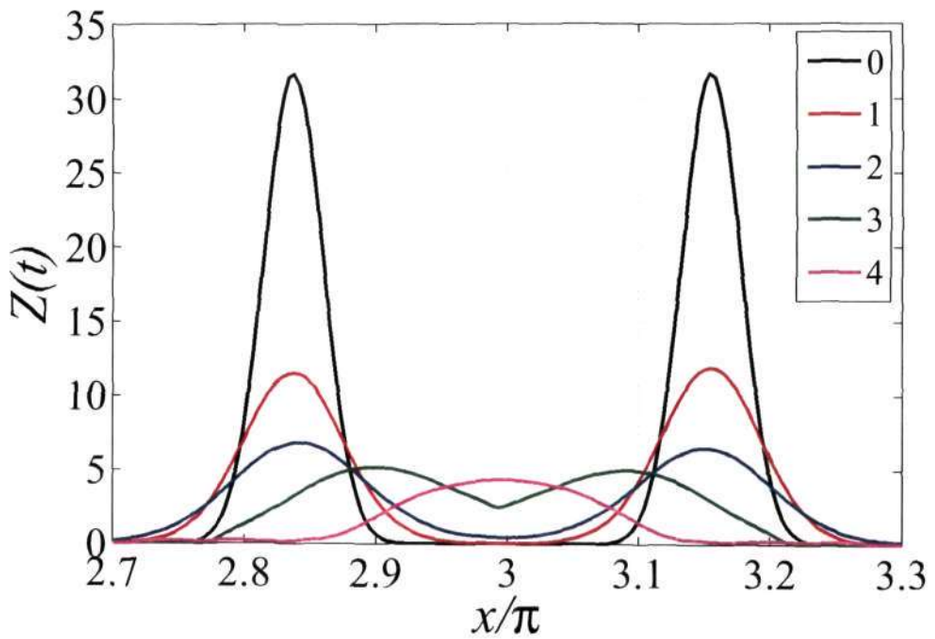

Figure 6.11: Instantaneous vorticity profiles at various times drawn along a line connecting the two vorticity maxima.

such that the constant vanishes, i.e. at $t^* = 0$, the evolution consists of two point vortices. Rewriting ν in terms of Re, the above equation reduces to

$$\frac{a^2}{b_0^2} = \frac{8\pi^2}{Re} t^*. \tag{6.34}$$

The critical core size, a_c and time, t_c^* are the size of the vortex core and time respectively at which convective merger begins. Using the above formula, these two quantities are related by the equation

$$\frac{a_c^2}{b_0^2} = \frac{8\pi^2}{Re} t_c^* \Rightarrow t_c^* \equiv CRe, \tag{6.35}$$

where C is a constant. This equation just states that the larger the Re, the smaller is the diffusion, and therefore, it takes more time to reach the critical core radius, a_c. This procedure makes it simple for the vortex merger process to be broken into two separate stages. Since the second stage is assumed to be purely of convective nature, the time it takes for the initial separation distance to decrease from its initial value b_0 to a certain fraction x of b_0, is therefore assumed to depend purely on x, independent of Re. The fraction x can be chosen arbitrarily, and we choose three different values of 0.5, 0.6 and 0.75. The "merging time" for the three different values of x are plotted as a function of Re in figure (6.13). The constant slope indicates that the merger time is truly independent of Re, and that t^* increase with Re owing to a purely viscous diffusion

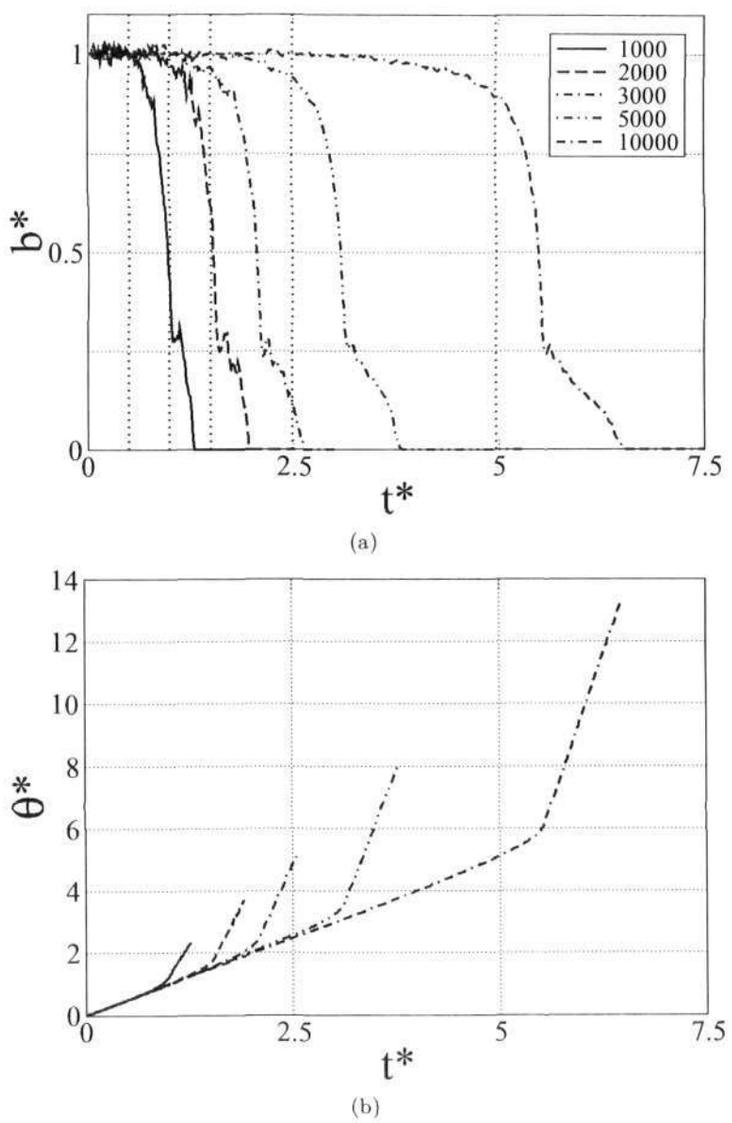

(a)

(b)

Figure 6.12: (a) Variation of separation distance between vortex maxima with time in a homogeneous fluid for various Reynolds numbers. The vertical dotted lines indicate the time when convective merger begins. See text for more details. (b) Variation with time of the total angle subtended by the line joining the vortices and the x-axis for various Re normalized by 2π. This is equivalent to the number of revolutions made by each vortex. In stage 1, the angular velocity of revolution of the vortices is constant, and is similar to an equivalent point vortex system. A distinct change in angular velocity can be noticed at the beginning of the convective merger process.

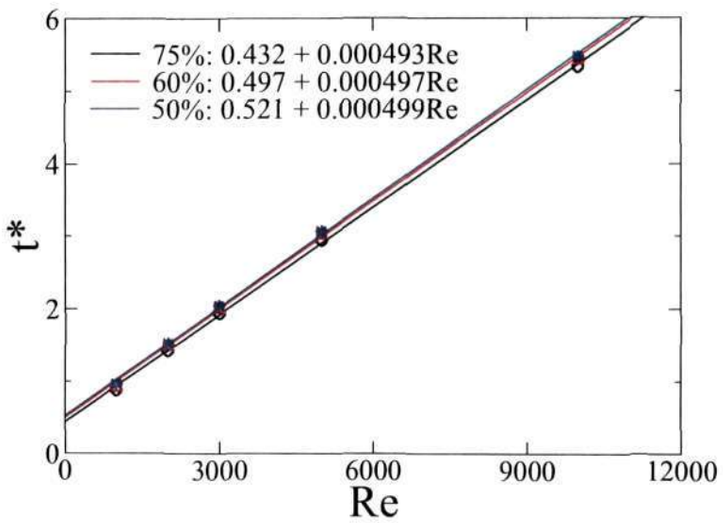

Figure 6.13: Convective merger time as a function of the Reynolds number for $Fr = \infty$ obtained by using three different fractions x. The straight lines are least-square fits to the data shown with symbols and the slopes are also indicated.

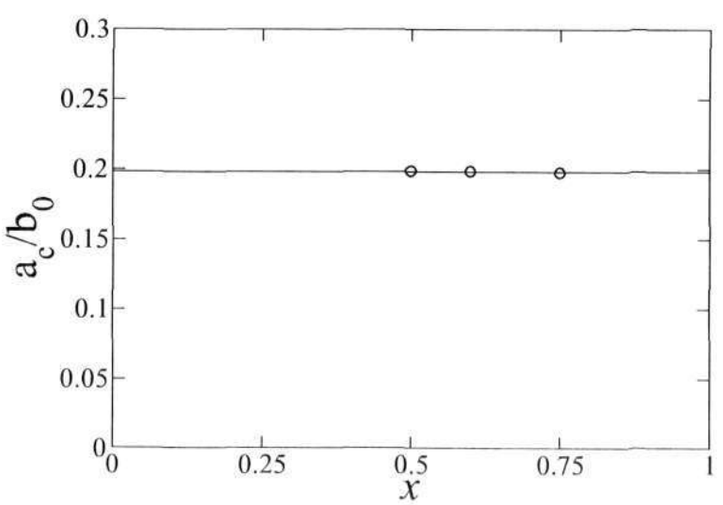

Figure 6.14: Estimation of the critical core size as a function of fraction x of the separation distance for $Fr = \infty$. The straight line corresponds to a mean value of $a_c/b_0 = 0.198$.

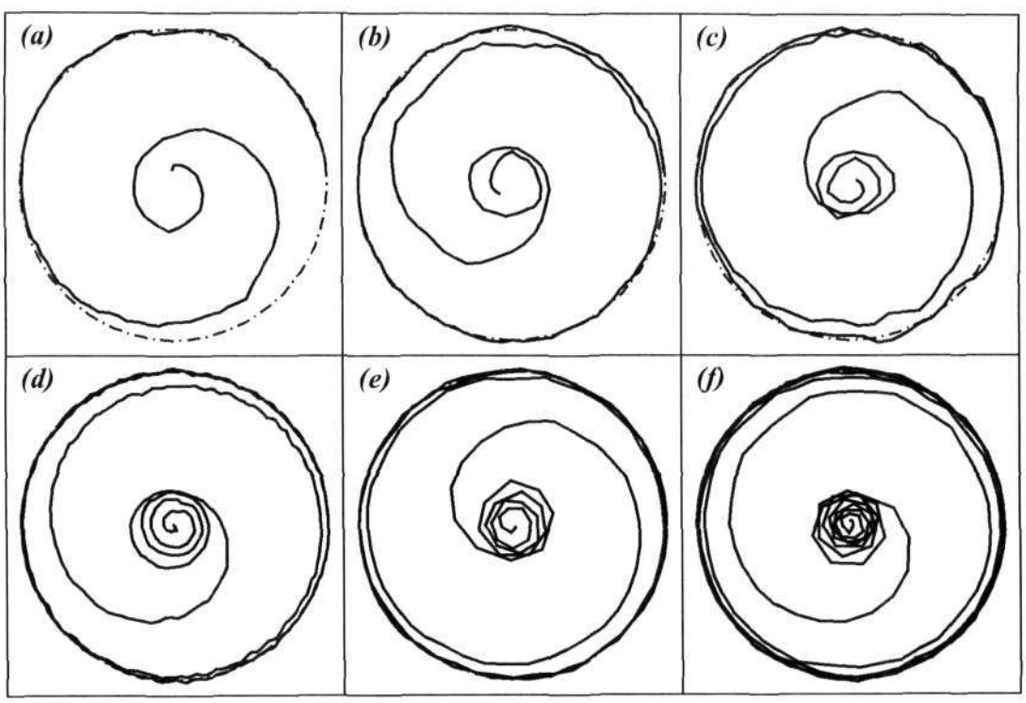

Figure 6.15: Trajectory of one of the vortices with time for various Re with $Fr = \infty$, (a) 1000, (b) 2000, (c) 3000, (d) 4000, (e) 5000, (f) 10000. All figures are to the same scale, and the dashed-dot circle indicates the trajectory of an equivalent point vortex.

of the vortex cores in stage 1. From the slope C of the three lines, the calculated cores size are plotted in figure (6.14). An average value of core size obtained is

$$\frac{a_c}{b_0} \approx 0.198. \tag{6.36}$$

This value is slightly lower than the previous estimates obtained by Meunier *et al.* (2002) (≈ 0.24), Cerretelli & Williamson (2003*b*) and others. But those studies estimate the merger time for a much shorter range of Re than has been done here. Knowing the critical core size, we can now calculate the critical time, t_c using equation (6.35), to be

$$t_c \approx 4.964 \times 10^{-4} Re. \tag{6.37}$$

The vertical dotted lines in figure (6.12(a)) show t_c for various Reynolds numbers. As mentioned earlier, the earlier stage of the merger process is similar to that of a point vortex, and therefore, two vortices describe circular orbits around a common centroid of vorticity. When convective merger begins, the trajectory of each vortex deviates from this circular trajectory and the vortices spiral inwards towards the vorticity centroid obeying the basic symmetries in the system. This is shown in figure (6.15) for various Reynolds numbers. This symmetry is also obeyed by a stratified flow under Boussinesq

approximation, and will serve to illustrate the effects of non-Boussinesq equations dealt with in later sections.

6.5.1 Merger mechanism in an unstratified fluid

We conclude this section examining some basic physical mechanism leading to merger. The first detailed examination of vortex merger was due to Melander *et al.* (1988). This pioneering work also used the idea of viewing the flow field in a rotating frame of reference. Figure (6.16) shows the streamlines in both fixed and rotating frames of reference for two positive (anti-clockwise rotation) vortices. The rotating frame streamfunction is related to the fixed frame streamfunction by the transformation

$$\psi_{rot} = \psi - \frac{\Omega_{ang}}{2} r^2, \tag{6.38}$$

where ψ and ψ_{rot} are the streamfunctions in the fixed and rotating frames respectively, and Ω_{ang} is the angular velocity of the system. Also shown in figure (6.16) are the separatrices, i.e. streamlines which divide different regions of the flow. As can be seen from figures (6.16(c)) and (6.16(d)), in addition to the hyperbolic point H_0, moving to a rotating frame creates additional saddle/hyperbolic points, H_1 and H_2 in the system. The curves joining these hyperbolic points creates various separatrices separating different regions of the flow. In dynamical systems parlance, the curve passing through H_0 would be referred to as a homoclinic orbit, and the curves joining H_1 and H_2 as a heteroclinic orbit.

In figure (6.16(d)), the region within the closed separatrices around the centres O_1 and O_2 are commonly referred to as the *inner core region*. In this region, fluid parcels rotate in an anticlockwise direction obeying the induced velocity field of the vortices. The squeezed region between the inner core regions and the separatrices connecting H_1 and H_2, i.e., between the homoclinic and heteroclinic orbits is referred to as the *exchange band region*. In this region, fluid parcels rotate around both the vortices. The two regions above and below the exchange band region, but within the outer separatrices are referred to as *ghost regions*. In these regions, fluid parcels rotate in an anti-clockwise direction. When the vortices are far apart, i.e. $a/b << 1$, all the vorticity is confined to the inner core regions as shown in figure (6.17(a)). Due to viscosity, the vortex core size increases as given by equation (6.34), and vorticity slowly diffuses across the separatrices into the exchange band region. In this way, the two vortices can exchange vorticity with each other, and hence the name for this region. This allows the two vortices to strongly strain each other. When vorticity slowly diffuses past the hyperbolic points H_1 and H_2, thin filaments are quickly peeled off along the outer separatrices. The filaments enter the ghost regions causing further straining of the flow field as shown in figure (6.17(b)). Meunier *et al.* (2002) argued that these filaments, which are essentially antisymmetric create a velocity field which causes the two vortices to approach each other. Due to the spread-out filamentary 'arms', to conserve angular momentum of the system (at large Re), the vortex cores rotate faster, as can be seen in a drastic change in rotation rate in figure (6.12(b)). Cerretelli & Williamson (2003*b*) interpreted this as fllows. They split the vorticity field into symmetric and antisymmetric parts and showed that the

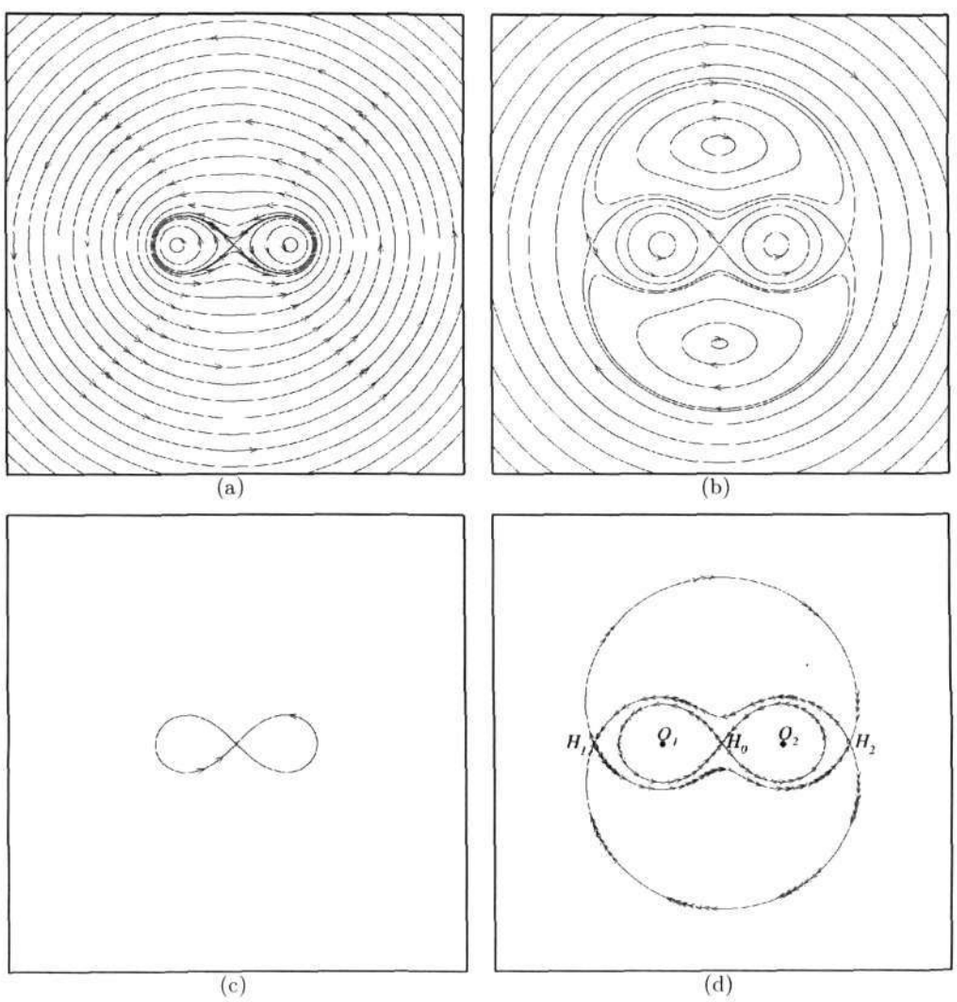

Figure 6.16: (a,b) Streamlines and (c,d) Separatrices in the fixed and rotating frame of reference. In (d) H_0, H_1 and H_2 are hyperbolic points and O_1 and O_2 are the centres. The separatrices divide the flow into various regions as discussed in the text.

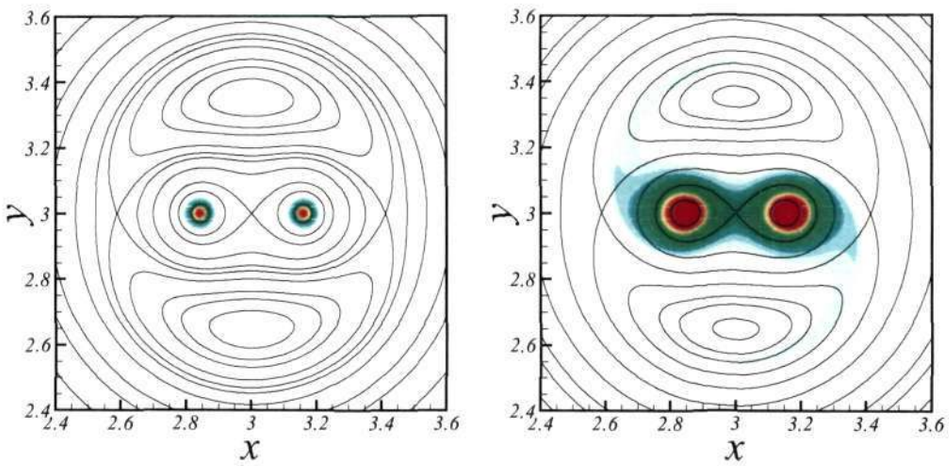

Figure 6.17: Vorticity contours along with corresponding streamlines in a rotating frame for $Re = 5000$ and $Fr = \infty$ at (a) $t^* = 0$ and (b) $t^* = 1.5$. Vorticity diffuses across the separatrices and peels off at the hyperbolic points H_1 and H_2 following the streamline.

antisymmetric part causes a disturbance field which makes the two vortices move into each other. The antisymmetric part was predominantly due to filaments. But the idea of describing merger in terms of filaments diverted the attention from the important point of asymmetry of the flow field. It was not clear at this stage whether filaments were the cause or the effect of vortex merger. In an important contribution, Fuentes (2005) showed that filamentation is the effect of merger, and convective merger begins before the onset of filamentation as discussed earlier. Brandt & Nomura (2006) calculated the induced velocity from various flow regions and showed that the exchange band region is responsible for the merger process, not the filaments. The vortices tilt creating an asymmetry in the flow field. At this stage, there are multiple explanations for the onset of merger. But, it is clear that during the convective merger stage, both filaments and the exchange band region contribute significantly to merger. Note that the former in fact owes its existence to the latter.

6.6 Stratified merger with Boussinesq approximation

We now study the effects of linear density stratification on the vortex merger problem, within the Boussinesq approximation. The vorticity equation has another source due to baroclinic torque and takes the form

$$\frac{\partial Z}{\partial t} + (\mathbf{u} \cdot \boldsymbol{\nabla} Z) = \nu \nabla^2 Z - \frac{g}{\rho_0} \frac{\partial \rho}{\partial x} \tag{6.39}$$

The last term in this equation is the additional vorticity generated due to to density

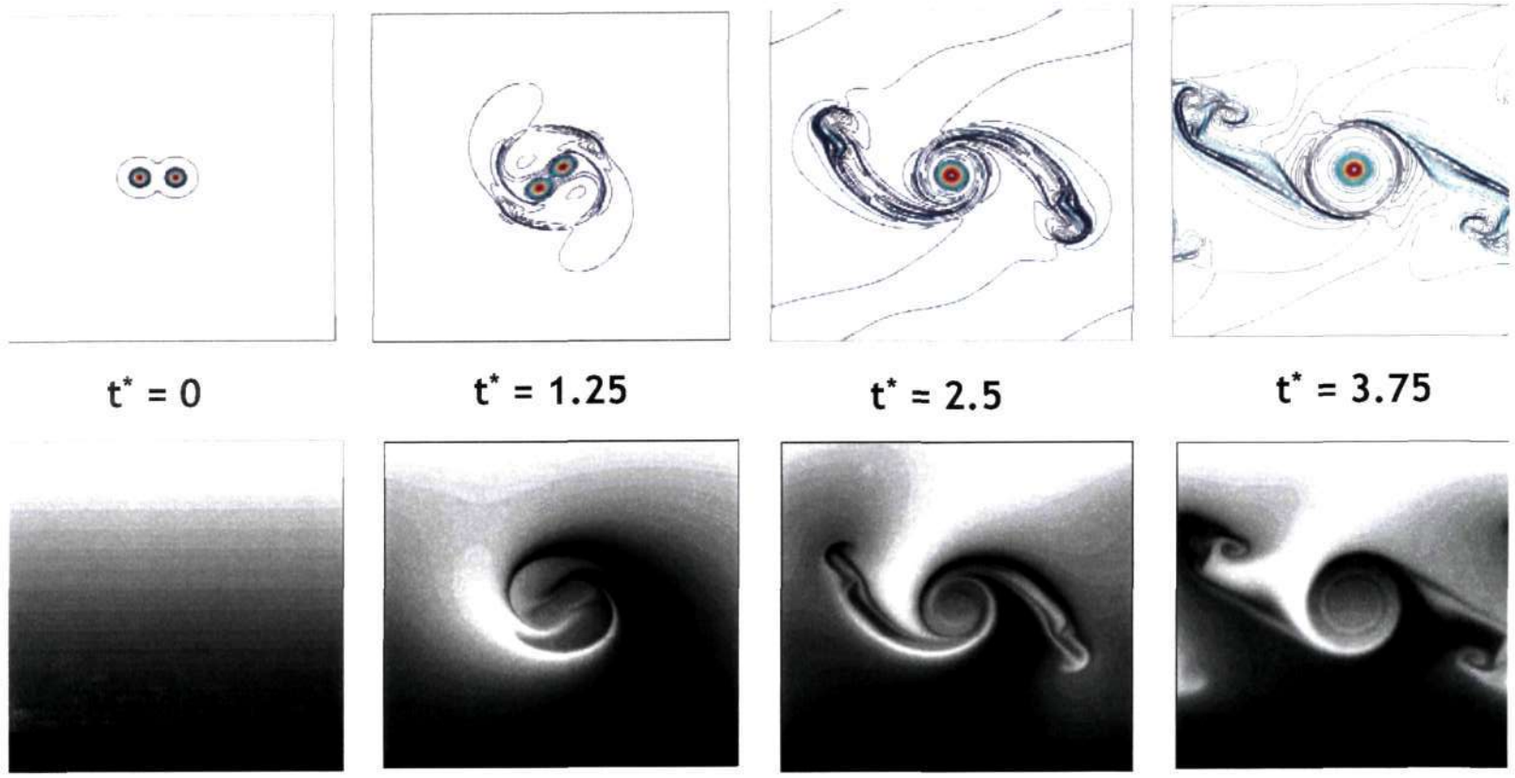

Figure 6.18: Time evolution of vorticity (colour) and density (gray scale) contours for merger in the presence of density stratification with $Re = 5000$, $Fr = 2$ and $Pr = 1$.

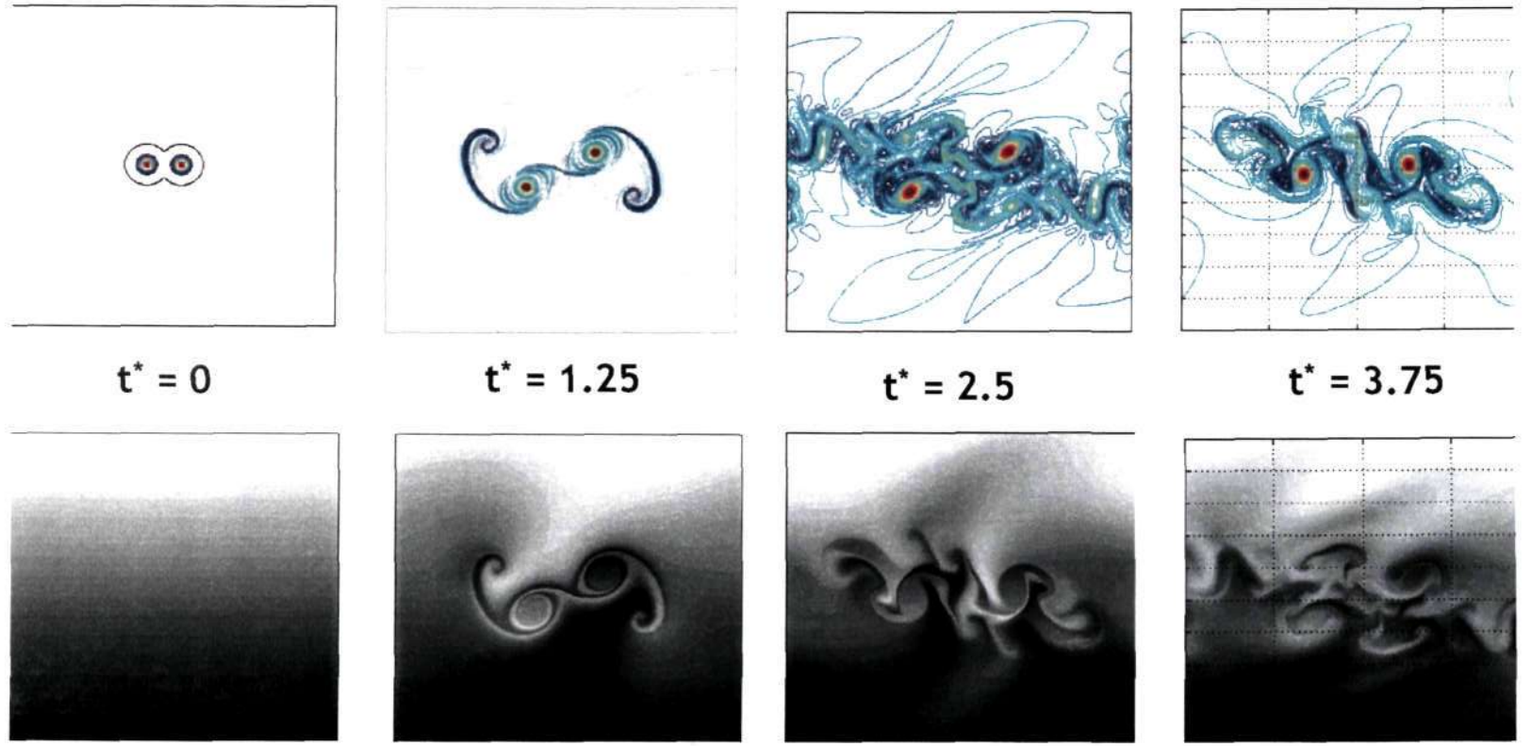

Figure 6.19: Time evolution of Vorticity (colour) and density (gray scale) contours for merger at higher levels of stratification than in figure (6.18) with $Re = 5000$, $Fr = 1$ and $Pr = 1$. Significant generation of small scales can be observed.

stratification. Note that horizontal gradients of density contribute to vorticity generation. As the two vortices rotate, they churn the entire density field around them such that horizontal density gradients are established. These in turn influences the evolution of the two vortices themselves. It can be easily imagined that both positive and negative vorticity will be created due to density effects. In a recent work, Brandt & Nomura (2007) treated exactly the same problem as the present one, but restricted their study to moderate stratification. At the Froude numbers they imposed, merger always occurred. For larger stratification, where baroclinic torque can dominate the flow field, it will be shown that merger can be completely prevented. Figures 6.18 and 6.19 show time evolution of vorticity (upper panel) and density (lower panel) fields. This can be contrasted with the unstratified case considered earlier (see figure 6.10). Additional filaments created due to baroclinic vorticity can be clearly seen in figure 6.18(b). The orientation and sign of this additional vorticity can either accelerate or decelerate the merger process. When stratification increases further to $Fr \approx 1$, in all our simulations with $Pr \approx 1$, merger was always completely prevented. But for very small Pr, things can be different, and therefore, the role of Pr is separately discussed. In addition, the two vortices gradually drifted away from each other. One such scenario with $Re = 5000$, $Fr = 1$ and $Pr = 1$ is shown in figure (6.19). Notice that baroclinically generated filaments are now much stronger than before, and are predominantly of negative sign. This additional vorticity not only causes the vortices to drift away from each other, but also causes breakdown of the flow into a turbulence-like state. A kinematic view of the flow field and the role of various time scales in the flow will be examined later in this section, and this will help us understand the reasons behind merger/non-merger.

6.6.1 Effect of Froude number

To understand the role of Froude number on the flow, we have carried out a parametric study for various Fr at different Re and a fixed $Pr = 1$. The effect of Prandtl number is considered separately in the next section. The variation of separation distance with time for three different Fr is shown in figure (6.20). For moderate stratifications (figure 6.20(a) and 6.20(b)), merger was always found to occur for all Re considered in this study. Notice that the separation distance does not decrease monotonically with time like in the unstratified case. This non-monotonicity is due to the effect of baroclinic torque on the two vortices, and depends on the exact orientation of baroclinic vorticity generated in the flow.

A series of numerical simulations were carried out for many different Fr for a fixed $Re = 1000$ and $Pr = 1$. The separation distance with time for this case is shown in figure (6.21(a)). At this Reynolds number, as Fr decreases, it takes longer to complete the merger process. For comparison, the $Re = 5000$ case with different Fr is also shown in figure (6.21(b)). In this case, at low stratification levels, the merger process is accelerated with increasing stratification, an effect opposite to the $Re = 1000$ case. This is in broad agreement with Brandt & Nomura (2007). But in both the cases, for $Fr \approx 1$, merger is completely prevented. Therefore, a cross-over exists in the $Re - Fr$ plane as can be seen figure (6.22).

We will briefly discuss the energetics of the system. As the vortices rotate, the density

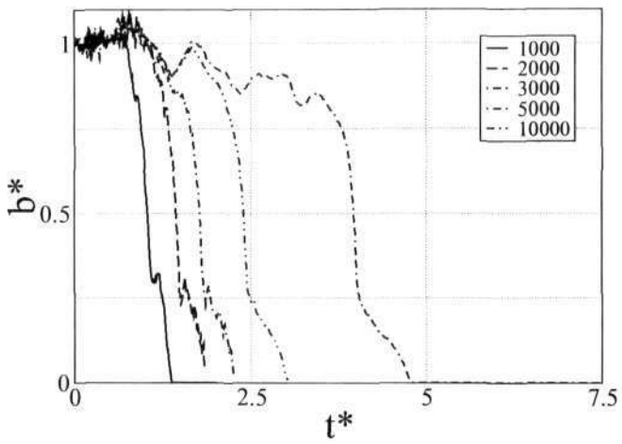

(a)

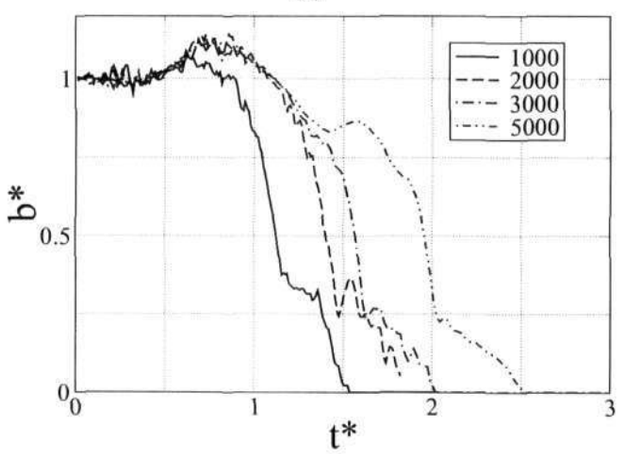

(b)

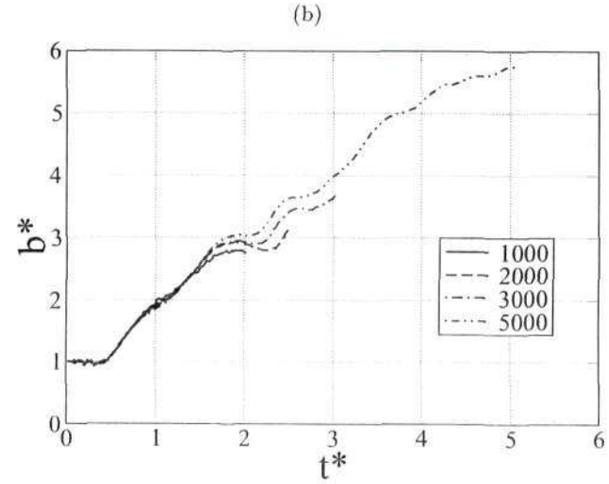

(c)

Figure 6.20: Effect of Froude number on the separation distance for a fixed $Pr = 1$ and various Re as shown in the legend boxes, (a) $Fr = 3$, (b) $Fr = 2$, (c) $Fr = 1$. The horizontal scale for the figures are different.

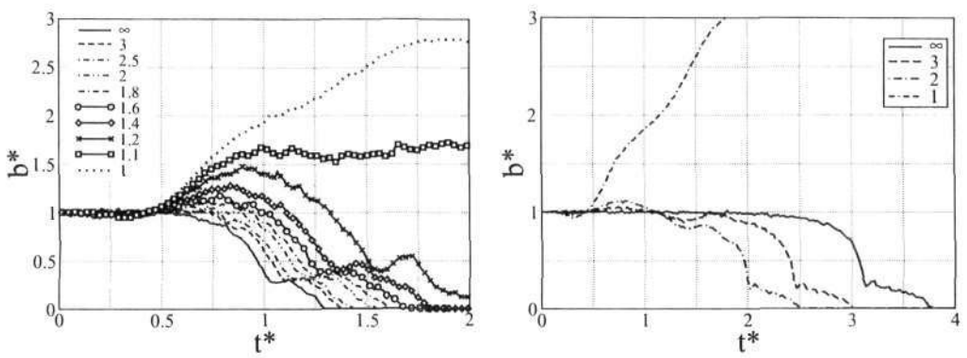

Figure 6.21: Effect of Froude number shown in the legend on the separation distance for a fixed $Pr = 1$ with (a) $Re = 1000$ and (b) $Re = 5000$. In both (a) and (b), merger is completely prevented for $Fr = 1$,

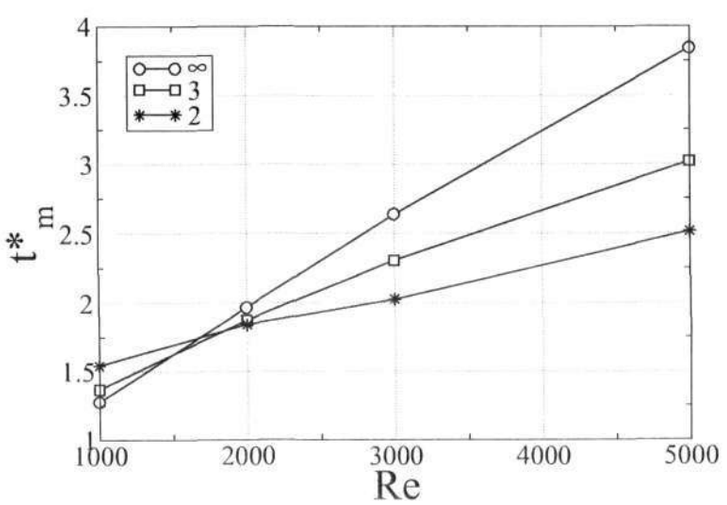

Figure 6.22: Variation of merging time as a function of Re for three different Fr. A cross-over occurs between $Re = 1000 - 2000$.

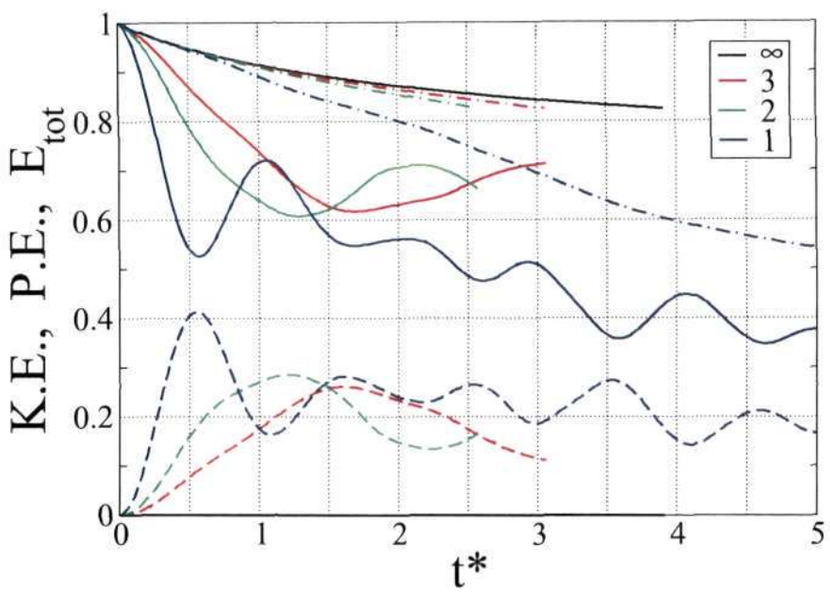

Figure 6.23: Evolution of kinetic ($K.E.$ - solid), potential ($P.E.$ - dashed) and total (E_{tot} - dash-dot lines) for $Re = 5000$ and $Pr = 1$ for four different Froude numbers indicated with different colours. The kinetic and potential energies are always in anti-phase with each other.

field is rotated creating a large scale overturning. Thus rotation of the vortices creates disturbances in the density field, and small perturbations would oscillate with the Brunt-Vaisala frequency. The ratio of timescales of rotation of vortices to the time scale of density oscillations is given by the inverse of Froude number. By time scale of density oscillations, we mean the time it takes for a small parcel of fluid slightly heavier than its surroundings to rise upwards and the sink downwards again. This would hold for a lighter fluid too. For example, with $Fr = 3$, the vortices would have completed approximately three complete rotations for one complete oscillation of the density field. During the first half of density oscillation, the heavier fluid rises upwards and lighter fluid sinks downwards. This causes an increase in potential energy (P.E.) at the expense of kinetic energy (K.E.) of the vortices. During the second half of oscillation, the heavier fluid sinks downwards and lighter fluid rises back upwards. This causes the potential energy to decrease. Now the kinetic energy increases at the expense of potential energy. In addition, viscosity causes a net dissipation of kinetic energy of the system. Indeed, this is seen to happen in our simulations as shown in figure (6.23), though small differences exist in the timescales observed. The kinetic and potential energies are in anti-phase with each other. Owing to viscous diffusion, the total energy decreases in all the cases, but a much larger dissipation is observed with $Fr = 1$. This is due to a significant generation of small scales in the flow, as shown in figure (6.19), which makes viscous diffusion more effective, whereas for higher Fr, the final state is a single large vortex, with fewer small scales, in the form of weak filaments in the flow.

6.6.2 Effect of Prandtl number

In the previous sub-section, the Prandtl number was fixed at unity. The Prandtl number is a measure of the rate at which density field diffuses in relation to diffusion of momentum. Small Pr denotes fast diffusion of density field. Therefore, for a low Pr fluid, any density inhomogeneities are rapidly erased, thus removing the source of baroclinic torque. Figure (6.24) shows the effect of Pr for three different stratifications. With $Pr = 1$, it was shown that merger gets progressively delayed for $Re = 1000$ as stratification is increased. Therefore as Pr is decreased, due to the reduction of baroclinic effects, we would expect this delay to be minimized. In the limit of $Pr \to 0$, where the density field is instantaneously homogenized, no baroclinic torque would be generated, and the merger process would be similar to that in a constant density fluid. In figure (6.24), it can be seen that merger time decreases with increasing stratification, eventually approaching the $Fr = \infty$ limit for very small Pr. In this small Pr limit, merger was always found to occur, even for very large stratification's, i.e. $Fr = 1$ as can be seen in figure (6.24(c)).

6.7 Merger in a non-Boussinesq system

The Boussinesq approximation employed in the previous section and in the earlier work of Brandt & Nomura (2007) preserves basic symmetries in the system, as discussed in section 6.3 and showed quantitatively in section 6.6. In this section, we consider the effect of non-Boussinesq terms on the merger process. By the adjective non-Boussinesq, we only refer here to inertial effects of density stratification, and all transport coefficients are held constant for simplicity. Two cases are separately studied: one, where purely inertial effects of density variation are considered with gravity being absent, and two, where combined inertial-gravity effects are present in the system. This will help us compare and contrast Boussinesq and non-Boussinesq effects on the merger process. To do this, we choose a fixed mean density profile and adjust gravity such that a desired Froude number is attained. In figure (6.25), we compare variation of separation distance with time for unstratified flow, a Boussinesq fluid with $Fr = 3$, a non-Boussinesq fluid with $Fr = 3$ and a purely inertial case where baroclinic vorticity is generated from inertial effects of density stratification and gravity is set to zero. Clearly, purely inertial effects do not affect the separation distance when compared with an unstratified case.

To observe symmetry breaking due to inertial effects, we consider a higher Reynolds number, viz., $Re = 10000$. At this Re, the two vortices complete approximation 5 rotations before convective merger begins. This provides ample time for baroclinic torque to act on the vortices and symmetry breaking to become noticeable. In figure (6.26), the trajectory of a single vortex is plotted as a function of time. For clarity, the curves are shifted in the vertical scale. It can be seen that for a system governing by purely inertial effects of density stratification, the centroid of vorticity is no longer an invariant. The vortices are shown to drift leftwards in this case. The exact direction and rate of drift depends both on Re and the density stratification employed. The same result can be obtained by monitoring the x-coordinate of the two vortices as shown in figure (6.27). These results show that for large density stratifications, where inertial effects of density field become important, symmetry breaking can lead to large scale meandering

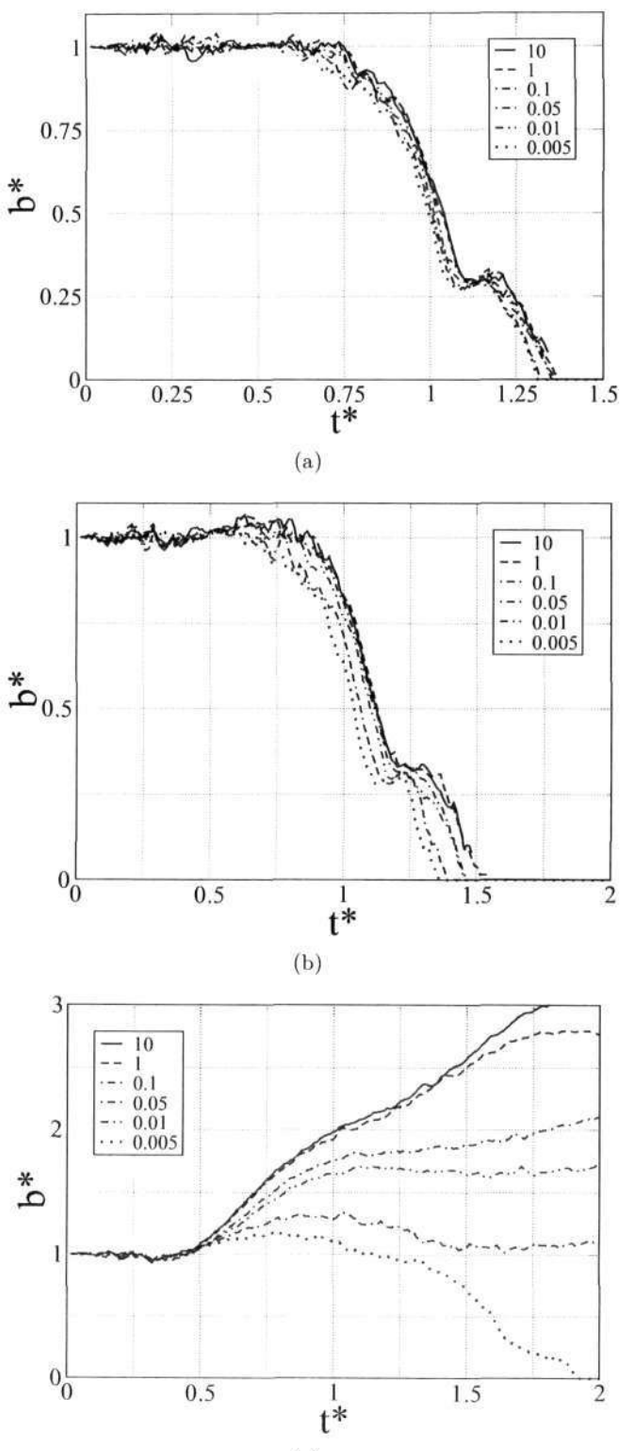

Figure 6.24: Effect of Prandtl number on the separation distance for a fixed $Re = 1000$ and different Froude numbers, (a) $Fr = 3$, (b) $Fr = 2$ and (c) $Fr = 1$.

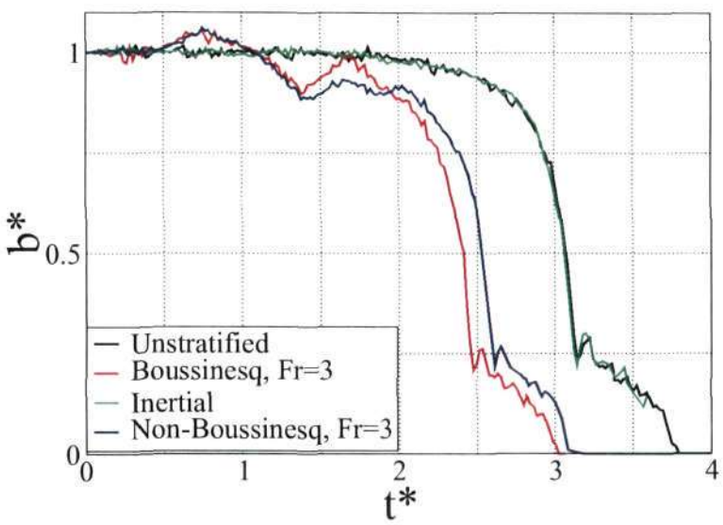

Figure 6.25: Variation of separation distance with time for $Re = 5000$ with a mean density gradient of $(b_0/\rho_0)(d\bar{\rho}/dy) = 0.095$. For a purely Boussinesq fluid, gravity is chosen to give $Fr = 3$. In a purely inertial case, gravity is neglected and baroclinic torque is generated only from non-linear terms in the governing equation.

of vortices.

6.7.1 Merger mechanism in a stratified fluid

We briefly examine some aspects of the physical mechanism in a stratified vortex merger. We first discuss merger in a Boussinesq fluid. Figure (6.20) showed that upto $t^* \approx 0.5$, the variation of b^* in a stratified fluid is similar to that in an unstratified case. Figure (6.28) shows the vorticity and density field at $t^* = 0.5$ for various Fr. For comparison, an unstratified case is also presented. Clearly, the vorticity and density fields are similar in structure in all the cases, but the magnitudes significantly vary. For example, the maximum baroclinic vorticity in figures (6.28(b)), (6.28(c)) and (6.28(d)) for $Fr = 3,\ 2,\ 1$ are approximately 0.013, 0.022 and 0.11 respectively. In the Boussinesq approximation, vorticity generation is proportional to g, i.e., $1/Fr^2$ all the other parameters being kept the same. In fact, the observed maximum vorticity values indeed closely follow this scaling. At this time ($t^* \approx 0.5$), the orientation of this baroclinic vorticity is such that the vortices are pushed away from each other as shown schematically in figure (6.29). This only explains the initial separation of the vortices as can be seen for $t^* > 0.5$. In the case of $Fr = 1$, due to the much larger baroclinic vorticity, the vortices are strongly repelled from each other preventing merger. But for $Fr = 3,\ 2$, the vortices approach each other for $t^* > 1$. In this case, the orientation of the baroclinic vorticity is such that a net inward velocity is induced on the two primary vortices, but it is difficult to precisely show this as both the positve and negative baroclinic vortices stronly overlap with each other. Hence a simple kinematic mechanism becomes increasingly difficult.

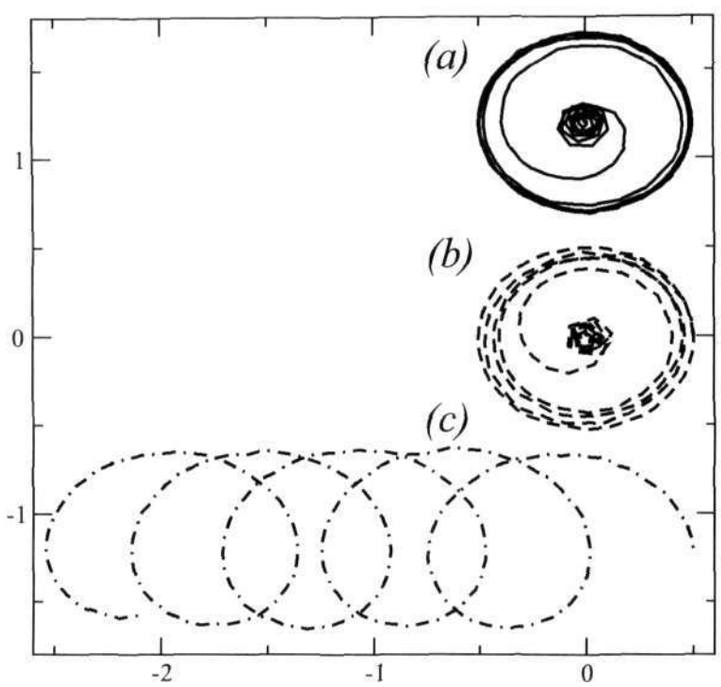

Figure 6.26: Trajectory of a single vortex for (a) Unstratified fluid, (b) Boussinesq fluid, (c) non-Boussinesq fluid.

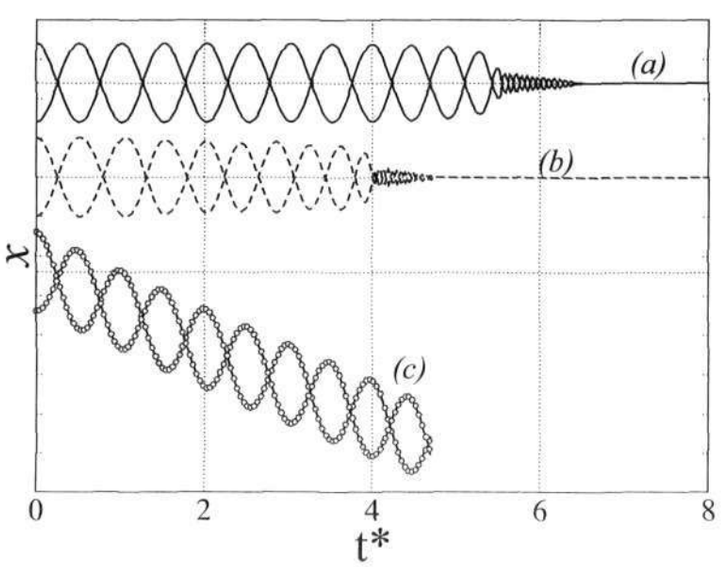

Figure 6.27: Same as figure (6.26), but showing the x-coordinate of both the vortices as a function of time. (a) Unstratified fluid, (b) Boussinesq fluid, (c) non-Boussinesq fluid.

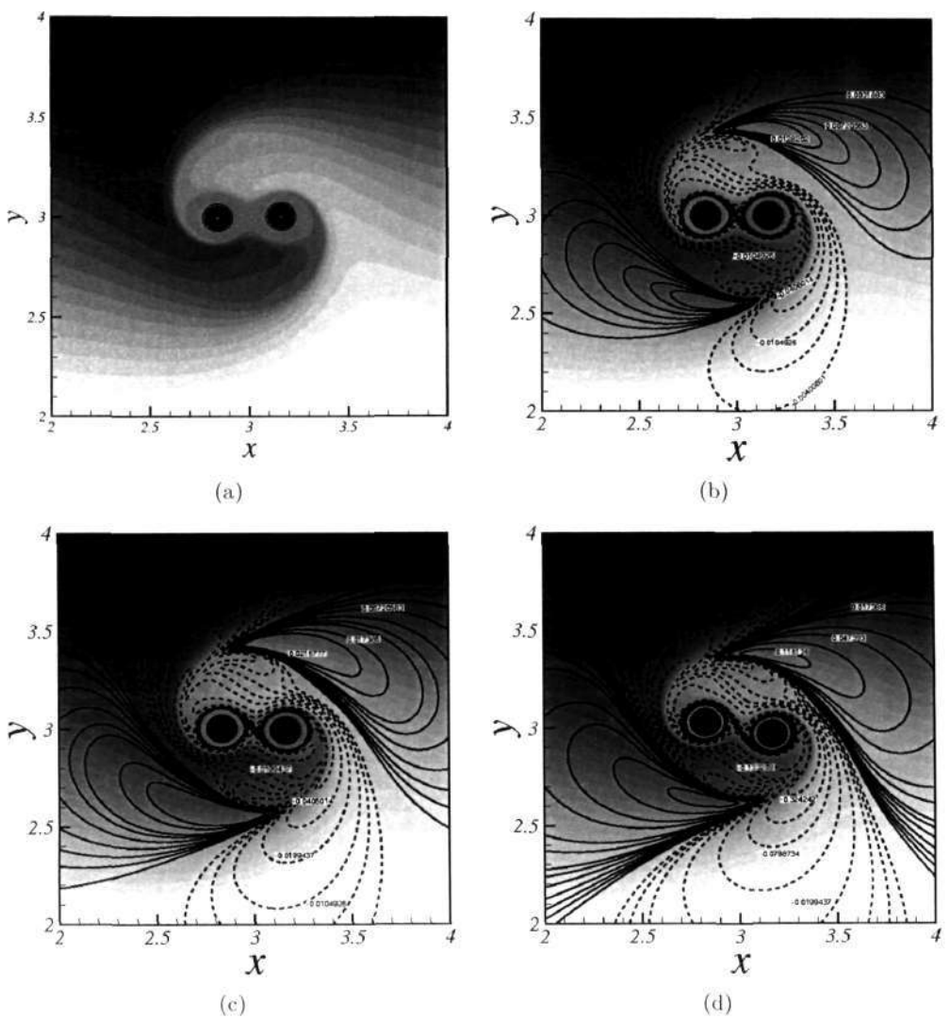

Figure 6.28: Vorticity (lines) and density (gray scale) contours for $Re = 5000$, $Pr = 1$ at various Fr: (a) $Fr = \infty$, (b) $Fr = 3$, (c) $Fr = 2$, (d) $Fr = 1$. Solid and negative lines represent positive and negative vorticity levels. Note that in (a), the density field is a passive scalar.

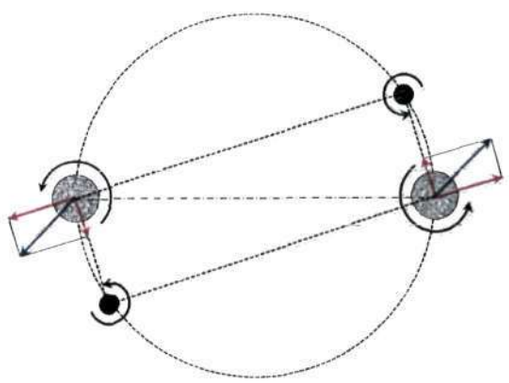

Figure 6.29: A schematic of the dominant vorticity based on figure (6.28). The two primary vortices are shown in grey circles and the baroclinic vorticity is shown by black circles. The red arrows show the induced velocity field due to baroclinic vorticity on the two vortices, and the result velocity field is shown in blue arrows. Note that the net velocity at the vorticity centroid is identically zero from symmetry.

We can construct a simple model with two Gaussian vortices and a single flat density interface placed along the line joining the two vortices. This interface can be viewed as an approximation of one single isopycnal in a linearly stratified flow or a sharp density interface. We first move into a rotating frame of reference where the vortices are stationary, and advect this interface passively. But, knowing that density jump discontinuously, we can calculate $\partial\rho/\partial x$. In this case, it will be a δ-function at the interface. We assume that the new vorticity is initially too weak to alter the motion of the primary vortices themselves. We are primarily interested in knowing the sign and orientation of the vorticity produced, not so much in its magnitude. In any case, it would not be possible in this model to predict the vorticity produced quantitatively. To calculate the net baroclinic vorticity generated, we move into a Lagrangian frame of reference, where each particle on the interface is advected by the equations

$$\frac{dx}{dt} = u_{rot}, \tag{6.40a}$$

$$\frac{dy}{dt} = v_{rot} \tag{6.40b}$$

where u_{rot} and v_{rot} are the x and y component of the velocity field in a rotating frame of reference. For a Gaussian vortex system, this can be written as

$$u_{rot} = -\frac{\Xi y}{2\pi l_1}\left(1-\exp\left[\frac{-l_1}{\delta^2}\right]\right) - \frac{\Xi y}{2\pi l_2}\left(1-\exp\left[\frac{-l_2}{\delta^2}\right]\right) + \frac{\Xi y}{\pi b_0^2}, \tag{6.41a}$$

$$v_{rot} = \frac{\Xi(x-b_0/2)}{2\pi l_1}\left(1-\exp\left[\frac{-l_1}{\delta^2}\right]\right) + \frac{\Xi(x+b_0/2)}{2\pi l_2}\left(1-\exp\left[\frac{-l_2}{\delta^2}\right]\right) + \frac{\Xi x}{\pi b_0^2} \tag{6.41b}$$

where $l_1 = \left((x-b_0/2)^2+y^2\right)$ and $l_2 = \left((x+b_0/2)^2+y^2\right)$. Initial baroclinic vorticity

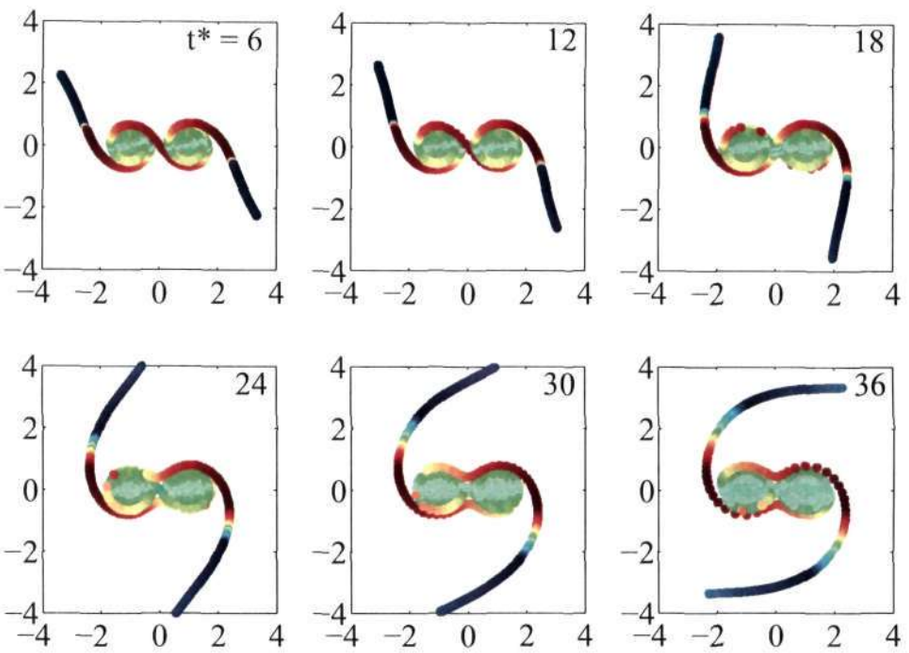

Figure 6.30: Evolution of a passive interface due to a co-rotating Gaussian vortex pair viewed in a rotating frame of reference. The color coding represent the strength of baroclinic vorticity than can be produced at this interface, where red denotes positive values and blue denoted negative values.

along the interface is taken to be zero. The non-dimensional vorticity equation for each particle on the interface takes the form

$$\frac{d\zeta}{dt} = -\cos\left(\frac{\pi}{2} - \theta\right) \tag{6.42}$$

where ζ is the baroclinic vorticity generated as each particle on the interface is advected by the background flow and θ is the angle made by the interface with the horizontal. This equation is obtained by knowing that the interface is a material contour across which density changes discontinuously, and therefore, $\partial\rho/\partial x$ can be related to the interface orientation. Since we are interested in the sign of the vorticity, the prefactor in the above equation is taken to be unity. Therefore, the generated vorticity, ζ can be taken to be suitably normalized. The angle θ can be calculated from the slope made by the interface with the horizontal, i.e.,

$$\theta = \tan^{-1}\left(\frac{dy}{dx}\right) = \tan^{-1}\left(\frac{v_{rot}}{u_{rot}}\right) \tag{6.43}$$

The position of the interface at various times is shown in figure (6.30). The color coding shows the sign and strength of the baroclinic vorticity generated, where blue indicates regions of negative vorticity and red, regions of positive vorticity. The symmetry

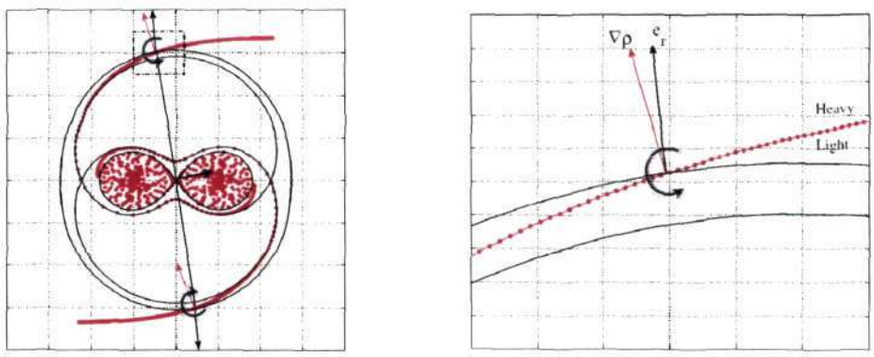

Figure 6.31: (a) Position of a passive interface (red circles) and the streamlines for a Gaussian co-rotating vortex pair at $t^* = 36$. The red arrow is normal to the interface, and the black arrow shows the direction of centrifugal acceleration. (b) Close-up of (a) indicated by a dash-dot rectangle. $\nabla\rho$ and e_r are the density gradient vector and normal vector to the streamline respectively at the point of intersection of the interface with the streamline.

of the Boussinesq approximation is clearly seen in this figure. Each point on this interface can be treated like a point vortex, and the induced velocity from these point vortices at the centroid of the system is identically zero, due to cancellations from either side of the interface.

We repeat the same analysis with only inertial effect of stratification, neglecting gravity. The interface position and the streamlines at some arbitrary time is shown in figure (6.31). An obvious and striking difference in this case is the reversal of the acceleration vector shown with a black arrow. This is absent in the Boussinesq case where the direction of gravity is fixed. The induced velocity at the upper and lower interfaces, proportional to $\nabla\rho \times \dfrac{D\mathbf{u}}{Dt}$ can be approximated as $\nabla\rho \times \dfrac{U^2}{r}\hat{e}_r$ where U is the total velocity. It is possible to avoid this approximation, but has not been done here for simplicity. Since the vorticity on either side of the interface is of opposite sign, as shown by blue circles, a net vorticity is created at the centroid of the system. The direction of this induced velocity at the centroid of the system is shown by a blue arrow. The above analysis is carried out in a rotating frame of reference. As the interface continues to wind, greater amount of baroclinic vorticity gets generated at the density interface such that a net drift arises in the system. To predict quantitatively, the direction and magnitude of the drift, more careful modelling is required.

The above models are constructed capturing only the essential physics in the problem. Though highly simplistic in nature, they explain the basic effect of density stratification in the merging process.

6.8 Summary

The present chapter is part of an ongoing work to understand the effect of density stratification on the vortex merging process. The first part of the study dealt with vortex merger in a homogeneous flow, and this served as a validation exercize, and also to compare the differences upon introduction of stratification. In stratified merger, both Boussinesq and non-Boussinesq situations were considered. It is shown that certain symmetries are allowed in a Boussinesq fluid. More importantly, a key finding of this work is that at high stratifications, baroclinic vorticity generated at the density interface can be sufficient to prevent the merger process. A detailed parametric study concerning effects of Froude and Prandtl numbers has been carried out. We then dealt with inertial effects of stratification, the non-Boussinesq effects on the merger process. Since the symmetries allowed by a Boussinesq system need no longer be obeyed, a drift of the entire system was observed. A simple kinematic model is constructed to explain the observed feature in stratified merger, especially, the process of drift in a non-Boussinesq system.

CHAPTER 7

CONCLUSIONS

In this thesis, a study on the effect of density stratification on the structure and stability of vortices was carried out. Conclusions for each chapter has already been made, but me summarize here the main findings of this thesis.

In chapter 2, the wave interaction mechanism has been examined closely to show how stable density stratification can sometimes destabilize a flow in the presence of shear. We construct a simple flow with a single vorticity jump and a single density jump separated from each other. Though these two interfaces support neutral waves themselves when considered in isolation, their interaction can give rise to an instability. This result was then extended to a Rankine vortex geometry with a circular density jump in chapter 3, where the interaction is between Kelvin waves of a Rankine vortex and internal waves from the density jump. For smooth profiles which do not possess discrete Kelvin modes, the wave-interaction mechanism can be attributed to the presence of quasi-modes. For the first time, we show that a light-cored vortex can be unstable, and the physical mechanism causing this instability is explained. Quasi-mode properties of a wide range of vortex profiles with varying steepness are studied and we recover the Rankine Kelvin mode for steep vortex profiles. Direct numerical simulations reveal the presence of stable non-linear non-axisymmetric vortex structures.

In chapter 5, we show the importance of retaining non-Boussinesq effects, i.e., inertial effects of density when dealing with flows with sharp density interfaces. The Atwood number can be small, but the gradient of density can be large generating significant baroclinic torque. A key finding of this chapter is the presence of a new spiral Kelvin-Helmholtz instability at a density interface caused solely by inertial effects of stratification, and also the classical Rayleigh-Taylor instability, similar to the one studied in chapter 3. Using direct numerical simulations, we show that these instabilities can degrade the flow generating turbulence and small scale structures in the flow.

The last chapter deals with vortex merger in a stratified medium. This is part of an ongoing work, and some sample results are presented in this chapter. The main finding of this chapter is that for large stratifications, vortex merger is completely prevented. At large Reynolds number, with increasing stratification, vortex merger is accelerated, up to a threshold value, beyond which, stratification prevents merger. A more detailed analysis is beyond the scope of this thesis.

A Derivation of Rankine vortex dispersion relation

In the three regions for a Rankine vortex with a density jump given by equation (3.20), the general solutions of equation (3.15) take the form, r^{m-1} and r^{-m-1}. The complete solution can be written as

$$u_r = \begin{cases} A_1 r^{m-1}, & \text{if } r < a, \\ A_2 r^{m-1} + A_3 r^{-m-1}, & \text{if } a < r < r_j, \\ r^{-m-1}, & \text{if } r > r_j. \end{cases} \tag{A-1}$$

The constants A_1, A_2 and A_3 can be found by matching radial velocity at $r = a$ and $r = r_j$ and pressure across $r = a$, and this gives

$$A_1 = \frac{(\omega - m\Omega_0)a^{-2m}}{\left[\left(\frac{r_j}{a}\right)^{2m}(\omega - (m-1)\Omega_0) - \Omega_0\right]}, \tag{A-2}$$

$$A_2 = \frac{(\omega - (m-1)\Omega_0)a^{-2m}}{\left[\left(\frac{r_j}{a}\right)^{2m}(\omega - (m-1)\Omega_0) - \Omega_0\right]}, \tag{A-3}$$

$$A_3 = \frac{-\Omega_0}{\left[\left(\frac{r_j}{a}\right)^{2m}(\omega - (m-1)\Omega_0) - \Omega_0\right]}. \tag{A-4}$$

Finally, matching pressure across the density jump gives us equation 3.21, a cubic dispersion relation in the eigenvalue ω. From the continuity equation, the azimuthal velocity perturbation can be written as

$$u_\theta = \frac{ir}{m}\mathcal{D}^* u_r. \tag{A-5}$$

The form of u_r on either side of the two interfaces shows that there exists a jump in u_θ at $r = a$ and $r = r_j$, i.e., there is a vortex sheet at each of the two interfaces. The vortex sheet strength is given by

$$\Delta u_\theta|_{r=a} = \frac{2i\Omega_0 a^{-m-1}}{\left[\left(\frac{r_j}{a}\right)^{2m}(\omega - (m-1)\Omega_0) - \Omega_0\right]}, \tag{A-6}$$

$$\Delta u_\theta|_{r=r_j} = -2ir_j^{-m-1}\frac{\left[\left(\frac{r_j}{a}\right)^{2m}(\omega - (m-1)\Omega_0)\right]}{\left[\left(\frac{r_j}{a}\right)^{2m}(\omega - (m-1)\Omega_0) - \Omega_0\right]}. \tag{A-7}$$

References

ABRAMOWITZ, M. & STEGUN, I. A. 1965 *Handbook of Mathematical Functions*. Dover Publications.

ACHESON, D. J. 1976 On over-reflection. *J. Fluid Mech.* **44**, 433–472.

ANDERSON, J. D. 2001 *Fundamentals of Aerodynamics*. McGraw-Hill.

ASH, R. L. & KHORRAMI, M. R. 1995 Vortex stability. In *Fluid Vortices* (ed. S. I. Green), pp. 317–372. Kluwer.

BAINES, P. G. & MITSUDERA, H. 1994 On the mechanism of shear flow instabilities. *J. Fluid Mech.* **276**, 327–342.

BAJER, K., BASSOM, A. P. & GILBERT, A. D. 2001 Accelerated diffusion in the centre of a vortex. *J. Fluid Mech.* **437**, 395–411.

BAJER, K., BASSOM, A. P. & GILBERT, A. D. 2004 Vortex motion in a weak background shear flow. *J. Fluid Mech.* **509**, 281–304.

BASSOM, A. P. & GILBERT, A. D. 1998 The spiral wind-up of vorticity in an inviscid planar vortex. *J. Fluid Mech.* **371**, 109–140.

BATCHELOR, G. K. 1980 *An Introduction to Fluid Dynamics*. Cambridge University Press.

BAYLY, B. J. 1986 Three-dimensional instability of elliptical flow. *Phys. Rev. Lett.* **57**, 2160–2163.

BENJAMIN, T. B. 1963 Classification of unstable disturbances in flexible surfaces bounding inviscid flows. *J. Fluid Mech.* **16**, 436–450.

BILLANT, P. & CHOMAZ, J.-M. 2000 Experimental evidence for a new instability of a vertical columnar vortex pair in a strongly stratified fluid. *J. Fluid Mech.* **418**, 167–188.

BILLANT, P. & LE DIZÉS, S. 2009 Waves on a columnar vortex in a strongly stratified fluid. *Phys. Fluids* **21**, 106602.

BOOKER, J. R. & BRETHERTON, F. P. 1967 The critical layer for internal gravity waves in a shear flow. *J. Fluid Mech.* **27**, 513–539.

BRANDT, L. K. & NOMURA, K. K. 2006 The physics of vortex merger: Further insight. *Phys. Fluids* **18**, 051701.

BRANDT, L. K. & NOMURA, K. K. 2007 The physics of vortex merger and the effects of ambient stable stratification. *J. Fluid Mech.* **592**, 413–446.

BRIGGS, R. J., DAUGHERTY, J. D. & LEVY, R. H. 1970 Role of landau damping in crossed-field electron beams and inviscid shear flow. *Phys. Fluids* **13** (2), 421–432.

CAIRNS, R. A. 1979 The role of negative energy waves in some instabilities of parallel flows. *J. Fluid Mech.* **92**, 1-14.

CANUTO, C., HUSSAINI, M. Y., QUARTERONI, A. & ZANG, T. A. 1988 *Spectral Methods in Fluid Dynamics*. Springer.

CARNEVALE, G. F., MCWILLIAMS, J. C., POMEAU, Y., WEISS, J. B. & YOUNG, W. R. 1991 Evolution of vortex statistics in two-dimensional turbulence. *Phys. Rev. Lett.* **66**, 2735–2737.

CARPENTER, J. R., TEDFORD, E. W., RAHMANI, M. & LAWRENCE, G. A. 2010 Holmboe wave fields in simulation and experiment. *J. Fluid Mech.* **648**, 205-223.

CARTON, X. J., FLIERL, G. R. & POLVANI, L. M. 1989 The generation of tripoles from unstable axisymmetric isolated vortex structures. *Europhys. Lett.* **9**, 339–344.

CASE, K. M. 1960 Stability of an inviscid plane Couette flow. *Phys. Fluids* **3**, 143–148.

CERRETELLI, C. & WILLIAMSON, C. H. K. 2003*a* A new family of uniform vortices related to vortex configurations before merging. *J. Fluid Mech.* **493**, 219–229.

CERRETELLI, C. & WILLIAMSON, C. H. K. 2003*b* The physical mechanism for vortex merging. *J. Fluid Mech.* **475**, 41–77.

CHAN, J. C. L. 2005 The physics of tropical cyclone motion. *Ann. Rev. Fluid Mech.* **37**, 99–128.

CHANDRASEKHAR, S. 1961 *Hydrodynamic and hydromagnetic stability*. Oxford: Clarendon Press.

COHEN, I. M. & KUNDU, P. K. 2004 *Fluid Mechanics*. Academic Press.

COQUART, L., SIPP, D. & JACQUIN, L. 2005 Mixing induced by Rayleigh-Taylor instability in a vortex. *Phys. Fluid* **17**, 021703–.

CRAIK, A. D. D. 1985 *Wave interactions and fluid flow*. Cambridge University Press.

CROW, S. C. 1970 Stability theory for a pair of trailing vortices. *AIAA J.* **8**, 2172–2179.

CROW, S. C. 1974 Motion of a vortex pair in a stably stratified fluid. *Tech. Rep.* 1. Poseidon Research Rep., Santa Monica, CA.

DAHM, W. J. A., SCHEIL, C. M. & TRYGGVASON, G. 1989 Dynamics of vortex interaction with a density interface. *J. Fluid Mech.* **205**, 1–43.

DEEM, G. S. & ZABUSKY, N. J. 1978 Vortex waves: Stationary "v states", interactions, recurrence and breaking. *Phys. Rev. Lett.* **40**, 859–862.

DIXIT, H. N. & GOVINDARAJAN, R. 2010 Vortex-induced instabilities and accelerated collapse due to inertial effects of density stratification. *J. Fluid Mech.* **646**, 415–439.

DRAZIN, P. G. & REID, W. H. 1981 *Hydrodynamic Stability*. Cambridge University Press.

DRITSCHEL, D. G. 1985 The stability and energetics of corotating uniform vortices. *J. Fluid Mech.* **157**, 95–134.

DUFF, R. E., HARLOW, F. H. & HIRT, C. W. 1962 Effects of diffusion on interface instability between gases. *Phys. Fluid* **5**, 417–425.

FABRE, D., SIPP, D. & JACQUIN, L. 2006 Kelvin waves and the singular modes of the Lamb–Oseen vortex. *J. Fluid Mech.* **551**, 235–274.

FABRIKANT, A. L. & STEPANYANTS, Y. A. 1998 *Propagation of waves in shear flows*. World Scientific series on Nonlinear Science.

FLOHR, P. & VASSILICOS, J. C. 1997 Accelerated scalar dissipation in a vortex. *J. Fluid Mech.* **348**, 295–317.

FONTANE, J. & JOLY, L. 2008 The stability of the variable-density Kelvin-Helmholtz billow. *J. Fluid Mech.* **612**, 237–260.

FREYMUTH, P. 1966 On transition in a separated laminar boundary layer. *J. Fluid Mech.* **25**, 683–704.

FUENTES, O. V. 2005 Vortex lamentation: its onset and its role on axisymmetrization and merger. *Dyn. Atmos. Oceans* **40**, 23–42.

FUKUMOTO, Y. 2003 The three-dimensional instability of a strained vortex tube revisited. *J. Fluid Mech.* **493**, 287–318.

FUNG, Y. T. 1983 Non-axisymmetric instability of a rotating layer of fluid. *J. Fluid Mech.* **127**, 83–90.

FUNG, Y. T. & KURZWEG, U. H. 1975 Stability of swirling flows with radius-dependent density. *J. Fluid Mech.* **72**, 243–255.

GANS, R. F. 1975 On the stability of a shear flow in a rotating gas. *J. Fluid Mech.* **68**, 403–412.

GILBERT, A. D. 1988 Spiral structures and spectra in two-dimensional turbulence. *J. Fluid Mech.* **193**, 475–497.

GILL, A. E. 1982 *Atmosphere-ocean dynamics*. Academic Press.

GOLDSTEIN, S. 1931 On the stability of superposed streams of fluid of different densities. *Proc. R. Soc. Lond. A.* **132**, 524–548.

GOVINDARAJAN, R. 2004 Effect of miscibility on the linear stability of a two-fluid channel. *Intl. J. Multiphase Flow* **30**, 1177–1192.

GREENSPAN, H. P. 1968 *The theory of rotating fluids*. Cambridge University Press.

GRIFFITHS, R. W. & HOPFINGER, E. J. 1987 Coalescing of geostrophic vortices. *J. Fluid Mech.* **178**, 73–97.

HALL, I. M., BASSOM, A. P. & GILBERT, A. D. 2003 The effect of ne structure on the stability of planar vortices. *Eur. J. Mech. B Fluids* **22**, 179–198.

HARNIK, N., HEIFETZ, E., UMURHAN, O. M. & LOTT, F. 2008 A buoyancy-vorticity wave interaction approach to stratified shear flow. *J. Atm. Sci.* **65**, 2615–2630.

HAURWITZ, B. 1931 Zur Theorie der Wellenbewegungen in Luft und Wasser. *Veroff. Geophys. Inst. Univ. Leipzig* **6**.

VAN HEIJST, G. J. F. & KLOOSTERZIEL, R. C. 1989 Tripolar vortices in a rotating fluid. *Nature* **338**, 569–571.

VAN HEIJST, G. J. F., KLOOSTERZIEL, R. C. & WILLIAMS, C. W. M. 1991 Laboratory experiments on the tripolar vortex in a rotating fluid. *J. Fluid Mech.* **225**, 301–331.

HIDE, R. 1953 Some experiments on thermal convection in a rotating liquid. PhD thesis, Cambridge University.

HIDE, R. 1957 An experimental study of thermal convection in a rotating fluid. *Phil. Trans. Royal Soc. London A* **250**, 441–478.

HIDE, R. 1967 Theory of axisymmetric thermal convection in a rotating fluid annulus. *Phys. Fluids* **10**, 56–68.

HIDE, R. 1977 Experiments with rotating fluids. *Quart. J. R. Met. Soc.* **103**, 1–28.

HOLMBOE, J. 1966 On the instability of stratified shear flow. *Geofysiske Publikasjoner* **26**, 1–27.

HOSKINS, B. J., MCINTYRE, M. E. & ROBERTSON, A. W. 1985 On the use and significance of isentropic potential vorticity maps. *Quart. J. Roy. Met. Soc.* **111**, 877–946.

HOWARD, L. N. 1961 Note on a paper of John W. Miles. *J. Fluid Mech.* **10**, 509–512.

HOWARD, L. N. & GUPTA, A. S. 1962 On the hydrodynamic and hydromagnetic stability of swirling flows. *J. Fluid Mech.* **14**, 463–476.

HOWARD, L. N. & MASLOWE, S. A. 1973 Stability of stratified shear flows. *Boundary-Layer Meteorology* **4**, 511–523.

HUANG, M. J. 2005 The physical mechanism of symmetric vortex merger: A new viewpoint. *Phys. Fluids* **17**, 074105.

ITANO, T. 2004 Stability of an elliptic flow with a horizontal axis under stable stratification. *Phys. Fluid* **16**, 1164–1167.

JACQUIN, L., FABRE, D., SIPP, D., THEOFILIS, V. & VOLLMERS, H. 2003 Instability and unsteadiness of wake vortices. *Aero. Sci. Tech.* **7**, 577593.

JOLY, L., FONTANE, J. & CHASSAING, P. 2005 The Rayleigh-Taylor instability of two-dimensional high-density vortices. *J. Fluid Mech.* **537**, 415–431.

JOSSERAND, C. & ROSSI, M. 2007 The merging of two co-rotating vortices: a numerical study. *Eur. J. Mech. B/Fluids* **26**, 779–794.

VON KÁRMÁN, T. 1954 *Aerodynamics*. McGraw-Hill, New York.

KELVIN, L. 1867 On vortex atoms. *Phil. Mag.* **34**, 15–24.

KELVIN, L. 1880 Vibrations of a columnar vortex. *Phil. Mag.* **10**, 155–168.

KERSWELL, R. R. 2002 Elliptical instability. *Ann. Rev. Fluid Mechanics* **34**, 83–113.

KHORRAMI, M. R., MALIK, M. R. & ASH, R. L. 1989 Application of spectral collocation techniques to the stability of swirling flows. *J. Comp. Physics* **81**, 206–229.

KIMURA, Y. & HERRING, J. R. 2001 Gradient enhancement and filament ejection for a non-uniform elliptic vortex in two-dimensional turbulence. *J. Fluid Mech.* **439**, 43–56.

KOCHAR, G. T. & JAIN, R. K. 1979 Note on Howard's semicircle theorem. *J. Fluid Mech.* **91**, 489–491.

KURZWEG, U. H. 1969 A criteria for the stability of heterogenous swirling flows. *Z. Angew. Math. Phys.* **20**, 141–143.

LANDAHL, M. T. 1962 On the stability of a laminar incompressible boundary layer over a flexible surface. *J. Fluid Mech.* **13**, 609–632.

LE DIZÈS, S. 2000 Non-axisymmetric vortices in two-dimensional flows. *J. Fluid Mech.* **406**, 175–198.

LE DIZÈS, S. 2008 Inviscid waves on a Lamb-Oseen vortex in a rotating stratified fluid: consequences for the elliptic instability. *J. Fluid Mech.* **597**, 283–303.

LE DIZÈS, S. & BILLANT, P. 2009 Radiative instability in stratified vortices. *Phys. Fluids* **21**, 096602 (1–8).

LE DIZÈS, S. & VERGA, A. 2002 Viscous interactions of two co-rotating vortices before merging. *J. Fluid Mech.* **467**, 389–410.

LEES, L. 1958 Note on the stabilizing effect of centrifugal forces on the laminar boundary layer over convex surfaces. *J. Aero. Sci.* **25**, 407–408.

LEIBOVICH, S. 1969 Stability of density stratified rotating flows. *AIAA J.* **7**, 177–178.

LIN, C. C. 1955 *The Theory of Hydrodynamic Stability*. Cambridge University Press.

LINDEN, P. F. 1973 The interaction of a vortex ring with a sharp density interface: a model for turbulent entrainment. *J. Fluid Mech.* **60**, 467–480.

LOON, H. V. 1979 The association between latitudinal temperature gradient and eddy transport. Part i: Transport of sensible heat in winter. *Mon. Wea. Rev.* **107**, 525–534.

MCWILLIAMS, J. C., GRAVES, L. P. & MONTGOMERY, M. T. 2003 A formal theory for vortex Rossby waves and vortex evolution. *Geophys. Astro. Fluid Dyn.* **97**, 275–309.

MELANDER, M. V., ZABUSKY, N. J. & MCWILLIAMS, J. C. 1988 Symmetric vortex merger in two dimensions: causes and conditions. *J. Fluid Mech.* **195**, 303–340.

MEUNIER, P., EHRENSTEIN, U., LEWEKE, T. & ROSSI, M. 2002 A merging criterion for two-dimensional co-rotating vortices. *Phys. Fluids* **14**, 2757–2766.

MEUNIER, P., LE DIZÈS, S. & LEWEKE, T. 2005 Physics of vortex merging. *C. R. Phys.* **6**, 431–450.

MIYAZAKI, T. & FUKUMOTO, Y. 1992 Three dimensional instability of strained vortices in a stably stratified fluid. *Phys. Fluids A* **4**, 2515–2522.

MOFFATT, H. K. & KAMKAR, H. 1983 The time-scale associated with flux expulsion. In *Stellar and Planetary Magnetism* (ed. A. M. Soward), pp. 91–97. Gordon and Breach.

MOORE, D. W. & SAFFMAN, P. G. 1971 Structure of a line vortex in an imposed strain. In *Proc. Symp. Aircraft Wave Turbulence, Seattle, Washington*, pp. 339–354.

MOORE, D. W. & SAFFMAN, P. G. 1973 Axial flow in laminar trailing vortices. *Proc. R. Soc. Lond. A.* **333**, 491–508.

MOORE, D. W. & SAFFMAN, P. G. 1975 The instability of a straight vortex filament in a strain field. *Proc. R. Soc. Lond. A* **346**, 413–425.

NADIGA, B. T. & AURNOU, J. M. 2008 A tabletop demonstration of Atmospheric Dynamics: Baroclinic Instability. *Oceanography* **21**, 196–201.

NAPPO, C. J. 2002 *An Introduction to Atmospheric Gravity Waves*. Academic Press.

NARAIN, J. P. & UBEROI, M. S. 1974 The motion of a trailing vortex-wake in a stratified medium. *Atmospheric Environment* **8**, 459–473.

NAYFEH, A. H. 1985 *Problems in Perturbation*. Wiley-Interscience.

NEILSEN, A. H., HE, X., RASMUSSEN, J. J. & BOHR, T. 1996 Vortex merging and spectral cascade in two-dimensional flows. *Phys. Fluids* **8**, 2263–2265.

OSTROVSKII, L. A., RYBAK, S. A. & TSIMRING, L. S. 1986 Negative energy waves in hydrodynamics. *Sov. Phys. Usp.* **29**, 1040–1052.

OVERMAN, E. D. & ZABUSKY, N. J. 1982 Evolution and merger of isolated vortex structures. *Phys. Fluids* **25**, 1297–1305.

PEDLOSKY, J. 1987 *Geophysical Fluid Dynamics*. Springer-Verlag, New York.

PIERREHUMBERT, R. T. 1986 Universal short-wave instability of two-dimensional eddies in an inviscid fluid. *Phys. Rev. Lett.* **57**, 2157–2160.

PRESS, W. H., TEUKOLSKY, S. A., VETTERLING, W. T. & FLANNERY, B. P. 1992 *Numerical Recipes in C: The art of Scientific Computing*. Cambridge Univ. Press.

RAYLEIGH, J. W. S. 1894 *The Theory of Sound, Vol. 2*. Macmillan (Dover, NY, 1945, reprint of 2nd edn).

REINAUD, J., JOLY, L. & CHASSAING, P. 2000 The baroclinic secondary instability of the two-dimensional shear layer. *Phys. Fluid* **12**, 2489–2505.

RHINES, P. B. & YOUNG, W. R. 1983 How rapidly is a passive scalar mixed within closed streamlines? *J. Fluid Mech.* **133**, 133–145.

RIND, D. 1998 Latitudinal temperature gradients and climate change. *J. Geophysical Res.* **103**, 5943–5971.

ROMANOVA, N. N. 2008 Resonant interaction of waves of continuous and discrete spectra in the simplest model of a stratified shear flow. *Izvestiya, Atmospheric and Oceanic Physics* **44**, 53–63.

ROMANOVA, N. N. & SHRIRA, V. I. 1988 Explosive generation of surface waves by wind. *Izv. Atmos. Ocean. Phys.* **24**, 528–535.

ROSSI, M. 2000 Of vortices and vortical layers: An overview. In *Vortex Structure and Dynamics* (ed. A. Maurel & P. Petitjeans), *Lecture Notes in Physics*, vol. 555, pp. 40–123. Springer.

ROSSOW, V. J. 1977 Convective merging of vortex cores in lift-generated wakes. *J. Aicraft* **14**, 283–290.

ROY, A. & SUBRAMANIAN, G. 2009 Linearized oscillations of an inviscid vortex column: the non-Kelvin modes. *preprint* .

SAFFMAN, P. G. 1972 The motion of a vortex-pair in a stratified atmosphere. *SIAM* **L1**, 107–119.

SAFFMAN, P. G. 1992 *Vortex Dynamics*. Cambridge University Press.

SAFFMAN, P. G. & SZETO, R. 1980 Equilibrium shapes of a pair of equal uniform vortices. *Phys. Fluids* **23**, 2339–2342.

SARPKAYA, T. 1983 Trailing vortices in homogeneous and density-stratified media. *J. Fluid Mech.* **136**, 85–109.

SAUNDERS, P. M. 1973 The instability of a baroclinic vortex. *J. Physical Oceanography* **3**, 61–65.

SAZONOV, I. A. 1989 Interaction of continuous-spectrum waves with each other and with discrete-spectrum waves. *Fluid Dynamics* **24**, 586–592.

SCHECTER, D. A., DUBIN, D. H. E., CASS, A. C., DRISCOLL, C. F., LANSKY, I. M. & O'NEIL, T. M. 2000 Inviscid damping of asymmetries on a two-dimensional vortex. *Phys. Fluids* **12**, 2397–2412.

SCHECTER, D. A. & MONTGOMERY, M. T. 2003 On the symmetrization rate of an intense geophysical vortex. *Dyn. Atm. Oceans* **37**, 55–88.

SCHECTER, D. A. & MONTGOMERY, M. T. 2004 Damping and pumping of a vortex rossby wave in a monotonic cyclone: Critical layer stirring versus inertia-buoyancy wave emission. *Phys. Fluids* **16**, 1334.

SCHMID, P. J. & HENNINGSON, D. S. 2001 *Stability and Transition in Shear Flows*. Springer.

SCORER, R. S. & DAVENPORT, L. J. 1970 Contrails and aircraft downwash. *J. Fluid Mech.* **43**, 451–464.

SEN, S., SHARMA, P. K. & STORER, R. G. 1998 Role of flow shear and flow curvature in the supression of low-frequency fluctuations. *Phys. Plasmas* **5**, 2637–2641.

SEN, S. & STORER, R. G. 1997 Suppression of Rayleigh-Taylor instability by flow curvature. *Phys. Plasmas* **4**, 3731–3733.

SHRIRA, V. I. & SAZONOV, I. A. 2001 Quasi-modes in boundary-layer-type-flows. Part 1. Inviscid two-dimensional spatially harmonic perturbations. *J. Fluid Mech.* **446**, 133–171.

SIPP, D., FABRE, D., MICHELIN, S. & JACQUIN, L. 2005 Stability of a vortex with a heavy core. *J. Fluid Mech.* **526**, 67–76.

SIPP, D. & JACQUIN, L. 2003 Widnall instabilities in vortex pairs. *Phys. Fluids* **15**, 1861–1874.

SPALART, P. R. 1996 On the motion of laminar wing wakes in a stratified fluid. *J. Fluid Mech.* **327**, 139–160.

TAYLOR, G. I. 1931 Effect of variation in density on the stability of superposed streams of fluid. *Proc. R. Soc. Lond. A.* **132**, 499–523.

TSAI, C. Y. & WIDNALL, S. E. 1976 The stability of short waves on a straight vortex filament in a weak externally imposed strain field. *J. Fluid Mech.* **73**, 721–733.

TSANG, G. 1971 Laboratory study of line thermals. *Atmospheric Environment* **5**, 445–471.

TURNER, J. S. 1973 *Buoyancy Effects in Fluids*. Cambridge University Press.

TURNER, M. R. & GILBERT, A. D. 2007 Linear and nonlinear decay of cat's eyes in two-dimensional vortices, and the link to landau poles. *J. Fluid Mech.* **593**, 255–279.

UBEROI, M. S., CHOW, C. Y. & NARAIN, J. P. 1972 Stability of coaxial rotating jet and vortex of different densities. *Phys. Fluid* **15**, 1718–1727.

VALLIS, G. K. 2006 *Atmospheric and Oceanic Fluid Dynamics*. Cambridge University Press.

VANNESTE, J. 1996 Rossby wave interaction in a shear flow with critical levels. *J. Fluid Mech.* **323**, 317–338.

VILLERMAUX, E. 1998 On the role of viscosity in shear instabilities. *Phys. Fluid* **10**, 368–373.

VORONOVICH, A. G. & RYBAK, S. A. 1978 Explosive instability of stratified currents. *Dokl. Acad. Sci. USSR* **239**, 1457–1460.

VORONOVICH, V. V., PELINOVSKY, D. E. & SHRIRA, V. I. 1998*a* On the internal waves shear flow resonance in shallow water. *J. Fluid Mech.* **354**, 209–237.

VORONOVICH, V. V., SHRIRA, V. I. & STEPANYANTS, Y. A. 1998*b* Two-dimensional modes for nonlinear vorticity waves in shear flows. *Stud. Appl. Math.* **100**, 1–32.

WALEFFE, F. 1990 On the three-dimensional instability of strained vortices. *Phys. Fluids* **2**, 76–80.

WHITHAM, G. B. 1974 *Linear and nonlinear waves*. Wiley, NY.

WINANT, C. D. & BROWAND, F. K. 1974 Vortex pairing: the mechanics of turbulent mixing-layer growth at moderate reynolds number. *J. Fluid Mech.* **63**, 237–255.

YIH, C. S. 1961 Dual role of viscosity in the instability of revolving fluids of variable density. *Phys. Fluids* **4**, 806–811.

YIH, C. S. 1973 *Dynamics of inhomogeneous fluids*. Cambridge University Press.